Dissertation zur Erlangung des Doktorgrades

der Fakultät für Chemie und Pharmazie

der Ludwig-Maximilians-Universität München

Functional Covalent Organic Frameworks for Redox- and Adsorption Processes

Katharina Iulscha Maria Muggli

aus

München, Deutschland

2024

Erklärung

Diese Dissertation wurde im Sinne von § 7 der Promotionsordnung vom 28. November 2011 von Herrn Prof. Dr. Thomas Bein betreut.

Eidesstattliche Versicherung

Diese Dissertation wurde eigenständig und ohne unerlaubte Hilfe erarbeitet.

München, 02.04.2024

……

Katharina Muggli

Dissertation eingereicht am 03.04.2024

1. Gutachter: Prof. Dr. Thomas Bein

2. Gutachter: Prof. Dr. Konstantin Karaghiosoff

Mündliche Prüfung am 10.05.2024

Abstract

Ever since their development in the early 2000s, covalent organic frameworks (COFs) have been established as a new class of porous materials. As the name already indicates, COFs are fully organic materials consisting of light-weight elements, such as carbon, hydrogen, nitrogen, oxygen, boron, or sulfur. Characteristics of COFs are their high crystallinity with a clearly and regularly ordered structure and their high porosity, leading to large surface areas. Covalent organic frameworks are formed from secondary building units (SBUs) in reversible condensation reactions. The reversibility of these reaction plays a crucial role for the successful formation of these organic polymers, as it allows for error correction and self-healing processes throughout the synthesis. Being constructed from small yet highly functional and versatile building blocks, COFs can assume various geometries, dependent on the choice of SBU. Given the virtually unlimited number of these building units through vast combinations of molecular subunits, there is a sheer infinite number of possible COF structures, following predefined schematic diagrams. It is, for example, possible to determine dimensionality (2D or 3D) of the materials by choosing a suitable building block. Furthermore, the linkage types in the framework structure can be selected and altered by equipping the bare building unit with appropriate functional groups. With COFs exhibiting a highly porous structure, it is also possible to engineer the material's pores in terms of size, side chains or wetting properties. This adjustability and tunability of COF building blocks, and in consequence COFs, has been successfully used for designing materials exhibiting desired properties, such as optical, optoelectronic, electric, redox, catalytic, adsorption, or wetting properties.

In the course of this thesis, new covalent organic frameworks were synthesized and characterized for their application as adsorbents and redox active materials.

Firstly, larger thienoisoindigo (TII) building blocks were further developed extending the by then already known smaller thienoisoindigo core building unit. Given that structural planarity promotes π-conjugation, which is important for high-performing (opto-)electronic properties, two thienoisoindigo building blocks exhibiting a high degree of planarity, due to little steric hinderance between the core and the side moieties, were further developed and characterized. In order to also tune their redox behavior, the electron-deficient thienoisoindigo core was extended by an electron-rich moiety (thienothiophene (tt) or

naphthalene (n)) on both sides, yielding a donor-acceptor-donor structure. This electronic configuration of the building block allows for intramolecular charge transfer (ICT) between donor and acceptor moieties, causing a strong redshift of the absorption onset in the electromagnetic spectrum. Incorporating these specifically tailored building blocks into covalent organic frameworks by combining them with the well-known pyrene (Py) as the tetragonal node yields dark-green and low-band gap powders with strong vis-NIR absorption. The successful growth of both thienoisoindigo COFs, Py-ttTII and Py-nTII, as oriented thin films on different substrates furthermore allowed for the investigation of their electrochromic behavior. The highly oriented structure of the thin films promotes good electronic connectivity of the COF layers and the free diffusion of counter ions in and out of the pores, when oxidizing and reducing the COF in an electrochromism experiment, leading to a strong and fully reversible electrochromic behavior with very fast switching speeds and high coloration efficiencies.

The fact that Py-ttTII exhibited strong optical and redox active properties, whilst maintaining its high crystallinity, motivated us to use this building block to develop further ttTII-based COFs by exchanging the pyrene node with another tetradentate building block. To further support the excellent properties of the ttTII building block, a new carbazole-based building block was developed. Carbazole is an established building unit in organic electronics, due to its electron-rich character, its aromaticity and hence planarity, which is beneficial for opto-electronic and redox applications of COFs. The new linker exhibits a rectangular structure and is synthesized by fusing two carbazole moieties *via* a phenyl ring and extending the core with an aniline moiety on each of its four sides, yielding the highly crystalline Cz-ttTII COF when combined with ttTII. In addition, another ttTII-based COF with a hexagonal geometry was developed to demonstrate the versatility of the ttTII building block. The COFs showed a broad vis-NIR absorption in the electromagnetic spectrum. Furthermore, both materials were successfully grown as oriented thin films and exhibited good vertical electrical conductivities taking advantage of the oriented stacking of the COF layers and the consequent good electronic connectivity. The following electrochromic experiments demonstrated a good performance with strong absorption changes, fast switching speeds and a high cycle stability, also emphasizing the versatility and high suitability of the ttTII building block when used in different COF geometries.

Targeted design for specific application purposes is an overall major goal when developing new COFs. As shown in the above projects, properties of a materials are highly dependent on the choice of building blocks and can therefore be altered by adjusting the chosen SBUs. In this context, pore engineering is an important principle for achieving desired material properties. Here, the incorporation of side chains or molecular moieties can enhance the material's performance in different applicational fields. To build on this principle and by combining it with our prior research, the newly developed carbazole building block was linked with two small linear building blocks: terephthalaldehyde and dimethoxy terephthalaldehyde, yielding two structurally highly similar COFs. When investigating the adsorption features of a material, adjusting the wetting properties for the targeted adsorbate is of utter importance. The incorporation of polar methoxy groups into the otherwise highly water repellent COF pores allows for deliberate pore surface engineering. The adjustability of COF wetting properties was investigated in water and dye adsorption experiments, showing an overall improved adsorption performance and adsorption efficiency for the surface-modified COF. Dye adsorption cycling experiments confirmed a good reusability of the COF powders. Furthermore, adsorption kinetic experiments emphasized the importance of adsorbent-adsorbate interactions for achieving a good adsorption performance.

Table of Contents

1. Introduction

Porous materials have been an integral part of human life for centuries. We use these materials on a daily basis – often without noticing – when filtering tea or coffee, vacuum cleaning or doing the laundry. Even in ancient times the porosity of clay pots and charcoal was used to purify water and air, with charcoal also being used as a reducing agent for steel production in the Middle Ages. Then, in 1756, the Swedish mineralogist Baron Axel Frederick von Cronstedt for the first time described zeolites,[1] which have ever since become crucial parts in modern industry and which are still widely researched for various applicational fields such as catalysis, adsorption, and molecular storage and separation.[2-4]

With a growing need for porous materials for highly specific applications, the research has advanced, trying to find methods for more directed synthetic strategies. In this context, the concept of reticular chemistry was developed at the end of the previous millennium, paving the way to the generation of novel material classes within the realm of porous materials.

1.1 Reticular Chemistry and the Origins of COFs

Up until the end of the 20th century, the chemistry of solids was characterized by a lack of control over the characteristics of the product from a traditional synthetic reaction. Here, the generation of new materials predominantly was serendipitous and often the result of 'shake and bake', 'mix and wait', and 'heat and beat' procedures.[5] These methods did indeed generate a vast number of novel compounds, however, exercising control was merely possible in zero dimensions, such as nanoparticles, and later in one dimension as shown by polymer chemists.[6] Achieving control over the structure of solids in two and three dimensions was for a long time deemed highly challenging or impossible or – positively spoken – a challenge of the future, and was widely referred to as the *crystallization problem*.[7] An approach for the realization of materials featuring deterministic control is represented by surfactant templating, i.e. the generation of mesoporous materials with structural control via surfactant aggregates. Here, the formation of ordered mesoporous materials using micelle templates and sol-gel processing was reported.[8, 9] Nevertheless, the lack of structural determinability in the synthesis of new solid materials, which is needed for generating structures with specific functions, remained a major challenge.[10, 11]

That was the scene when *reticular chemistry* came into play, a principle introduced to tackle the challenge of structural determinability with a different conceptual approach necessary for the predetermination of a material's characteristics and features. In its definition, reticular chemistry is about the 'geometry that atoms and molecules adopt in space',[12] and thus already emphasizes the significance of choosing appropriate building units for the reticulation process. To avoid the degradation of the starting material, judiciously designed rigid and stable secondary building units (SBUs) are selected and then linked *via* strong bonds to form the desired network.[5, 13] Following this principle, Yaghi and Li reported the synthesis of the first MOF (metal organic framework) in 1995, exhibiting a crystalline and open framework with an extended channel system, based on single metal ions and organic building units.[14]
This first coordination network was soon further developed by incorporating chelating units into the network, providing increased stability.[15] In 1998, Yaghi reported the first MOF based on a metal cluster that further increased the network's stability and which marked the beginning of MOFs as we know them nowadays.[16]
MOFs hence offer a great robustness (depending on structure and conditions), a highly crystalline structure with large pore sizes and a high surface area. The choice of the SBUs used for a given MOF also enables the directed tailoring, not only of its geometry/symmetry, but also of its properties. Here, for instance the capability of including guest molecules in the porous network can be designed according to the respective requirements.[17]

To demonstrate their versatility, Figure 1.1 exhibits 16 isoreticular metal organic frameworks (IRMOFs) that are based on the basic zinc acetate SBU and varying counterparts and exhibit a cubic topology with the space group *Fm*-3*m*. In case of MOFs 1-7, the linear (organic) linkers differ in their pending groups, altering the functionality, polarity, and reactivity of the respective material. For the syntheses of MOFs 8-16, linear linkers of increasing length were chosen, leading to a gain in pore size, however, also causing catenation in some cases, which describes the intergrowth of two or more identical frameworks and therefore a loss of pore volume.[17]

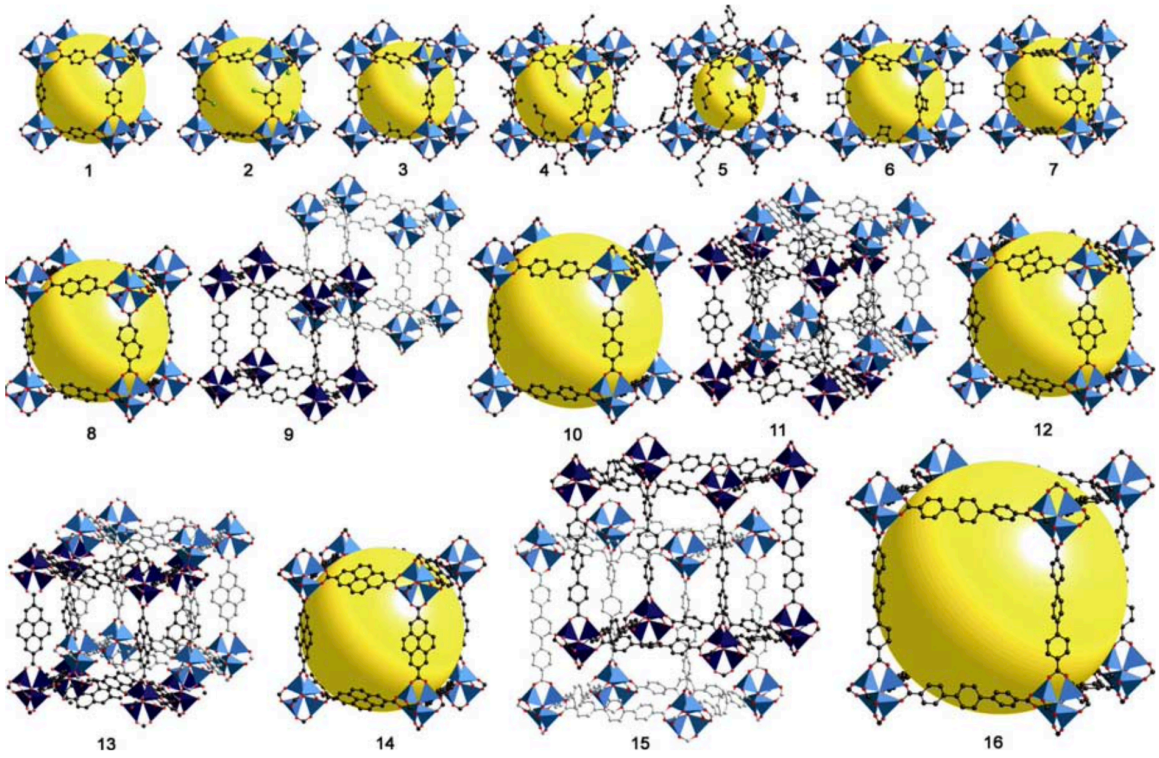

Figure 1.1. A series of 16 MOFs based on the zinc acetate SBU connected with varying counterparts (linear linkers). The MOFs all exhibit a cubic topology (space group *Fm*-3*m*). For the formation of MOFs 1-7, different pending groups were used on the linear linkers, altering the materials' functionalities. In MOFs 8-16, the length of the linear linkers was increased, leading to larger pores, whilst also causing catenation in some cases. [17-19] Copyright (2004) Elsevier.

This series exemplarily shows the immense diversity that can be achieved using the modular concept of MOFs. Alteration of the metal clusters or the organic linkers provides access to a plethora of new porous materials with predetermined structures and tailored properties.

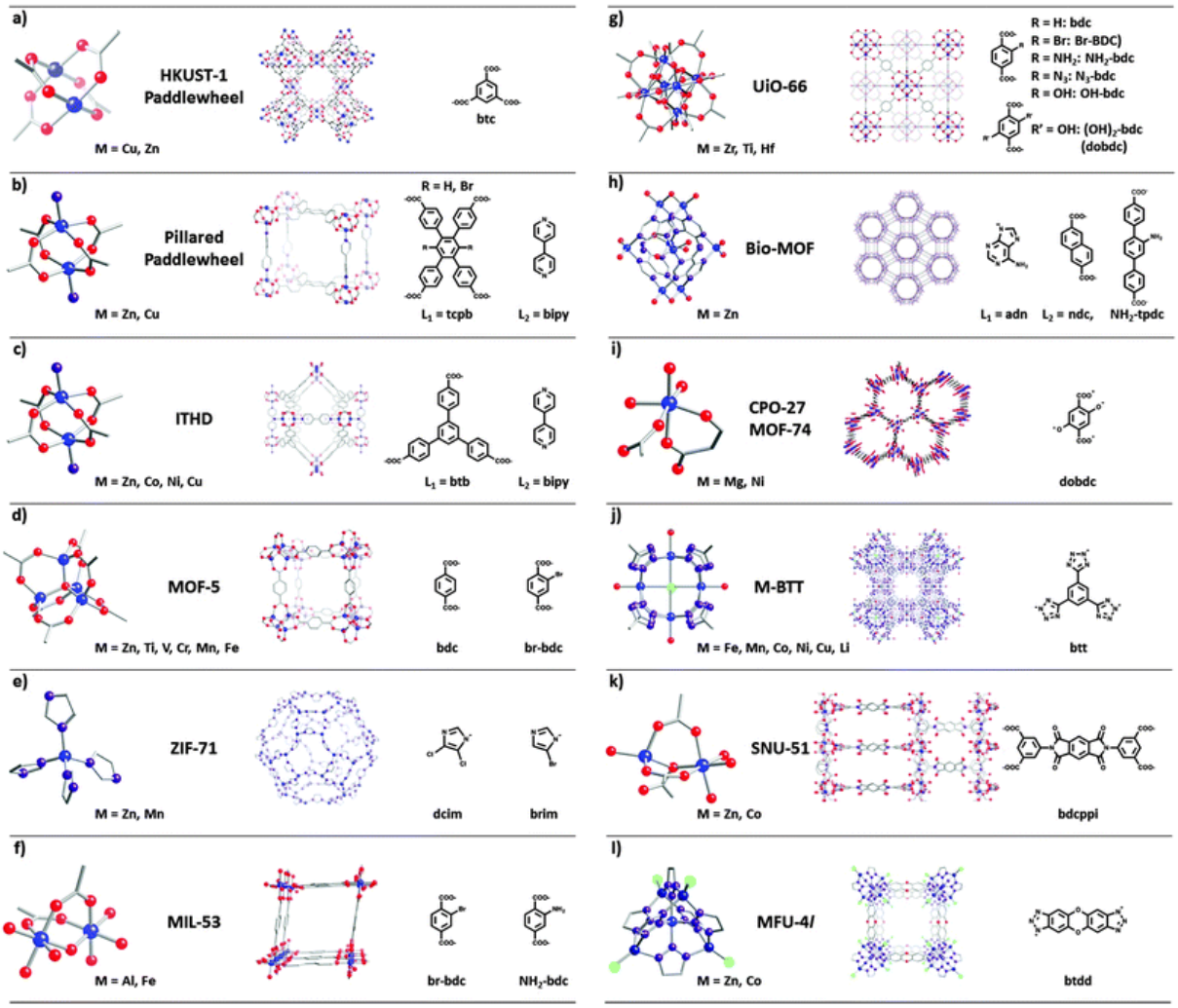

Figure 1.2. Selection of different topologies of metal organic frameworks (middle), based on the respective metal clusters (left) and organic linkers (right).[20] Reproduced with permission from the Royal Society of Chemistry.

Here, Figure 1.2 illustrates a selection of metal clusters and organic linkers used to form a variety of lattice structures of MOFs. This structural versatility has made metal organic frameworks highly interesting materials for many chemical, biochemical and physical applications, such as catalysis,[21] drug delivery,[22] or sensing.[23] Furthermore, MOFs are applied in water harvesting from desert air[24, 25] or as photodetectors in the UV-NIR region.[26]

In 2005, Yaghi and coworkers introduced the first covalent organic frameworks (COFs), COF-1 and COF-5, the first representatives of a new class of crystalline porous polymers, that is entirely constructed from organic building blocks, which are connected *via* strong covalent bonds.[27]

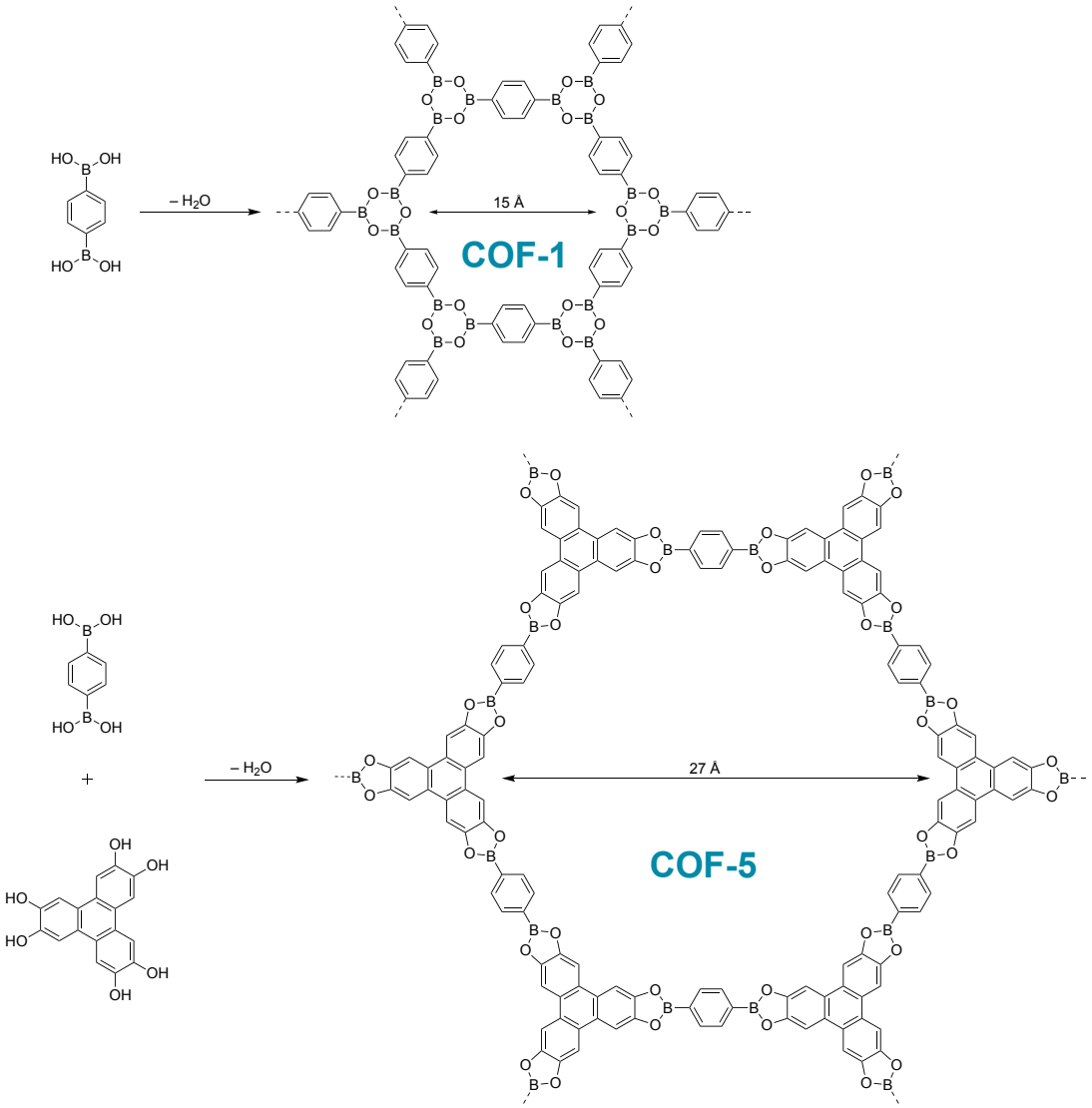

Scheme 1.1. Synthesis route of COF-1 and COF-5 as published by Yaghi and coworkers. COF-1 is generated in a condensation reaction of diboronic acid, whilst COF-5 is synthesised by co-condensing diboronic acid and hexahydroxy triphenylene. Both frameworks exhibit boronic ester linkages.[27]

Scheme 1.1 depicts the respective synthesis routes for COF-1 and COF-5. Here, the former is derived in a condensation reaction of diboronic acid, whilst the latter is generated by condensing diboronic acid and hexahydroxy triphenylene. Both COFs are linked *via* boronic ester linkages. With this research, Omar Yaghi and his coworkers opened the door to an entirely new research field that has been strongly expanding ever since.

Generally, covalent organic frameworks are a group of materials made from light-weight elements (e.g. C, N, O, B, S, H) that exhibits high crystallinity, permanent porosity, large surface areas, strong covalent bonding, high thermal stability and chemical stability depending on the

linkage chemistry chosen.[13] A vital aspect for the formation of crystalline COFs is the (slight) reversibility of the synthesis reaction, which allows for a self-healing process needed to correct defects/disorder occurring throughout the synthesis and for finally creating crystalline frameworks. This error correction mechanism is inalienable for the generation of highly crystalline materials, as purification of the final COFs is not possible due to their insolubility. Hence, the significance of finding appropriate synthesis conditions that promote the reversibility of the COF formation reactions, and thus the self-healing ability, must be stressed.[28]

Another great advantage of covalent organic frameworks is the possibility to predesign their lattice structures according to the choice of rigid organic building blocks employed in the synthesis.

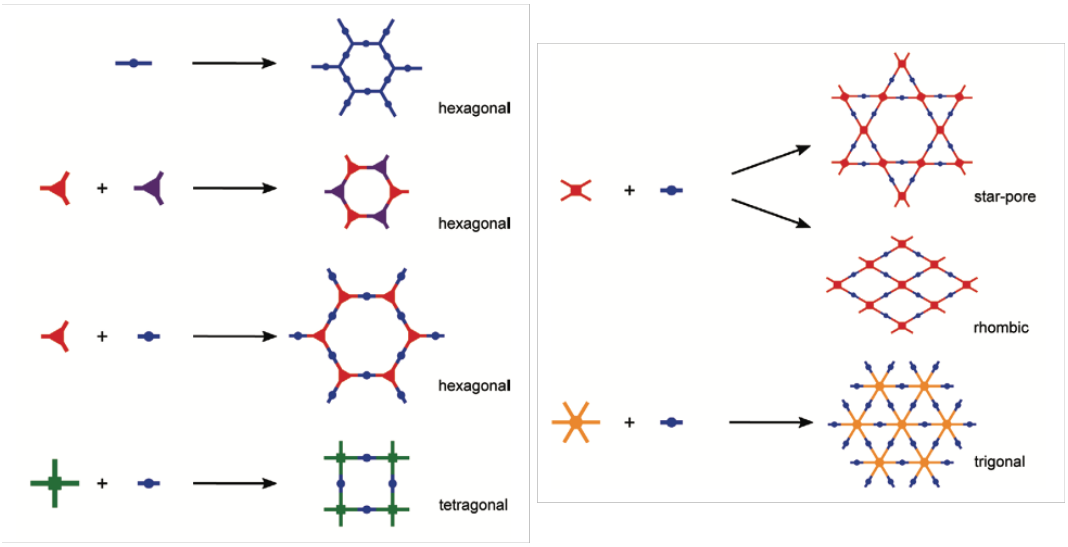

Figure 1.3. Illustration of different 2D COF topologies, realized according to the choice of molecular building blocks.[29] Copyright (2018) Maria Lohse and Thomas Bein. Publisher: WILEY-VCH Verlag GmbH & Co.

Dependent on the building block geometries chosen for the COF synthesis, a multitude of different topologies can be realized, as exemplified in Figure 1.3. Here, the respective combinations of linear, trigonal, tetragonal, or other multidentate building blocks lead to trigonal, tetragonal, hexagonal, or Kagome (star-shaped) structures amongst others.

All structures depicted in Figure 1.3 are examples of two-dimensional (2D) COFs. In 2D COFs, the individual COF sheets exhibit covalent linkages in the crystallographic *a*-*b* plane, but are stacked *via* π-interactions along the *c*-axis. As a consequence of this non-covalent stacking,

separation distances of adjacent layers are fairly short, usually measuring merely several Angstroms and thus can promote electronic connectivity along the *c*-axis.

In 2007 the young but growing group of covalent organic frameworks was expanded by the first three-dimensional COFs, also introduced by Yaghi and coworkers.[30]

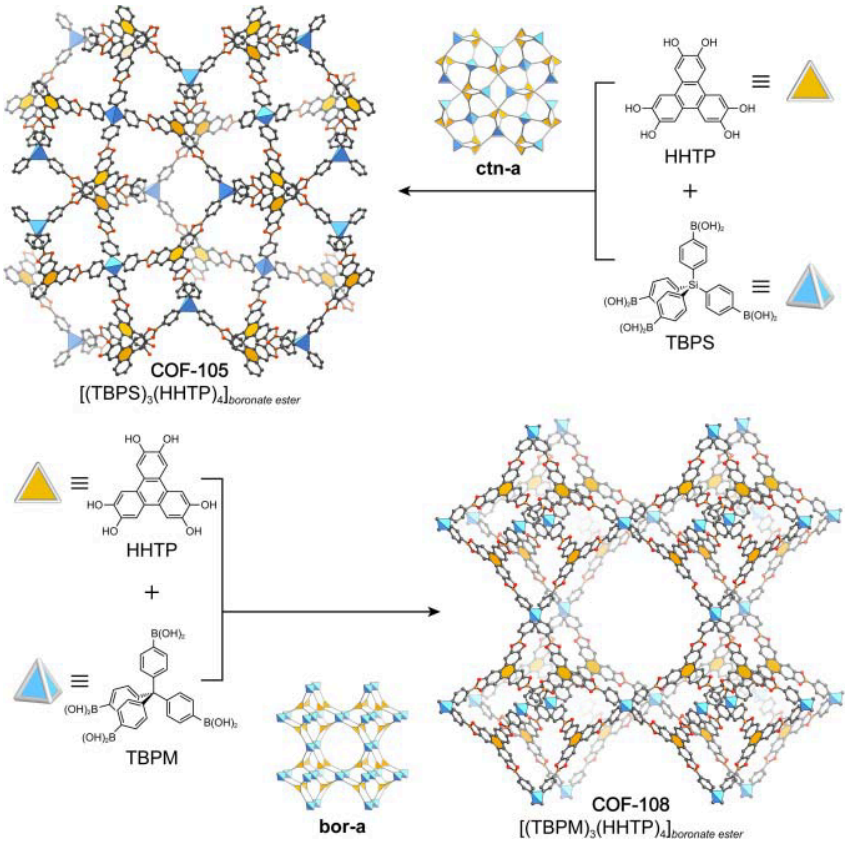

Figure 1.4. Synthesis scheme of COF-105 and COF-108. COF-105 was formed in a condensation reaction of the tetrahedral tetra(4-dihydroxyborylphenyl)silane with the triangular 2,3,6,7,10,11-hexahydroxytriphenylene. In the case of COF-108, the tetrahedral tetra(4-dihydroxyborylphenyl)methane was co-condensed with 2,3,6,7,10,11-hexahydroxy-triphenylene.[28] Copyright (2019) Omar M. Yaghi, Markus J. Kalmutzki and Christian S. Diercks. Publisher: WILEY-VCH Verlag GmbH & Co.

Figure 1.4 depicts the synthesis schemes for COF-105 and COF-108, with the respective building blocks being covalently connected in all three dimensions. Here, COF-105 is formed in a condensation reaction of the tetrahedral tetra(4-dihydroxyborylphenyl)silane with the triangular 2,3,6,7,10,11-hexahydroxytriphenylene and COF-108 in an analogous reaction of tetra(4-dihydroxyborylphenyl)methane and 2,3,6,7,10,11-hexahydroxytriphenylene. Both materials exhibit high thermal stabilities exceeding 450 °C. Ever since being reported in the

literature for the first time, research on 3D COFs has further developed. Here, 3D COFs have been, amongst others, applied for gas storage,[31, 32] gas separation,[33, 34] catalysis,[35, 36] or in a perovskite solar cell.[37]

Nearly 20 years after their first mention, covalent organic frameworks have been studied and tested for a multitude of applications in diverse research areas, such as catalysis,[38] sensing,[39] energy storage[40], biomedical applications[41], or adsorption (see Chapter 1.3). Their adjustability and tunability allows for the targeted design also in optoelectronic applications, such as electrochromic materials. Here, electrochromism describes the phenomenon of a color change as the response to an electrically induced stimulus. Electrochromic materials have, amongst others, been used for stimuli-responsive coatings,[42] and electrochromic displays or smart windows[43-45] and are envisioned to find application in optical information processing, and thermal control purposes. The first electrochromic COFs, however, only showed moderate coloration efficiencies and switching speeds.[46, 47] With the work described in this thesis, we succeeded in expanding the scope of electrochromic covalent organic frameworks, whilst also enhancing the materials' performance.

1.2 Linkages in Covalent Organic Frameworks

Ever since their first report in the literature, the field of COFs has been developing and expanding rapidly and a large number of COFs have been synthesized. A major difference between these frameworks is the linkage type used for fusing the individual building blocks. Scheme 1.2 provides a non-exhaustive list of bonding types of two-dimensional COFs.

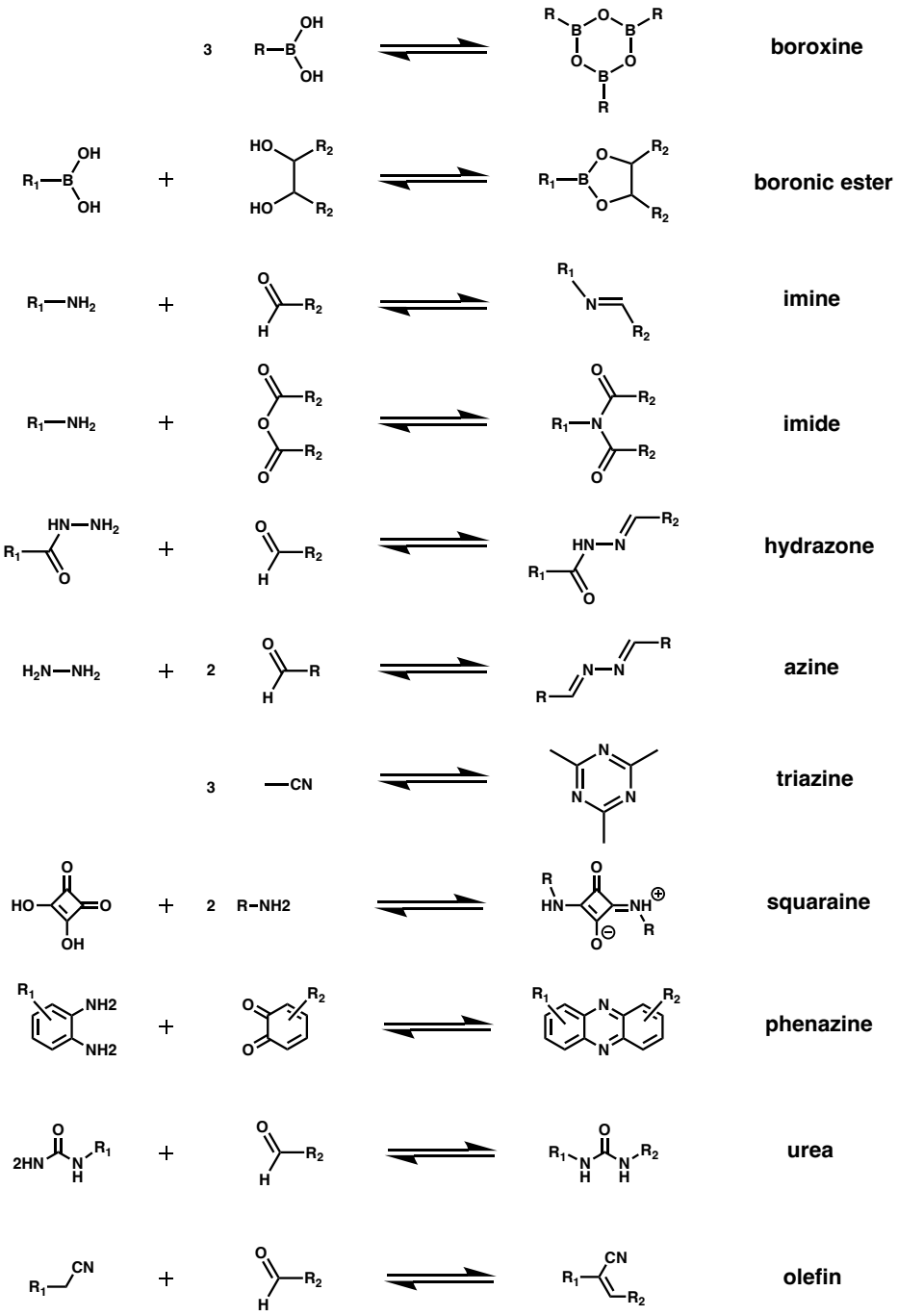

Scheme 1.2. Selection of common linkage types of two-dimensional covalent organic frameworks formed in condensation reactions.

Here, the SBUs must be equipped with the appropriate functional groups required for forming the respective COF linkage. Again, it is vital to choose reaction conditions that allow for a (slightly) reversible linkage formation reaction, enabling the above-mentioned error correction mechanism.[28]

With the boronic ester linkages of the original COF-105 and COF-108, being prone to hydrolysis and decomposition when exposed to protic solvents, and therefore suffering from a lack of

stability,[48] more resistant COF linkages were investigated. In 2016 Zhang and co-workers hence reported spiroborate-linked COFs that exhibit a superior stability towards aqueous and basic conditions.[49] Triazine linkages also offer a superior stability to boron-containing bonds, but require harsh synthesis conditions and therefore only a limited range of rigid and thermally stable building blocks can be used for their formation. Acid-catalyzed Schiff-base reactions represent a method for reversible synthesis under milder conditions, thus expanding the choice of possible COF building blocks. In 2009, Yaghi and coworkers reported the synthesis of COF-300 using this method, successfully condensing tetrahedral tetra-(4-anilyl)methane with terephthalaldehyde to a three-dimensional and imine-linked framework.[50]

Due to an improved chemical stability coupled with the milder synthesis conditions, imine linkages have ever since been widely chosen for the formation of new COFs and were also used for the COFs described in this thesis.

Scheme 1.3 illustrates the proposed reaction mechanism for the acid-catalyzed formation of imine linkages in covalent organic frameworks, emphasizing the reversibility of every reaction step.

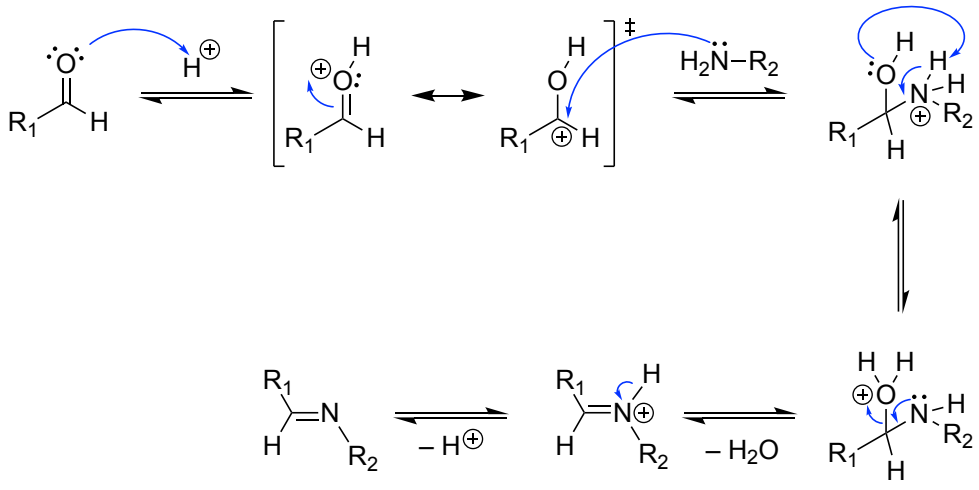

Scheme 1.3. Proposed reaction mechanism of an acid-catalyzed imine linkage formation.

In a first step, the aldehyde group is protonated, rendering the carbonyl carbon more electrophilic. In the following step, the free electron pair of the amine's nitrogen atom attacks the carbonyl carbon. After an internal proton transfer, H_2O is eliminated, yielding the positively charged iminium ion, which is deprotonated in the last step, affording the imine bond.

In addition to an enhanced chemical stability, imine bonds also offer an improved π-conjugation, facilitating charge transport and thus making them beneficial for electrical, electrochemical, or optoelectronic applications.

Ever since the development of imine-linked COF, further bonding types, such as hydrazone,[51-53] azine,[54-56] imide,[57-59] β-ketoenamine,[60-62] squaraine,[63-65] phenazine,[66-68] or urea[69-71] have been reported. Moreover, the generation of olefin-linked COFs was realized in 2016 *via* a Knoevenagel condensation, yielding fully π-conjugated frameworks with sp^2-hybridized carbons, exhibiting enhanced stability.[40, 72, 73]

1.3 Covalent Organic Frameworks as Adsorbents

In addition to the aforementioned applications, the field of adsorption and separation represents another intriguing research field for COFs. Here, the term adsorption describes the enrichment of atoms, ions, or molecules in a gaseous, liquid or dissolved solid state in the vicinity of an interface.[74]

Due to their highly porous structures and their large surface areas, COFs are well-suited materials for this kind of application. The possibility to design and adjust the frameworks according to predefined needs enables the targeting of specific molecules. Here, pore engineering, that is the design of the pore size, the pore shape, and the overall pore environment, plays a vital role. In this context, COFs for the (sometimes selective) adsorption of different gases, such as hydrogen,[75, 76] methane,[32, 77] ammonia,[78, 79] or carbon dioxide[80, 81] have been developed. Here, Yaghi and coworkers emphasize the importance of a large and accessible pore volume and the adequate pore size for a high gas uptake.[75] Furthermore, the choice of linkage can strongly influence the uptake capacity, as for example in the case of ammonia, where COFs with Lewis acidic boronate ester bonds exhibit a superior uptake of the Lewis basic ammonia.[79]

In addition to solely capturing and storing gas molecules, covalent organic frameworks have also been developed for the capture of water in arid conditions, referred to as *sorption-based atmospheric water harvesting (SAWH)*. With an estimated amount of 13000 trillion liters of water being available in the atmosphere at any given time, this method is expected to help address global water problems in the future.[82] Here, the performance of *SAWH* is strongly

dependent on the adsorbent, which not only needs an affinity to water to ensure a successful water uptake, but at the same time must enable its release at tolerable regeneration energies. Given these requirements, covalent organic frameworks have been developed as promising materials for *SAWH*, offering the possibility to specifically tailor the pore size and its hydrophilicity.[83-85] Recently, Sun et al. published a hexagonal COF incorporating hydrophilic and hydrophobic sites in its structure for fast capture and release of atmospheric water (Figure 1.5).[86]

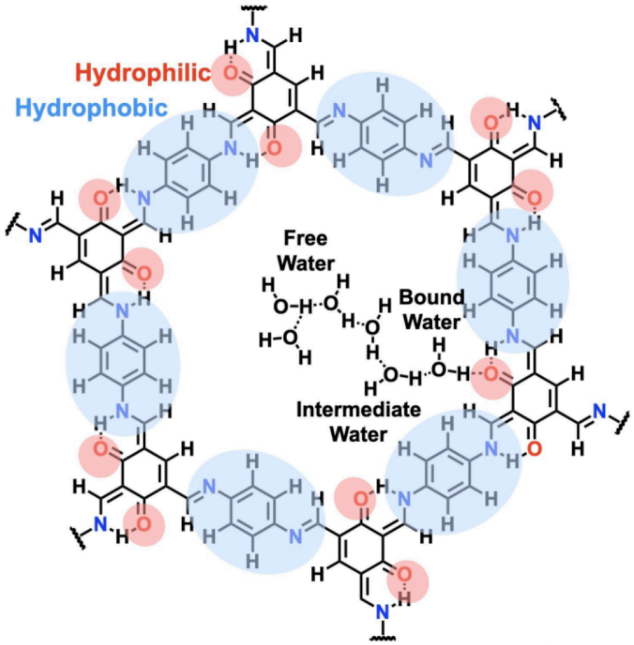

Figure 1.5. Schematic illustration of DHTA-Pa COF with alternatively arranged hydrophilic and hydrophobic sites for fast atmospheric water adsorption and desorption kinetics. Adapted with permission.[86] Copyright (2023) John Wiley and Sons.

Similarly, Chen et al. also reported a COF structure balancing hydrophilic and hydrophobic moieties, so that the formation of water clusters within the framework is promoted whilst maintaining a low regeneration energy.[87]

Generally, dependent on the target atom, ion, or molecule, the wetting properties of the materials are highly significant for a successful adsorption process. This is not only the case for *SAWH* applications, but also plays a crucial role for the separation of water and oily residues, which represents another intriguing applicational field for COFs being used as adsorbents. With ever-growing industrialization, global population and transport, environmental damage resulting from oil-contaminated water, e.g. due to oil spillages, has become a major threat. To tackle this problem, different approaches for the separation of oil and water have been investigated.[88-93] Again, the adjustability of COFs allows for the targeted

generation of materials with specifically designed wetting properties. Here, the full or partial fluorination of COF building blocks represents an option for controllable superhydrophobicity (Figure 1.6a).[94]

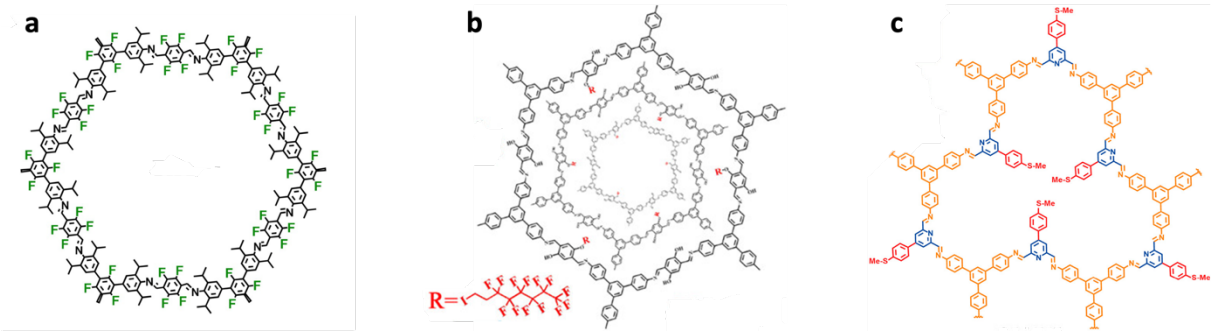

Figure 1.6. Selection of published COFs with superhydrophobic wetting properties based on targeted pore engineering strategies. **(a)** Fluorination of the COF building blocks. Adapted with permission.[94] Copyright (2022) John Wiley and Sons. **(b)** Post-synthetic pore modification with perfluorooctane side chain. Adapted with permission.[95] Copyright American Chemical Society. **(c)** Incorporation of thioanisole moieties into the pores. Adapted with permission.[96] Copyright American Chemical Society.

Another method for tuning the wetting properties of COFs is pore modification with side chains or small molecules. Han et al. report the successful formation of a hexagonal imine-linked COF that is post-synthetically modified by a perfluorooctane side chain, rendering it superhydrophobic (Figure 1.6b). Using the COF for treatments of different materials, such as foam, fabric or glass exhibits very good water repellency properties.[95] Trifluoromethyl side chains were used for the generation of a superhydrophobic COF by Chu et al., who successfully used the material for the separation of oil from water with high permeation fluxes.[97] Another reported method for tuning the wetting properties is the incorporation of thioanisole groups in an otherwise hydrophilic COF, rendering it hydrophobic and suitable for the removal of different oily pollutants from water (Figure 1.6c).[96] Moreover, Wang et al. published a stable COF-treated melamine sponge substrate that was post-synthetically modified by an octadecane-amine side chain to generate a superhydrophobic material, which was used for oil-water separation.[98]

The possibility to use covalent organic frameworks for separating oil from water has furthermore been elaborated for not only targeting oils and non-polar solvents, but also for the adsorption of organic molecules, such as organic dyes that are environmentally harmful. In this context, Xu et al. reported a hexagonal imine-linked and triazine-based COF with large pores that was used for the successful removal of rhodamine B dye from wastewater,[99] while Li et al. published a cage-based COF and used it for the removal of malachite green from wastewater with a high adsorption capacity.[100] In another approach, Anbazhagan et al. published a covalent organic polymer nanosheet on a melamine sponge substrate and used it for the selective adsorption of crystal violet and methylene blue, also taking advantage of the material's superhydrophobic nature.[101] In contrast, Qi and coworkers synthesized a hexagonal, imine-linked and anionic COF by introducing sulfonic acid groups into the structure, rendering the material hydrophilic. The group demonstrated the removal of cationic dyes from aqueous solution *via* electrostatic interactions.[102]

Overall, given the virtually unlimited number of possible designs, COFs for various adsorption and separation applications have been developed over the years. Considering the increasing complexity of industrial processes and global population and the resulting environmental impact, the need for sustainable materials for targeted applications such as those described above will rise, necessitating the investigation and further development of new functional materials.

1.4 Carbazole – a Versatile Building Block

With ever-advancing research on covalent organic frameworks, the list of possible building blocks has been growing enormously over the years. Originally, COFs were predominantly synthesized from commercially available and simple molecules with the main focus on the generation of highly crystalline frameworks. Gradually, the focus shifted from solely forming crystalline frameworks to specifically designing materials targeting pre-defined purposes. For this, the development of novel building blocks with customized features and properties plays a vital role in modern COF research.

Carbazole is a small heterocyclic, organic, and aromatic molecule with a planar tricyclic structure. Here, a pyrrole moiety is extended by two benzene rings at its [2,3]- and [4,5]-position.

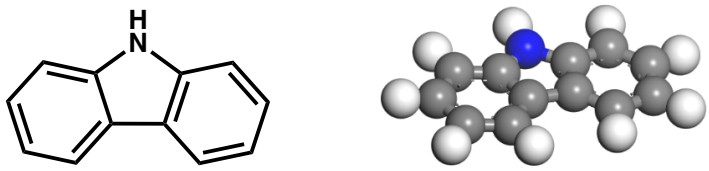

Figure 1.7. Structure of the carbazole molecule (color code: grey: carbon, blue: nitrogen, white: hydrogen).

Carbazole was originally discovered in 1872 by Carl Graebe and Carl Glaser, who isolated the compound from coal tar.[103] The molecule exhibits several advantageous features, which make it a widely researched building unit for optoelectronic applications. Firstly, carbazole is a cheap and easily available starting material. Secondly, it is facile to functionalize the nitrogen atom with many different substituents in order to alter its optical or electrical properties, whilst maintaining structural freedom at the molecule's backbone.[104] Thirdly, it is possible to generate linkages at different positions at the backbone such as the 3,6-, and the 2,7-position. Whilst linkages at the 3,6-position are chemically easily feasible and therefore very common, modifications at the 2,7-positions still are synthetically challenging and therefore more expensive.[105] Last but not least, due to its aromaticity, carbazole exhibits a high chemical stability.[104] This full aromaticity furthermore leads to an extensive electron delocalization within the molecule, which is beneficial for efficient charge transport.[106]

Hence, today carbazole has become an important and widely researched component in materials used for organic electronics, such as organic light emitting diodes (OLEDs),[104, 107, 108] and photovoltaics.[109, 110] Here, carbazole-based hole transporting materials (HTMs) exhibit an improved energy level alignment for effective hole extraction and an enhanced solution processability needed for successful thin layer generation.[111] Furthermore, carbazole-based HTMs offer reduced electron-hole recombination and therefore show enhanced charge separation and hole transport properties.[112] Another advantage of these HTMs is an increased photocurrent generation with reduced charge losses, due to a facilitated electronic coupling between donor and acceptor moieties.[111] In 2015, Gratia et al. report a hole transporting material (HTM) based on carbazole, 3,6-substituted with

methoxydiphenylamine, which they used in perovskite solar cells, exhibiting a power conversion efficiency (PCE) of 17% (at that time being almost as efficient as the widely used spiro-OMeTAD HTM).[113] Two years later, in 2017, Daskeviciene et al. published a low-cost and straightforward synthesis of the carbazole-based enamine HTM V950, exhibiting a PCE of 17.80% in perovskite solar cells[114], which was even outperformed by Lu et al., who reported an easy and cheap synthesis route for three star-shaped carbazole-based HTMs. Used in perovskite solar cells, these HTMs exhibited power conversion efficiencies of up to 18.87%.[115] Magomedov et al. nearly also achieved this PCE value with a series of branched HTMs with two diphenylamine-substituted carbazole moieties, bridged by a non-conjugated methylenebenzene unit, used in perovskite solar cells and showing a performance of up to 18.78%.[116] In 2020, Gao et al. studied the impact of metal ion-free dopants in carbazole-based HTMs. They successfully synthesized low-cost and stable materials, which, when used in perovskite solar cells, exhibited a power conversion efficiency of nearly 18 %, similar to spiro-OMeTAD, but with improved stability.[106] Two years after this, in 2022, Liu et al. reported the carbazole-based D-A type HTM KZRD, substituted at the 3,6-positions, in which carbazole functions as the electron-donor, exhibiting a high power conversion efficiency of 20.40% in a perovskite solar cell.[117]

Not only being used for photovoltaics, carbazole-based materials are also applied in modern OLEDs. In 2022, Cheng et al. reported a multiple resonance thermally activated delayed fluorescence (MR-TADF) emitter based on a carbazole-modified MR core unit for high-efficiency orange-red emission, almost achieving an external quantum efficiency (EQE) of 40 %.[118] Even more recently, Zhang et al. published a carbazole-modified organoboron MR core unit for a MR-TADF emitter with low-lying HOMO levels used in narrowband pure blue hyperfluorescence OLED devices with a record EQE for this kind of device of 29.2%.[119]

Because of the favorable properties performance of carbazole-based materials in organic electronics, paired with its abundance and stability, researchers have also successfully implemented it in different framework materials.

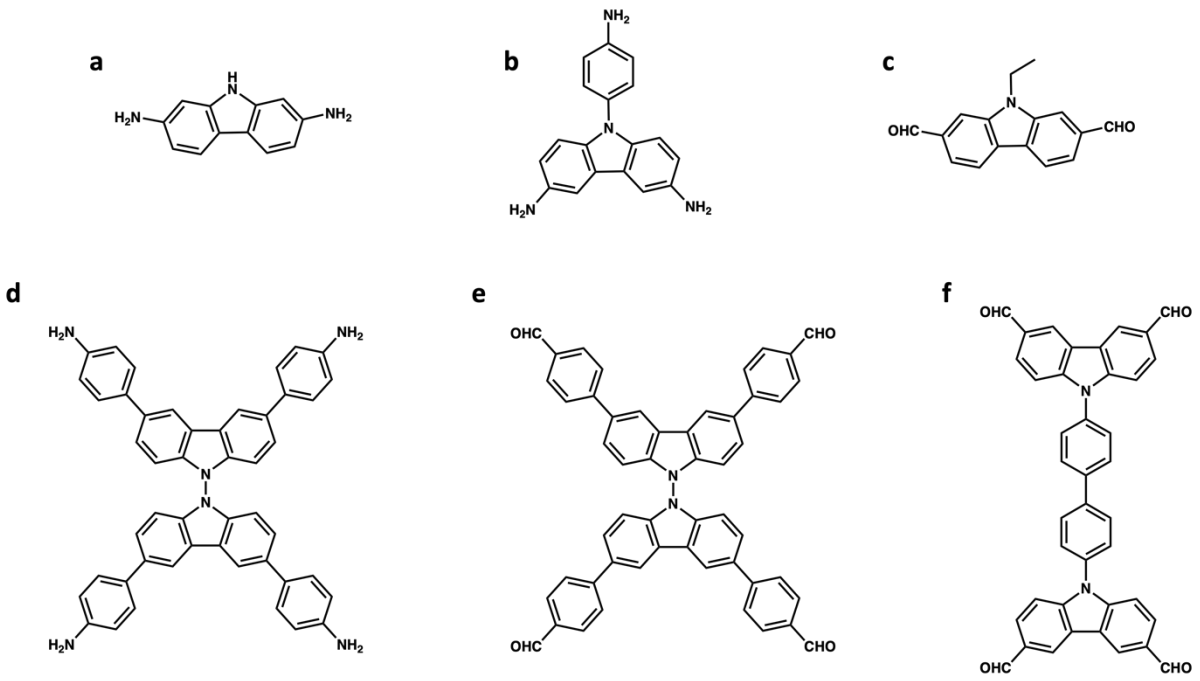

Scheme 1.4. Examples of carbazole-based building blocks that have been incorporated into covalent organic frameworks. **(a)** 2,7-Diaminocarbazole, **(b)** 9-(4-aminophenyl)-carbazole-3,6-diamine, **(c)** 9-ethyl-9H-carbazole-2,7-dicarboxaldehyde, **(d)** 4,4',4'',4'''-([9,9'-bicarbazole]-3,3',6,6'-tetrayl)tetraaniline (BTTA), **(e)** 4,4',4'',4'''-([9,9'-bicarbazole]-3,3',6,6'-tetrayl)tetrabenzaldehyde (BCTB) , **(f)** 4,4'-bis(3,6-diformyl-9H-carbazo-9-yl)-1,1'-biphenyl.

Here, the first COFs using carbazole-based building blocks were published in 2019. An et al. reported the successful generation of the hexagonal Cz-COF, solvothermally condensing 2,7-diaminocarbazole (Scheme 1.4a) with 1,3,5-triformylbenzene, and its usage for CO_2 capture.[120] In the same year, El-Mahdy et al. studied a series of three hexagonal COFs based on the 9-(4-aminophenyl)-carbazole-3,6-diamine motif (Scheme 1.4b). The COFs exhibit a high CO_2 uptake and also show redox activity, used for electrochemical energy storage.[121] In 2020, Lei et al. published a carbazole-based donor-acceptor type COF, with the carbazole units (Scheme 1.4c) acting as the electron donating sites, for visible light-driven photocatalytic CO_2 reduction and H_2O oxidation.[122] Furthermore, El-Mahdy et al. continued his research on carbazole-based COFs with the successful formation of a series of three thermally stable COFs, both using amino-functionalized (Scheme 1.4d) and aldehyde-functionalized (Scheme 1.4e) carbazole-based building blocks. Here, the influence of π-stacking on the materials' fluorescence behavior was investigated. Moreover, the potential application of one COF for fast and solution-based HCl chemosensing was shown.[123] Another COF based on a building block incorporating two carbazole moieties fused *via* a biphenylene bridge (Scheme 1.4f) was

reported by Kaskel and coworkers in 2021. Here, the COF exhibited a good performance for humidity control applications, taking advantage of the material's optical response to changes in the relative humidity.[124] Only recently, Chen et al. published a stable and fluorescent COF based on the BTTA building block (Scheme 1.4d) with hydrophobic pores and studied its application for the selective detection and adsorption of the pertechnetate and perrhenate anions.[125] Also in 2023, Liu et al. chose the aldehyde-functionalized version of the building block, BCTB (Scheme 1.4e), for the formation of tetragonal and olefin-linked JUC-557 COF nanosheets, exhibiting good performance in different molecular sensing applications.[126]

Concerning optoelectronic applications, a strongly π-conjugated COF network with a high degree of planarity and therefore closely stacked layers (in case of a 2D structure), is highly desirable. In this context, the carbazole building block used for the COF structures of this thesis was designed so that the individual carbazole moieties are nearly coplanar.

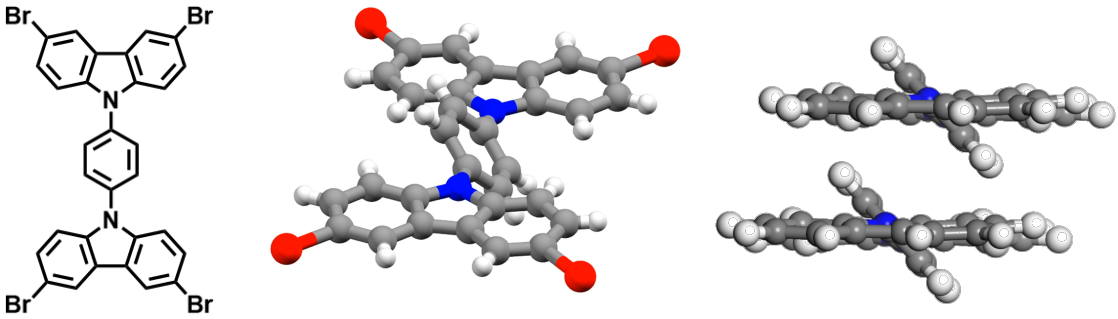

Figure 1.8. Structure of the 9,9'-(1,4-phenylene)bis(3,6-dibromo-9H-carbazole) molecule **(left)**, showing the virtual coplanarity of the carbazole moieties **(middle)** and the slightly offset and close stacking of two such molecules **(right)**. Color code: grey: C, blue: N, red: Br, white: H.[127, 128]

The 9,9'-(1,4-phenylene)bis(3,6-dibromo-9H-carbazole) molecule displayed in Figure 1.8 illustrates the core unit, chosen for the new building block (see Sections 4 and 5 of this thesis). The almost full coplanarity of the two carbazole units promotes an extended π-conjugation across the structure and allows for a fairly close stacking of 3.957 Å between the inner phenyl rings of the molecules,[127] which is also favorable for an optoelectronically active material that is based on this molecule. Here, the significance for the appropriate selection and design of the chosen building blocks is highlighted and was also a focal point for the COF developments described in this thesis.

1.5 References

1. Colella, C.; Gualtieri, A. F., Cronstedt's zeolite. *Microporous Mesoporous Mater.* **2007,** *105*, 213-221.
2. Corma, A.; Nemeth, L. T.; Renz, M.; Valencia, S., Sn-zeolite beta as a heterogeneous chemoselective catalyst for Baeyer–Villiger oxidations. *Nature* **2001,** *412*, 423-425.
3. Adeoye, J. B.; Balogun, D. O.; Etemire, O. J.; Ezeh, P. N.; Tan, Y. H.; Mubarak, N. M., Rapid adsorptive removal of eosin yellow and methyl orange using zeolite Y. *Sci. Rep.* **2023,** *13*, 21373.
4. Du, P.; Zhang, Y.; Wang, X.; Canossa, S.; Hong, Z.; Nénert, G.; Jin, W.; Gu, X., Control of zeolite framework flexibility for ultra-selective carbon dioxide separation. *Nat. Commun.* **2022,** *13*, 1427.
5. Yaghi, O. M.; O'Keeffe, M.; Ockwig, N. W.; Chae, H. K.; Eddaoudi, M.; J., K., Reticular synthesis and the design of new materials. *Nature* **2003,** *423*, 705-714.
6. Hoffmann, R., How should chemists think? *Sci. Am.* **1993,** *268*, 66-73.
7. O'Keeffe, M., Design of MOFs and intellectual content in reticular chemistry: a personal view. *Chem. Soc. Rev.* **2009,** *38*, 1215-1217.
8. Li, H.; Luk, Y.-Y.; Mrksich, M., Catalytic Asymmetric Dihydroxylation by Gold Colloids Functionalized with Self-Assembled Monolayers. *Langmuir* **1999,** *15*, 4957-4959.
9. Cao, G.; Wang, Y., *Nanostructures and Nanomaterials*. World Scientific: 2011; Vol. Volume 2, p 596.
10. Yaghi, O. M.; O'Keeffe, M.; Kanatzidis, M. G., Design of solids from molecular building blocks: golden opportunities for solid state chemistry. *J. Solid State Chem.* **2000,** *152*, 1-2.
11. Stein, A.; Keller, S. W.; Mallouk, T. E., Turning down the heat: Design and mechanism in solid-state synthesis. *Science* **1993,** *259*, 1558-1563.
12. Yaghi, O. M., Reticular Chemistry in All Dimensions. *ACS Cent. Sci.* **2019,** *5*, 1295-1300.
13. Yaghi, O. M., Reticular Chemistry—Construction, Properties, and Precision Reactions of Frameworks. *J. Am. Chem. Soc.* **2016,** *138*, 15507-15509.
14. Yaghi, O. M.; Li, H., Hydrothermal Synthesis of a Metal-Organic Framework Containing Large Rectangular Channels. *J. Am. Chem. Soc.* **1995,** *117*, 10401 - 10402.
15. Yaghi, O. M.; Li, G.; Li, H., Selective binding and removal of guests in a microporous metal–organic framework. *Nature* **1995,** *378*, 703 - 706.

16. Li, H.; Eddaoudi, M.; Groy, T. L.; Yaghi, O. M., Establishing Microporosity in Open Metal-Organic Frameworks: Gas Sorption Isotherms for Zn(BDC). *J. Am. Chem. Soc.* **1998,** *120*, 8571-8572.

17. Rowsell, J. L. C.; Yaghi, O. M., Metal–organic frameworks: a new class of porous materials. *Microporous Mesoporous Mater.* **2004,** *73*, 3-14.

18. Eddaoudi, M.; Kim, J.; Rosi, N.; Vodak, D.; Wachter, J.; apos; Keeffe, M.; Yaghi, O. M., Systematic design of pore size and functionality in isoreticular MOFs and their application in methane storage. (Reports). *Science* **2002,** *295*, 469+.

19. Li, H.; Eddaoudi, M.; O'Keeffe, M.; Yaghi, O. M., Design and synthesis of an exceptionally stable and highly porous metal-organic framework. *Nature* **1999,** *402*, 276-279.

20. Deria, P.; Mondloch, J. E.; Karagiaridi, O.; Bury, W.; Hupp, J. T.; Farha, O. K., Beyond post-synthesis modification: evolution of metal–organic frameworks via building block replacement. *Chem. Soc. Rev.* **2014,** *43*, 5896-5912.

21. Bavykina, A.; Kolobov, N.; Khan, I. S.; Bau, J. A.; Ramirez, A.; Gascon, J., Metal–Organic Frameworks in Heterogeneous Catalysis: Recent Progress, New Trends, and Future Perspectives. *Chem. Rev.* **2020,** *120*, 8468-8535.

22. Lawson, H. D.; Walton, S. P.; Chan, C., Metal–Organic Frameworks for Drug Delivery: A Design Perspective. *ACS Appl. Mater. Interfaces* **2021,** *13*, 7004-7020.

23. Kreno, L. E.; Leong, K.; Farha, O. K.; Allendorf, M.; Van Duyne, R. P.; Hupp, J. T., Metal–Organic Framework Materials as Chemical Sensors. *Chem. Rev.* **2012,** *112*, 1105-1125.

24. Fathieh, F.; Kalmutzki, M. J.; Kapustin, E. A.; Waller, P. J.; Yang, J.; Yaghi, O. M., Practical water production from desert air. *Sci. Adv. 4*, eaat3198.

25. Service, R. F., Crystalline nets snare water and make fuel from thin air. *Science* **2019,** *365*, 964-965.

26. Arora, H.; Dong, R.; Venanzi, T.; Zscharschuch, J.; Schneider, H.; Helm, M.; Feng, X.; Cánovas, E.; Erbe, A., Demonstration of a Broadband Photodetector Based on a Two-Dimensional Metal–Organic Framework. *Adv. Mater.* **2020,** *32*, 1907063.

27. Côté, A. P.; Benin, A. I.; Ockwig, N. W.; O'Keeffe, M.; Matzger, A. J.; Yaghi, O. M., Porous, Crystalline, Covalent Organic Frameworks. *Science* **2005,** *310*, 1166-1170.

28. Yaghi, O. M.; Kalmutzki, M. J.; Diercks, C. S., *Introduction to Reticular Chemistry: Metal-Organic Frameworks and Covalent Organic Frameworks*. Wiley-VCH: Weinheim, 2019.

29. Lohse, M. S.; Bein, T., Covalent Organic Frameworks: Structures, Synthesis and Application. *Adv. Funct. Mater.* **2018,** *28*, 1705553.

30. El-Kaderi, H. M.; Hunt, J. R.; Mendoza-Cortés, J. L.; Côté, A. P.; Taylor, R. E.; O'Keeffe, M.; Yaghi, O. M., Designed Synthesis of 3D Covalent Organic Frameworks *Science* **2007,** *316*, 268-272.

31. Cao, D.; Lan, J.; Wang, W.; Smit, B., Lithium-Doped 3D Covalent Organic Frameworks: High-Capacity Hydrogen Storage Materials. *Angew. Chem. Int. Ed.* **2009,** *48*, 4730-4733.

32. Mercado, R.; Fu, R.-S.; Yakutovich, A. V.; Talirz, L.; Haranczyk, M.; Smit, B., In Silico Design of 2D and 3D Covalent Organic Frameworks for Methane Storage Applications. *Chem Mater.* **2018,** *30*, 5069-5086.

33. Fu, J.; Das, S.; Xing, G.; Ben, T.; Valtchev, V.; Qiu, S., Fabrication of COF-MOF Composite Membranes and Their Highly Selective Separation of H2/CO2. *J. Am. Chem. Soc.* **2016,** *138*, 7673-7680.

34. Gao, C.; Li, J.; Yin, S.; Lin, G.; Ma, T.; Meng, Y.; Sun, J.; Wang, C., Isostructural Three-Dimensional Covalent Organic Frameworks. *Angew. Chem. Int. Ed.* **2019,** *58*, 9770-9775.

35. Li, H.; Pan, Q.; Ma, Y.; Guan, X.; Xue, M.; Fang, Q.; Yan, Y.; Valtchev, V.; Qiu, S., Three-Dimensional Covalent Organic Frameworks with Dual Linkages for Bifunctional Cascade Catalysis. *J. Am. Chem. Soc.* **2016,** *138*, 14783-14788.

36. Fang, Q.; Gu, S.; Zheng, J.; Zhuang, Z.; Qiu, S.; Yan, Y., 3D Microporous Base-Functionalized Covalent Organic Frameworks for Size-Selective Catalysis. *Angew. Chem. Int. Ed.* **2014,** *53*, 2878-2882.

37. Wu, C.; Liu, Y.; Liu, H.; Duan, C.; Pan, Q.; Zhu, J.; Hu, F.; Ma, X.; Jiu, T.; Li, Z.; Zhao, Y., Highly Conjugated Three-Dimensional Covalent Organic Frameworks Based on Spirobifluorene for Perovskite Solar Cell Enhancement. *J. Am. Chem. Soc.* **2018,** *140*, 10016-10024.

38. Banerjee, T.; Gottschling, K.; Gökcen, S.; Ochsenfeld, C.; Lotsch, B. V., H 2 Evolution with Covalent Organic Framework Photocatalysts. *ACS Energy Lett.* **2018,** *3*, 400-409.

39. Ascherl, L.; Evans, E. W.; Gorman, J.; Orsborne, S.; Bessinger, D.; Bein, T.; Friend, R. H.; Auras, F., Perylene-Based Covalent Organic Frameworks for Acid Vapor Sensing. *J. Am. Chem. Soc.* **2019,** *141*, 15693-15699.

40. Peng, H.; Huang, S.; Montes-García, V.; Pakulski, D.; Guo, H.; Richard, F.; Zhuang, X.; Samorì, P.; Ciesielski, A., Supramolecular Engineering of Cathode Materials for Aqueous Zinc-ion Energy Storage Devices: Novel Benzothiadiazole Functionalized Two-Dimensional Olefin-Linked COFs. *Angew. Chem. Int. Ed* **2023,** *62*, e202216136.

41. Shi, Y.; Yang, J.; Gao, F.; Zhang, Q., Covalent Organic Frameworks: Recent Progress in Biomedical Applications. *ACS Nano* **2023,** *17*, 1879-1905.

42. Malik, N.; Elool Dov, N.; de Ruiter, G.; Lahav, M.; van der Boom, M. E., On-Surface Self-Assembly of Stimuli-Responsive Metallo-Organic Films: Automated Ultrasonic Spray-Coating and Electrochromic Devices. *ACS Applied Materials & Interfaces* **2019,** *11*, 22858-22868.

43. Wang, K.; Wu, H.; Meng, Y.; Zhang, Y.; Wei, Z., Integrated energy storage and electrochromic function in one flexible device: an energy storage smart window. *Energy & Environmental Science* **2012,** *5*, 8384-8389.

44. Wu, W.; Poh, W. C.; Lv, J.; Chen, S.; Gao, D.; Yu, F.; Wang, H.; Fang, H.; Wang, H.; Lee, P. S., Self-Powered and Light-Adaptable Stretchable Electrochromic Display. *Advanced Energy Materials* **2023,** *13*, 2204103.

45. Zhang, W.; Li, H.; Elezzabi, A. Y., Electrochromic Displays Having Two-Dimensional CIE Color Space Tunability. *Advanced Functional Materials* **2022,** *32*, 2108341.

46. Hao, Q.; Li, Z.-J.; Lu, C.; Sun, B.; Zhong, Y.-W.; Wan, L.-J.; Wang, D., Oriented Two-Dimensional Covalent Organic Framework Films for Near-Infrared Electrochromic Application. *J. Am. Chem. Soc.* **2019,** *141*, 19831-19838.

47. Yu, F.; Liu, W.; Ke, S.-W.; Kurmoo, M.; Zuo, J.-L.; Zhang, Q., Electrochromic two-dimensional covalent organic framework with a reversible dark-to-transparent switch. *Nat. Commun.* **2020,** *11*, 5534.

48. Lanni, L. M.; Tilford, R. W.; Bharathy, M.; Lavigne, J. J., Enhanced Hydrolytic Stability of Self-Assembling Alkylated Two-Dimensional Covalent Organic Frameworks. *J. Am. Chem. Soc.* **2011,** *133*, 13975-13983.

49. Du, Y.; Yang, H.; Whiteley, J. M.; Wan, S.; Jin, Y.; Lee, S.-H.; Zhang, W., Ionic Covalent Organic Frameworks with Spiroborate Linkage. *Angew. Chem. Int. Ed.* **2016,** *55*, 1737-1741.

50. Uribe-Romo, F. J.; Hunt, J. R.; Furukawa, H.; Klock, C.; O'Keeffe, M.; Yaghi, O. M., A Crystalline Imine-Linked 3-D Porous Covalent Organic Framework. *J. Am. Chem. Soc.* **2009,** *131*, 4570-4571.

51. Uribe-Romo, F. J.; Doonan, C. J.; Furukawa, H.; Oisaki, K.; Yaghi, O. M., Crystalline Covalent Organic Frameworks with Hydrazone Linkages. *J. Am. Chem. Soc.* **2011,** *133*, 11478-11481.

52. Stegbauer, L.; Schwinghammer, K.; Lotsch, B. V., A hydrazone-based covalent organic framework for photocatalytic hydrogen production. *Chem. Sci.* **2014,** *5*, 2789-2793.

53. Yang, Y.-X.; Tang, X.-H.; Wu, J.-L.; Dong, Z.-Y.; Yan, Y.-L.; Zheng, S.-R.; Fan, J.; Li, X.; Cai, S.; Zhang, W.-G., Transformation of a Hydrazone-Linked Covalent Organic Framework into a Highly Stable Hydrazide-Linked One. *ACS Appl. Polym. Mater.* **2022,** *4*, 4624-4631.

54. Dalapati, S.; Jin, S.; Gao, J.; Xu, Y.; Nagai, A.; Jiang, D., An Azine-Linked Covalent Organic Framework. *J. Am. Chem. Soc.* **2013,** *135*, 17310-17313.

55. Alahakoon, S. B.; Thompson, C. M.; Nguyen, A. X.; Occhialini, G.; Mccandless, G. T.; Smaldone, R. A., An azine-linked hexaphenylbenzene based covalent organic framework. *Chem. Commun.* **2016,** *52*, 2843-2845.

56. Li, Z.; Zhi, Y.; Feng, X.; Ding, X.; Zou, Y.; Liu, X.; Y., M., An Azine-Linked Covalent Organic Framework: Synthesis, Characterization and Efficient Gas Storage. *Chem. Eur. J.* **2015,** *21*, 12079-12084.

57. Maschita, J.; Banerjee, T.; Savasci, G.; Haase, F.; Ochsenfeld, C.; Lotsch, B. V., Ionothermal Synthesis of Imide-Linked Covalent Organic Frameworks. *Angew. Chem. Int. Ed.* **2020,** *59*, 15750-15758.

58. Shi, J.; Su, M.; Li, H.; Lai, D.; Gao, F.; Lu, Q., Two-Dimensional Imide-Based Covalent Organic Frameworks with Tailored Pore Functionality as Separators for High-Performance Li–S Batteries. *ACS Appl. Mater. Interfaces* **2022,** *14*, 42018-42029.

59. Pei, B.; Liu, D.; Tian, Z.; Huang, J., Imide-Based Covalent Organic Frameworks/Carbon Nanotube Composites as Anode Materials for Potassium Storage. *ChemistrySelect* **2022,** *7*, e202200656.

60. DeBlase, C. R.; Silberstein, K. E.; Truong, T.-T.; Abruña, H. D.; Dichtel, W. R., β-Ketoenamine-Linked Covalent Organic Frameworks Capable of Pseudocapacitive Energy Storage. *J. Am. Chem. Soc.* **2013,** *135*, 16821-16824.

61. Daugherty, M. C.; Vitaku, E.; Li, R. L.; Evans, A. M.; Chavez, A. D.; Dichtel, W. R., Improved synthesis of β-ketoenamine-linked covalent organic frameworks via monomer exchange reactions. *Chem. Commun.* **2019,** *55*, 2680-2683.

62. Wang, H.; Zou, W.; Liu, C.; Sun, Y.; Xu, Y.; Sun, W.; Wang, Y., β-Ketoenamine-Linked Covalent Organic Framework with Co Intercalation: Improved Lithium-Storage Properties and Mechanism for High-Performance Lithium-Organic Batteries. *Batter. Supercaps* **2023,** *6*, e202200434.

63. Nagai, A.; Chen, X.; Feng, X.; Ding, X.; Guo, Z.; Jiang, D., A Squaraine-Linked Mesoporous Covalent Organic Framework. *Angew. Chem. Int. Ed.* **2013,** *52*, 3770-3774.

64. Xue, R.; Gou, H.; Zheng, Y.; Zhang, L.; Liu, Y.; Rao, H.; Zhao, G., A New Squaraine-Linked Triazinyl-Based Covalent Organic Frameworks: Preparation, Characterization and Application for Sensitive and Selective Determination of Fe3+ Cations. *ChemistrySelect* **2020,** *5*, 10632-10636.

65. Wang, S.; Li, M.; Yan, G.; Yang, Z.; Guo, Y.; Sun, X.; Wang, Y.; Feng, Y.; Ding, H.; Zhang, X., Squaraine-linked zwitterionic COF modified LLZTO nanoparticles for high performance polymer composite electrolytes in Li–S batteries. *Nanoscale* **2023,** *15*, 12961-12971.

66. Vitaku, E.; Gannett, C. N.; Carpenter, K. L.; Shen, L.; Abruña, H. D.; Dichtel, W. R., Phenazine-Based Covalent Organic Framework Cathode Materials with High Energy and Power Densities. *J. Am. Chem. Soc.* **2020,** *142*, 16-20.

67. Tavakoli, E.; Kakekhani, A.; Kaviani, S.; Tan, P.; Ghaleni, M. M.; Zaeem, M. A.; Rappe, A. M.; Nejati, S., In Situ Bottom-up Synthesis of Porphyrin-Based Covalent Organic Frameworks. *J. Am. Chem. Soc.* **2019,** *141*, 19560-19564.

68. Kandambeth, S.; Jia, J.; Wu, H.; Kale, V. S.; Parvatkar, P. T.; Czaban-Jóźwiak, J.; Zhou, S.; Xu, X.; Ameur, Z. O.; Abou-Hamad, E.; Emwas, A.-H.; Shekhah, O.; Alshareef, H. N.; Eddaoudi, M., Covalent Organic Frameworks as Negative Electrodes for High-Performance Asymmetric Supercapacitors. *Adv. Energy Mater.* **2020,** *10*, 2001673.

69. Zhao, C.; Diercks, C. S.; Zhu, C.; Hanikel, N.; Pei, X.; Yaghi, O. M., Urea-Linked Covalent Organic Frameworks. *J. Am. Chem. Soc.* **2018,** *140*, 16438-16441.

70. Cao, H.-L.; Yang, C.; Qian, H.-L.; Yan, X.-P., Urea-linked covalent organic framework functionalized polytetrafluoroethylene film for selective and rapid thin film microextraction of rhodamine B. *J. Chromatogr. A* **2022,** *1673*, 463133.

71. Basu, A.; Banerjee, R., Chemically stable urea based COF for size selective heterogeneous catalysis. *Acta. Cryst. A* **2017,** *73*, C1146.

72. Zhuang, X.; Zhao, W.; Zhang, F.; Cao, Y.; Liu, F.; Bi, S.; Feng, X., A two-dimensional conjugated polymer framework with fully sp2-bonded carbon skeleton. *Polym. Chem.* **2016,** *7*, 4176-4181.

73. Wang, Z.; Yang, Y.; Zhao, Z.; Zhang, P.; Zhang, Y.; Liu, J.; Ma, S.; Cheng, P.; Chen, Y.; Zhang, Z., Green synthesis of olefin-linked covalent organic frameworks for hydrogen fuel cell applications. *Nat. Commun.* **2021,** *12*, 1982.

74. Thommes, M.; Kaneko, K.; Neimark, A. V.; Olivier, J.; Rodriguez-Reinoso, F.; Rouquerol, J.; Sing, K. S. W., Physisorption of gases, with special reference to the evaluation of surface area and pore size distribution. *Pure Appl. Chem.* **2015,** *87*, 1051-1069.

75. Furukawa, H.; Yaghi, O. M., Storage of Hydrogen, Methane, and Carbon Dioxide in Highly Porous Covalent Organic Frameworks for Clean Energy Applications. *J. Am. Chem. Soc.* **2009,** *131*, 8875-8883.

76. Han, S. S.; Furukawa, H.; Yaghi, O. M.; Goddard, W. A., Covalent Organic Frameworks as Exceptional Hydrogen Storage Materials. *J. Am. Chem. Soc.* **2008,** *130*, 11580-11581.

77. Mendoza-Cortes, J. L.; Pascal, T. A.; Goddard, W. A., III, Design of Covalent Organic Frameworks for Methane Storage. *J. Phys. Chem. A* **2011,** *115*, 13852-13857.

78. Yang, Y.; Faheem, M.; Wang, L.; Meng, Q.; Sha, H.; Yang, N.; Yuan, Y.; Zhu, G., Surface Pore Engineering of Covalent Organic Frameworks for Ammonia Capture through Synergistic Multivariate and Open Metal Site Approaches. *ACS Cent. Sci.* **2018,** *4*, 748-754.

79. Doonan, C. J.; Tranchemontagne, D. J.; Glover, T. G.; Hunt, J. R.; Yaghi, O. M., Exceptional ammonia uptake by a covalent organic framework. *Nat. Chem.* **2010,** *2*, 235-238.

80. Lyu, H.; Li, H.; Hanikel, N.; Wang, K.; Yaghi, O. M., Covalent Organic Frameworks for Carbon Dioxide Capture from Air. *J. Am. Chem. Soc.* **2022,** *144*, 12989-12995.

81. Zeng, Y.; Zou, R.; Zhao, Y., Covalent Organic Frameworks for CO2 Capture. *Adv. Mater.* **2016,** *28*, 2855-2873.

82. Kalmutzki, M. J.; Diercks, C. S.; Yaghi, O. M., Metal–Organic Frameworks for Water Harvesting from Air. *Adv. Mater.* **2018,** *30*, 1704304.

83. Nguyen, H. L.; Hanikel, N.; Lyle, S. J.; Zhu, C.; Proserpio, D. M.; Yaghi, O. M., A Porous Covalent Organic Framework with Voided Square Grid Topology for Atmospheric Water Harvesting. *J. Am. Chem. Soc.* **2020,** *142*, 2218-2221.

84. Nguyen, H. L.; Gropp, C.; Hanikel, N.; Möckel, A.; Lund, A.; Yaghi, O. M., Hydrazine-Hydrazide-Linked Covalent Organic Frameworks for Water Harvesting. *ACS Cent. Sci.* **2022,** *8*, 926-932.

85. Grunenberg, L.; Savasci, G.; Emmerling, S. T.; Heck, F.; Bette, S.; Cima Bergesch, A.; Ochsenfeld, C.; Lotsch, B. V., Postsynthetic Transformation of Imine- into Nitrone-Linked Covalent Organic Frameworks for Atmospheric Water Harvesting at Decreased Humidity. *J. Am. Chem. Soc.* **2023,** *145*, 13241-13248.

86. Sun, C.; Zhu, Y.; Shao, P.; Chen, L.; Huang, X.; Zhao, S.; Ma, D.; Jing, X.; Wang, B.; Feng, X., 2D Covalent Organic Framework for Water Harvesting with Fast Kinetics and Low Regeneration Temperature. *Angew. Chem. Int. Ed.* **2023,** *62*, e202217103.

87. Chen, L.-H.; Han, W.-K.; Yan, X.; Zhang, J.; Jiang, Y.; Gu, Z.-G., A Highly Stable Ortho-Ketoenamine Covalent Organic Framework with Balanced Hydrophilic and Hydrophobic Sites for Atmospheric Water Harvesting. *ChemSusChem* **2022,** *15*, e202201824.

88. Sarkar, A.; Mahapatra, S., Novel hydrophobic vaterite particles for oil removal and recovery. *J. Mater. Chem. A* **2014,** *2*, 3808-3818.

89. Jiang, J.; Zhang, Q.; Zhan, X.; Chen, F., A multifunctional gelatin-based aerogel with superior pollutants adsorption, oil/water separation and photocatalytic properties. *Chem. Eng. J.* **2019,** *358*, 1539-1551.

90. Yang, J.; Wang, H.; Tao, Z.; Liu, X.; Wang, Z.; Yue, R.; Cui, Z., 3D superhydrophobic sponge with a novel compression strategy for effective water-in-oil emulsion separation and its separation mechanism. *Chem. Eng. J.* **2019,** *359*, 149-158.

91. Saleh, T. A.; Baig, N.; Alghunaimi, F. I.; Aljuryyed, N. W., A flexible biomimetic superhydrophobic and superoleophilic 3D macroporous polymer-based robust network for the efficient separation of oil-contaminated water. *RSC Adv.* **2020,** *10*, 5088-5097.

92. Mähringer, A.; Hennemann, M.; Clark, T.; Bein, T.; Medina, D. D., Energy Efficient Ultrahigh Flux Separation of Oily Pollutants from Water with Superhydrophilic Nanoscale Metal–Organic Framework Architectures. *Angew. Chem. Int. Ed.* **2021,** *60*, 5519-5526.

93. Yu, Z.-P.; Zhan, B.; Dong, L.-M.; Jiang, W.; Song, Y.-Y.; Hu, S.-A., Self-Healing Structured Graphene Surface with Reversible Wettability for Oil–Water Separation. *ACS Appl. Nano Mater.* **2019,** *2*, 1505-1515.

94. Liu, Y.; Li, W.; Yuan, C.; Jia, L.; Liu, Y.; Huang, A.; Cui, Y., Two-Dimensional Fluorinated Covalent Organic Frameworks with Tunable Hydrophobicity for Ultrafast Oil–Water Separation. *Angew. Chem. Int. Ed.* **2022,** *61*, e202113348.

95. Han, N.; Zhang, Z.; Gao, H.; Qian, Y.; Tan, L.; Yang, C.; Zhang, H.; Cui, Z.; Li, W.; Zhang, X., Superhydrophobic Covalent Organic Frameworks Prepared via Pore Surface Modifications for Functional Coatings under Harsh Conditions. *ACS Appl. Mater. Interfaces* **2020,** *12*, 2926-2934.

96. Das, G.; Skorjanc, T.; Prakasam, T.; Garai, B.; Abubakar, S.; Zalch, C. S.; Gándara, F.; Pasricha, R.; Sharma, S. K.; Varghese, S.; Jagannathan, R.; Olson, M. A.; Trabolsi, A., Hydrophobicity Tuning in Isostructural Urchin-Shaped Covalent Organic Framework Nanoparticles by Pore Surface Engineering for Oil–Water Separation. *ACS Appl. Ener. Mater.* **2022,** *5*, 13745-13751.

97. Chu, J.-Q.; Lu, Y.; Gan, S.-X.; Qi, Q.-Y.; Jia, C.; Yao, J.; Zhao, X., A Superhydrophobic Trifluoromethyl-Containing Covalent Organic Framework Membrane for Efficient Oil/Water Separation. *Macromol. Rapid Commun.* **2023,** *44*, 2200641.

98. Wang, J.; Wang, F.; Zhou, Y.; Zhou, Y.; Gao, P.; Men, X., Facile fabrication of covalent organic framework functionalized superhydrophobic porous sponges for highly efficient water/oil separation. *Sci. China Inf. Sci.* **2022,** *65*, 2631-2640.

99. Xu, T.; An, S.; Peng, C.; Hu, J.; Liu, H., Construction of Large-Pore Crystalline Covalent Organic Framework as High-Performance Adsorbent for Rhodamine B Dye Removal. *Ind. Eng. Chem.* **2020,** *59*, 8315-8322.

100. Li, M.; Ma, J.; Pan, B.; Wang, J., Cage-Based Covalent Organic Framework for the Effective and Efficient Removal of Malachite Green from Wastewater. *ACS Appl. Mater. Interfaces* **2022,** *14*, 57180-57188.

101. Anbazhagan, R.; Krishnamoorthi, R.; Thankachan, D.; Van Dinh, T. T.; Wang, C.-F.; Yang, J. M.; Chang, Y.-H.; Tsai, H.-C., Fluorine-Free Superhydrophobic Covalent-Organic-Polymer Nanosheet Coating for Selective Dye and Emulsion Separation. *Langmuir* **2022,** *38*, 4310-4320.

102. Zheng, W.; Li, A.; Wang, X.; Li, Z.; Zhao, B.; Wang, L.; Kan, W.; Sun, L.; Qi, X., Construction of hydrophilic covalent organic frameworks and their fast and efficient adsorption of cationic dyes from aqueous solution. *New J. Chem.* **2022,** *46*, 22185-22194.

103. Graebe, C.; Glaser, C., Ueber Carbazol. *Justus Liebigs Annalen der Chemie* **1872,** *163*, 343-360.

104. Blouin, N.; Leclerc, M., Poly(2,7-carbazole)s: Structure–Property Relationships. *Acc. Chem. Res.* **2008,** *41*, 1110-1119.

105. Radhakrishna, K.; Manjunath, S. B.; Devadiga, D.; Chetri, R.; Nagaraja, A. T., Review on Carbazole-Based Hole Transporting Materials for Perovskite Solar Cell. *ACS Appl. Energy Mater.* **2023,** *6*, 3635-3664.

106. Gao, L.; Schloemer, T. H.; Zhang, F.; Chen, X.; Xiao, C.; Zhu, K.; Sellinger, A., Carbazole-Based Hole-Transport Materials for High-Efficiency and Stable Perovskite Solar Cells. *ACS Appl. Energy Mater.* **2020,** *3*, 4492-4498.

107. Wex, B.; Kaafarani, B. R., Perspective on carbazole-based organic compounds as emitters and hosts in TADF applications. *J. Mater. Chem. C* **2017,** *5*, 8622-8653.

108. de Jong, F.; Daniels, M.; Vega-Castillo, L.; Kennes, K.; Martín, C.; de Miguel, G.; Cano, M.; Pérez-Morales, M.; Hofkens, J.; Dehaen, W.; Van der Auweraer, M., 5,10-Dihydrobenzo[a]indolo[2,3-c]carbazoles as Novel OLED Emitters. *J. Phys. Chem. B* **2019,** *123*, 1400-1411.

109. Puckyte, G.; Schmaltz, B.; Tomkeviciene, A.; Degbia, M.; Grazulevicius, J. V.; Melhem, H.; Bouclé, J.; Tran-Van, F., Carbazole-based molecular glasses for efficient solid-state dye-sensitized solar cells. *J. Power Sources* **2013,** *233*, 86-92.

110. Li, J.; Grimsdale, A. C., Carbazole-based polymers for organic photovoltaic devices. *Chem. Soc. Rev.* **2010,** *39*, 2399-2410.

111. Zahid, W. A.; Ahmad, M. F.; Akram, W.; Shaaban, I. A.; Assiri, M. A.; Elmushyakhi, A.; Iqbal, J., Probing the Effect of Acceptor Moiety Engineering in Carbazole-Based Hole-Transporting Materials for Efficient Perovskite Solar Cells. *Adv. Theory Simul.* **2023,** *6*, 2300495.

112. Keremane, K. S.; Rao, R.; Adhikari, A. V., Simple 3,6-disubstituted Carbazoles as Potential Hole Transport Materials: Photophysical, Electrochemical and Theoretical Studies. *Photochem. Photobiol.* **2021,** *97*, 289-300.

113. Gratia, P.; Magomedov, A.; Malinauskas, T.; Daskeviciene, M.; Abate, A.; Ahmad, S.; Grätzel, M.; Getautis, V.; Nazeeruddin, M. K., A Methoxydiphenylamine-Substituted Carbazole Twin Derivative: An Efficient Hole-Transporting Material for Perovskite Solar Cells. *Angew. Chem. Int. Ed.* **2015,** *54*, 11409-11413.

114. Daskeviciene, M.; Paek, S.; Wang, Z.; Malinauskas, T.; Jokubauskaite, G.; Rakstys, K.; Cho, K. T.; Magomedov, A.; Jankauskas, V.; Ahmad, S.; Snaith, H. J.; Getautis, V.; Nazeeruddin, M. K., Carbazole-based enamine: Low-cost and efficient hole transporting material for perovskite solar cells. *Nano Energy* **2017,** *32*, 551-557.

115. Lu, C.; Choi, I. T.; Kim, J.; Kim, H. K., Simple synthesis and molecular engineering of low-cost and star-shaped carbazole-based hole transporting materials for highly efficient perovskite solar cells. *J. Mater. Chem. A* **2017,** *5*, 20263-20276.

116. Magomedov, A.; Paek, S.; Gratia, P.; Kasparavicius, E.; Daskeviciene, M.; Kamarauskas, E.; Gruodis, A.; Jankauskas, V.; Kantminiene, K.; Cho, K. T.; Rakstys, K.; Malinauskas, T.; Getautis, V.; Nazeeruddin, M. K., Diphenylamine-Substituted Carbazole-Based Hole Transporting Materials for Perovskite Solar Cells: Influence of Isomeric Derivatives. *Adv. Funct. Mater.* **2018,** *28*, 1704351.

117. Liu, H.; He, B.; Lu, H.; Tang, R.; Wu, F.; Zhong, C.; Li, S.; Wang, J.; Zhu, L., Carbazole-based D–A type hole transport materials to enhance the performance of perovskite solar cells. *Sustain. Energy Fuels* **2022,** *6*, 371-376.

118. Cheng, Y.-C.; Fan, X.-C.; Huang, F.; Xiong, X.; Yu, J.; Wang, K.; Lee, C.-S.; Zhang, X.-H., A Highly Twisted Carbazole-Fused DABNA Derivative as an Orange-Red TADF Emitter for OLEDs with Nearly 40 % EQE. *Angew. Chem. Int. Ed.* **2022,** *61*, e202212575.

119. Zhang, K.; Wang, X.; Chang, Y.; Wu, Y.; Wang, S.; Wang, L., Carbazole-Decorated Organoboron Emitters with Low-Lying HOMO Levels for Solution-Processed

Narrowband Blue Hyperfluorescence OLED Devices. *Angew. Chem. Int. Ed.* **2023,** *62*, e202313084.

120. An, S.; Xu, T.; Hu, J.; Liu, H., Rational design of functionalized covalent organic frameworks and their performance towards CO2 capture. *RSC Adv.* **2019,** *9*, 21438-21443.
121. El-Mahdy, A. F. M.; Young, C.; Kim, J.; You, J.; Yamauchi, Y.; Kuo, S.-W., Hollow Microspherical and Microtubular [3 + 3] Carbazole-Based Covalent Organic Frameworks and Their Gas and Energy Storage Applications. *ACS Appl. Mater. Interfaces* **2019,** *11*, 9343-9354.
122. Lei, K.; Wang, D.; Ye, L.; Kou, M.; Deng, Y.; Ma, Z.; Wang, L.; Kong, Y., A Metal-Free Donor–Acceptor Covalent Organic Framework Photocatalyst for Visible-Light-Driven Reduction of CO2 with H2O. *ChemSusChem* **2020,** *13*, 1725-1729.
123. El-Mahdy, A. F. M.; Lai, M.-Y.; Kuo, S.-W., A highly fluorescent covalent organic framework as a hydrogen chloride sensor: roles of Schiff base bonding and π-stacking. *J. Mater. Chem. C* **2020,** *8*, 9520-9528.
124. Gilmanova, L.; Bon, V.; Shupletsov, L.; Pohl, D.; Rauche, M.; Brunner, E.; Kaskel, S., Chemically Stable Carbazole-Based Imine Covalent Organic Frameworks with Acidochromic Response for Humidity Control Applications. *J. Am. Chem. Soc.* **2021,** *143*, 18368-18373.
125. Chen, X.-R.; Zhang, C.-R.; Liu, X.; Liang, R.-P.; Qiu, J.-D., Ionic covalent organic framework for selective detection and adsorption of TcO4−/ReO4−. *Chem. Comm.* **2023,** *59*, 9521-9524.
126. Liu, Y.; Ren, J.; Wang, Y.; Zhu, X.; Guan, X.; Wang, Z.; Zhou, Y.; Zhu, L.; Qiu, S.; Xiao, S.; Fang, Q., A Stable Luminescent Covalent Organic Framework Nanosheet for Sensitive Molecular Recognition. *CCS Chemistry* **2022,** *5*, 2033-2045.
127. Colin-Molina, A.; Pérez-Estrada, S.; Roa, A. E.; Villagrana-Garcia, A.; Hernández-Ortega, S.; Rodríguez, M.; Brown, S. E.; Rodríguez-Molina, B., Isotropic rotation in amphidynamic crystals of stacked carbazole-based rotors featuring halogen-bonded stators. *Chem. Comm.* **2016,** *52*, 12833-12836.
128. Cambridge-Crystallographic-Data-Centre https://www.ccdc.cam.ac.uk/structures/search?id=doi:10.5517/ccdc.csd.cc1ll98r&sid=DataCite (accessed 12/18/2023).

2. Characterization Techniques

2.1 Powder X-Ray Diffraction

Powder X-ray Diffraction (PXRD) is a powerful tool for the structural characterization of crystalline materials such as covalent organic frameworks. It represents a non-destructive method for the analysis of powders, thin films, and single crystals, providing insight concerning the phase composition. Furthermore, it is a prerequisite for the structural simulation and refinement of crystalline samples.

X-Ray radiation with typical wavelengths of 10 pm to 10 nm was discovered by Wilhelm Röntgen in 1895 in Würzburg. In the experimental PXRD setup, X-ray beams are generated by directing voltage-accelerated electrons onto a metal target anode. Here, atoms of the metal target are ionized. Resulting inner shell electron vacancies are refilled by higher shell electrons, leading to the generation of X-ray radiation. So, for instance, if an electron is knocked out of the *K*-shell, and subsequently refilled by an electron from the *L*-shell, characteristic K_α-radiation is emitted. K_β-radiation is generated if the vacancy is refilled with an electron from the *M*-shell. The energy of the resultant X-ray beam is hence equal to the energy difference of the respective shells, and dependent on the metal target material. For the experimental measurement, the X-ray beam is filtered to make it monochromatic, and collimated towards the sample.[1-3]

Bragg's law describes the diffraction processes that occur when the collimated X-ray beam interferes with the crystalline sample.

$$n\,\lambda = 2d\,sin\theta$$

where *n* represents the order of reflection, λ the wavelength of the monochromatic X-ray beam, *d* the lattice spacing, and θ the diffraction angle.

With the crystal lattice spacing *d* being in the range of the X-ray's wavelength, the crystal acts as a three-dimensional diffraction grating, where X-rays are diffracted by sample electron shells, as visualized in Figure 2.1.

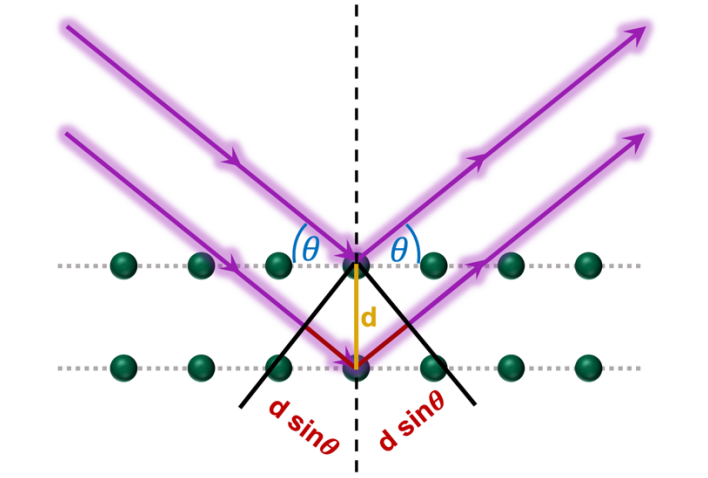

Figure 2.1. Schematic visualization of Bragg's law for constructive interference. The incoming X-ray beams (violet) are diffracted by the sample electron shells (green).

Bragg's law describes the condition for constructive interference in a crystal sample. With a fixed lattice spacing d and a specific wavelength λ, constructive interference only occurs for diffraction angles θ with values such that $2d\ sin\theta$ is an integer multiple of the wavelength λ.[4]

The resultant constructive interference pattern is subsequently transformed into diffraction patterns where the intensity is plotted against the diffraction angle 2θ.

It is also possible to estimate the size of the sample's crystallites from the diffraction pattern. In case of small crystallite domains, the individual reflections of the diffraction pattern appear broadened compared to larger crystallites. Here, the Scherrer equation can be used for the estimation of the crystal domain sizes *D*.

$$D = \frac{k\,\lambda}{\beta \cos\theta}$$

Where λ is the wavelength of the monochromatic X-ray beam, β is the FWHM (full width at half maximum) of the respective reflection, θ is the diffraction angle, and k is the Scherrer constant at the order of unity.[5]

Powder X-ray diffractograms were measured on a BRUKER D8 Discover with Ni-filtered Cu-K_α radiation and a LynxEye position-sensitive detector. The visualization of the simulated covalent organic frameworks was conducted using the Materials Studio 7.0 software package.

2.2 Grazing Incidence X-Ray Scattering

Grazing Incidence Wide Angle X-Ray Scattering (GIWAXS) is a highly convenient method for the characterization of thin crystalline samples, such as nanostructured COF thin films, as standard XRD geometries do not provide enough signal due to the small sample thickness. Here, GIWAXS gives information on the crystallinity and the preferred orientation of the thin film's crystalline domains. A schematic illustration of a GIWAXS set-up geometry is depicted in Figure 2.2.

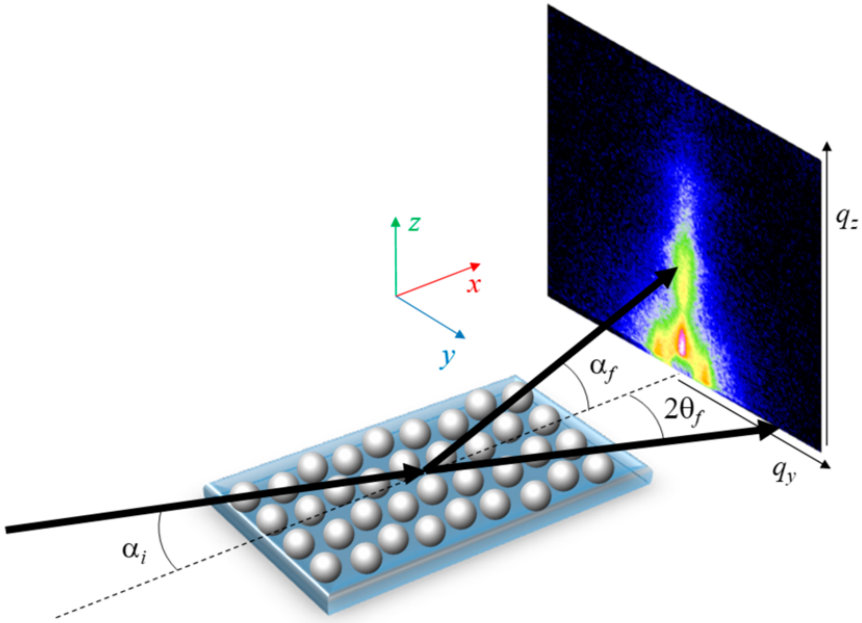

Figure 2.2. Schematic illustration of a GIWAXS set-up geometry with a thin film sample.[6]

A monochromatic X-ray beam with the wavelength λ is directed onto the sample surface under an incident angle α_i, which is below the critical angle of the sample. Probing the sample surface, the incoming beam is scattered vertically with the exit angle α_f, and horizontally with the in-plane angle $2\theta_f$. With the incident X-ray beam being below the critical angle, it is totally externally reflected on the sample surface, creating an exponentially decreasing evanescent wave that only penetrates a short distance into the sample. A 2D area detector collects the intensity information of the scattered X-rays as a function of α_f and $2\theta_f$. Whilst GIWAXS set-ups are operated at short sample-detector distances, GISAXS (grazing incidence small angle X-ray scattering) use large distances of often two meters or more.[7] The positions of the scattering spots are typically displayed via the wavelength-independent scattering vector q, enabling the comparison of data from different devices. The q-values are correlated to 2θ angles by the following equation:[8]

$$q = \frac{4\pi}{\lambda} \sin\theta$$

Analyzing samples, such as COF thin films with GIWAXS allows for the examination of the film's preferential orientation. Here, a preferential orientation of the crystalline domains yields distinct scattering spots, while arcs with a homogeneous intensity distribution would be obtained for non-oriented samples.

2D grazing-incidence wide angle X-ray scattering (GIWAXS) data were recorded with an Anton Paar SAXSpoint 2.0 system equipped with a Primux 100 micro Cu K_α source and a Dectris EIGER R 1M detector.

2.3 Nuclear Magnetic Resonance

Nuclear magnetic resonance (NMR) spectroscopy is a powerful analytical method for the structural characterization of organic molecules, whilst also providing information on the sample's purity. Phase-purity of the secondary building blocks is of great importance for COF synthesis, which makes NMR an indispensable analytical method.

Using NMR spectroscopy, the existence of suitable isotopes is a prerequisite, as only nuclei with an intrinsic nuclear spin *p* can be measured. It is therefore necessary for the nuclei to have an odd number of protons, neutrons, or both, such as ^{1}H, ^{13}C, or ^{14}N. The following equation describes the relationship between the nuclear spin *p* and the magnetic moment μ.

$$\mu = \gamma\, p$$

where γ is the gyromagnetic ratio, a unique constant, characteristic for the respective isotope. The magnetic moment μ is a quantum-chemical quantity described as follows:

$$\mu = \gamma\, (\sqrt{I(I+1)}\ \frac{h}{2\pi})$$

where *I* is the azimuthal quantum number of the nucleus with an integer or half-integer number and *h* is the Planck constant. In a homogeneous, static magnetic field B_0, the angular momentum is quantized, so that

$$p_B = m\,\frac{h}{2\pi}$$

with *m* being the magnetic quantum number.[9]

$$m = +I,\ I-1,\ I-2,\ \ldots,\ -I+1,\ -I$$

When exposed to an external magnetic field, there is only a limited number of orientations for the magnetic moment of a nucleus. For each azimuthal quantum number *I*, 2*I*+1 eigenstates are energetically split, exhibiting the so-called *Zeeman effect*. With *I* of a proton being $\frac{1}{2}$, *m* can assume the values $+\frac{1}{2}$ and $-\frac{1}{2}$ (Figure 2.3).

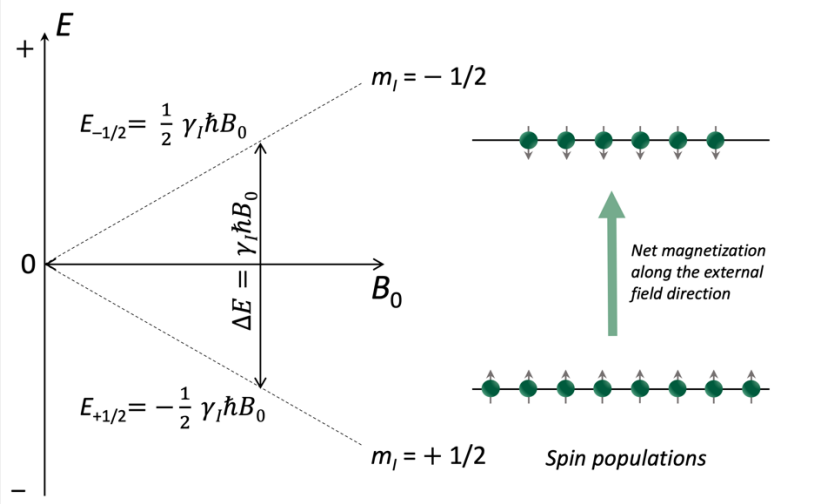

Figure 2.3. Schematic illustration of the *Zeeman* splitting of ^{1}H nuclei in an external magnetic field. The spin state distribution shows a slightly greater population of the lower energy state in comparison to the higher energy state, leading to a longitudinal net magnetization (green arrow) with $\hbar = \frac{h}{2\pi}$ and B_0 being the external magnetic field.[10]

In thermal equilibrium, there is merely a small energy difference between the system's eigenstates, resulting in a Boltzmann distribution of the protons, where the lower energy state is only slightly more populated than the higher energy state, leading to the longitudinal net magnetization M_0. The exposure of the nuclei to radiofrequency radiation at the so-called Larmor frequency leads to spin inversion, with the following resonance condition:[11]

$$\Delta E = h\upsilon = \gamma \frac{h}{2\pi} B_0$$

As a result of the spin inversion, the net magnetization moves away from B_0, with a predominant in-phase precession of the magnetic moments, generating a transversal magnetization M_{xy}.

Switching off the radiofrequency pulse, the induced transversal magnetization starts to relax and precess back to the initial state in thermal equilibrium at a static magnetic field B_0. The resulting fluctuations of the magnetic field generate a current in a receiver coil.

Two main types of relaxation processes can be differentiated: On the one hand, the longitudinal relaxation, indicated by the relaxation time *T1*, describes the return of the excited spin states to the thermal equilibrium with the slightly higher population of lower energy states, resuming the predominant longitudinal net magnetization. On the other hand, the

spin-spin relaxation or transversal relaxation, which describes the dephasing of the phase-coherent precessing magnetic moments, due to entropic effects.

The detection of NMR signals is based on the induction of a current in a receiver coil. Here, the oscillation of the precessing net magnetization resulting from the radiofrequency pulse generates a current, which decreases exponentially due to the aforementioned relaxation processes, yielding a spectrum in the time-domain, referred to as the free induction decay (FID). The FID is then transformed to the frequency-domain *via* Fourier transformation, providing the conventionally known NMR spectrum. With NMR signals being referenced to a particular compound, chemical shifts are independent of the applied *B*-field, enabling the differentiation of atoms and protons based on their chemical environments.[9, 11, 12]

NMR spectra were recorded on BRUKER Avance III HD spectrometers.

2.4 UV-vis-NIR Spectroscopy

UV-vis-NIR spectroscopy is a powerful tool for the quantitative characterization of a material's optical properties in liquid or solid samples or as thin films. Here, the sample is irradiated with monochromatic ultra-violet (UV), visible (vis) and near-infrared (NIR) light, leading to the excitation of valence electrons from the ground state S_0 to higher, excited states S_n with n>0.[9]

When investigating semiconducting materials, such as covalent organic frameworks, UV-vis-NIR spectroscopy provides information concerning the band structure of the samples. If the frequency, and thus the energy, of the incoming photon matches the energy gap between the ground state and the excited states, the photon can be absorbed by the sample.[9]

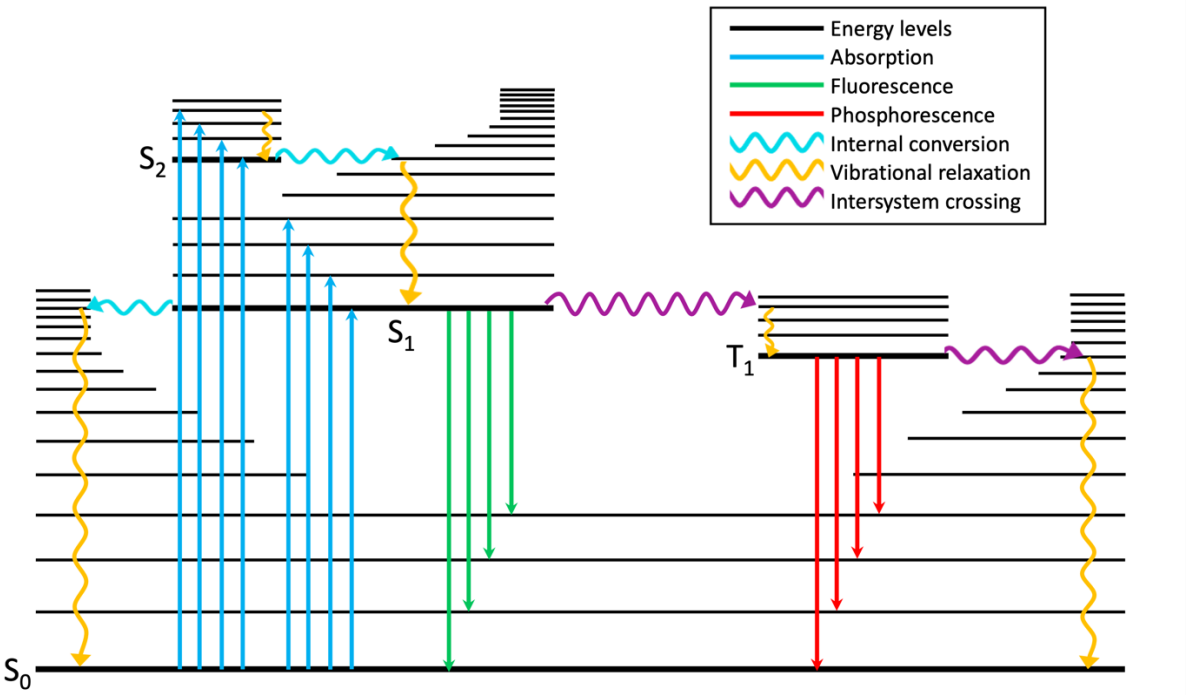

Figure 2.4. Simplified illustration of the absorption and relaxation processes occurring after photoexcitation of the examined sample.

The Jablonski diagram shown in Figure 2.4 visualizes absorption and relaxation processes following the irradiation of a sample with monochromatic light. After absorbing the photon's energy (blue arrows), radiative and non-radiative relaxation processes can occur, leading to fluorescence (green arrows), phosphorescence (red arrows), or vibrational relaxation processes (yellow arrows).

When examining a homogeneously diluted sample, the attenuation of the incoming light beam can be described with the following equation:

$$I(\lambda) = I_0(\lambda) - I_{abs}(\lambda),$$

where $I(\lambda)$ describes the transmitted intensity of the light, $I_0(\lambda)$ the intensity of the incoming light beam, and $I_{abs}(\lambda)$ the intensity absorbed by the sample.

Using Lambert Beer's law, it is now possible to determine the absorbance ($A(\lambda)$ by correlating the measured attenuation of the incoming light with the concentration *c*, the molar extinction coefficient $\varepsilon(\lambda)$ and the path length *d*:

$$A(\lambda) = log\frac{I_0(\lambda)}{I(\lambda)} = \varepsilon(\lambda) \cdot c \cdot d$$

Whilst it is possible to measure the absorption of COF building blocks in solution, the final COF materials are insoluble and are therefore often examined with diffuse reflectance measurements based on the Kubelka-Munk (KM) theory. Here, the sample is diluted with barium sulfate and the diffuse reflectance R is determined. The data are then referenced to barium sulfate as the white standard, and converted into a spectrum using the Kubelka-Munk equation:

$$KM = \frac{(1-R)^2}{2R}$$

For the analysis of thin films on a substrate, the transmission and reflection spectra of the sample are recorded. Here, the film is respectively placed in a small aperture in front of an integrating sphere (transmission), or behind the integrating sphere (reflectance). The absorbance of the sample is then calculated with the following equation:

$$\%T + \%R + \%A = 1$$

UV-Vis spectra were recorded on a PERKIN-ELMER Lambda 1050 spectrometer equipped with a 150 mm integrating sphere featuring an InGaAs detector. Absorbance spectra of the starting materials were measured with 50 µM chloroform solutions. Diffuse reflectance spectra were recorded with a HARRICK Praying Mantis accessory kit and were referenced to barium sulfate powder as the white standard.

2.5 Nitrogen Sorption

Nitrogen sorption represents a very important analytical method for porous materials such as COFs. In a nitrogen sorption measurement, the sample is probed with an inert gas, usually nitrogen, which then provides information concerning the pore size, the pore volume, and the surface area. Furthermore, conclusions regarding the pore accessibility of the investigated material can be drawn. In nitrogen sorption analysis, the gaseous nitrogen molecules, referred to as the adsorptive, reversibly bind to the surface of the sample, referred to as the adsorbent. The nitrogen molecules merely are attached to the sample surface *via* weak *van-der-Waals* forces, which represents a physisorption process, in contrast to chemisorption, a process where chemical bonds are formed between adsorptive and adsorbent, and which therefore can be irreversible.[13]

The nitrogen sorption analysis is conducted at 77 K, the boiling temperature of nitrogen, and both an adsorption and desorption isotherm are recorded at predetermined relative pressure values p/p_0, where p describes the equilibrium pressure and p_0 the saturation vapor pressure. Here, the volume of the adsorbed gas is measured at each relative pressure value using preset equilibration conditions. Keeping the temperature constant, the adsorption isotherm is obtained by the gradual increase of the relative pressure and thus the amount of adsorptive, whilst the desorption isotherm is measured whilst reducing the relative pressure.

According to the IUPAC, pores of porous materials are divided into three size categories:[13]

I. macroporous materials: pore size $>$ 50 nm
II. mesoporous materials: pore size between 2 nm and 50 nm
III. microporous materials: pore size $<$ 2 nm

Furthermore, the isotherms obtained from the physisorption analysis are also categorized into eight different types, shown in Figure 2.5.

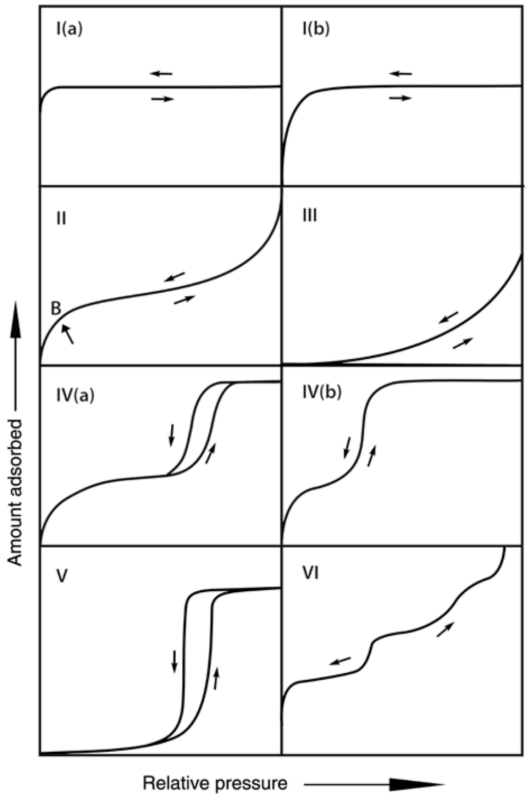

Figure 2.5. Physisorption isotherm types according to IUPAC. Reprinted with permission.[14] Copyright (2015) IUPAC & De Gruyter.

Type I Microporous material. Maximum filling of the pores is reached at low relative pressure values. Strong interactions occur between the adsorptive and the adsorbent. Type I(a) represents a micropore width below 1 nm; Type I(b) is found for larger micropores and small mesopores of up to 2.5 nm.

Type II Non-porous or macroporous materials. The monolayer adsorption at point B is followed by multilayer adsorption at higher relative pressure values.

Type III Nonporous or macroporous materials. Weak interactions between the adsorbent and the adsorbate (adsorbed gas molecules) cause no identifiable monolayer formation point.

Type IV Mesoporous materials. The initial monolayer formation resembles the type II isotherm and is then followed by pore condensation, where the gas condenses to a liquid-like phase at a pressure p below the saturation pressure p_0. At higher relative pressure values type IV isotherms reach a final saturation plateau. Type

IV(a): Hysteresis due to capillary condensation, which occurs for pores exceeding a certain critical width. Type IV(b): Smaller mesopores.

Type V — Mesoporous materials. The lower relative pressure range resembles type III isotherms with weak interactions between adsorbent and adsorbate. Condensation and pore filling at higher relative pressure values cause the hysteresis.

Type VI — Nonporous material. The cascade-shaped isotherm represents a layer-by-layer adsorption behavior. The respective layer capacities are shown by the step height.[14]

Most covalent organic frameworks exhibit pore sizes between larger micropores and smaller mesopores. Typically, mesoporous COFs show type IV isotherms, sometimes including a hysteresis based on capillary condensation (type IV(a)) if the pore size exceeds a certain value.

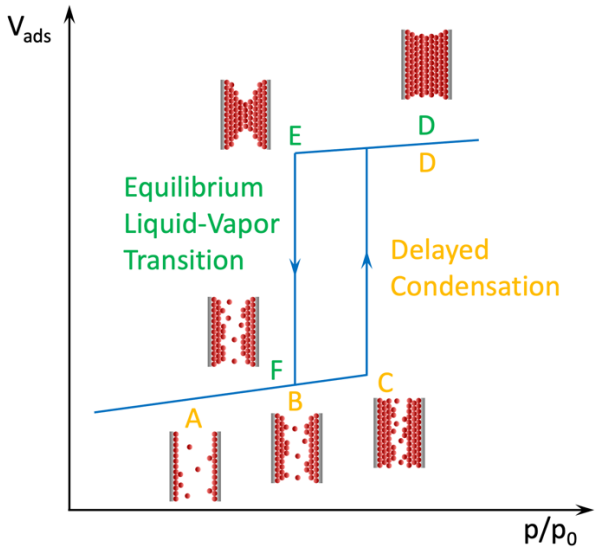

Figure 2.6. Schematic illustration of a type IV(a) isotherm showing hysteresis due to capillary condensation in the mesopores. Adapted with permission.[15] Copyright (2021) Carola Schlumberger and Matthias Thommes. Publisher: WILEY-VCH GmbH.

Figure 2.6 schematically illustrates the capillary condensation process leading to a type IV(a) isotherm with hysteresis. Here, the hysteresis results from a delayed condensation in the adsorption process (A – D). The metastable multilayer adsorption stops at a vapor-liquid spinodal, when the pore fluid spontaneously condenses to a liquid-like state (point C). In case

of the desorption (D – F), the process is in thermodynamic equilibrium and the liquid-vapor transition proceeds *via* a receding meniscus with an evaporation without nucleation. Hence, the equilibrium phase transition occurs at point E.[15]

For the interpretation of physisorption measurements, most frequently the Brunauer-Emmett-Teller (BET) equation is applied, allowing for a quantitative determination of the material's surface area. The BET method further developed the original Langmuir model, which only assumed a monolayer adsorption. The BET model expands this concept for a multilayer adsorption, assuming the adsorption enthalpy of the first adsorbed layer to exceed that of the following layers. Hence, the monolayer capacity n_m^a can be calculated using the BET equation:

$$\frac{p}{n^a\,(p_0 - p)} = \frac{1}{n_m^a} + \frac{(C-1)\,p}{n_m^a\,C\,p_0},$$

where *p* is the equilibrium pressure, n^a the amount of adsorptive, p_0 the saturation vapor pressure, and *C* the BET constant.[13]

Here, a linear relationship between $\frac{p}{n^a\,(p_0 - p)}$ and $\frac{p}{p_0}$ is vital for the correct calculation of the monolayer capacity. This linear relationship usually is found for relative pressure values between 0.05 and 0.30.[16]

The BET surface area a_s (BET) can be determined according to the following equation:

$$a_s\,(BET) = n_m^a\,\sigma_m\,\frac{N_A}{m}$$

with σ_m being the molecular cross-sectional area and N_A the Avogadro constant.[13]

Nitrogen sorption measurements were performed at 77 K on a QUANTACHROME INSTRUMENTS Autosorb-IQ within a pressure range of $p/p_0 = 10^{-5}$ – 0.98. The samples were preheated in vacuo at 100 °C for 60 min to 24 hours. ASiQwin Version 3.0 was used for data analysis. BET surface areas were calculated based on the pressure range between 0.05 and 0.2 p/p_0. The calculation of the pore size distribution was conducted using the QSDFT equilibrium model with a carbon kernel for cylindrical pores.

2.6 Infrared Spectroscopy

Infrared (IR) spectroscopy is based on the absorption of electromagnetic radiation with frequencies of around 400 – 4000 cm^{-1}, thus from the infrared spectral region.[9] This technique provides useful information about chemical bonds and functional groups in a system. Dependent on these bonds or groups, radiation of a specific frequency, matching that of the energy difference of the respective vibrational (and possibly rotational) quantum numbers, is absorbed, leading to an excitation of vibrational and rotational modes and thus to a movement of the sample atoms. The extent of this excitation depends on the atomic masses and the bond strengths, with bonds acting like springs of varying stiffness connecting different atoms. Here, an increased bond strength and a lower atomic weight require more excitation energy and therefore lead to higher vibrational frequencies.[17] This relationship can be illustrated by the approximation of the classical harmonic oscillator with two masses m_1 and m_2, connected by an elastic spring with fixed spring constant *k*. The corresponding vibrational frequency ν_{osc} is given by the following equation:

$$\nu_{osc} = \frac{1}{2\pi}\sqrt{\frac{k}{\mu}}$$

where μ the reduced mass.

Figure 2.7 schematically depicts the curves for a harmonic oscillator (solid line) and an anharmonic oscillator (dashed line), the latter featuring non-constant *k*.

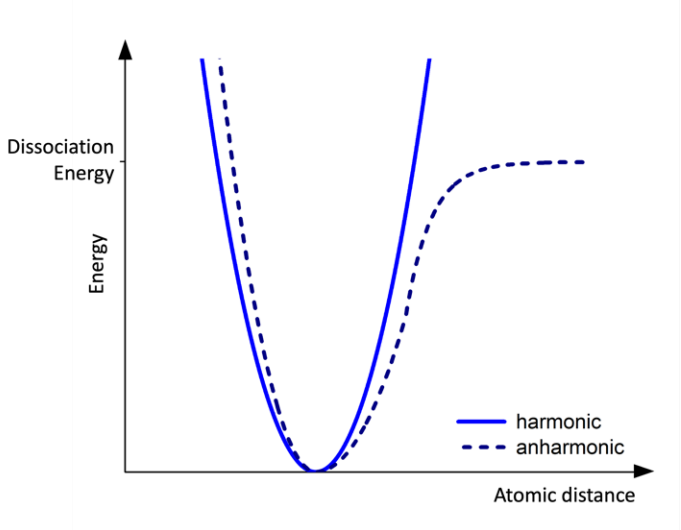

Figure 2.7. Schematic illustration of the relationship between energy and atomic distance in a harmonic oscillator (solid line) and an anharmonic oscillator (dashed line).

In contrast to the harmonic oscillator, which does not account for the possibility of dissociation or repulsion depending on the atomic distance, the model of the anharmonic oscillator incorporates this option. Here, reaching the dissociation energy will cause the dissociation, and thus the breaking, of the atomic bond.[17]

Given that many chemical bonds, functional groups, and organic molecules exhibit characteristic vibrations, it is possible to identify and distinguish them with IR spectroscopy, as well as to investigate the overall molecular constitution of the sample. In contrast to UV-vis spectroscopy, where spectra are often plotted as function of wavelength, the use of wavenumbers in IR spectroscopy is more common, and advantageous due to the direct relationship of wavenumbers to frequency and thus energy.

A key selection rule identifies the prerequisites for IR spectroscopy: only molecular vibrations that show a temporary change of the electronic dipole moment during the vibration are allowed, or IR-active. In case of a centrosymmetric molecule, molecular vibrations that are symmetric to the center of symmetry are forbidden, or IR-inactive. Only if a dipole moment is induced in a centrosymmetric molecule by an antisymmetric molecular vibration, these modes can be observed in the IR spectrum. [17, 18]

Fourier-transform infrared (FT-IR) spectroscopy represents an enhanced measuring technique, offering fast collection of spectra and high resolution.

Fourier-transform infrared (FTIR) spectra were recorded on a Bruker Vertex 70 FTIR instrument using a liquid nitrogen-cooled MCT detector and a germanium ATR crystal.

2.7 Electron Microscopy

Recording microscopy images is an important analysis method for gaining structural and morphological information of a material. In the case of nanostructured samples, conventional light microscopy cannot be applied for this image acquisition due to the spatial resolution limit of this technique, the so-called Abbe limit, which restricts the resolution to approximately 200 nm. Hence, for imaging nanomaterials such as covalent organic frameworks, shorter wavelength radiation analysis techniques are chosen. Electrons in electron microscopes exhibit a significantly shorter wavelength than visible light, which allows one to achieve sub-nanometer resolution. The wavelength of the electrons, as shown by the de-Broglie relation, is dependent on the acceleration voltage *V*, with a higher acceleration voltage resulting in a shorter electron wavelength λ.[2, 19]

$$\lambda = \frac{h}{p} = \frac{h}{\sqrt{2m_e qV}}$$

with the Planck constant *h*, the electron mass m_e, and the elementary charge *q*.

In an electron microscopy set-up, electrons are accelerated under high vacuum, and focused onto the sample using a set of electromagnetic lenses. The interaction of the electrons with the sample causes a variety of signals, such as secondary electrons (SE), backscattered electrons (BSE), and transmitted primary electrons, amongst others (Figure 2.8).[20]

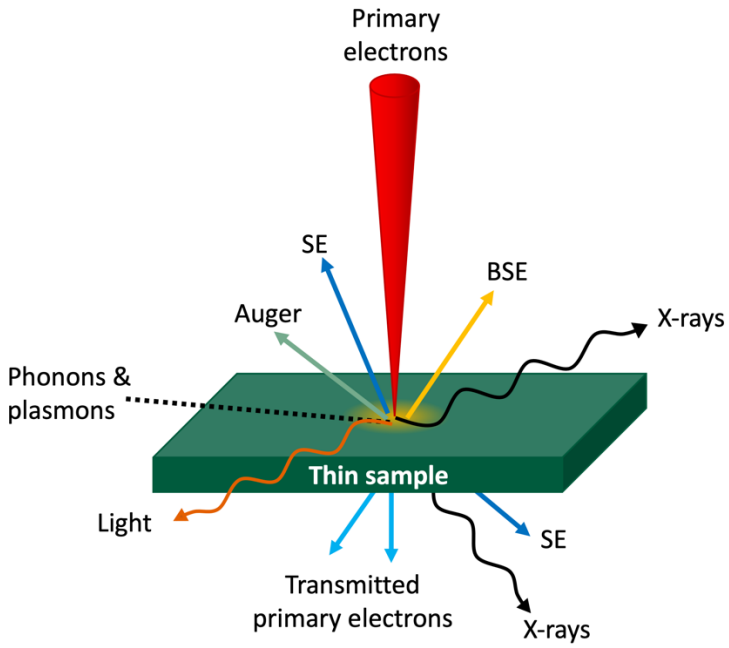

Figure 2.8. Schematic illustration of different possible interactions between an incoming primary electron beam and the sample.

2.7.1 Scanning Electron Microscopy

Scanning electron microscopy (SEM) enables the morphological investigation of a material, providing information on surface properties and topography. As indicated by the name, the incoming primary electron beam scans, or rasters, the sample, causing different interactions in the investigated material (Figure 2.8). Typically, acceleration voltages of 1 – 30 kV are chosen, with the voltages for the examination of fully organic materials, such as covalent organic frameworks, generally being below 5 kV. Figure 2.9 illustrates the set-up of a typical scanning electron microscope.

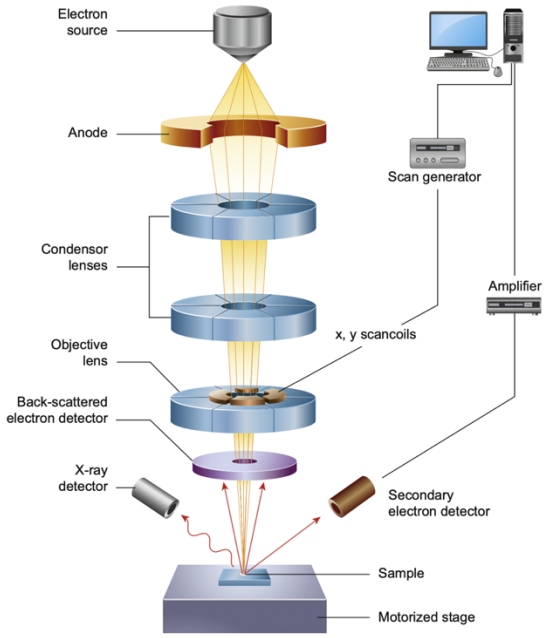

Figure 2.9. Schematic illustration of a scanning electron microscope set-up. Reprinted with permission.[21] Copyright (2016) Elsevier.

Electrons are generated in the electron source, which is either a thermionic emitter (W or LaB_6) or a field emission gun (FEG). The primary electrons are then accelerated towards the anode and focused by a set of electromagnetic lenses, directing the electron beam onto the sample. Depending on the operation mode, different detectors are used for the detection of emitted signals. In the common operation modes, secondary electrons (SE) or backscattered electrons (BSE) are detected for the generation of an image. The former result from inelastic scattering of the primary electrons, which most likely happens at outer-shell electrons at the sample surface. In contrast, the latter are defined as primary electrons that are elastically scattered at an angle greater than 90° and possess a kinetic energy above 50 eV. The detection of BSE furthermore offers the possibility to image the compositional contrast of the sample, with heavier elements with larger atomic numbers appearing brighter due to the larger number of BSE.

Apart from SE and BSE, it is also possible to detect X-rays that are generated when a sample atom is ionized due to the interaction with the primary electron beam, and the resulting electron vacancy is refilled by a higher-shell electron. The generated X-ray radiation is used for energy-dispersive X-ray spectroscopy (EDX), as it is characteristic for the respective sample elements, providing information on the elementary composition of the material. [22, 23]

SEM images were recorded on an FEI Helios NanoLab G3 UC scanning electron microscope equipped with a field emission gun operated at 1 - 30 kV.

2.7.2 Transmission Electron Microscopy

In transmission electron microscopy (TEM), unlike SEM, transmitted primary electrons are detected and used for image generation. Therefore, samples examined by TEM have to be very thin, allowing electrons to pass through the specimen. Using this technique, images with high resolution down to the atomic level can be obtained. Here, the primary electron beam with energies of typically up to 400 keV is not scanned across the sample as in SEM, but evenly focused on the sample. Figure 2.10 exemplarily shows a schematic set-up of a transmission electron microscope.

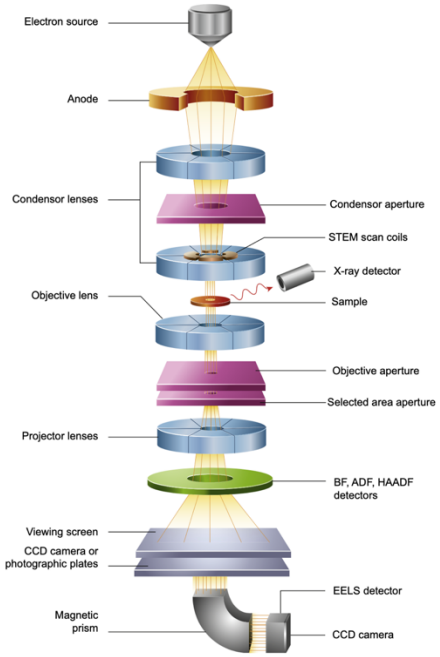

Figure 2.10. Schematic illustration of a transmission electron microscope set-up. Reprinted with permission.[21] Copyright (2016) Elsevier.

As for SEM, electrons are generated by the electron source, a thermionic emitter or a field emission gun, accelerated towards the anode, and focused *via* a set of electromagnetic lenses onto the sample. The transmitted electrons are focused by the objective lens behind the sample, creating a diffraction pattern in the back-focal plane. TEM can be conducted in different operation modes: bright-field (BF), dark-field (DF) and high-resolution TEM (HRTEM). For the BF mode, the objective aperture is adjusted in a way that solely allows unscattered

electrons to pass. Hence, areas with less scattering events, i.e. with light-weight atoms and smaller thickness, appear brighter than areas causing more scattering events. The reverse is true for the DF mode, where the objective aperture blocks the directly transmitted electron beam and only scattered electrons are detected. In this case areas producing more scattered electrons appear brighter. HRTEM is a complex operation mode for the acquisition of images with resolutions at the atomic level. Here, the image generation is based on the interference of the transmitted electron wave in the image plane.[22-24] Transmission electron microscopy not only enables the generation of real space images that give information on the sample's morphology and atomic lattice structure, but also provides electron diffraction patterns, which can be used to gain structural information in the reciprocal space.[24]

TEM images were recorded on an FEI Titan Themis transmission electron microscope equipped with a field emission gun run at 300 kV.

2.8 Cyclic voltammetry

Cyclic voltammetry (CV) is a commonly used measurement technique for the investigation of a material's electrochemical properties. Cyclic voltammograms shed light on the redox behavior and the reversibility of redox cycles of the examined sample. CV experiments usually are performed in a three-electrode set-up, comprising a working electrode, a counter electrode, and a reference electrode, immersed in an electrolyte solution. Here, the material under investigation functions as the working electrode and is reduced/oxidized, while the counter electrode is needed for the balancing of these redox reactions and the closing of the electric circuit. The reference electrode is crucial for avoiding undesired potential fluctuations throughout the measurements. In a CV experiment, a continuous potential sweep between two vertex potentials (Figure 2.11, a) is applied with a fixed scan speed, and the current response is recorded and analyzed (Figure 2.11, b).[25, 26]

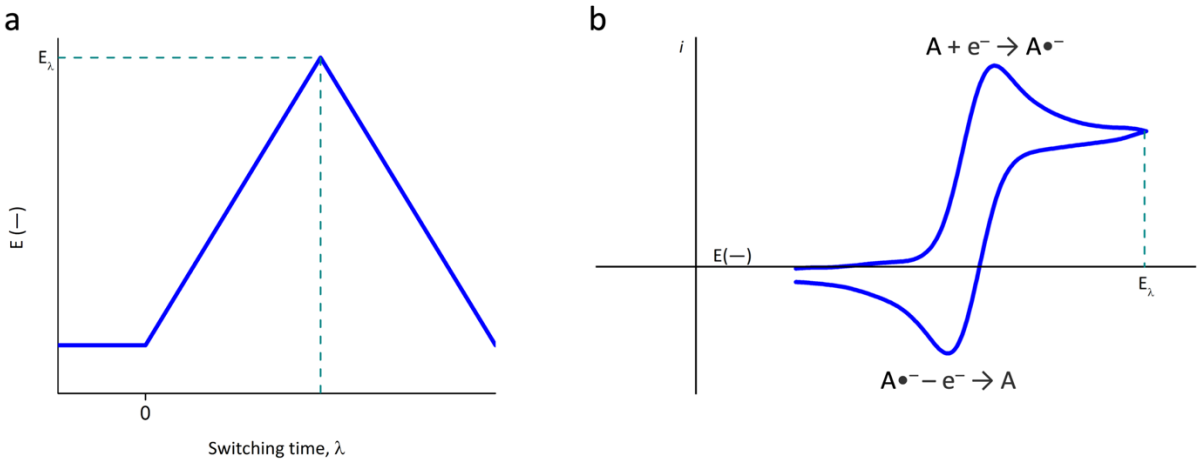

Figure 2.11. (a) Continuous triangular potential wave as a function of time, swept between two vertex potential values. **(b)** Schematic cyclic voltammogram, showing the current response *i* as a function of the applied potential *E*. Adapted with permission.[26] Copyright (2000) John Wiley and Sons.

In the cyclic voltammogram (Figure 2.11, b), an increase of the negative potential *E* eventually leads to a current response *i*, indicating the reduction of the examined material at the working electrode ($A + e^- \rightarrow A^{\bullet -}$), which is illustrated by the distinct reduction peak. After the completion of the reduction process, the current response drops, and the scanning direction is reversed at E_λ. Gradually decreasing the applied potential at the fixed scan rate leads to the corresponding oxidation of the material back to the original neutral state ($A^{\bullet -} - e^- \rightarrow A$), indicated by the distinct oxidation peak.[26]

Cyclic voltammograms can be plotted according to two different conventions. The above-described CV curve (Figure 2.11, b) is an example for the US convention, where potentials are plotted from high to low (negative) and the cathodic current of the reduction process is shown in positive direction on the ordinate axis. In contrast, in cyclic voltammograms following the IUPAC convention, potentials are indicated from low to high (positive) along the abscissa, and the anodic current of the oxidation process is shown on the ordinate in positive direction.[26-28] In this thesis, cyclic voltammograms are plotted according to the IUPAC convention (Figure 2.12).

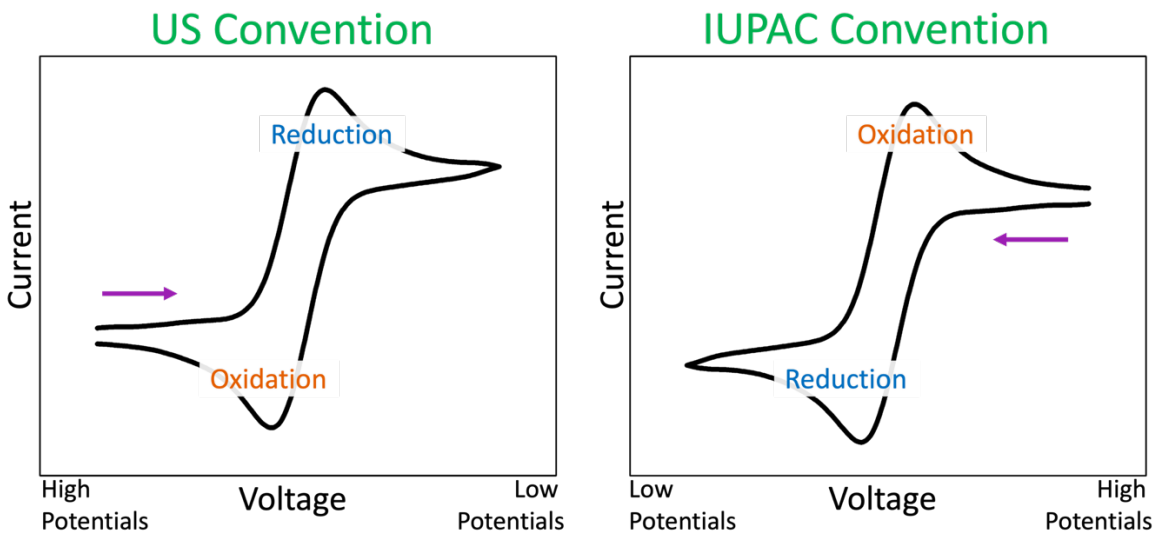

Figure 2.12. Comparison of the US convention (left) and the IUPAC convention (right) for the presentation of cyclic voltammograms.[25]

The measured current response is the sum of faradaic currents that describe the currents deriving from electron transfer, hence redox reactions, and potential capacitive effects, such as accumulation or dissipation processes of charge carriers at interfaces.[29]

For the measurement of the cyclic voltammograms in this thesis, a three-electrode set-up with COF thin films grown on ITO or Au/glass substrates as the working electrode and a platinum wire counter electrode was used. The reference electrode consisted of an Ag/AgCl electrode or an Ag wire. All electrodes were immersed in a 0.1 M tetrabutylammonium hexafluorophosphate ($TBAPF_6$) electrolyte solution in acetonitrile. 0.1 mM Ferrocene (fc) solution was used as a standard in control experiments with a blank ITO working electrode. All potentials are referenced to the fc/fc^+ redox pair. All electrochemical measurements were performed with a Metrohm Autolab PGSTAT potentiostat/galvanostat.

2.9 References

1. Waseda, Y.; Matsubara, E.; Shinoda, K., *X-Ray Diffraction Crystallography*. Springer-Verlag Berlin: Heidelberg, 2011.
2. Cao, G.; Wang, Y., *Nanostructures and Nanomaterials*. World Scientific: 2011; Vol. Volume 2, p 596.
3. Cullity, B. D., *Elements of X-ray Diffraction*. 2nd ed.; Addison-Wesley Publishing Company: Reading, Massachusetts, 1978.
4. Elton, L. R. B.; Jackson, D. F., X-Ray Diffraction and the Bragg Law. *Am. J. Phys.* **1966,** *34*, 1036-1038.
5. Scherrer, P., Bestimmung der Größe und der inneren Struktur von Kolloidteilchen mittels Röntgenstrahlen. *Nachrichten von der Gesellschaft der Wissenschaften zu Göttingen, Mathematisch-Physikalische Klasse* **1918**, 98-100.
6. Saxena, V.; Portale, G., Nanomaterials. **2020,** *10*, 2240.
7. Müller-Buschbaum, P., A Basic Introduction to Grazing Incidence Small-Angle X-Ray Scattering. In *Applications of Synchrotron Light to Scattering and Diffraction in Materials and Life Sciences*, Gomez, M.; Nogales, A.; Garcia-Gutierrez, M. C.; Ezquerra, T. A., Eds. Springer Berlin Heidelberg: Berlin, Heidelberg, 2009; pp 61-89.
8. Birkholz, M., *Thin Film Analysis by X-Ray Scattering*. Wiley-VCH: Weinheim, 2006.
9. Hesse, M.; Meier, H.; Zeeh, B., *Spektroskopische Methoden in der organischen Chemie*. Thieme: Stuttgart, 2005; Vol. 7.
10. *NMR and MRI of Electrochemical Energy Storage Materials and Devices*. The Royal Society of Chemistry: 2021.
11. Ward, R. L., A Complete Introduction to Modern NMR Spectroscopy (Macomber, Rodger S.). *J. Chem Educ.* **1999,** *76*, 473.
12. Levitt, M. H., *Spin Dynamics - Basics of Nuclear Magnetic Resonance*. 2nd ed.; John Wiley & Sons Ltd.: Chichester, 2008.
13. Sing, K. S. W.; Everett, D. H.; Haul, R. A. W.; Moscou, L.; Pierotti, R. A.; Rouquerol, J.; Siemieniewska, T., Reporting Physisorption Data for Gas/Solid Systems with Special Reference to the Determination of Surface Area and Porosity. *Pure Appl. Chem.* **1985,** *57*, 603-619.
14. Thommes, M.; Kaneko, K.; Neimark, A. V.; Olivier, J.; Rodriguez-Reinoso, F.; Rouquerol, J.; Sing, K. S. W., Physisorption of gases, with special reference to the

evaluation of surface area and pore size distribution. *Pure Appl. Chem.* **2015,** *87*, 1051-1069.

15. Schlumberger, C.; Thommes, M., Characterization of Hierarchically Ordered Porous Materials by Physisorption and Mercury Porosimetry—A Tutorial Review. *Adv. Mater. Interfaces* **2021,** *8*, 2002181.
16. Brunauer, S.; Emmett, P. H.; Teller, E., Adsorption of Gases in Multimolecular Layers. *J. Am. Chem. Soc.* **1938,** *60*, 309-319.
17. Günzler, H.; Gremlich, H.-U., *IR-Spektroskopie: Eine Einführung*. 4th ed.; Wiley-VCH: Weinheim, 2003.
18. Weidlein, J.; Müller, U.; Dehnicke, K., *Schwingungsspektroskopie, Eine Einführung*. 2nd ed.; Georg Thieme Verlag: Stuttgart, 1988.
19. Atkins, P. W.; de Paula, J., *Physikalische Chemie*. 4th ed.; Wiley-VCH: Weinheim, 2006.
20. Brandon, D.; Kaplan, W. D., *Microstructural Characterization of Materials*. 2nd ed.; John Wiley & Sons: 2008.
21. Inkson, B. J., *Materials Characterization Using Nondestructive Evaluation (NDE) Methods*. Woodhead Publishing: 2016.
22. Dehm, G.; Howe, J. M.; Zweck, J., *In-situ Electron Microscopy*. Wiley-VCH: Weinheim, 2012.
23. Williams, D. B.; Carter, C. B., *Transmission Electron Microscopy*. 2nd ed.; Springer: New York, 2009.
24. Sun, L.; Xu, T.; Zhang, Z., *In-Situ Transmission Electron Microscopy*. Springer: Nanjing, 2023.
25. Elgrishi, N.; Rountree, K. J.; McCarthy, B. D.; Rountree, E. S.; Eisenhart, T. T.; Dempsey, J. L., A Practical Beginner's Guide to Cyclic Voltammetry. *J. Chem Educ.* **2018,** *95*, 197-206.
26. Bard, A. J.; Faulkner, L. R., *Electrochemical Methods: Fundamentals and Applications*. Wiley: 2000.
27. Bates, R. G.; al., e., Recommendations for Sign Conventions and Plotting of Electrochemical Data. *Pure & Appl. Chem.* **1976,** *45*, 131-134.
28. Comption, R. G.; Banks, C. E., *Understanding Voltammetry*. 3rd ed.; World Scientific: London, 2018.

29. Hamann, C. H.; Hamnett, A.; Vielstich, W., *Electrochemistry*. 2nd ed.; Wiley-VCH: Weinheim, 2007.

3. Fast-Switching Vis-IR Electrochromic Covalent Organic Frameworks

This chapter is based on the following publication:

Derya Bessinger, Katharina Muggli, Michael Beetz, Florian Auras*, Thomas Bein*

J. Am. Chem. Soc. **2021**, *143*, 7351−7357

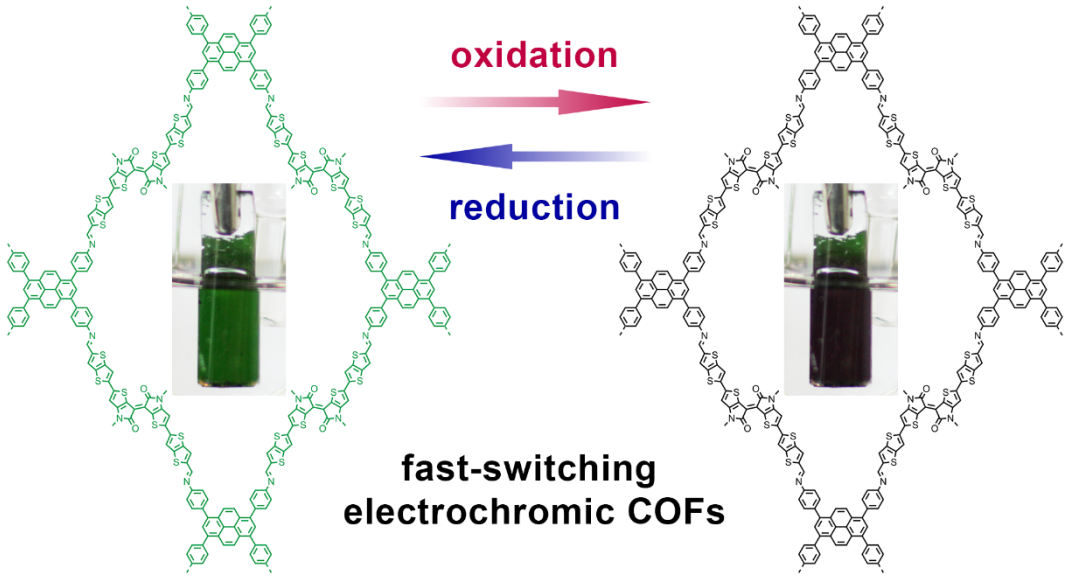

The development, synthesis, and characterization of the nTII building block, and the Py-nTII COF were carried out by K. Muggli. Furthermore, K. Muggli contributed to the development and synthesis of the Py-N COF and to the syntheses of the ttTII building block, the Py-ttTII COF and the Py-TII COF. All electrochromism and electrochromism-related experiments, measurements and analyses were conducted in equal parts by K. Muggli, D. Bessinger, and F. Auras.

* corresponding authors

3. Fast-Switching Vis-IR Electrochromic Covalent Organic Frameworks

The article was published with the Supplementary Cover Art in issue 19 from May 2021.

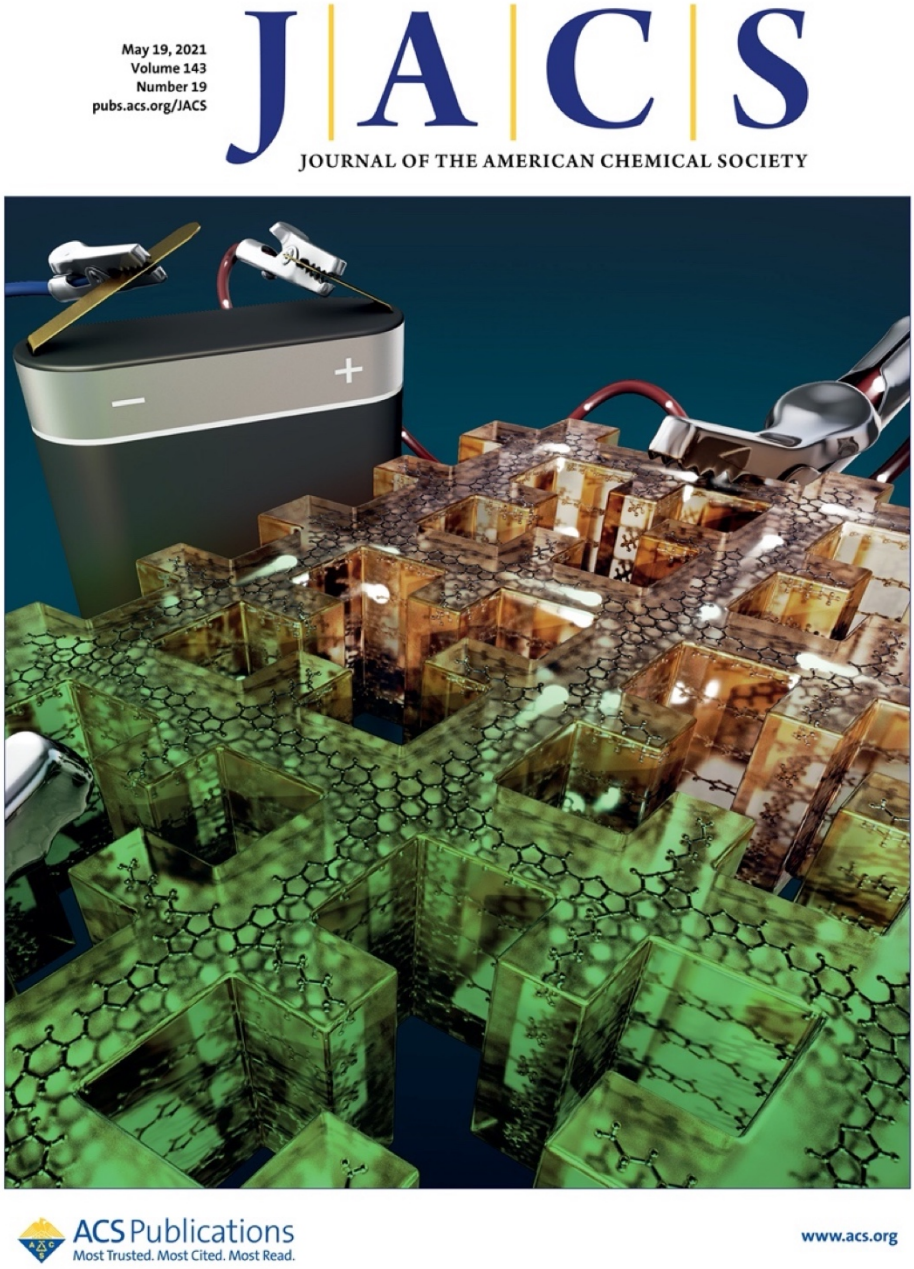

Cover artwork: Vera Hiendl (e-conversion cluster)

based on an idea of F. Auras, D. Bessinger, and V. Hiendl

3.1 Abstract

Electrochromic coatings are promising for applications in smart windows or energy-efficient optical displays. However, classical inorganic electrochromic materials such as WO_3 suffer from low coloration efficiency and slow switching speed. We have developed highly efficient and fast-switching electrochromic thin films based on fully organic, porous covalent organic frameworks (COFs). The low-bandgap COFs have strong Vis-NIR absorption bands in the neutral state, which shift significantly upon electrochemical oxidation. Fully reversible absorption changes by close to 3 OD can be triggered at low operating voltages and low charge per unit area. Our champion material reaches an electrochromic coloration efficiency of 858 cm^2 C^{-1} at 880 nm and retains >95% of its electrochromic response over 100 oxidation/reduction cycles. Furthermore, the electrochromic switching is extremely fast with response times below 0.4 s for the oxidation and around 0.2 s for the reduction, outperforming previous COFs by at least an order of magnitude and rendering these materials some of the fastest-switching frameworks to date. This combination of high coloration efficiency and very fast switching reveals intriguing opportunities for applications of porous organic electrochromic materials.

3.2 Introduction

Since their first development in 2005, covalent organic frameworks (COFs) have emerged into a very active research field of tailor-made functional nanostructures.[1-3] Constructed from rigid organic building blocks, COFs combine high crystallinity with a precisely defined porosity and large internal surface area.[4-6] A wide range of functional building blocks enable the design of bespoke networks with well-defined catalytic, optical and electronic properties.[7-11]

Electrochromism describes reversible color changes of a material in response to an external electronic stimulus. Electrochromic materials have been applied in smart windows, optical displays, and molecular imaging.[12-14] In addition to well-established inorganic electrochromic materials such as WO_3, research focuses increasingly on organic molecular compounds and polymers.[15-17] Organic materials offer higher coloration efficiencies and better tunability owing to their broad range of possible chemical modifications, while the higher diffusion rates of charge-compensating counterions allow for faster switching times.[18, 19]

Due to their permanent porosity on a molecular length scale, every building block throughout a COF domain can be brought into contact with an electrolyte, enabling very fast and efficient electrochromic switching. However, first examples of electrochromic COFs based on triphenylamine dyes have not yet reached their full potential as they show only moderate coloration efficiencies and switching speeds.[20, 21]

Here we present a series of fast-switching electrochromic 2D-COFs with panchromatic UV-Vis-IR response and high coloration efficiency. Key to this performance is our linker design strategy where we combine a central thienoisoindigo moiety with more electron-rich units while fully retaining its favorable stacking interactions (Figure 1). This donor-acceptor-donor electronic setup promotes intramolecular charge transfer, leading to strong light absorption across the visible and near IR regions and an increased sensitivity of the absorption spectra towards electrochemical oxidation. COFs constructed from the new building blocks are highly crystalline frameworks with large one-dimensional pores for optimal accessibility of every building block throughout the material. Oriented COF thin films of the best-performing framework are stable over at least 200 oxidation/reduction cycles. They retain >95% of their electrochromic response over 100 cycles, show very rapid switching with response times below 0.4 s (oxidation) and around 0.2 s (reduction), and have coloration efficiencies of up to 858 $cm^2\ C^{-1}$.

3.3 Results

In order to maximize the electrochromic response across the visible and near-infrared (NIR) spectral regions, we constructed building blocks with a donor-acceptor-donor (D-A-D) electronic configuration. This design not only provides a sufficiently small bandgap to push the absorption onset well into the NIR (Supporting Information, Figure 4.11), but also renders the charge-transfer (CT) and π–π* transitions very sensitive to electronic changes such that significant electrochromic response can be expected over a wide spectral range.[18, 22-24] We chose the highly electron-deficient thienoisoindigo (TII) unit as the acceptor and combined it with the more electron-rich thienothiophene (TT) or naphthalene (N) donors, yielding the extended, NIR-absorbing ttTII$(CHO)_2$ and nTII$(CHO)_2$ building blocks, respectively (Figure 4.1). For comparison purposes, we also constructed the dicarboxaldehyde building blocks of the individual components (TII, TT, and N).

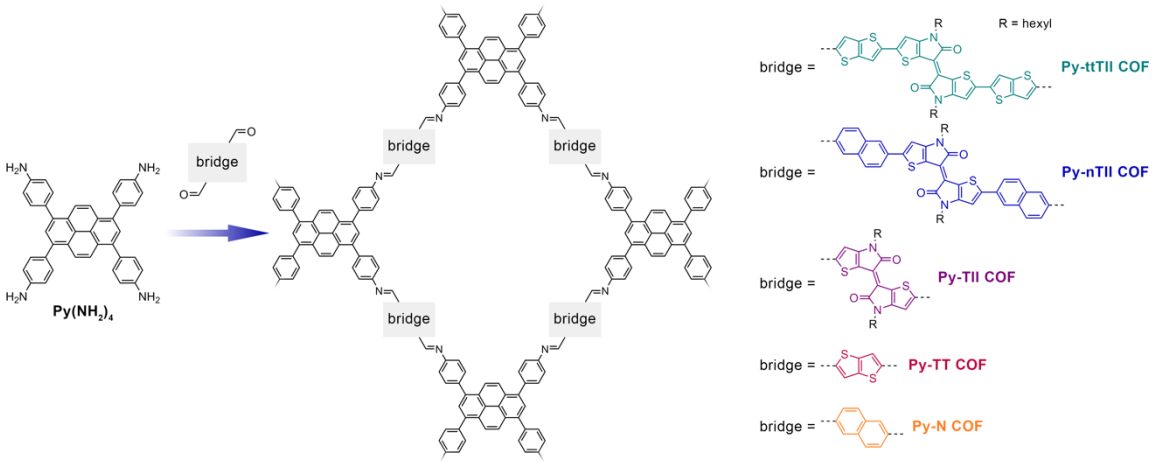

Figure 4.1. Construction of the new thienoisoindigo COFs and the Py-TT and Py-N COF reference materials. The co-condensation of the linear dicarboxaldehydes with the pyrene tetraaniline yields a series of isostructural frameworks with a pseudosquare geometry and slip-stacked 2D layers.

For COF construction we selected the well-established pyrene tetraaniline ($Py(NH_2)_4$) as the tetradentate counterpart. This building block is known to generate exceptionally crystalline and stable 2D-COFs with a broad range of linear linkers and, most importantly, is compatible with heteroaromatic moieties where strong electrostatic interactions enforce slip-stacked arrangements.[25-27] Moreover, the pyrene building block enables the synthesis of very well-oriented COF films on a variety of substrates.[28, 29]

The Py-ttTII, Py-nTII, Py-TII, Py-TT, and Py-N COFs were synthesized under solvothermal conditions with aqueous acetic acid as the catalyst (see the SI, Section B for experimental details). The isoreticular COFs feature a pseudosquare geometry with slip-stacked 2D layers.

When synthesized as a bulk material, the Py-ttTII COF is a dark green powder. Its powder X-ray diffraction pattern exhibits a series of sharp reflections with only minimal background, confirming the formation of a highly crystalline framework (Figure 4.2a). Rietveld refinement carried out in the monoclinic space group *C*2/*m* and using the structure model shown in Figure 4.2b provides a very good fit to the experimental pattern. The refined lattice parameters are a = 6.33 ± 0.02 nm, b = 5.89 ± 0.02 nm, c = 0.39 ± 0.02 nm, and β = 60 ± 5°. Due to the large number of atoms per unit cell and the inherent flexibility of the COF backbone and alkyl chains, it is not possible to refine individual atom positions. Thus, slight differences between the structure model and the actual COF structure are unavoidable, causing the deviations in intensity observed for some of the higher-index reflections.

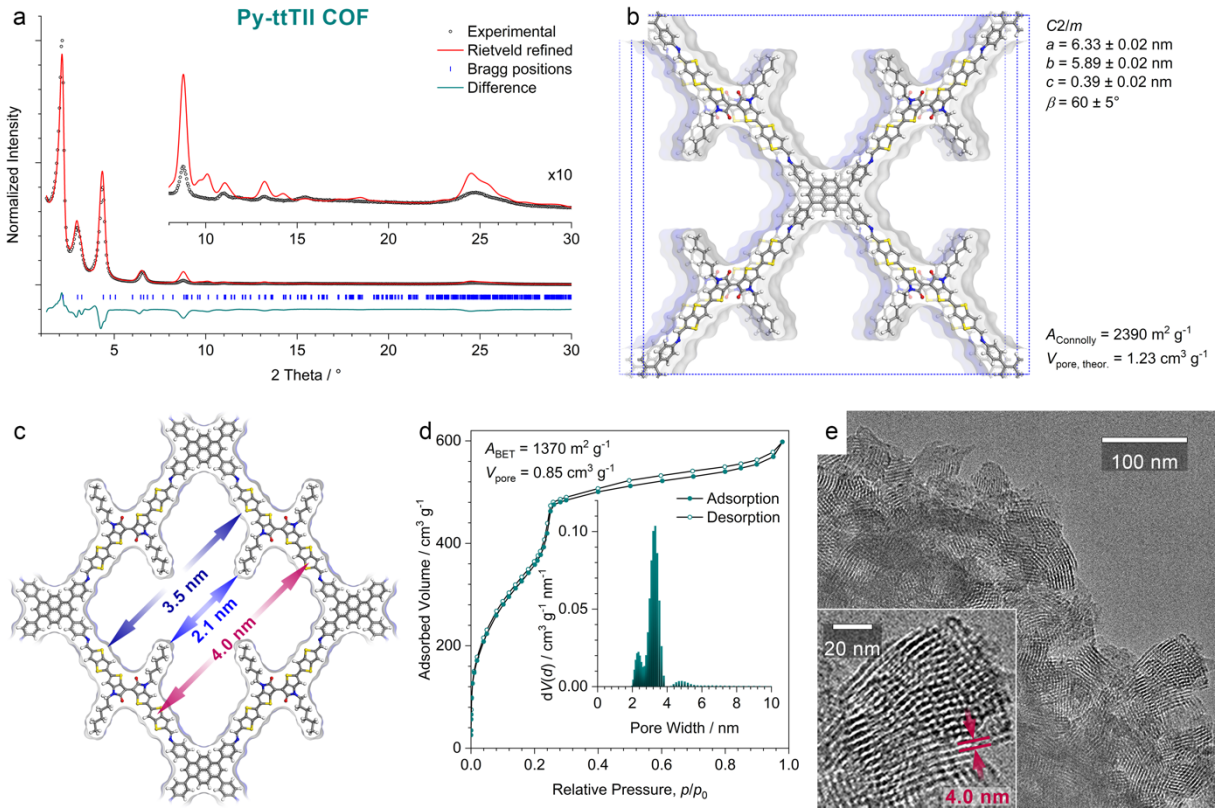

Figure 4.2. Structure analysis of the Py-ttTII COF. (**a**) Experimental PXRD pattern of the Py-ttTII COF bulk material (black dots). Rietveld refinement (red line) using the monoclinic (space group *C*2/*m*) structure model displayed in (b) provides a good fit with only minor differences between the experimental and refined patterns (green line) arising mainly from the flexibility of the alkyl chains. R_{wp} = 12.3%, R_p = 20.9%. Bragg positions are indicated by blue ticks. Inset: Magnified view of the $2\vartheta > 8°$ region. (**b**) The Rietveld-refined structure model of the Py-ttTII COF viewed perpendicular to the crystallographic *a*-*b* plane. The COF has a pseudosquare geometry with slip-stacked layers. The structure is highly porous with a Connolly surface area of 2390 $m^2 g^{-1}$ and a pore volume of 1.23 $cm^3 g^{-1}$. (**c**) Illustration of the pore structure of the COF viewed along the *c*-axis. The structure refinement indicates that in this COF the alkyl chains extend relatively straight into the pores, producing a shamrock-shaped pore cross section. The wall-to-wall distances (blue arrows) are 2.1 nm and 3.5 nm including and excluding the alkyl chains, respectively. The periodicity of the COF in this orientation is 4.0 nm (red arrows). (**d**) Nitrogen sorption isotherm recorded at 77 K. Inset: Fitting the isotherm with a QSDFT equilibrium model for cylindrical pores produces a bimodal pore size distribution (PSD) with peaks at 2.3 nm and 3.4 nm. These values are in good agreement with the wall-to-wall distances including and excluding the alkyl chains derived from the refined structure model, confirming the shamrock-shaped pore cross section. (**e**) High-resolution TEM image of a Py-ttTII COF bulk powder sample showing crystallites of approximately 50 nm diameter. Inset: A crystallite viewed along the pores (i.e., along the crystallographic *c*-axis) showing a periodicity of 4.0 nm in excellent agreement with the structure model.

While the refinement of individual atoms is not possible, the data quality is sufficient to refine the overall orientation of the alkyl chains. In the case of the Py-ttTII COF, the alkyl chains were found to extend straight into the pores, creating a shamrock-shaped pore cross section with

wall-to-wall distances of 3.5 nm and 2.1 nm without and with alkyl chains, respectively (Figure 4.2c). This configuration is very similar to the geometries found in molecular crystals of thienoisoindigos with linear alkyl chains, and is further supported by gas sorption analysis (see below).[30, 31]

The nitrogen sorption isotherm recorded at 77 K exhibits a type IVb isotherm shape with a sharp step at p/p_0 = 0.24, confirming the mesoporosity of the framework (Figure 4.2d).[32] Analysis of the isotherm using the quenched solid density functional theory (QSDFT) method and an equilibrium model for cylindrical pores yields a bimodal pore size distribution (PSD). Bimodal PSDs have been observed previously for alkyl-containing COFs and are the result of the QSDFT method trying to describe a non-cylindrical pore shape.[27] The maxima at 2.3 nm and 3.4 nm are in very good agreement with the wall-to-wall distances with and without alkyl chains, respectively, and further confirm the shamrock-shaped pore cross section with two predominant diagonals. The Py-ttTII COF has a Brunauer-Emmett-Teller (BET) surface area of 1370 $m^2 g^{-1}$ with a total pore volume of 0.85 $cm^3 g^{-1}$. The experimental surface area is about 60% of the Connolly surface area calculated from the idealized structure model. This reduction in porosity is frequently observed for alkyl-chain containing COFs and is mainly attributed to the enhanced trapping of oligomers due to the complex pore shape.[27, 33] However, at 60% of the theoretical porosity, the accessibility throughout the framework is expected to be sufficient for efficient electrochemical switching (see below).

High-resolution transmission electron microscopy (TEM) images reveal the nanocrystalline morphology of the Py-ttTII COF powder with domain sizes of 50 – 100 nm (Figure 4.2e). Crystallites that are oriented with their crystallographic *c*-axis (i.e., along the pores) parallel to the viewing direction confirm the pseudo-square topology with a periodicity of 4.0 nm, which is in excellent agreement with the refined structure model.

The naphthalene-containing Py-nTII COF has a very similar structure and features the same shamrock-shaped pore cross section (SI, Figure 4.5). In contrast, due to the shorter $TII(CHO)_2$ building block, the alkyl chains of the Py-TII COF cannot extend straight into the pore, but are forced to collapse onto the pore walls (SI, Figures 4.6, 4.7). Hence, this COF has significantly narrower pores with a single maximum in the corresponding PSD. The Py-N and Py-TT COFs are highly crystalline frameworks with very similar overall topology but relatively small diamond-shaped pores (SI, Figure 4.9).[28]

For the electrochemistry and spectroelectrochemistry experiments, oriented COF thin films were grown on transparent and conductive indium-tin-oxide (ITO) coated glass (Py-ttTII, Py-TII, Py-TT and Py-N COFs) or 10 nm Au on glass (Py-nTII COF) substrates using modified solvothermal protocols (see the SI, section B for details).

2D grazing-incidence wide-angle X-ray scattering (GIWAXS) measurements confirm that the COF films are crystalline and strongly textured (Figure 4.3a and SI, Figures 4.12, 4.13). For all COFs, the *hk*0 reflections show the highest intensity close to the sample horizon, indicating a preferred orientation of the *a*-*b* plane parallel to the substrate surface. Consistently, the intensity of the 001 and other low-index *hk*1 reflections is concentrated within a 60° segment centered at q_x = 0 / q_z = 18 nm^{-1}. This preferential orientation is highly desired, as the COF pores extend towards the film surface and are fully accessible.

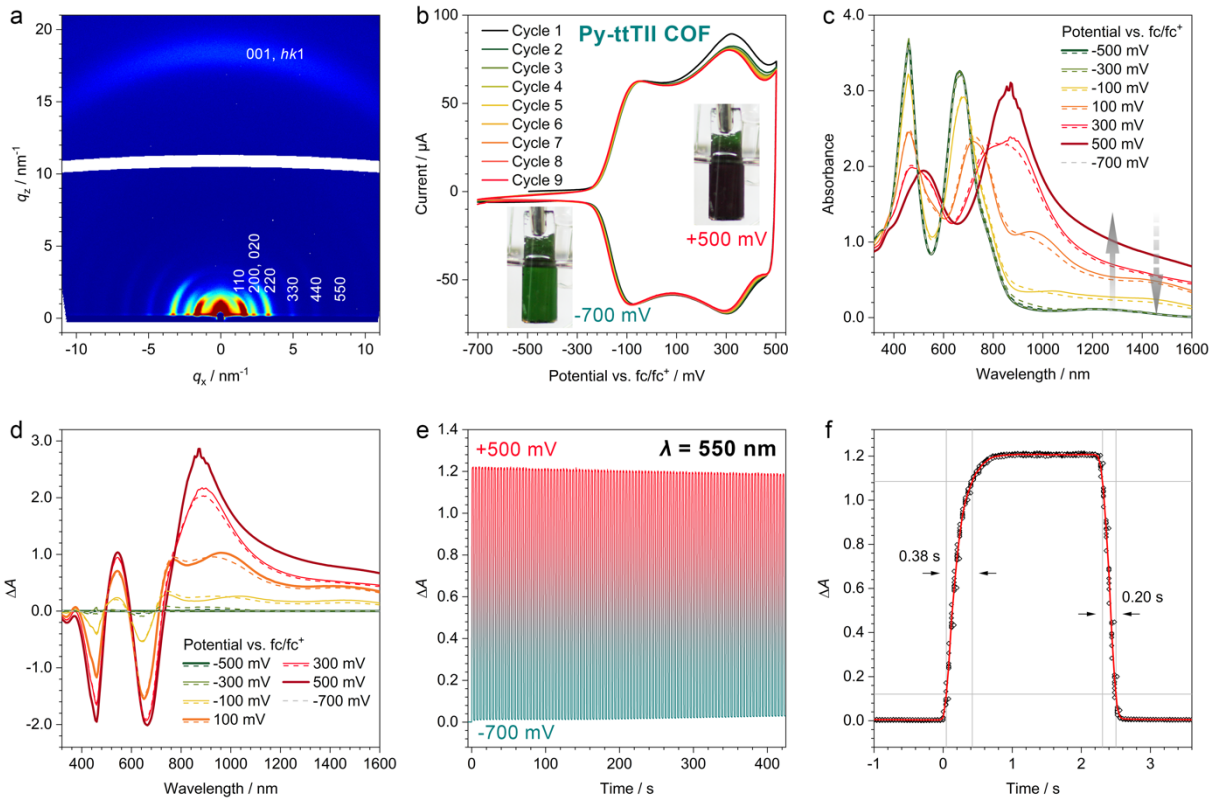

Figure 4.3. Electrochromism of Py-ttTII COF thin films. (**a**) GIWAXS pattern of a 430 nm thick Py-ttTII COF film grown on ITO/glass. Color scaling is logarithmic. The intensities of the *hk*0 reflections are concentrated directly above the sample horizon, confirming the anticipated strong texture with a predominant orientation of crystallites with their *a*-*b* plane parallel to the substrate surface. The 001 and other low-index *hk*1 reflections form an arc with the highest intensity in the middle segment close to the substrate normal. (**b**) Cyclic voltammetry scans of a Py-ttTII film on ITO/glass recorded at a scan rate of 20 mV s^{-1} in a three-electrode-setup. The COF shows two very well-defined oxidation waves at

−100 and +300 mV vs. fc/fc^+, respectively, with negligible drift over nine oxidation/reduction cycles. Insets: Photographs of the COF film in the neutral (−700 mV) and oxidized (+500 mV) states. (**c**) Spectroelectrochemical characterization of a Py-ttTII COF film. UV-Vis-NIR spectra are recorded at increasing (oxidation; solid lines) and decreasing (reduction; dashed lines) potentials. The electrochromic color changes are fully reversible with only minimal hysteresis. After reduction back to the neutral state (−700 mV; grey dashed line), the spectrum is indistinguishable from the initial spectrum (green). (**d**) Plot of the absorption difference between the spectra shown in (c) after stepwise oxidation and the initial spectrum. The first oxidation step produces an absorption band at 1000 nm (orange line), which is replaced by an even stronger band at 900 nm after the second oxidation step (dark red). The emergence of the new absorption bands is accompanied by two strong bleach bands that correspond to the absorption of the neutral Py-ttTII COF at 450 and 650 nm. (**e**) Electrochromic switching stability over 100 oxidation/reduction cycles. The applied potential is switched between −700 and +500 mV with 2 s dwell time after each potential step. Upon oxidation, the absorbance at 550 nm changes by 1.2 OD with only minimal drift (<5%) over 100 cycles. (**f**) Switching speed at 550 nm extracted from ten oxidation/reduction cycles (symbols: data points, red line: average). The electrochromic response of the Py-ttTII COF film is very fast with 0.38 s for the oxidation and 0.20 s for the reduction, determined between 10% and 90% Δ*A* thresholds.

The optical properties of the thienoisoindigo COFs are largely dominated by the strong absorption features of the ttTII, nTII, and TII building blocks (SI, Figure 4.11). The higher-energy absorption bands between 350 and 500 nm can be attributed to π–π* transitions, while the longer-wavelength absorption is due to intramolecular charge transfer (ICT) between the electron-rich and -deficient moieties of the building blocks.[23, 34] Both π–π* and ICT bands appear red-shifted and broadened compared to the respective building blocks due to aggregation effects across the closely-packed, slip-stacked layers in the COF.[35]

In order to study the electrochromic behavior of our COFs, we integrated the COF thin film coated electrodes in a three-electrode electrochemical setup with a Pt wire as the counter electrode and a Ag/AgCl reference electrode (see the SI, section A for details). 0.1 M tetrabutylammonium hexafluorophosphate ($TBAPF_6$) in acetonitrile was used as the electrolyte. The applied potentials were calibrated against the ferrocene fc/fc^+ redox couple. Cyclic voltammetry (CV) scans of the Py-ttTII COF show two very well-defined oxidation waves at around −100 and +300 mV, respectively, which appear mirrored when the scan direction is reversed (Figure 4.3b). The respective anodic and cathodic peak positions are shifted by only about 20 mV, suggesting that the redox processes in the COF are fully reversible with fast electron transfer kinetics. The reversibility is further illustrated by the absence of any major drift or changes in curve shape during repeated redox cycles.

Electrochemical oxidation of the Py-ttTII COF film causes a gradual color change form initially dark green to black (SI, Figure 4.14). The corresponding UV-Vis-NIR spectra recorded in 200 mV intervals reveal the progressive bleaching of the two main absorption bands of the neutral COF, accompanied by the appearance of a new feature around 550 nm and a massive absorption band in the near-infrared (Figures 4.3c, d). The first oxidation step (−100 to +100 mV) produces a spectral feature at 1000 nm, which is replaced by an even stronger absorption band around 900 nm after the second oxidation step. The spectral changes are fully reversible with only minimal hysteresis. The spectrum recorded at −700 mV is indistinguishable from the initial spectrum of the neutral COF.

The charge density extracted from a 430 nm thick COF film during the oxidation scan is 0.0032 C cm^{-2}, which is very close to the theoretical charge density of 0.0030 C cm^{-2} calculated for the two-electron oxidation of every ttTII unit in the COF film (see the SI, section I). We thus can assign the two oxidation waves in the CV scans and the corresponding 1000 nm and 900 nm absorption features to the $ttTII^{+}$ and $ttTII^{2+}$ species, respectively.

The two-electron oxidation leads to very strong absorption and bleach bands (absorption changes of up to 2.8 OD), and requires only slightly more charge per unit area than the theoretical limit discussed above. Thus, the electrochromic color changes are highly efficient with coloration efficiencies (CEs) of 318 cm^2 C^{-1} at 550 nm, 620 cm^2 C^{-1} at 660 nm, and 858 cm^2 C^{-1} at 880 nm, respectively (see the SI, section I). These values are several times higher than the CEs of previously reported electrochromic COFs,[20, 21] rendering the Py-ttTII COF, to the best of our knowledge, the most efficient electrochromic organic framework to date.[36, 37]

In order to further investigate the stability and response times, we alternated the applied potential between +500 mV (oxidized COF) and −700 mV (neutral COF). The Py-ttTII COF retains >95% of its initial electrochromic response over 100 oxidation/reduction cycles (Figure 4.3e and SI, Figure 4.19), and >85% over 200 cycles (SI, Figure 4.21). Furthermore, the framework crystallinity remains unaffected during these experiments. GIWAXS patterns of the COF film before and after 200 oxidation/reduction cycles are virtually identical (SI, Figure 4.12).

The response to step changes in the applied potential is extremely fast with response times of 0.38 s for the oxidation (coloration) and 0.2 s for the reduction (bleaching) at 550 nm (Figure 4.3f). Response times at 660 nm and 900 nm are similarly fast (SI, Figure 4.19e). To the best of our knowledge, the Py-ttTII COF is the fastest electrochromic framework to date,

outcompeting published COFs and inorganic competitors such as WO_3 by more than an order of magnitude.[20, 21, 38]

As an illustration for a potential application of our electrochromic COFs, we employed a Py-ttTII COF film as an electrochromic window that can rapidly switch between transmitting (neutral COF) and blocking (oxidized COF) light from a green LED. A video of this is included as Supporting Information (viewable at: https://doi.org/10.1021/jacs.0c12392).

The electronically and topologically very similar Py-nTII COF shows an overall comparable electrochromic performance, but with slightly less defined oxidation and reduction waves, and weaker coloring due to its reduced film thickness (SI, Figure 4.15). Owing to their more electron-deficient and/or wider band gap building blocks, the Py-TII, Py-TT and Py-N COFs require more positive potentials for oxidation (SI, Figures 4.16, 4.17, 4.18). Moreover, the color changes are much less pronounced and there is significant drift in the CV curves.

3.4 Discussion

Comparing the five electrochromic COFs, we can formulate a set of design rules:

(I) Response and coloration efficiency critically depend on a building block design that combines high extinction coefficients with significant spectral differences between the neutral building block and its oxidized forms. The D-A-D electronic configuration of the ttTII and nTII building blocks has proven very efficient in fulfilling both criteria.

(II) Framework stability during repeated oxidation/reduction seems to depend on two factors. There is a general trend that for a given linker length the more rigid building blocks generate more robust frameworks. This factor works in favor of the flat and almost linear ttTII building block over the slightly non-planar, more flexible nTII and the angled TII. Moreover, stability over repeated electrochromic switching cycles seems to depend critically on the pore size. The COF pores need to be sufficiently large to accommodate the counterions required for overall charge neutrality (i.e., four counter ions per pore and COF layer for the two-electron oxidation of every bridge unit). They must also enable fast diffusion of electrolyte ions into and out of the pores during the electrochemical oxidation and reduction. Among the frameworks in this study, the Py-ttTII and Py-nTII COFs fulfil this criterion, whereas the smaller-pore COFs show significant drift during repeated CV scans, likely due to a build-up of ions in the pores.

(III) Rapid response requires unimpeded diffusion of ions in the pores as well as electronic connectivity throughout the COF film. The Py-ttTII COF films have a unique pillar-like morphology (SI, Figure 4.12c). Every pillar appears to be a continuous COF nanocrystal, ensuring best possible electronic coupling to the ITO electrode and uninterrupted pores for fast electrolyte diffusion.

3.5 Conclusion

We have developed highly efficient, fast-switching and stable electrochromic covalent organic frameworks based on modified thienoisoindigo building blocks. With a donor-acceptor-donor electronic setup, the low-bandgap COFs have strong Vis-NIR absorption bands in the neutral state, which shift significantly upon electrochemical oxidation. Absorption changes by close to 3 OD can be triggered at low operating voltages and are fully reversible. The champion Py-ttTII COF reaches an electrochromic coloration efficiency of 858 $cm^2\ C^{-1}$ at 880 nm and retains >95% of its electrochromic response over 100 oxidation/reduction cycles. Furthermore, the electrochromic switching of our oriented COF films is extremely fast with response times below 0.4 s for the oxidation and around 0.2 s for the reduction, outperforming previous COFs by at least an order of magnitude and rendering these materials, to the best of our knowledge, the fastest-switching frameworks to date.

3.6 Supporting Information

Abbreviations

BET	Brunauer-Emmett-Teller
CV	cyclic voltammetry
dba	dibenzylideneacetone
DCM	dichloromethane
DMF	*N*,*N*-dimethylformamide
DMSO	dimethyl sulfoxide
eq.	equivalents
fc	ferrocene
ICT	intramolecular charge transfer
ITO	indium tin oxide
LDA	lithium diisopropylamide
NBS	*N*-bromosuccinimide
NIR	near-infrared
OD	optical density
PSD	pore size distribution
PTFE	poly(tetrafluoroethylene)
QSDFT	quenched solid density functional theory
rt	room temperature
SPhos	dicyclohexylphosphino-2',6'-dimethoxybiphenyl
$TBAPF_6$	tetrabutylammonium hexafluorophosphate
TFA	trifluoroacetic acid
THF	tetrahydrofuran
tol	tolyl

COF building blocks

$Py(NH_2)_4$	1,3,6,8-tetrakis(4-aminophenyl)pyrene
$N(CHO)_2$	naphthalene-2,6-dicarbaldehyde
$nTII(CHO)_2$	5,5'-bis(2-formylnaphthalen-6-yl)-*N*,*N*'-dihexyl-thienoisoindigo
$TII(CHO)_2$	5,5'-diformyl-*N*,*N*'-dihexyl-thienoisoindigo
$TT(CHO)_2$	thieno[3,2-*b*]thiophene-2,5-dicarbaldehyde
$ttTII(CHO)_2$	5,5'-bis(2-formylthienothiophen-5-yl)-*N*,*N*'-dihexyl-thienoisoindigo

Section A – Methods

Nuclear magnetic resonance (NMR) spectra were recorded on Bruker Avance III HD spectrometers. Proton chemical shifts are expressed in parts per million (δ scale) and are calibrated using residual undeuterated solvent peaks as an internal reference (^{1}H NMR: $CDCl_3$: 7.26, DMSO-d_6: 2.50; ^{13}C NMR: $CDCl_3$: 77.2, DMSO-d_6: 39.5). Data for ^{1}H NMR spectra are reported in the following way: chemical shift (δ ppm) (multiplicity, coupling constant, integration). Multiplicities are reported as follows: s = singlet, d = doublet, t = triplet, q = quartet, m = multiplet, or combinations thereof.

Solid-state ^{13}C cross-polarization magic angle spinning (CP-MAS) NMR spectra were recorded with a Bruker Avance III-500 spectrometer using 4 mm diameter ZrO_2 rotors at a spinning frequency of 12 kHz.

Powder X-ray diffraction (PXRD) patterns were measured on a Bruker D8 Advance diffractometer equipped with a Cu K_α source (0.1 mm divergence slit, knife edge air scatter screen) and a LynxEye detector. K_β radiation was attenuated with a 0.0125 mm Ni filter.

2D grazing-incidence wide angle X-ray scattering (GIWAXS) data were recorded with an Anton Paar SAXSpoint 2.0 system equipped with a Primux 100 micro Cu K_α source and a Dectris EIGER R 1M detector. The COF films were positioned at a sample-detector distance of 140 mm and were measured with an incidence angle of 0.2°.

The **structure models of the COFs** were constructed using the Accelrys Materials Studio software package. For each COF, the highest possible symmetry was applied considering the rotation of the bridge units vs. the pyrene cores. The structure models were optimized using the Forcite module with the Dreiding force-field. **Structure refinements** were carried out with the Reflex module using the Rietveld method. Pseudo-Voigt peak profiles were used, and peak

asymmetry was corrected using the Finger-Cox-Jephcoat method. **Connolly surfaces** and accessible surfaces were generated using a N_2-sized probe (r = 0.184 nm) at a 0.025 nm grid interval.[39]

Nitrogen sorption isotherms were recorded with Quantachrome Autosorb 1 and Autosorb iQ instruments at 77 K. The samples were extracted with supercritical CO_2 for 1 h, followed by degassing at 100 °C under high vacuum for 1 h prior to the measurements. BET areas were calculated based on the pressure range $0.05 \leq p/p_0 \leq 0.2$. Pore size distributions were calculated using the QSDFT equilibrium model (desorption) with a carbon kernel for cylindrical pores.

Scanning electron microscopy (SEM) images were obtained with an FEI Helios NanoLab G3 UC microscope equipped with a Schottky field-emission electron source operated at 1 – 30 kV.

Transmission electron microscopy (TEM) images were obtained with an FEI Titan Themis microscope equipped with a field emission gun operated at 300 kV.

Infrared (IR) spectra were recorded on a Thermo Scientific Nicolet iN10 FT-IR spectrometer equipped with a MicroTip attenuated total reflection (ATR) unit and an MCT-detector. The spectra were analyzed with the OMNIC software package.

UV-Vis-NIR spectra were recorded on a Perkin-Elmer Lambda 1050 spectrometer equipped with a 150 mm InGaAs integrating sphere. Absorbance spectra of the starting materials were measured with 50 µM chloroform solutions. **Diffuse reflectance spectra** were recorded with a Harrick Praying Mantis accessory kit and were referenced to barium sulfate powder as the white standard.

Electrochemical measurements were performed with a Metrohm Autolab PGSTAT potentiostat/galvanostat. **Cyclic voltammetry (CV)** scans were recorded with the respective COF film on ITO or Au/glass as the working electrode, a Pt wire counter electrode and a Ag/AgCl reference electrode. 0.1 M tetrabutylammonium hexafluorophosphate ($TBAPF_6$) in MeCN was chosen as the electrolyte. 0.1 mM ferrocene solution was used as a standard in control experiments with a blank ITO working electrode. All potentials are referenced to the fc/fc^+ redox pair ($V_{fc/fc+}$ = +0.50 V vs. Ag/Ag^+).

For the **spectroelectrochemical measurements**, the COF films were placed inside a fused silica cuvette (20 mm path length) equipped with a Pt wire counter electrode, Ag/AgCl (3 M NaCl) reference electrode and 0.1 M $TBAPF_6$/MeCN electrolyte. The potential was

increased/decreased in 200 mV intervals using a 20 mV s^{-1} ramp and then held constant for the duration of the UV-Vis scan (ca. 5 min per spectrum). For the **stability and response time measurements**, the applied potential was switched between −200 mV and +1V vs. Ag/AgCl and held constant for 2 s between each step. In order to reduce the instrument response time, absorption changes were tracked with the Lambda 1050 photomultiplier tube (Vis) and InGaAs (NIR) detectors set to fixed gain mode.

Section B – COF syntheses

Reagents and solvents were obtained in high-purity grades from commercial suppliers and were, unless shipped under argon, degassed and saturated with argon prior to use. The COF building blocks were synthesized as detailed in Section C. Thieno[3,2-*b*]thiophene-2,5-dicarbaldehyde ($TT(CHO)_2$) was obtained from Merck and purified by recrystallization from hot DMF. 1,3,6,8-tetrakis(4-aminophenyl)pyrene ($Py(NH_2)_4(dioxane)_{1.5}$) and naphthalene-2,6-dicarbaldehyde ($N(CHO)_2$) were synthesized according to published procedures.[25, 29] Please refer to page 103 for a list of abbreviations for the COF building blocks and solvents.

COF bulk powder syntheses were performed under argon atmosphere in PTFE-sealed glass reaction tubes (6 mL volume).

COF thin films were synthesized in 100 mL autoclaves equipped with a 28 mm diameter glass liner. ITO-coated glass substrates were cleaned in detergent solution (Hellmanex III, 0.5% *v*/*v*), water, acetone, and isopropanol, and activated with an O_2-plasma for 5 min directly before use. Semi-transparent gold substrates were prepared by thermal evaporation of a 3 nm Ti layer, followed by a 10 nm Au layer. The gold substrates were activated with an O_2-plasma for 5 min directly before use. For the COF thin film syntheses, substrates were placed horizontally in PTFE sample holders with the activated surface face-down.

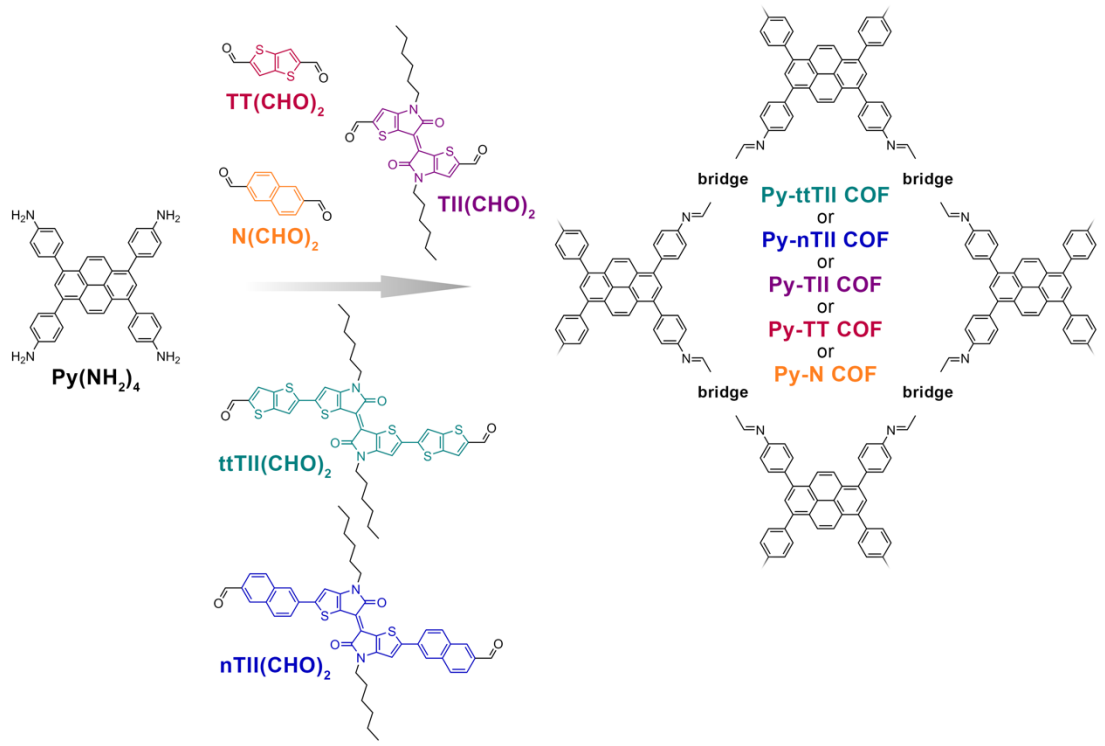

Figure 4.4. Construction of the new thienoisoindigo-based COFs and smaller-pore reference materials. The co-condensation of the tetradentate $Py(NH_2)_4$ with the linear dialdehyde building blocks yields the Py-ttTII, Py-nTII, Py-TII, Py-TT and Py-N COFs, respectively.

Py-ttTII COF. $Py(NH_2)_4(dioxane)_{1.5}$ (14.0 mg, 20 µmol, 1.0 eq.) and $ttTII(CHO)_2$ (31.0 mg, 40 µmol, 2.0 eq.) were filled into a 6 mL reaction tube, followed by the addition of mesitylene (667 µL), benzyl alcohol (333 µL), and 6 M acetic acid (100 µL). The tube was sealed and heated at 120 °C for 6 d. After cooling to room temperature, the precipitate was collected by filtration, washed with MeCN and dried in air. Extraction with supercritical CO_2 for 1 h yielded the COF as a dark green powder.

Elemental analysis (calculated, found for $C_{232}H_{180}N_{16}O_8S_{24}$): C (68.14, 67.48), H (4.44, 4.53), N (5.48, 5.23), S (18.81, 18.37).

Py-ttTII COF films. An autoclave was charged with $Py(NH_2)_4(dioxane)_{1.5}$ (3.5 mg, 5 µmol, 1.0 eq.), $ttTII(CHO)_2$ (7.8 mg, 10 µmol, 2.0 eq.), mesitylene (1333 µL) and benzyl alcohol (667 µL). An ITO/glass substrate was inserted, followed by the addition of 6 M acetic acid (200 µL). The autoclave was sealed and heated at 120 °C for 3 d. After cooling to room temperature, the COF film was rinsed with dry MeCN and dried with a stream of nitrogen.

The COF film thickness is 430 ± 30 nm (determined by cross-sectional SEM, sample-to-sample variation by UV-Vis).

Py-nTII COF. $Py(NH_2)_4(dioxane)_{1.5}$ (14.0 mg, 20 µmol, 1.0 eq.) and $nTII(CHO)_2$ (30.0 mg, 40 µmol, 2.0 eq.) were filled into a 6 mL reaction tube, followed by the addition of mesitylene (333 µL), 1,4-dioxane (667 µL), and 6 M acetic acid (100 µL). The tube was sealed and heated at 120 °C for 6 d. After cooling to room temperature, the precipitate was collected by filtration, washed with MeCN and dried in air. Extraction with supercritical CO_2 for 1 h yielded the COF as a dark green powder.

Elemental analysis (calculated, found for $C_{264}H_{212}N_{16}O_8S_8$): C (79.41, 77.13), H (5.35, 5.36), N (5.61, 5.35), S (6.42, 6.47).

Py-nTII COF films. An autoclave was charged with $Py(NH_2)_4(dioxane)_{1.5}$ (3.5 mg, 5 µmol, 1.0 eq.), $nTII(CHO)_2$ (7.5 mg, 10 µmol, 2.0 eq.), mesitylene (1333 µL) and benzyl alcohol (667 µL). A gold/glass substrate was inserted, followed by the addition of 6 M acetic acid (200 µL). The autoclave was sealed and heated at 120 °C for 3 d. After cooling to room temperature, the COF film was immersed in dry MeCN for 2 min and dried with a stream of nitrogen.
The COF film thickness is 280 ± 30 nm (determined by cross-sectional SEM; sample-to-sample variation by UV-Vis).

Py-TII COF. $Py(NH_2)_4(dioxane)_{1.5}$ (14.0 mg, 20 µmol, 1.0 eq.) and $TII(CHO)_2$ (20.0 mg, 40 µmol, 2.0 eq.) were filled into a 6 mL reaction tube, followed by the addition of mesitylene (667 µL), benzyl alcohol (333 µL), and 6 M acetic acid (100 µL). The tube was sealed and heated at 120 °C for 6 d. After cooling to room temperature, the precipitate was collected by filtration, washed with MeCN and extracted with supercritical CO_2 for 1 h to yield the COF as a dark teal powder.

Elemental analysis (calculated, found for $C_{184}H_{164}N_{16}O_8S_8$): C (74.06, 72.28), H (5.54, 5.49), N (7.51, 7.02), S (8.60, 8.35).

Py-TII COF films. An autoclave was charged with $Py(NH_2)_4(dioxane)_{1.5}$ (3.5 mg, 5 µmol, 1.0 eq.), $TII(CHO)_2$ (5.0 mg, 10 µmol, 2.0 eq.), mesitylene (1333 µL) and benzyl alcohol (667 µL). An ITO/glass substrate was inserted, followed by the addition of 6 M acetic acid (200 µL). The

autoclave was sealed and heated at 120 °C for 3 d. After cooling to room temperature, the COF film was immersed in dry MeCN for 2 min and dried with a stream of nitrogen.

Py-TT COF. This COF was prepared according to literature procedures.[28]

Py-TT COF films. COF thin films were prepared according to literature procedures.[28]

Py-N COF. $Py(NH_2)_4(dioxane)_{1.5}$ (14.0 mg, 20 µmol, 1.0 eq.) and $N(CHO)_2$ (7.4 mg, 40 µmol, 2.0 eq.) were filled into a 6 mL reaction tube, followed by the addition of mesitylene (667 µL), benzyl alcohol (333 µL), and 6 M acetic acid (100 µL). The tube was sealed and heated at 120 °C for 6 d. After cooling to room temperature, the precipitate was collected by filtration, washed with MeCN and dried in air. Extraction with supercritical CO_2 for 1 h yielded the COF as an orange-red powder.

Elemental analysis (calculated, found for $C_{128}H_{76}N_8$): C (89.07, 86.90), H (4.44, 4.29), N (6.49, 6.21)

Py-N COF films. An autoclave was charged with $Py(NH_2)_4(dioxane)_{1.5}$ (3.5 mg, 5 µmol, 1.0 eq.), $N(CHO)_2$ (1.8 mg, 10 µmol, 2.0 eq.), mesitylene (1333 µL) and benzyl alcohol (667 µL). An ITO/glass or fused silica substrate was inserted, followed by the addition of 6 M acetic acid (200 µL). The autoclave was sealed and heated at 120 °C for 3 – 4 d. After cooling to room temperature, the COF film was immersed in dry MeCN for 2 min and dried with a stream of nitrogen.

Section C – COF structure analysis

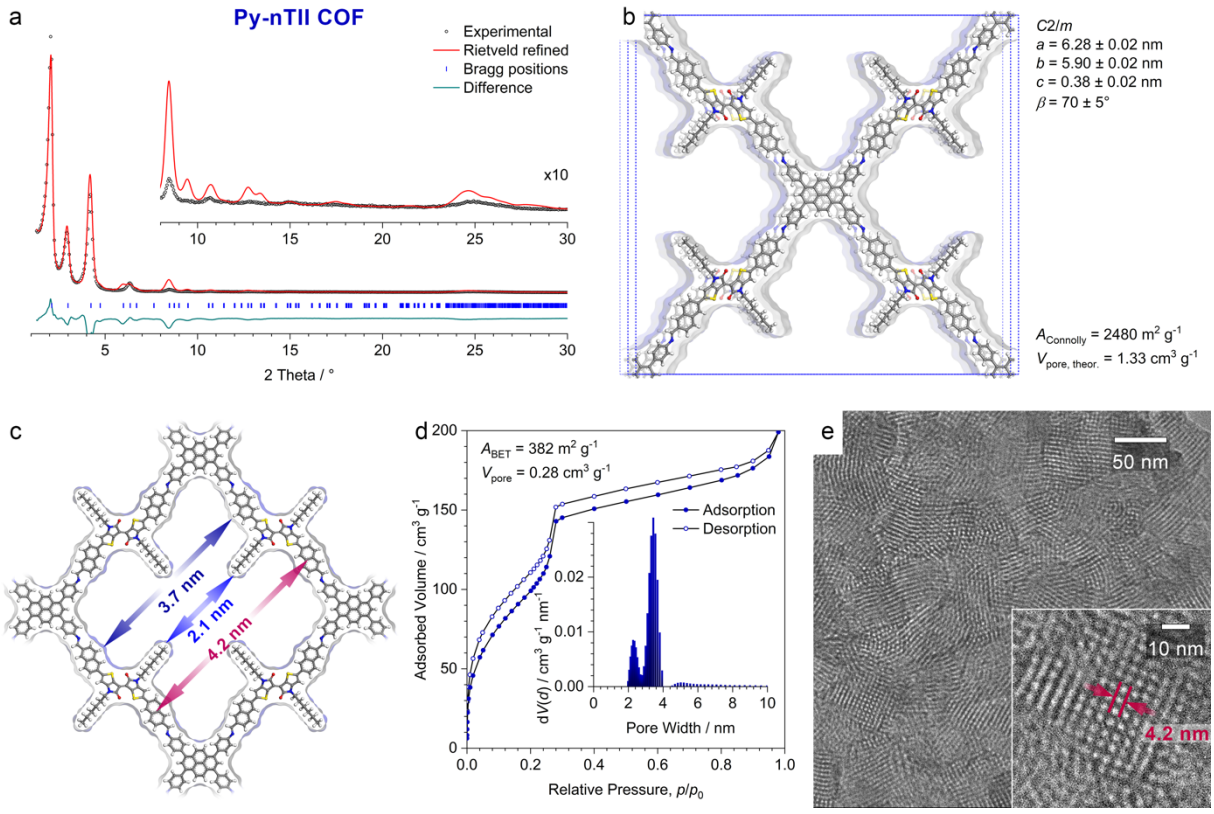

Figure 4.5. Structure analysis of the Py-nTII COF.

(**a**) PXRD pattern of the Py-nTII COF bulk material (black dots). Rietveld refinement (red line) using the monoclinic (space group *C*2/*m*) structure model shown on the right provides a good fit, with only small differences between the experimental and refined patterns (green line) arising mainly from the flexibility of the alkyl chains. R_{wp} = 13.7%, R_p = 23.5%. Bragg positions are indicated by blue ticks. Inset: Magnified view of the 2θ > 8° region.

(**b**) The Rietveld-refined structure model of the Py-nTII COF viewed perpendicular to the crystallographic *a*-*b* plane. The COF has a pseudo-square geometry with slip-stacked layers. The structure is highly porous with a Connolly surface of 2480 $m^2\ g^{-1}$ and a pore volume of 1.33 $cm^3\ g^{-1}$.

(**c**) Illustration of the pore structure of the COF viewed along the *c*-axis. The structure refinement indicates that in this COF the alkyl chains extend relatively straight into the pores, producing a shamrock-shaped pore cross section. The wall-to-wall distances (blue arrows) are 2.1 nm and 3.7 nm including and excluding the alkyl chains, respectively. The periodicity of the COF in this orientation is 4.2 nm (red arrows).

(**d**) Nitrogen sorption isotherm recorded at 77 K. The BET area and total pore volume are reduced compared to the structure model, most likely due to oligomeric fragments that were enclosed in the pores during the synthesis. This is a common challenge for COFs based on extended, bulky building blocks with low solubility.[9] Inset: Fitting the isotherm with a QSDFT equilibrium model for cylindrical pores produces a bimodal pore size distribution (PSD) with peaks at 2.3 nm and 3.5 nm. While unexpected at first glance, this PSD is a result of the algorithm trying to express the non-cylindrical pores as a superposition of cylindrical pores with the two contributions being in good agreement with the wall-to-wall distances including and excluding the alkyl chains. Bimodal PSDs have been observed previously for alkyl-containing COFs.[27] The sorption data and PSD analysis hence confirm the

shamrock-shaped pore cross section and provide an independent validation of the XRD-derived structure model of the Py-nTII COF.
(**e**) High-resolution TEM image of a Py-nTII COF bulk powder sample showing crystallites of 50 – 100 nm diameter. Inset: Magnified image of a crystallite viewed along the pores (i.e., along the crystallographic *c*-axis) showing a periodicity of 4.2 nm in excellent agreement with the structure model.

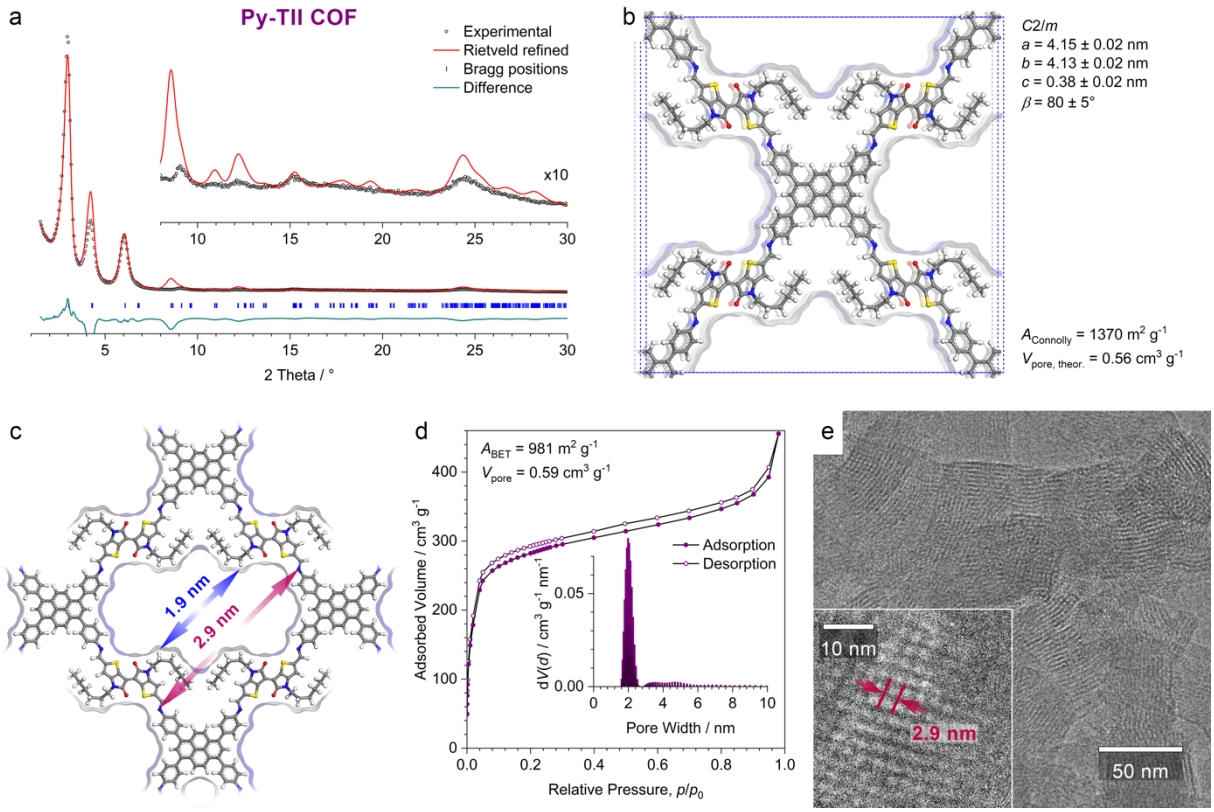

Figure 4.6. Structure analysis of the Py-TII COF.

(**a**) PXRD pattern of the COF bulk material (black dots). Rietveld refinement (red line) using the monoclinic (space group *C*2/*m*) structure model shown on the right provides a good fit, with only small differences between the experimental and refined patterns (green line). R_{wp} = 15.3%, R_p = 23.9%. Bragg positions are indicated by blue ticks. Inset: Magnified view of the 2θ > 8° region.

(**b**) The Rietveld-refined structure model of the Py-TII COF viewed perpendicular to the crystallographic *a*-*b* plane. The COF has a pseudo-square geometry with slip-stacked layers. The PXRD data quality is sufficient to refine the location of groups of atoms such as the hexyl chains. In this COF, the alkyl chains do not extend straight into the pore but collapse towards the neighboring pyrene units. This arrangement might be favorable because it avoids close contacts between the alkyl chains and the division of the pores into four small compartments. The COF is porous with a Connolly surface of 1370 $m^2\ g^{-1}$ and a pore volume of 0.56 $cm^3\ g^{-1}$.

(**c**) Illustration of the pore structure viewed along the *c*-axis. The collapsed alkyl chains produce a pore with 1.9 nm wall-to-wall distance (blue arrows). The periodicity of the COF in this orientation is 2.9 nm (red arrows).

(**d**) Nitrogen sorption isotherm recorded at 77 K. The BET area and pore volume are in good agreement with the porosity expected from the structure model. Inset: Fitting the isotherm with a QSDFT equilibrium model for cylindrical pores yields a narrow PSD with a maximum at 2.0 nm, in excellent agreement with the structure model. The fact that, in contrast to the larger Py-ttTII and Py-nTII COFs, the QSDFT analysis does not produce a bimodal distribution validates the XRD-derived structure model and confirms that the hexyl chains are collapsed to the pore walls in this COF.

(**e**) High-resolution TEM image of a Py-TII COF bulk powder sample showing crystallites of about 50 nm diameter. Inset: Magnified image of a crystallite viewed along the pores (i.e., along the crystallographic *c*-axis) showing a periodicity of 2.9 nm in excellent agreement with the structure model.

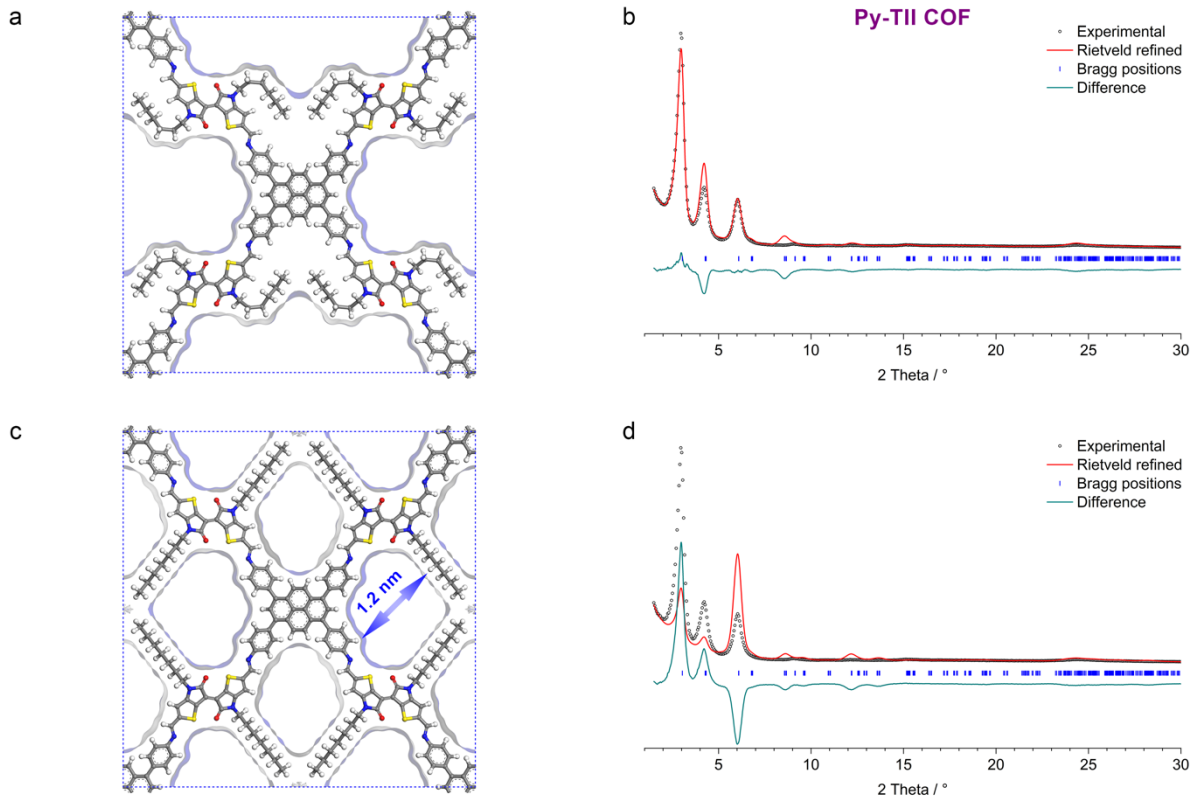

Figure 4.7. Comparison between the Py-TII COF structure models.
(**a**) Structure model of the Py-TII COF with collapsed alkyl chains. The Connolly surface calculated for an N_2-sized molecule is shown in blue. This arrangement of the alkyl chains leads to a large, slightly slit-like pore.
(**b**) This structure model provides a good fit to the experimental PXRD data and is further supported by the nitrogen sorption data (Figure 4.6d).
(**c**) Hypothetical structure model of the COF with the alkyl chains extending straight into the pore. In contrast to the larger COFs, this configuration would divide the pore of the Py-TII COF into four microporous compartments.
(**d**) Due to the very different distribution of electron density in the pores, this structure would lead to significantly different reflection intensities (red line) which do not match the experimental pattern. Moreover, straight alkyl chains can be excluded based on the nitrogen sorption, which clearly shows a pore width of around 2 nm (Figure 4.6d).

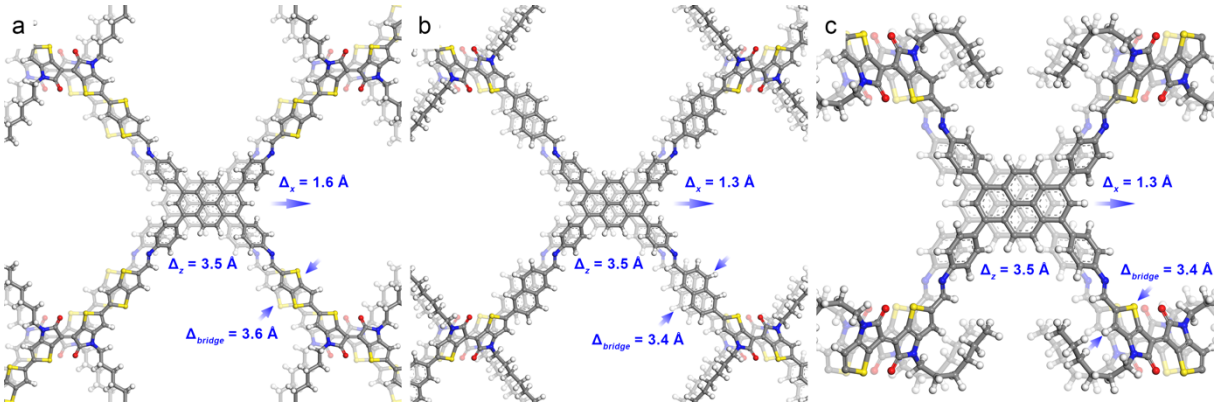

Figure 4.8. Stacking distances in the thienoisoindigo COFs. (a) Py-ttTII COF, (b) Py-nTII COF, (c) Py-TII COF. In all COFs, the pyrene-to-pyrene π-stacking distance (Δ_z; measured perpendicular to the pyrene planes) is 3.5 Å. The distance between the thienoisoindigo bridge units (measured perpendicular to the TII planes) ranges from 3.4 to 3.6 Å, confirming that also these moieties are closely packed in all three COFs. The lateral layer offset ranges from 1.3 Å in the Py-nTII and Py-TII COFs to 1.6 Å for the Py-ttTII COF. Given the very similar packing geometries, the electronic coupling across the COF layers is expected to be comparable in all three COFs.

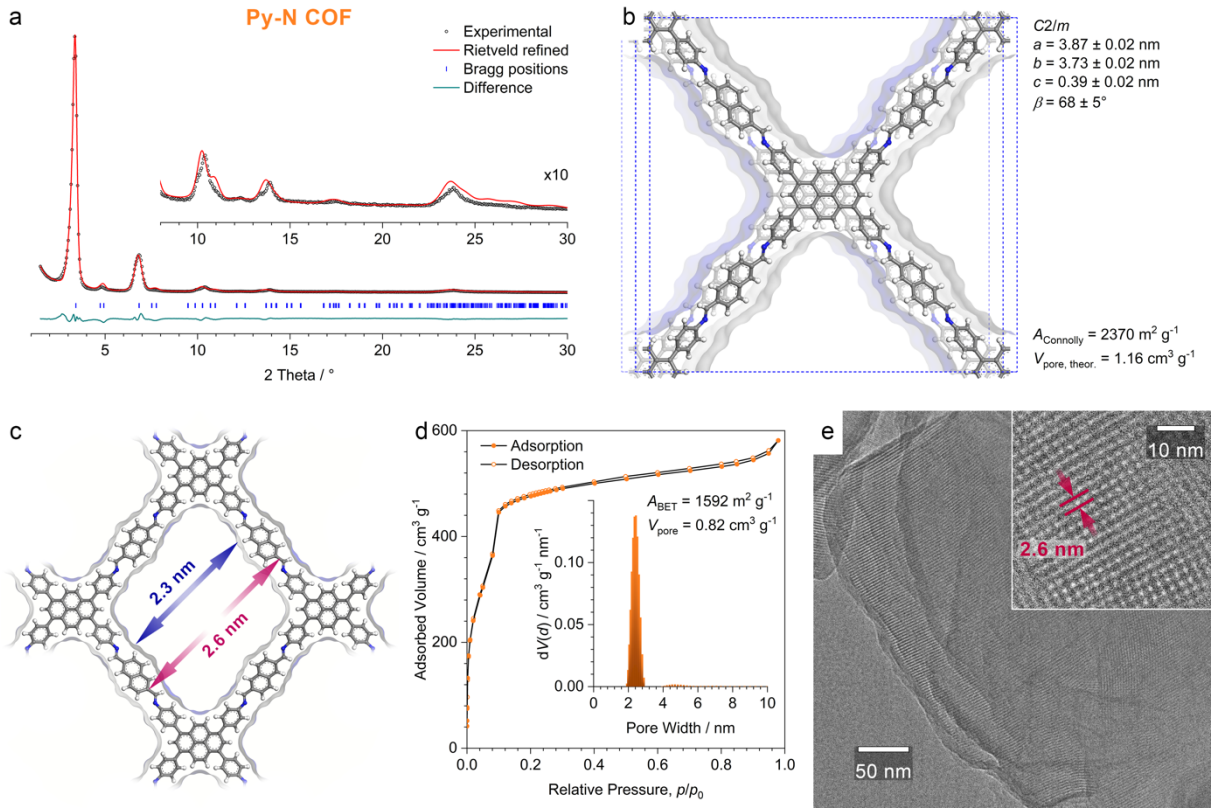

Figure 4.9. Structure analysis of the Py-N COF.

(**a**) PXRD pattern of the COF bulk material (black dots). Rietveld refinement (red line) using the monoclinic (space group *C*2/*m*) structure model shown on the right provides a very good fit, with only minimal differences between the experimental and refined patterns (green line). R_{wp} = 4.0%, R_p = 12.5%. Bragg positions are indicated by blue ticks. Inset: Magnified view of the 2θ > 8° region.

(**b**) The Rietveld-refined structure model of the Py-N COF viewed perpendicular to the crystallographic *a*-*b* plane. The COF has a pseudo-square geometry with slip-stacked layers. The COF is highly porous with a Connolly surface of 1910 $m^2\ g^{-1}$ and a pore volume of 0.61 $cm^3\ g^{-1}$.

(**c**) Illustration of the pore structure viewed along the *c*-axis. The pores have a pseudo-square cross section with a wall-to-wall distance of 2.3 nm. The periodicity of the COF in this orientation is 2.6 nm (red arrows).

(**d**) Nitrogen sorption isotherm recorded at 77 K. The BET area and pore volume are in good agreement with the porosity expected from the structure model. Inset: Fitting the isotherm with a QSDFT equilibrium model for cylindrical pores yields a narrow PSD with a maximum at 2.4 nm, which is in excellent agreement with the structure model.

(**e**) High-resolution TEM image of a Py-N COF bulk powder sample showing large crystal domains of about 400 nm. Inset: Magnified image of a crystallite viewed along the pores (i.e., along the crystallographic *c*-axis) showing a periodicity of 2.6 nm in excellent agreement with the structure model.

Other COFs:

See the manuscript for the structure analysis of the Py-ttTII COF.

The structure analysis of the Py-TT COF has been published previously.[28]

Section D – IR spectroscopy

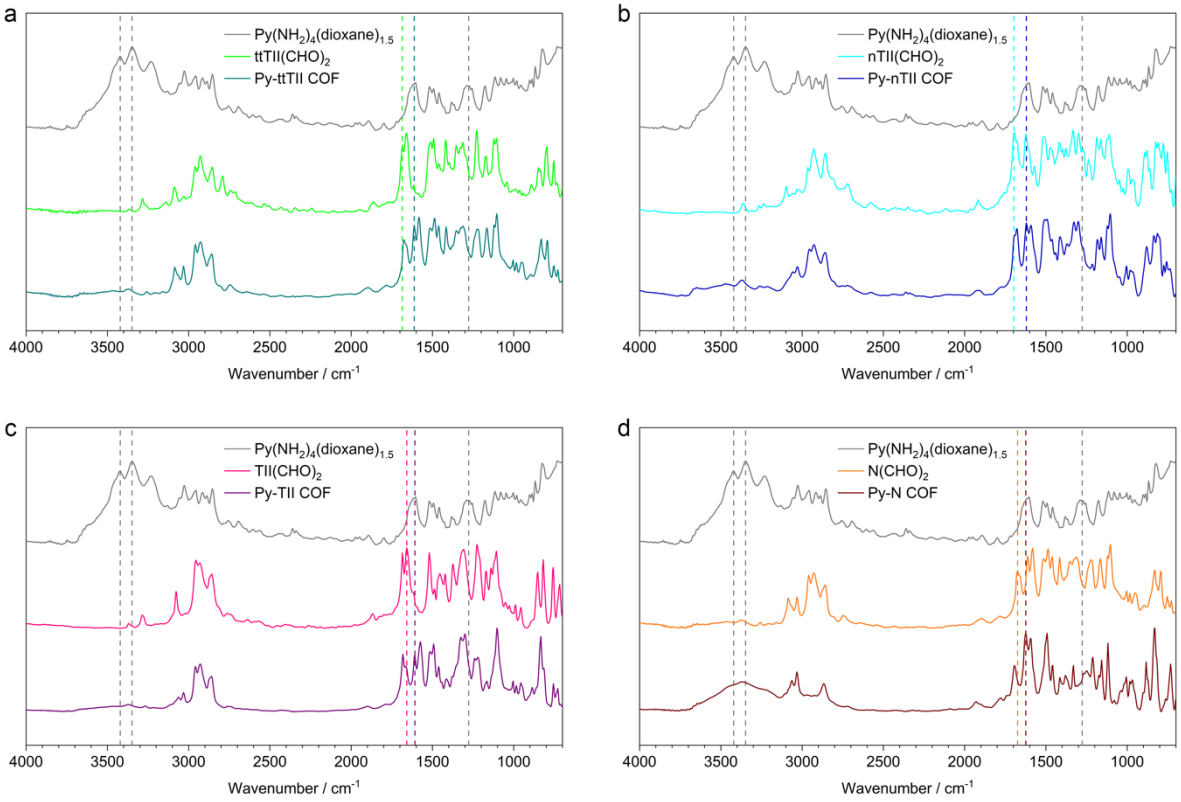

Figure 4.10. Comparison of IR spectra of the precursors and their COF powders. The IR spectra of the building blocks show the characteristic C-NH_2 and C=O stretching vibrations of the amine ($Py(NH_2)_4$) and aldehyde (linear precursors) functional groups, respectively. The attenuation of these absorption signals and the evolution of the C=N stretching vibrations of the imine bonds at around 1610 cm^{-1} confirm the successful COF formation.

Table 4.1. Assignments of selected IR signals.

	Wavenumber / cm^{-1}	Assignment
$Py(NH_2)_4(dioxane)_{1.5}$	1277 3348 3421	C–NH_2 stretching N-H stretching N-H stretching
$ttTII(CHO)_2$	1686	C=O stretching
Py-ttTII COF	1612	C=N stretching
$nTII(CHO)_2$	1697	C=O stretching
Py-nTII COF	1620	C=N stretching
$TII(CHO)_2$	1658	C=O stretching
Py-TII COF	1608	C=N stretching
$N(CHO)_2$	1674	C=O stretching
Py-N COF	1624	C=N stretching

Section E – UV-Vis spectroscopy

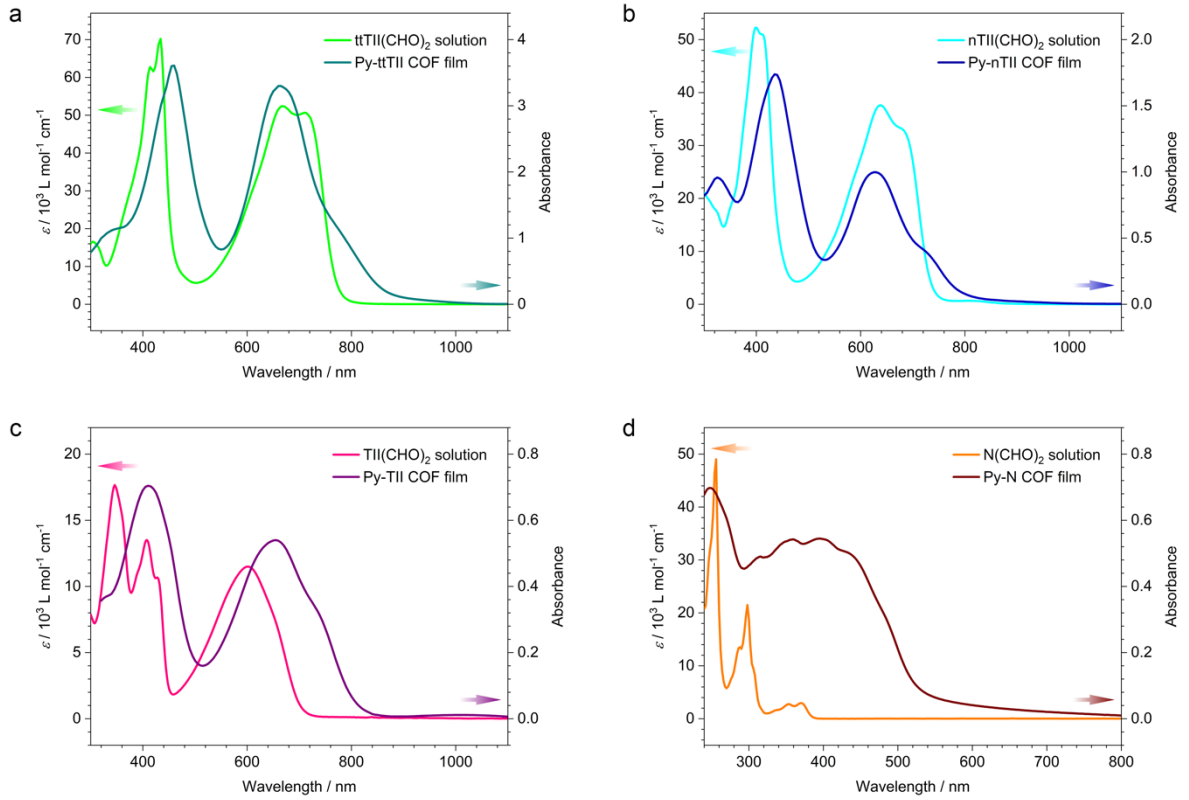

Figure 4.11. Comparison of the absorption spectra of the building blocks (50 µM solutions in $CHCl_3$) and the corresponding COF thin films. (**a**) Py-ttTII COF grown on ITO, (**b**) Py-nTII COF on a 10 nm Au layer, (**c**) Py-TII COF on ITO, (**d**) Py-N COF on fused silica.

The thienoisoindigo-containing building blocks have two characteristic absorption bands. The higher-energy band between 330 and 500 nm can be attributed to π–π^* transitions, whereas the strong absorption at longer wavelengths starting at 500 nm and ranging into the NIR is due to intramolecular charge transfer (ICT) between electron-rich and -deficient moieties. These ICT transitions are enabled by the structure design of the TII-based building blocks with their strongly electron-accepting ketopyrrole cores and the electron-donating fused thiophenes in the TII, or the coupled thienothiophenes and naphthalenes in the ttTII and nTII building blocks, respectively.

Section F – COF films GIWAXS analysis

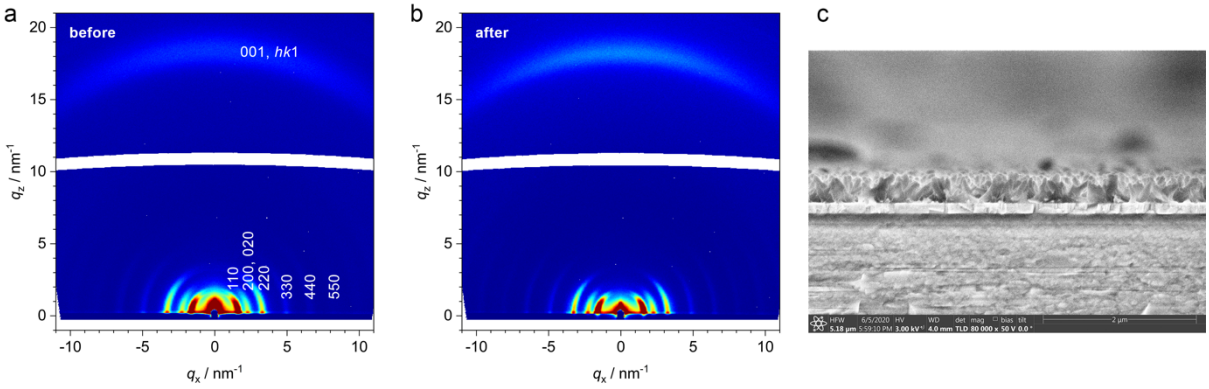

Figure 4.12. 2D GIWAXS patterns of a Py-ttTII COF film on ITO (**a**) before and (**b**) after 200 electrochemical oxidation/reduction cycles. The film is polycrystalline and highly textured with the COF *a*-*b* planes predominantly aligned parallel to the substrate. The crystallinity and orientation are fully retained during the electrochemical switching. (**c**) SEM cross-section of a Py-ttTII COF film. In contrast to other COFs, films of this COF are not dense, but have a pillar-like morphology.

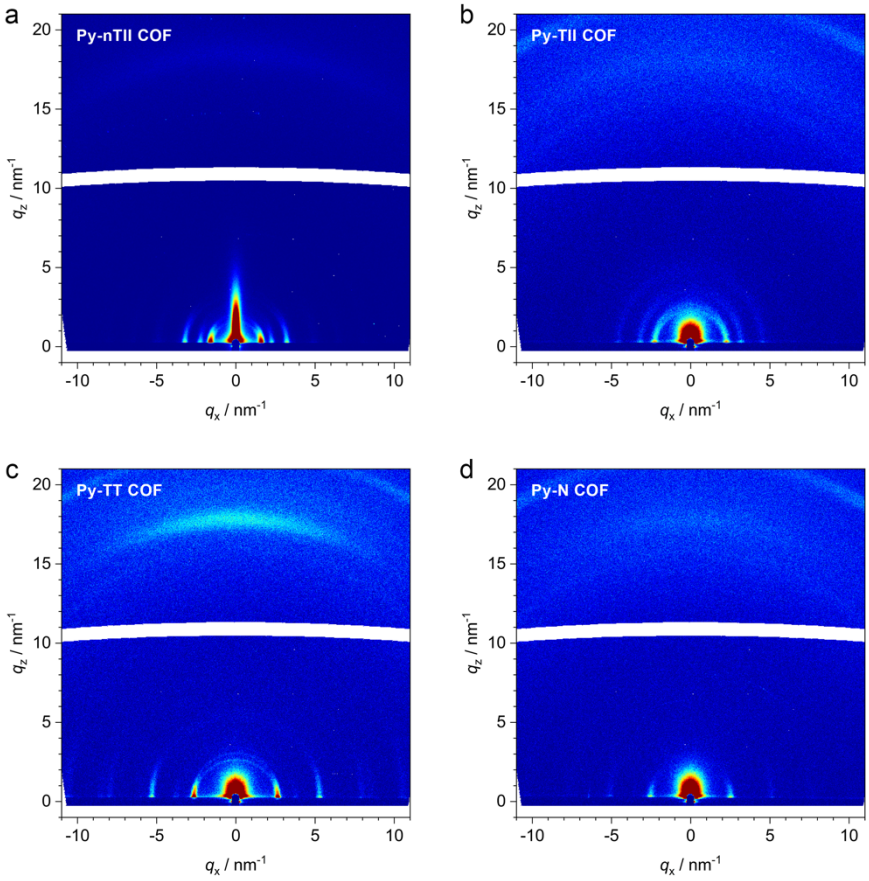

Figure 4.13. 2D GIWAXS patterns of the other COFs after ten oxidation/reduction cycles. (**a**) Py-nTII COF on a 10 nm Au/glass substrate. (**b**) Py-TII COF on ITO. (**c**) Py-TT COF on ITO. (**d**) Py-N COF on ITO. The COF films are polycrystalline and strongly textured with the *a*-*b* planes predominantly parallel to the substrate surface. Thus, the pores extend towards the film surface and are accessible.

Section G – Spectroelectrochemistry

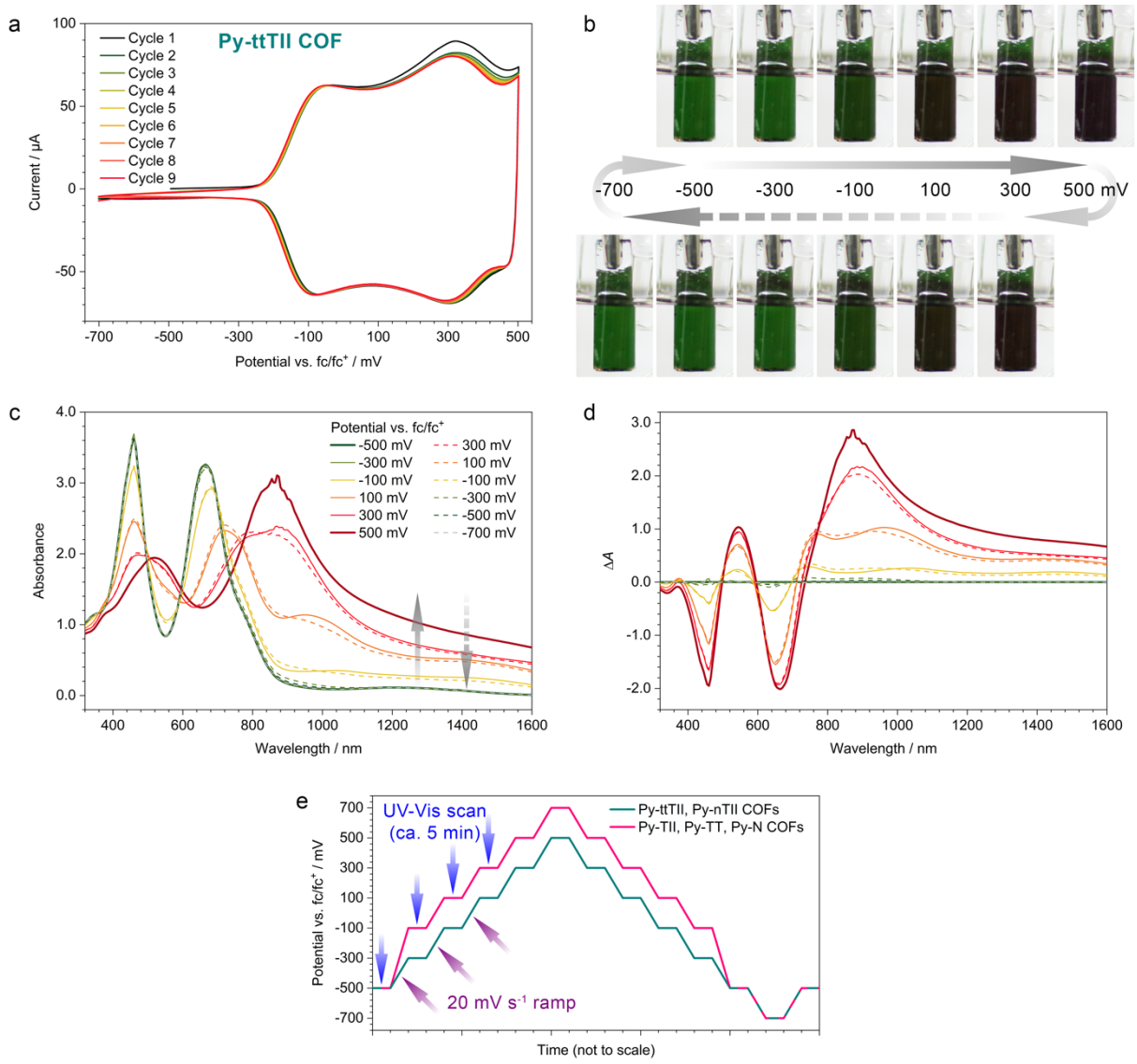

Figure 4.14. Electrochromic properties of the Py-ttTII COF. (**a**) Cyclic voltammetry scans of a COF film on ITO recorded at a scan rate of 20 mV s^{-1}. See the Methods section for experimental details. The Py-ttTII COF has two very well-defined oxidation waves at around −100 and +300 mV vs. fc/fc^+, respectively, and shows almost no drift over nine oxidation/reduction cycles. The stability of this COF over more oxidation/reduction cycles is analyzed in the next section.
(**b**) Photographs of the COF film taken during an oxidation (top row, left to right) / reduction (bottom row, right to left) cycle illustrating the electrochromic color changes.
(**c**) UV-Vis-NIR spectra recorded at different potentials using the ramp/dwell program shown in (**e**). The solid and dashed lines refer to spectra recorded at increasing (oxidation) and decreasing (reduction) potentials, respectively. The first oxidation step (+100 mV, orange line) produces a new absorption feature at 1000 nm, which is replaced by a strong absorption at 900 nm after the second oxidation step (+500 mV, dark red). The electrochromic color changes of the Py-ttTII COF are fully reversible with only minimal hysteresis (dashed lines). At −700 mV, the spectrum is indistinguishable from the initial spectrum (dashed grey line).

(**d**) Plot of the absorption difference between the oxidized COF and the initial spectrum. Oxidation of the Py-ttTII COF leads to the evolution of strong NIR absorption bands and a minor contribution at 550 nm, accompanied by two bleach bands at 450 and 650 nm.
(**e**) The voltage ramp programs used for the potential-dependent UV-Vis scans. Each UV-Vis scan (the first four scans are indicated by blue arrows) is followed by a 20 mV s^{-1} voltage ramp to the next potential (purple arrows). The larger-bandgap and/or more electron-deficient Py-TII, Py-TT and Py-N COFs require more positive potentials for oxidation. Hence, the potentials for the UV-Vis scans after the initial measurement are shifted by 200 mV (pink line).

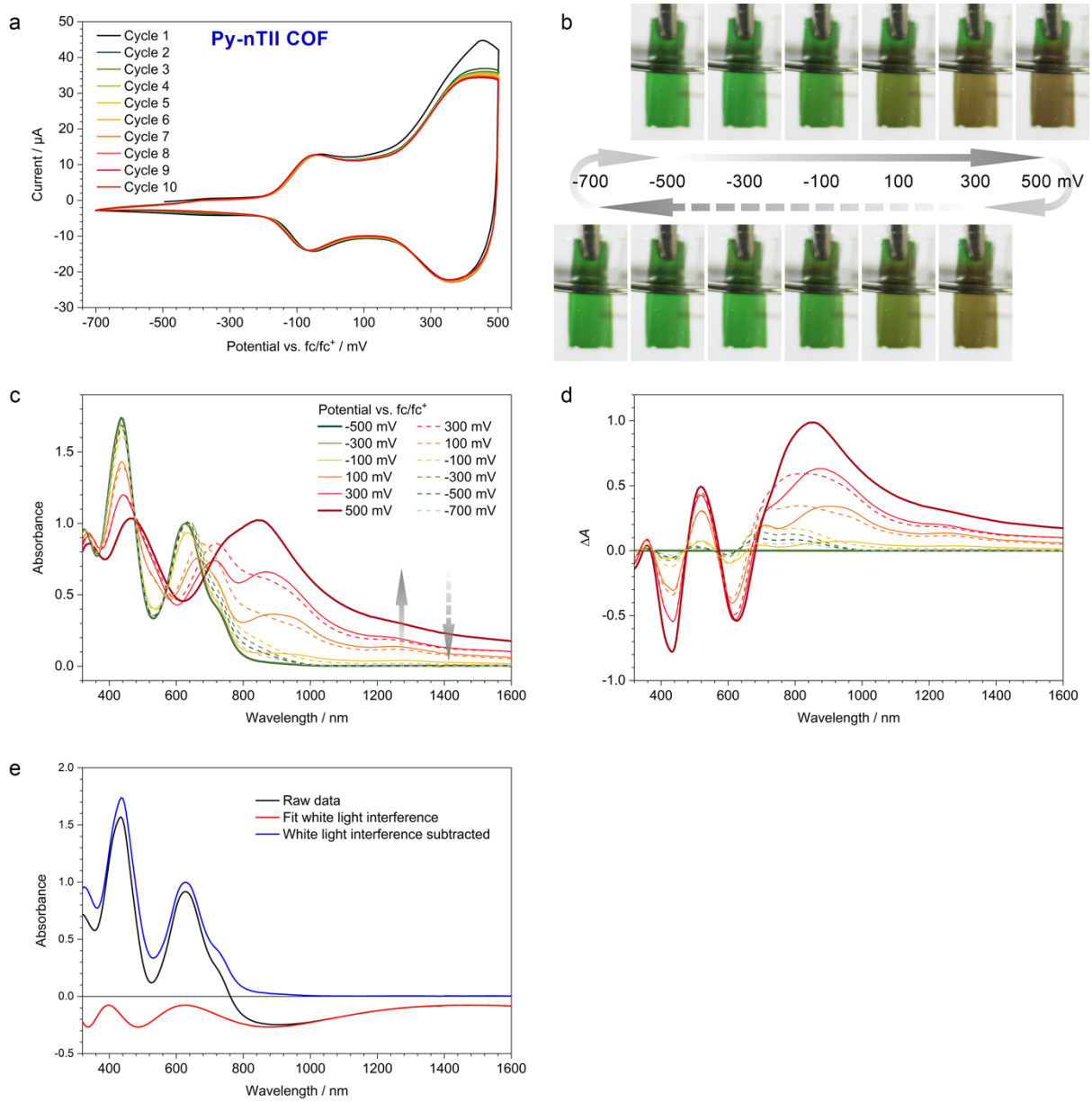

Figure 4.15. Electrochromic properties of the Py-nTII COF.

(**a**) Cyclic voltammetry scans of a COF film on a 10 nm Au/glass substrate, recorded at a scan rate of 20 mV s^{-1}. See the Methods section for experimental details. The Py-nTII COF has two very well-defined oxidation waves at around −50 and +350 mV vs. fc/fc^{+}, respectively, and shows almost no drift over ten oxidation/reduction cycles.

(**b**) Photographs of the COF film taken during an oxidation (top row, left to right) / reduction (bottom row, right to left) cycle illustrating the electrochromic color changes.

(**c**) UV-Vis-NIR spectra recorded at different potentials. The solid and dashed lines refer to spectra recorded at increasing (oxidation) and decreasing (reduction) potentials, respectively. The first oxidation step (+100 mV, orange line) produces a new absorption feature at 950 nm, which is replaced by a strong absorption at 900 nm after the second oxidation step (+500 mV, dark red line). The electrochromic color changes of the Py-nTII COF are almost fully reversible, however, with some hysteresis (dashed lines). At −700 mV, the spectrum follows the initial spectrum except for a minor residual absorption around 800 nm.

The effect of white light interference, which is pronounced for this sample due to the Au substrate, was removed from the absorption spectra (see below).
(**d**) Plot of the absorption difference between the oxidized COF and the initial spectrum. Oxidation of the Py-nTII COF leads to the evolution of strong NIR absorption bands and a minor contribution at 550 nm, accompanied by two bleach bands at 450 and 650 nm.
(**e**) Background correction of the spectra. White light interference (red line) was approximated by the expression $A = 0.095 \cos(4\pi \cdot 544/\lambda + 1.64) - 0.176$ and subtracted from all spectra. For clarity, only the spectrum at −500 mV is displayed.

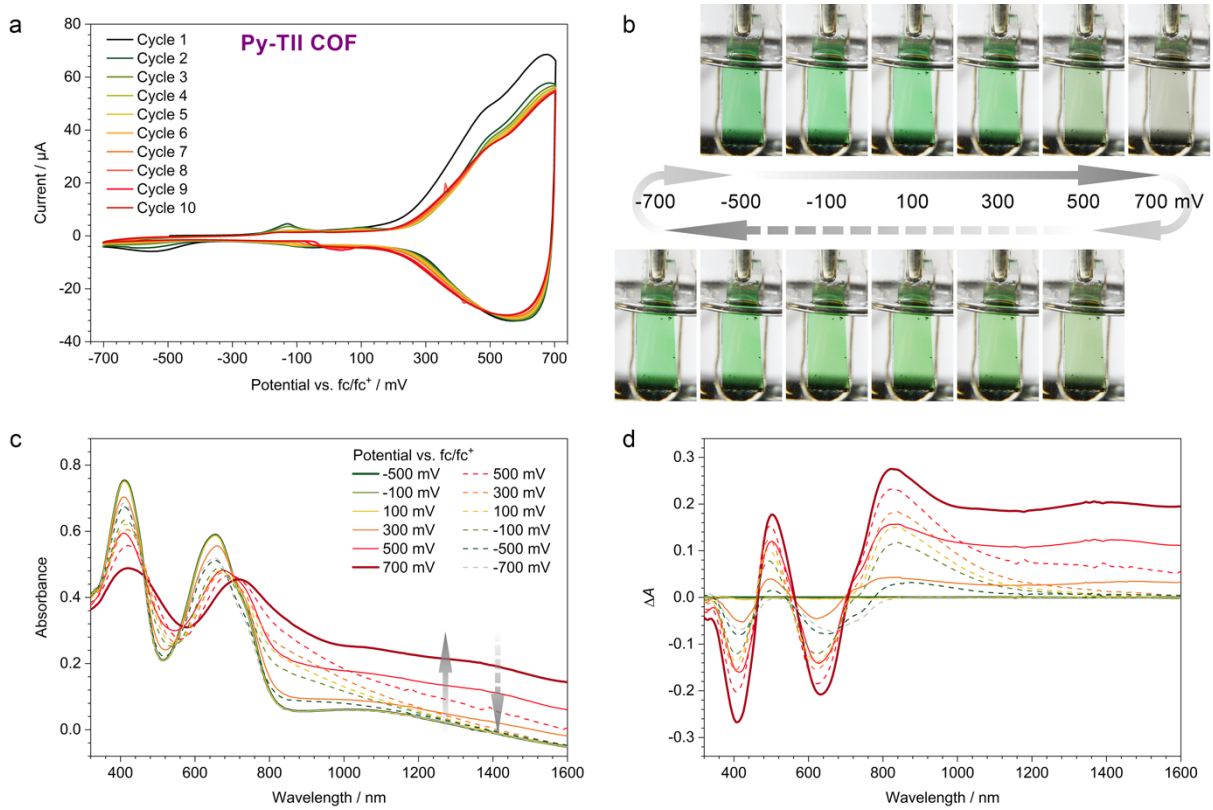

Figure 4.16. Electrochromic properties of the Py-TII COF.
(**a**) Cyclic voltammetry scans of a Py-TII COF film on ITO recorded at a scan rate of 20 mV s^{-1}. See the Methods section for experimental details. The Py-TII COF shows one oxidation wave at around +500 mV vs. fc/fc^+ and only moderate drift over ten oxidation/reduction cycles.
(**b**) Photographs of the COF film taken during an oxidation (top row, left to right) / reduction (bottom row, right to left) cycle illustrating the electrochromic color changes.
(**c**) UV-Vis-NIR spectra recorded at different potentials. The solid and dashed lines refer to spectra recorded at increasing (oxidation) and decreasing (reduction) potentials, respectively. Oxidation of the COF shifts the lowest-energy absorption band to about 800 nm and produces an additional very broad IR absorption that extends beyond the measurement range. In contrast to the COFs based on the larger and more electron-rich ttTII and nTII building blocks, the electrochromic color changes are not entirely reversible, probably due to pore blocking and a partial delamination of COF layers (see the manuscript for discussion).
(**d**) Plot of the absorption difference between the oxidized COF and the initial spectrum. Oxidation of the Py-TII COF leads to the evolution of strong NIR absorption bands and a minor contribution at 500 nm, accompanied by two bleach bands at 400 and 650 nm.

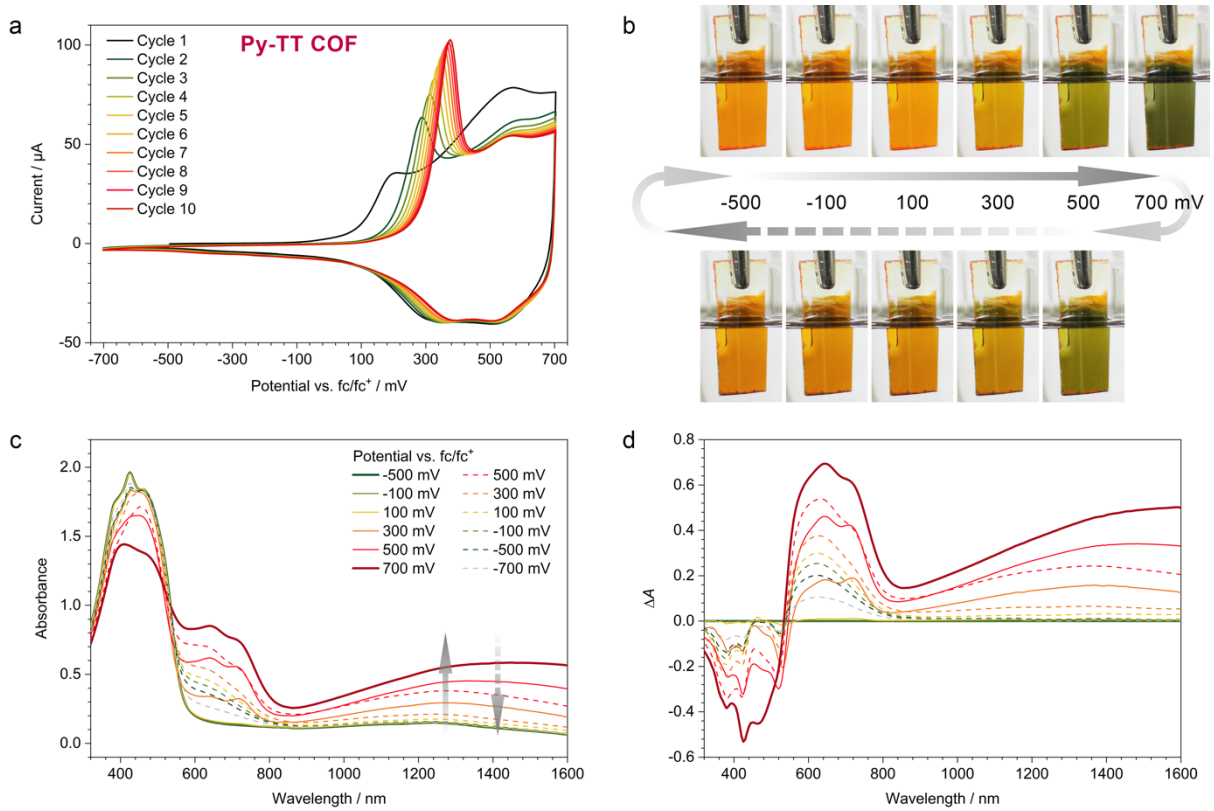

Figure 4.17. Electrochromic properties of the Py-TT COF.

(**a**) Cyclic voltammetry scans of a Py-TT COF film on ITO recorded at a scan rate of 20 mV s^{-1}. See the Methods section for experimental details. The Py-TT COF shows a well-defined oxidation wave at +200 mV during the first oxidation/reduction cycle, which shifts to higher potentials with every measurement cycle. We attribute this effect to limited diffusion of the electrolyte ions and a build-up of charged species in the considerably smaller pores of this COF (see the manuscript for discussion).

(**b**) Photographs of the COF film taken during an oxidation (top row, left to right) / reduction (bottom row, right to left) cycle illustrating the electrochromic color changes.

(**c**) UV-Vis-NIR spectra recorded at different potentials. The solid and dashed lines refer to spectra recorded at increasing (oxidation) and decreasing (reduction) potentials, respectively. Oxidation of the COF causes the evolution of two new absorption features between 600 and 800 nm as well as a broad IR absorption that extends beyond the measurement range. Unlike the large-pore Py-ttTII and Py-nTII COFs, the electrochromic color changes of the Py-TT COF are not entirely reversible, most likely due to pore blocking and a partial delamination of COF layers (see the manuscript for discussion).

(**d**) Plot of the absorption difference between the oxidized COF and the initial spectrum. Oxidation of the Py-TT COF leads to the evolution of a new absorption band between 600 and 800 nm that is accompanied by a bleach band around 400 nm.

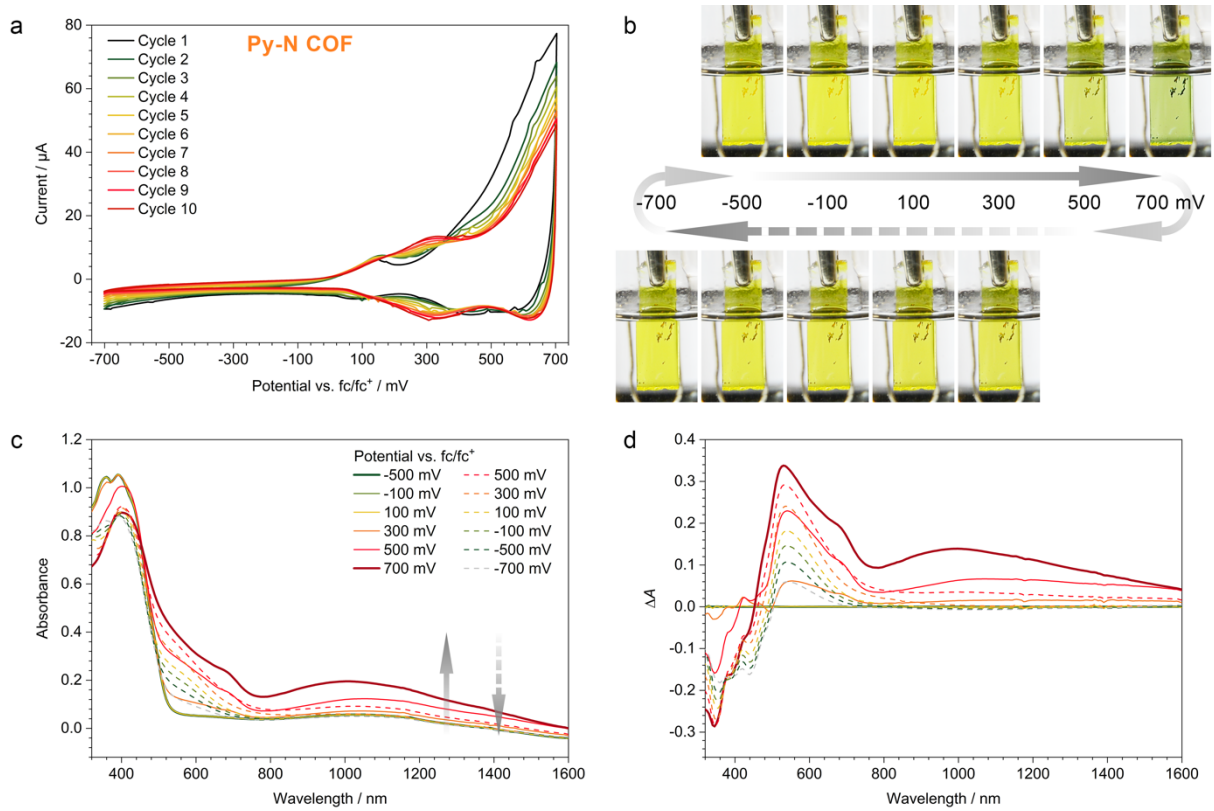

Figure 4.18. Electrochromic properties of the Py-N COF.

(**a**) Cyclic voltammetry scans of a Py-N COF film on ITO recorded at a scan rate of 20 mV s^{-1}. See the Methods section for experimental details. This COF shows an oxidation onset between 500 and 700 mV, which gradually shifts with every measurement cycle towards higher potentials. We attribute this effect to limited diffusion of the electrolyte ions and a build-up of charged species in the relatively small pores of this COF (see the manuscript for discussion). The small features at lower potentials are probably due to impurities or defects in the COF film.

(**b**) Photographs of the COF film taken during an oxidation (top row, left to right) / reduction (bottom row, right to left) cycle illustrating the electrochromic color changes.

(**c**) UV-Vis-NIR spectra recorded at different potentials. The solid and dashed lines refer to spectra recorded at increasing (oxidation) and decreasing (reduction) potentials, respectively. Oxidation of the COF causes the evolution of a new absorption feature around 600 nm as well as a broad IR absorption around 1000 nm. Unlike the large-pore Py-ttTII and Py-nTII COFs, the electrochromic color changes of the Py-N COF are not entirely reversible, most likely due to pore blocking and a partial delamination of COF layers (see the manuscript for discussion).

(**d**) Plot of the absorption difference between the oxidized COF and the initial spectrum. Oxidation of the Py-N COF leads to the evolution of a new absorption band around 600 nm that is accompanied by a bleach band around 380 nm.

Section H – Switching speed and stability

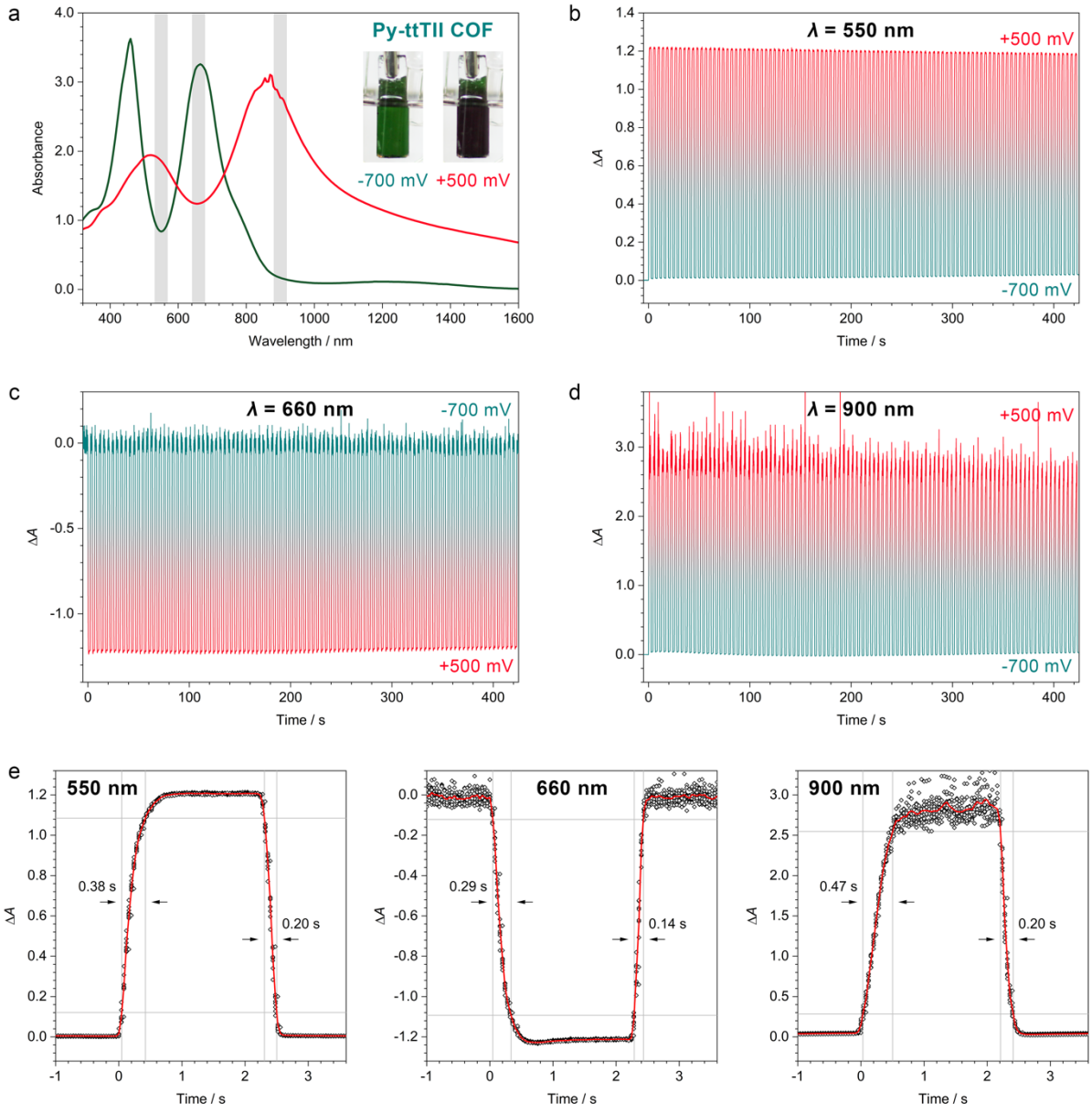

Figure 4.19. Electrochromic switching of the Py-ttTII COF. To avoid any "burn-in" effects, the switching experiments have been conducted with three freshly synthesized Py-ttTII COF samples from the same batch (one for each wavelength). Thus, time = 0 s corresponds to the first time that the samples are oxidized. Any differences between the Δ*A* values in (a) and (b)/(c)/(d) are due to slight variations in film thicknesses.

(**a**) Absorption spectra of a Py-ttTII COF film on ITO at −700 mV (green line) and +500 mV vs. fc/fc^+ (red line). The wavelengths used for the electrochromic switching experiments are indicated by grey lines. Insets: Photographs of the COF film.

(**b**) Electrochromic switching between the neutral and oxidized form of a Py-ttTII COF film over 100 cycles. The applied potential is switched between −700 and +500 mV vs. fc/fc^+ and held constant for 2 s after each potential step. The change of the absorbance is monitored at 550 nm. At this wavelength, the absorbance increases by 1.2 OD units upon oxidation with almost no degradation over 100 cycles.

(**c**) Electrochromic switching over 100 cycles recorded at 660 nm. At this wavelength, the absorbance of the Py-ttTII COF is reduced by ca. 1.2 OD upon oxidation.
(**d**) Electrochromic switching over 100 cycles monitored at 900 nm. Upon oxidation, the absorbance increases by almost 3 OD.
(**e**) Switching speed of the Py-ttTII COF films in response to potential steps at 550 nm (left), 660 nm (middle) and 900 nm (right). The respective datasets (black dots) of the first ten switching cycles shown in (b)/(c)/(d) are averaged (red lines). The response is extremely fast with response times of 0.29 – 0.47 s (coloration) and 0.14 – 0.20 s (bleaching) between the 10% and 90% boundaries (grey lines).

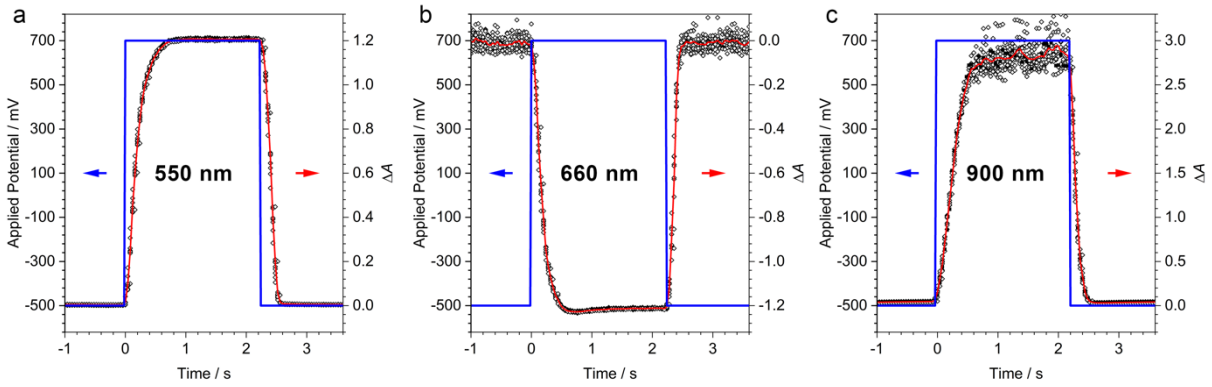

Figure 4.20. Overlay of the applied potential (blue, left *y*-axis) and the electrochromic response (black symbols and red line, right *y*-axis) of the Py-ttTII COF films at (**a**) 550 nm, (**b**) 660 nm, and (**c**) 900 nm.

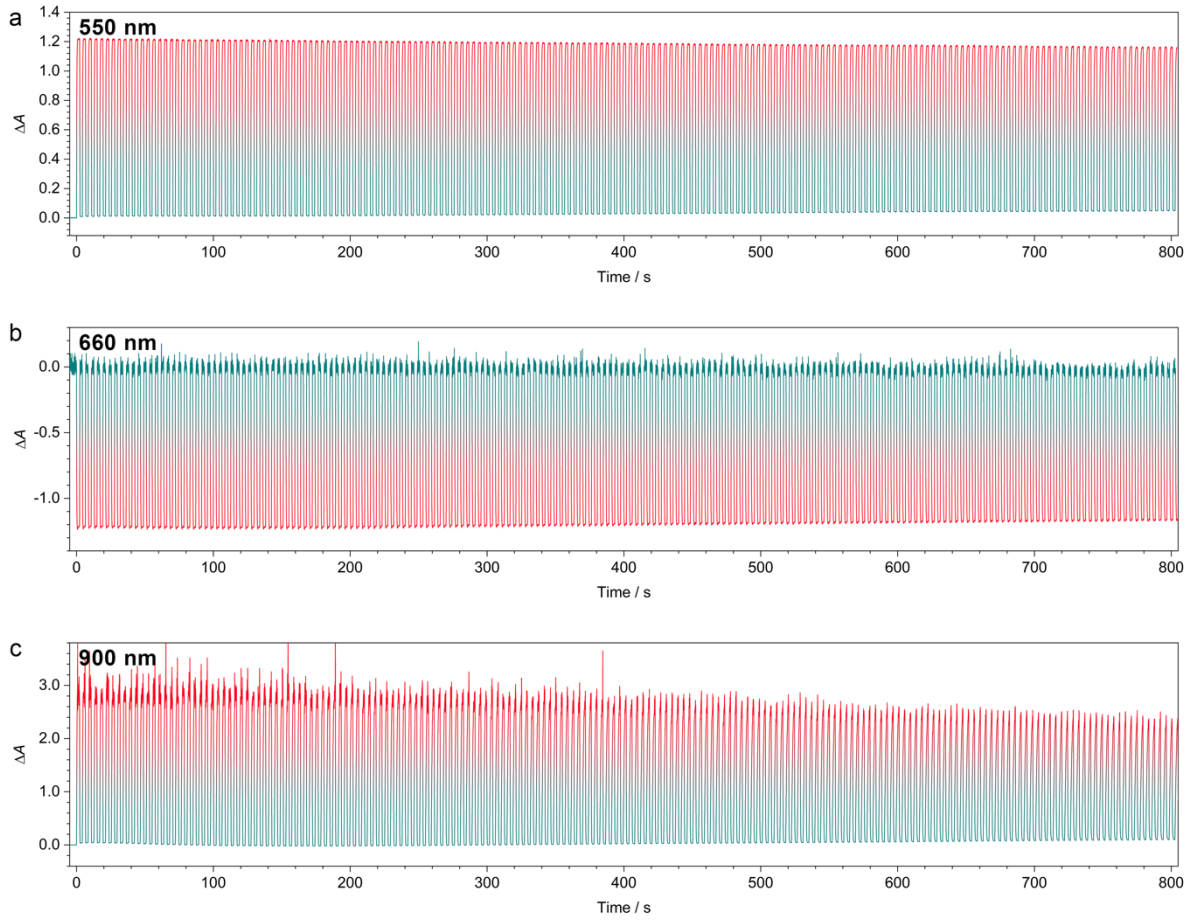

Figure 4.21. Electrochromic switching of the Py-ttTII COF over 200 cycles recorded at (**a**) 550 nm, (**b**) 660 nm, and (**c**) 900 nm. To avoid any "burn-in" effects, the switching experiments have been conducted with three freshly synthesized Py-ttTII COF samples from the same batch (one for each wavelength). Thus, time = 0 s corresponds to the first time that the samples are oxidized. The applied potential is switched between −700 and +500 mV vs. fc/fc^{+} and held constant for 2 s after each potential step.

Section I – Coloration efficiency and extracted charge

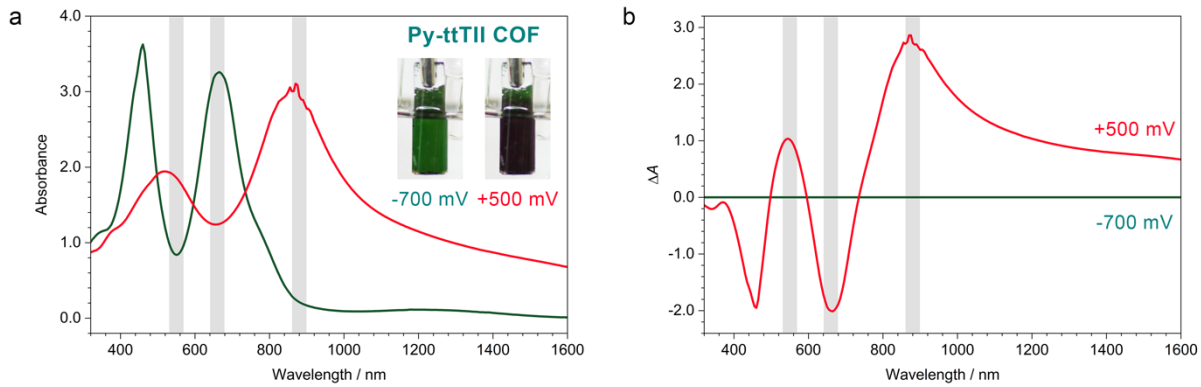

Figure 4.22. Spectra of the Py-ttTII COF in the neutral (green) and the 2x oxidized state (red). (**a**) Absorption spectra. (**b**) Absorption difference between the neutral and the oxidized COF. The wavelengths used for the calculation of the coloration efficiency are indicated by grey lines.

The electrochromic coloration efficiency (CE) relates the absorption change to the injected or extracted charge per unit area.

$$\mathrm{CE}(\lambda) = \frac{\Delta A(\lambda)}{Q/A}$$

ΔA is the absorption difference at the respective wavelength λ (Figure 4.22b).

ΔA(550 nm) = 1.03 ΔA(660 nm) = 2.01 ΔA(880 nm) = 2.78

A is the electrode area in contact with the electrolyte.

A = 11 mm × 6.3 mm = 0.69 cm^2

Q is the extracted charge, calculated from the oxidation scan shown in Figures 4.3b and 4.14a.

Q = 0.00223 C (0.00324 C cm^{-2}) for the two oxidation waves (−500 to +470 mV vs. fc/fc$^+$).

Using the above expression, the Py-ttTII COF has the following wavelength-dependent coloration efficiencies:

CE(550 nm) = 318 ± 32 cm^2 C^{-1}

CE(660 nm) = 620 ± 62 cm^2 C^{-1}

CE(880 nm) = 858 ± 86 cm^2 C^{-1}

These values are several times higher than the CEs of previous electrochromic COFs.[20, 21]

How much charge is extracted per unit cell?

The 430 nm thick Py-ttTII COF film has a volume of 2.95×10^{-11} m^3 using the electrode dimensions stated above and assuming a pinhole-free film with 70% density due to its unique pillar-like morphology (Figure 4.12c). Using the refined unit cell parameters (V = 1.27×10^{-26} m^3), this relates to 1.63×10^{15} unit cells. Hence, the maximum charge that can be extracted by oxidation of every ttTII unit (the unit cell contains four) is

$$Q_{ox1} = 4Ne = 0.00104 \text{ C } (0.00152 \text{ C cm}^{-2})$$

$$Q_{ox2} = 4Ne \times 2 = 0.00209 \text{ C } (0.00304 \text{ C cm}^{-2})$$

N is the number of unit cells per film (corresponding to 4N ttTII units).

e is the elementary charge (1.602×10^{-19} C).

Q_{ox1} and Q_{ox2} refer to the one-electron and two-electron oxidation, respectively.

This calculation confirms our assignment of the two oxidation waves in the CV scans and the two distinct absorption spectra at different potentials to the one-electron and two-electron oxidation steps. The charge determined from the measured electrical current is slightly higher than the theoretical value, because there is a non-zero current flow through the electrochemical cell under applied bias.

Coloration efficiencies of the other COFs

$$\mathrm{CE}(\lambda) = \frac{\Delta A(\lambda)}{Q/A}$$

Py-nTII COF

ΔA(520 nm) = 0.490 ΔA(630 nm) = 0.547 ΔA(850 nm) = 0.992

A = 10 mm × 6.7 mm = 0.67 cm^2 Q = 0.000814 C (0.00122 C cm^{-2})

CE(520 nm) = 400 ± 60 cm^2 C^{-1}

CE(630 nm) = 450 ± 70 cm^2 C^{-1}

CE(850 nm) = 820 ± 120 cm^2 C^{-1}

Py-TII COF

ΔA(500 nm) = 0.179 ΔA(630 nm) = 0.208 ΔA(820 nm) = 0.275

A = 13 mm × 5.8 mm = 0.75 cm^2 Q = 0.00103 C (0.00137 C cm^{-2})

CE(500 nm) = 130 ± 20 cm^2 C^{-1}

CE(630 nm) = 150 ± 20 cm^2 C^{-1}

CE(820 nm) = 200 ± 30 cm^2 C^{-1}

Py-TT COF

ΔA(645 nm) = 0.692

A = 11 mm × 7.5 mm = 0.83 cm^2 Q = 0.00163 C (0.00198 C cm^{-2})

CE(645 nm) = 350 ± 35 cm^2 C^{-1}

Py-N COF

ΔA(530 nm) = 0.336

A = 12 mm × 6.5 mm = 0.78 cm^2 Q = 0.000738 C (0.000946 C cm^{-2})

CE(530 nm) = 360 ± 50 cm^2 C^{-1}

The CEs of the Py-ttTII and Py-nTII COFs, which are based on donor-acceptor-donor building blocks, are significantly higher than the CEs of the other frameworks, highlighting the importance of a suitable electronic design.

Section J – Building block syntheses

All reactions were performed in oven-dried glassware under argon atmosphere using standard Schlenk and glovebox techniques. Reagents and solvents were obtained in high-purity grades from commercial suppliers and were, unless shipped under argon, degassed and saturated with argon prior to use. Flash column chromatography was performed using silica gel (Acros Organics, 60 Å, 35 – 70 µm) and was continuously monitored *via* thin layer chromatography (TLC) using silica gel coated aluminum plates (Merck, 60 Å, F254).

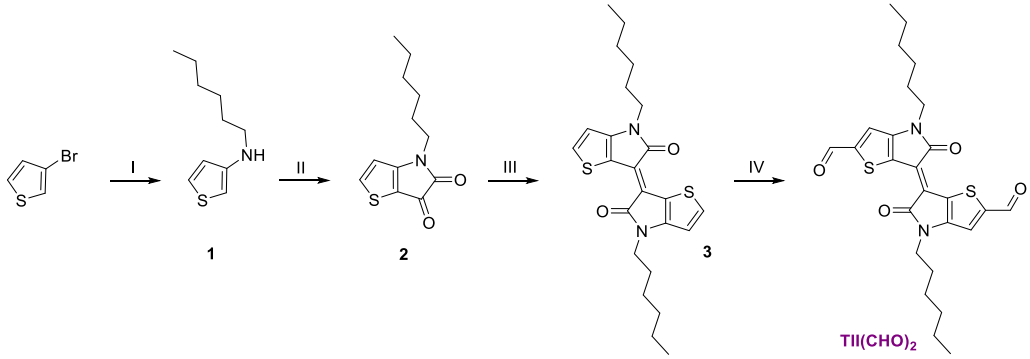

Figure 4.23. Syntheses of the hexyl-alkylated thienoisoindigo-core **3** and the TII(CHO)$_2$ building block. Reagents and conditions: (**I**) *n*-hexylamine, Cu, CuI, K_3PO_4, 2-dimethylaminoethanol, 80 °C, 65%. (**II**) oxalyl chloride, triethylamine, DCM, −15 °C/0°C/rt, 53%. (**III**) Lawesson's reagent, toluene, 100 °C, 5 min, 51%. (**IV**) LDA, DMF, THF, −78 °C/rt, 39%.

3-(hexylamino)thiophene (1)[27, 40]

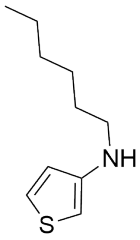

A reaction mixture containing 3-bromothiophene (12.2 g, 7.03 mL, 75.0 mmol, 1.0 eq.), *n*-hexylamine (11.4 g, 14.9 mL, 113 mmol, 1.5 eq.), copper powder (477 mg, 7.50 mmol, 10 mol%.), CuI (1.43 g, 7.50 mmol, 10 mol%) and K_3PO_4 (31.8 g, 150 mmol, 2.0 eq.) in anhydrous 2-dimethylaminoethanol (75 mL) were stirred under argon at 80 °C for 48 h. After cooling to room temperature, the supernatant was decanted and collected, and the solid residue was washed with anhydrous THF (4x 20 mL). The combined liquids were concentrated

under reduced pressure. Purification *via* high vacuum distillation (10^{-2} mbar, 68 °C) yielded the title compound as a colorless and highly air-sensitive liquid (8.98 g, 49.0 mmol, 65%).

Due to the high air- and moisture-sensitivity, no NMR spectra were recorded and the product was used directly in the following step.

4-hexyl-4*H*-thieno[3,2-*b*]pyrrole-5,6-dione (2)

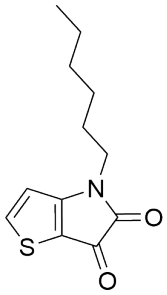

A solution of oxalyl chloride (9.95 g, 6.72 mL, 78.4 mmol, 1.6 eq.) in 49 mL of anhydrous DCM was cooled to −15 °C. Compound 1 (8.98 g, 49.0 mmol, 1.0 eq.) in 84 mL anhydrous DCM was slowly added *via* a syringe over 20 minutes under argon atmosphere. After the dropwise addition of triethylamine (14.9 g, 20.4 mL, 147 mmol, 3.0 eq.) at −15 °C, the resulting suspension was stirred for 1 h at 0 °C and allowed to warm to room temperature overnight. The reaction mixture was quenched with H_2O, and the product was extracted with DCM. The combined organic phases were washed with brine three times, dried over $MgSO_4$, and concentrated under reduced pressure. The product was purified by column chromatography (silica gel, DCM + 0.5% THF) to yield the title compound as a red oil (6.12 g, 25.8 mmol, 53%).

^{1}H-NMR (400 MHz, $CDCl_3$): 7.99 (d, *J* = 5.0 Hz, 1H), 6.78 (d, *J* = 5.0 Hz, 1H), 3.65 (t, *J* = 7.2 Hz, 2H), 1.73 – 1.61 (m, 2H), 1.41 – 1.24 (m, 6H), 0.88 (t, *J* = 7.1 Hz, 3H).

^{13}C-NMR (101 MHz, $CDCl_3$): 173.2, 165.3, 161.6, 144.0, 113.1, 111.2, 42.3, 31.5, 28.3, 26.6, 22.6, 14.1.

_N_,_N_'-dihexyl-thienoisoindigo (3)

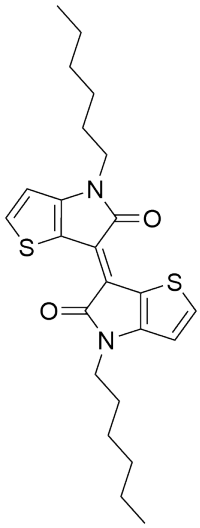

Compound **2** (4.68 g, 19.7 mmol, 2.0 eq.) was dissolved in 158 mL anhydrous toluene and added to Lawesson's reagent (3.99 g, 9.87 mmol, 1.0 eq.) under argon atmosphere at room temperature. In a preheated oil bath, the reaction mixture was stirred at 100 °C for 5 minutes. After cooling to room temperature, the product was concentrated under reduced pressure and all volatiles were removed under high vacuum. The crude product was purified by column chromatography (silica gel, DCM/*n*-hexane 2:1) to yield the title compound as a dark violet powder (2.23 g, 5.04 mmol, 51%).

^{1}H-NMR (400 MHz, $CDCl_3$): 7.53 (d, *J* = 5.2 Hz, 2H), 6.81 (d, *J* = 5.2 Hz, 2H), 3.80 (t, *J* = 7.3 Hz, 4H), 1.78 – 1.67 (m, 4H), 1.40 – 1.24 (m, 12H), 0.87 (t, *J* = 7.1 Hz, 6H).

^{13}C-NMR (101 MHz, $CDCl_3$): 171.1, 151.4, 134.5, 121.3, 114.3, 111.3, 42.0, 31.6, 28.7, 26.7, 22.7, 14.2.

5,5'-diformyl-*N*,*N*'-dihexyl-thienoisoindigo (TII(CHO)$_2$)

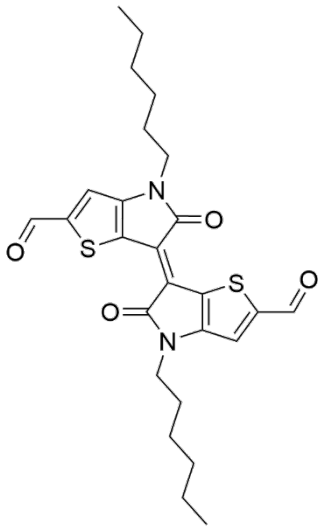

Following a literature procedure,[41] a solution of compound **3** (443 mg, 1.0 mmol, 1.0 eq.) in 40 mL anhydrous THF was added dropwise to a 1.0 M solution of LDA in THF/hexane (8.0 mmol, 8.0 eq.) cooled at −78 °C under argon atmosphere. The reaction mixture was stirred for 2 h at −78 °C. Anhydrous DMF (0.92 mL, 12 mmol, 12 eq.) was added dropwise and the resulting solution was stirred overnight, allowing the mixture to slowly warm to room temperature. The reaction was quenched with 100 mL of 0.5 M aqueous HCl, stirred for 1 h and extracted with DCM. The organic phase was washed with brine (2x), dried over $MgSO_4$ and concentrated under reduced pressure. The product was purified *via* column chromatography (silica gel, DCM + 2% EtOAc) to yield the title compound as an indigo blue solid (194 mg, 0.39 mmol, 39%).

^{1}H NMR (400 MHz, $CDCl_3$): 9.93 (s, 2H), 7.40 (s, 2H), 3.84 (t, *J* = 7.3 Hz, 4H), 1.80 – 1.70 (m, 4H), 1.42 – 1.26 (m, 12H), 0.89 (t, *J* = 7.1 Hz, 6H).

^{13}C NMR (101 MHz, $CDCl_3$): 183.0, 169.8, 152.3, 149.5, 123.8, 122.4, 115.1, 42.2, 31.5, 28.4, 26.7, 22.7, 14.1.

HR-EI-MS: *m*/*z* 498.16 (M^+, calculated for $C_{26}H_{30}N_2O_4S_2$: 498.16).

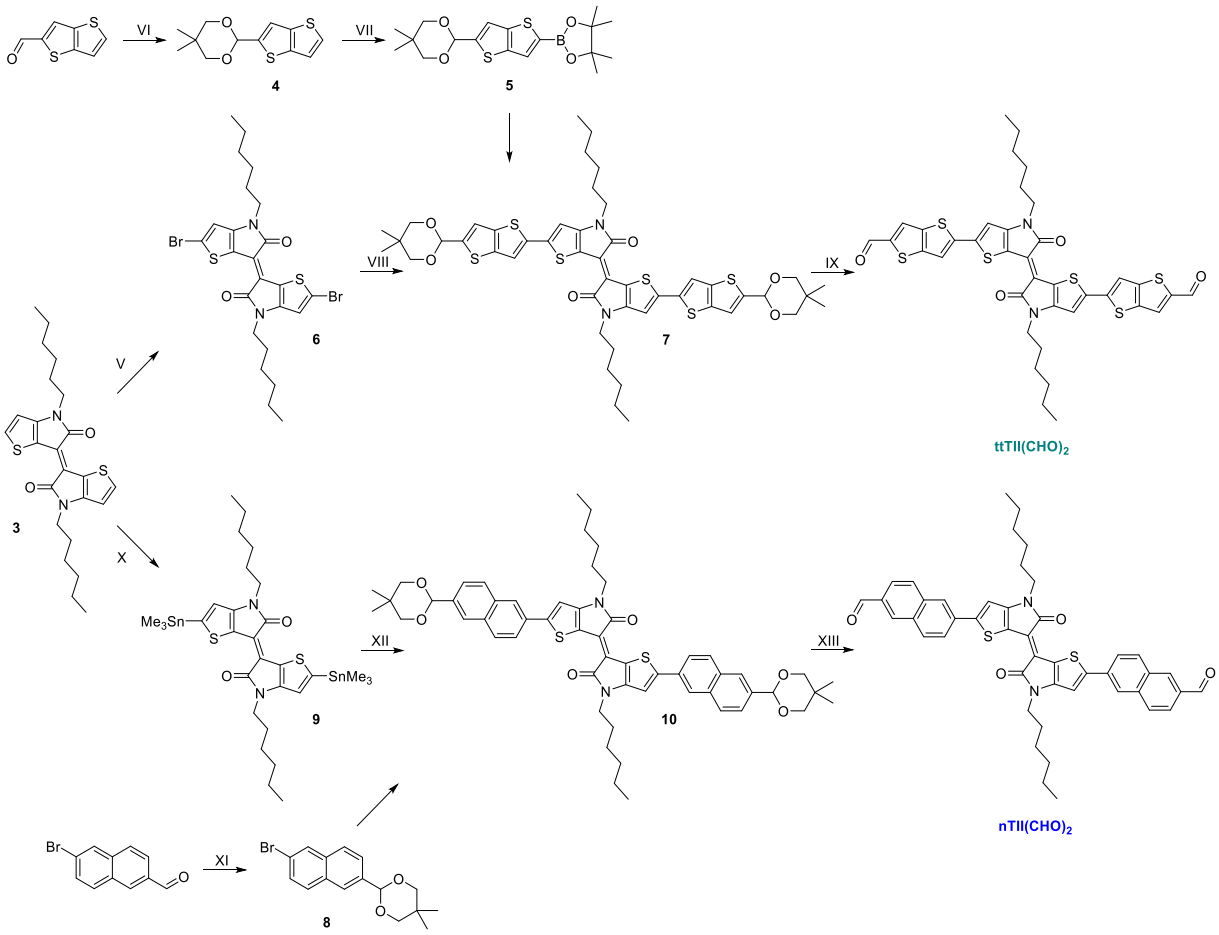

Figure 4.24. Syntheses of the new ttTII(CHO)$_2$ and nTII(CHO)$_2$ building blocks. Reagents and conditions: (**V**) NBS, THF, 0 °C, 84%. (**VI**) *p*-toluenesulfonic acid monohydrate, 2,2-dimethyl-1,3-propanediol, toluene, reflux, 97%. (**VII**) *n*-BuLi, 2-isopropoxy-4,4,5,5-tetramethyl-1,3,2-dioxaborolane, THF, −78 °C/rt, 58%. (**VIII**) $Pd_2(dba)_3{\cdot}CHCl_3$, SPhos, K_2CO_3, *o*-xylene/H_2O, 100 °C, 74%. (**IX**) TFA, H_2O, rt, 76%. (**X**) LDA, Me_3SnCl, THF, −78 °C/rt, 83%. (**XI**) *p*-toluenesulfonic acid monohydrate, 2,2-dimethyl-1,3-propanediol, toluene, reflux, 83%. (**XII**) $Pd_2(dba)_3$, P(*o*-tol)$_3$, toluene, 110 °C, 84%. (**XIII**) TFA, H_2O, $CHCl_3$, rt, 81%.

5,5-dimethyl-2-(thieno[3,2-*b*]thiophen-2-yl)-1,3-dioxane (4)

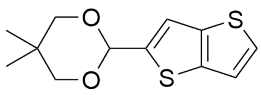

A reaction mixture containing thieno[3,2-*b*]thiophene-2-carboxaldehyde (1000 mg, 5.94 mmol, 1.0 eq.), 2,2-dimethyl-1,3-propanediol (1175 mg, 11.3 mmol, 1.9 eq.) and *p*-toluenesulfonic acid monohydrate (91.3 mg, 0.48 mmol, 8 mol%) in 59 mL toluene was refluxed at 110 °C for 2.5 h. After cooling to room temperature, the reaction mixture was poured into water, extracted with DCM and washed with brine (3x). The organic phase was dried over $MgSO_4$ and concentrated under reduced pressure. Purification *via* column

chromatography (silica gel, DCM/*n*-hexane 3:2) yielded the title compound as a white powder (1468 mg, 5.77 mmol, 97%).

^{1}H NMR (400 MHz, $CDCl_3$): 7.35 (d, *J* = 5.2 Hz, 1H), 7.32 (s, 1H), 7.24 (d, *J* = 5.3 Hz, 1H), 5.68 (s, 1H), 3.78 (d, *J* = 11.3 Hz, 2H), 3.66 (d, *J* = 10.8 Hz, 2H), 1.29 (s, 3H), 0.81 (s, 3H).

^{13}C NMR (101 MHz, $CDCl_3$): 143.4, 139.4, 138.5, 127.5, 119.7, 117.7, 98.5, 77.7, 30.4, 23.1, 22.0.

2-(5-(5,5-dimethyl-1,3-dioxan-2-yl)thieno[3,2-*b*]thiophen-2-yl)-4,4,5,5-tetramethyl-1,3,2-dioxaborolane (5)

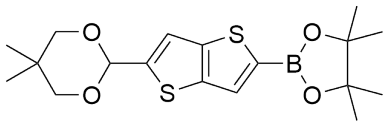

Compound **4** (715 mg, 2.81 mmol, 1.0 eq.) was dissolved in 23.5 mL THF and cooled to −78 °C. *n*-BuLi (2.0 M in cyclohexane, 4.22 mmol, 1.5 eq.) was added dropwise and the solution was stirred for 1.5 h at −78 °C. Subsequently, 2-isopropoxy-4,4,5,5-tetramethyl-1,3,2-dioxaborolane (785 mg, 0.86 mL, 4.22 mmol, 1.5 eq.) was added and the reaction mixture was stirred for 1 h at −78 °C. The resulting suspension was allowed to warm to room temperature and stirred overnight. The reaction was quenched with H_2O (25 mL) and stirred for 15 minutes. The product was extracted with diethyl ether and washed with brine three times. The organic phase was dried over $MgSO_4$ and concentrated under reduced pressure. The product was purified *via* recrystallization from *n*-hexane (75 mL, 70 °C to room temperature), collected by filtration and dried under high vacuum to yield the title compound as colorless needles (612 mg, 1.61 mmol, 58%).

^{1}H NMR (400 MHz, $CDCl_3$): 7.73 (s, 1H), 7.33 (s, 1H), 5.68 (s, 1H), 3.78 (d, *J* = 11.3 Hz, 2H), 3.66 (d, *J* = 10.7 Hz, 2H), 1.35 (s, 12H), 1.28 (s, 3H), 0.81 (s, 3H).

5,5'-dibromo-*N*,*N*'-dihexyl-thienoisoindigo (6)

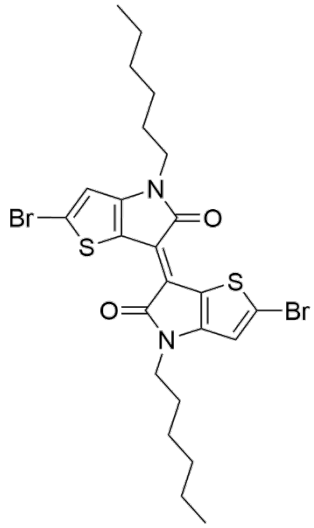

A solution of compound **3** (2230 mg, 5.04 mmol, 1.0 eq.) in 231 mL anhydrous THF was cooled to 0 °C. *N*-Bromosuccinimide (1883 mg, 10.6 mmol, 2.1 eq.) was added and the reaction mixture was stirred for 1.5 h at 0 °C in the dark. The reaction was quenched with H_2O, extracted with $CHCl_3$, and washed with brine (2x). The organic phase was dried over $MgSO_4$ and concentrated under reduced pressure. Purification *via* column chromatography (silica gel, $CHCl_3$/cyclohexane 1:1) yielded the title compound as a dark blue powder (2547 mg, 4.24 mmol, 84%).

^{1}H NMR (400 MHz, $CDCl_3$): 6.84 (s, 2H), 3.74 (t, *J* = 7.3 Hz, 4H), 1.75 – 1.63 (m, 4H), 1.40 – 1.24 (m, 12H), 0.88 (t, *J* = 7.1 Hz, 6H).

^{13}C NMR (101 MHz, $CDCl_3$): 170.2, 150.0, 123.4, 119.9, 115.0, 114.8, 42.0, 31.6, 28.7, 26.7, 22.7, 14.2.

5,5'-bis(5-(5,5-dimethyl-1,3-dioxane-2-yl)thienothiophen-2-yl)-*N*,*N*'-dihexyl-thienoisoindigo (7)

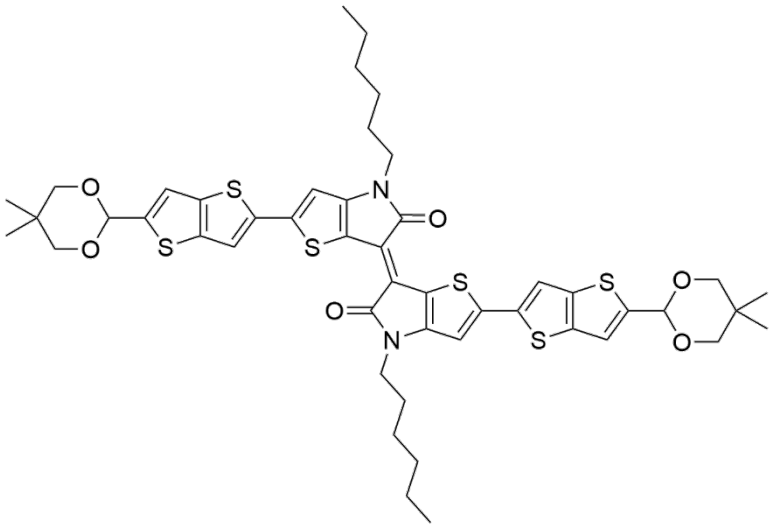

A reaction mixture containing compound **6** (143 mg, 0.24 mmol, 1.0 eq.), compound **5** (217 mg, 0.57 mmol, 2.4 eq.), $Pd_2(dba)_3 \cdot CHCl_3$ (24.6 mg, 0.024 mmol, 10 mol%), SPhos (19.5 mg, 0.05 mmol, 20 mol%), and K_2CO_3 (132 mg, 0.95 mmol, 4 eq.) in 7.6 mL *o*-xylene and 1.9 mL H_2O was stirred at 100 °C for 20 h under argon atmosphere. After cooling to room temperature, the mixture was poured into water and extracted with DCM. The organic phase was dried over $MgSO_4$ and concentrated under reduced pressure. Purification by column chromatography (silica gel, DCM) yielded the title compound as a dark green powder (168 mg, 0.18 mmol, 74%).

^{1}H NMR (400 MHz, $CDCl_3$): 7.53 (s, 2H), 7.29 (s, 2H), 6.91 (s, 2H), 5.68 (s, 2H), 3.86 – 3.75 (m, 8H), 3.67 (d, *J* = 11.0 Hz, 4H), 1.80 – 1.70 (m, 4H), 1.45 – 1.31 (m, 12H), 1.29 (s, 6H), 0.89 (t, *J* = 7.1 Hz, 6H), 0.82 (s, 6H).

5,5'-bis(2-formylthienothiophen-5-yl)-*N*,*N*'-dihexyl-thienoisoindigo (ttTII(CHO)$_2$)

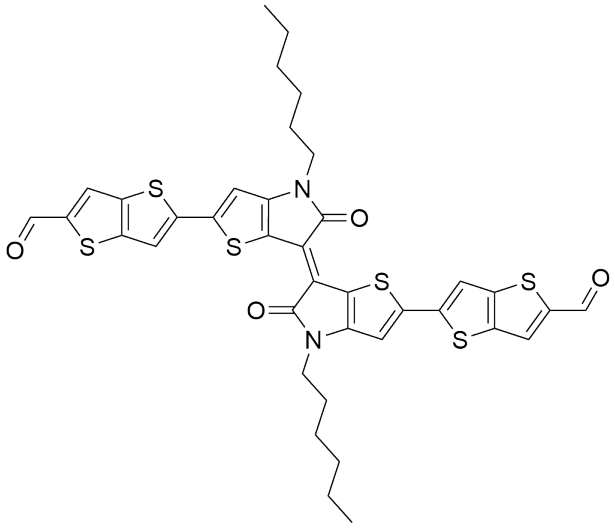

To a solution of compound **7** (160 mg, 0.17 mmol, 1.0 eq.) dissolved in 25 mL $CHCl_3$, trifluoroacetic acid (5 mL) and H_2O (0.5 mL) were added dropwise and left to stir at room temperature for 4 h under argon atmosphere. The reaction mixture was slowly added into saturated aqueous $NaHCO_3$ (100 mL) and extracted with $CHCl_3$. The combined organic phase was washed with brine, dried over $MgSO_4$ and concentrated to about 100 mL under reduced pressure. The product was precipitated by addition of MeOH (100 mL), collected by filtration, washed with $CHCl_3$ (20 mL) and dried under high vacuum to yield the title compound as a dark green powder (99 mg, 0.13 mmol, 76%).

^{1}H NMR (400 MHz, $CDCl_3$): 9.96 (s, 2H), 7.90 (s, 2H), 7.59 (s, 2H), 7.01 (s, 2H), 3.85 (t, *J* = 7.4 Hz, 4H), 1.83 – 1.73 (m, 4H), 1.41 – 1.29 (m, 12H), 0.90 (t, *J* = 7.0 Hz, 6H).

HR-EI-MS: *m*/*z* 774.08 (M^+, calculated for $C_{38}H_{34}N_2O_4S_6$: 774.08).

2-(6-bromonaphthalen-2-yl)-5,5-dimethyl-1,3-dioxane (8)

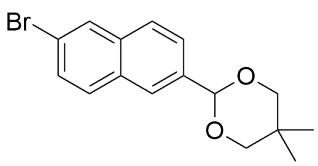

A reaction mixture containing 6-bromo-2-naphthaldehyde (500 mg, 2.1 mmol, 1.0 eq.), *p*-toluenesulfonic acid monohydrate (32.3 mg, 0.17 mmol, 8 mol%) and 2,2-dimethyl-1,3-propanediol (421 mg, 4.0 mmol, 1.9 eq.) in anhydrous toluene (21 mL) were refluxed at 110 °C for 2.5 h under argon atmosphere. After cooling to room temperature, the reaction mixture

was poured into water, extracted with DCM and washed with brine (3x). The organic phase was dried over $MgSO_4$, concentrated under reduced pressure, and purified *via* column chromatography (silica gel, DCM/cyclohexane 1:1) to yield the title compound as a white powder (589 mg, 1.83 mmol, 86%).

^{1}H NMR (400 MHz, $CDCl_3$): 8.00 (s, 1H), 7.95 (s, 1H), 7.79 – 7.70 (m, 4H), 7.65 (dd, *J* = 8.5, 1.7 Hz, 1H), 7.54 (dd, *J* = 8.7, 2.0 1H), 5.54 (s, 1H), 3.82 (d, *J* = 11.3, 2H), 3.72 (d, *J* = 10.6, 2H), 1.33 (s, 3H), 0.83 (s, 3H).

^{13}C NMR (101 MHz, $CDCl_3$): 136.6, 134.8, 131.6, 130.2, 129.9, 129.6, 127.4, 125.6, 125.1, 120.4, 101.7, 30.5, 27.1, 23.3, 22.1.

5,5'-bis(trimethylstannyl)-*N*,*N*'-dihexyl-thienoisoindigo (9)[41]

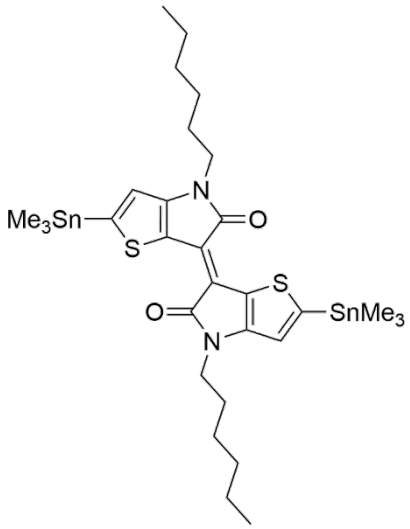

Compound **3** (443 mg, 1.0 mmol, 1 eq.) was dissolved in 50 mL anhydrous THF and added dropwise to LDA (1.0 M in THF/hexane, 8.0 mmol, 8.0 eq.) precooled to -78 °C under argon atmosphere. After stirring for 2 h at this temperature, Me_3SnCl (1.0 M in THF, 12 mmol, 12.0 eq.) was added and the reaction mixture was allowed to slowly warm to room temperature overnight. The reaction was quenched with H_2O and all volatiles were removed under high vacuum at 70 °C. The residue was dissolved in DCM, washed with brine (3x), dried over $MgSO_4$, and the solvent was removed under reduced pressure. The product was washed with MeOH (200 mL), filtrated and dried under high vacuum to yield the title compound as a purple powder (639 mg, 0.83 mmol, 83%).

^{1}H NMR (400 MHz, $CDCl_3$): 6.83 (s, 2H), 3.81 (t, *J* = 7.4 Hz, 4H), 1.79 – 1.68 (m, 4H), 1.42 – 1.24 (m, 12H), 0.88 (t, *J* = 7.1 Hz, 6H), 0.43 (s, with Sn coupling, 18H).

^{13}C NMR (101 MHz, $CDCl_3$): 171.8, 152.5, 151.1, 120.4, 120.2, 117.8, 42.0, 31.7, 28.8, 26.8, 22.7, 14.2, -7.9.

5,5'-bis(6-(5,5-dimethyl-1,3-dioxane-2-yl)naphthalen-2-yl)-*N*,*N*'-dihexyl-thienoisoindigo (10)

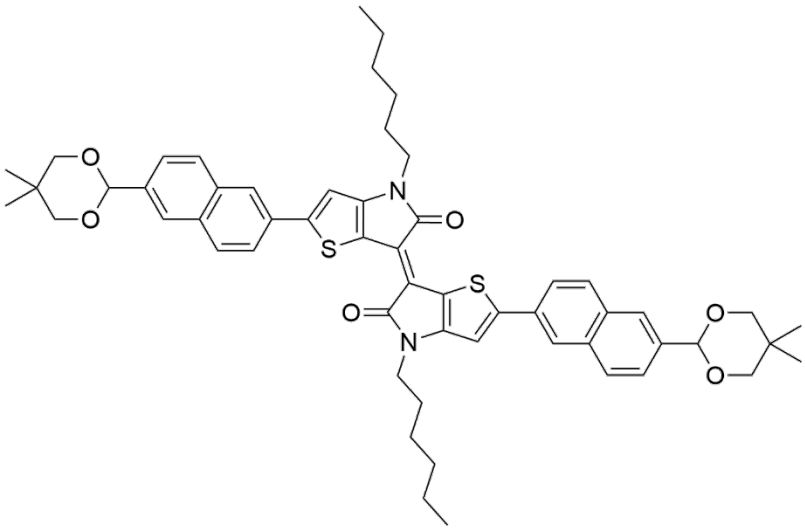

A reaction mixture containing compound **9** (230 mg, 0.3 mmol, 1.0 eq.), compound **8** (212 mg, 0.66 mmol, 2.2 eq.), $Pd_2(dba)_3$ (13.7 mg, 0.015 mmol, 5 mol%) and tri(*o*-tolyl)phosphine (36.5 mg, 0.12 mmol, 0.4 eq.) in 10 mL anhydrous toluene was heated to 110 °C for 4 d. After cooling to room temperature, all volatiles were removed under high vacuum at 60 °C. The solid residue was dissolved in DCM and purified by column chromatography (silica gel, DCM) to yield the title compound as a blue-green powder (234 mg, 0.25 mmol, 84%).

^{1}H NMR (400 MHz, $CDCl_3$): 8.22 (s, 2H), 7.96 (s, 2H), 7.91 – 7.81 (m, 6H), 7.67 (dd, *J* = 8.5, 1.7 Hz, 2H), 7.17 (s, 2H), 5.56 (s, 2H), 3.89 (t, *J* = 7.3 Hz, 4H), 3.84 (d, *J* = 11.2 Hz, 4H), 3.72 (d, *J* = 10.9 Hz, 4H), 1.88 – 1.77 (m, 4H), 1.42 – 1.29 (m, 18H), 0.91 (t, *J* = 7.1 Hz, 6H), 0.85 (s, 6H).

5,5'-bis(2-formylnaphthalen-6-yl)-*N*,*N*'-dihexyl-thienoisoindigo (nTII(CHO)$_2$)

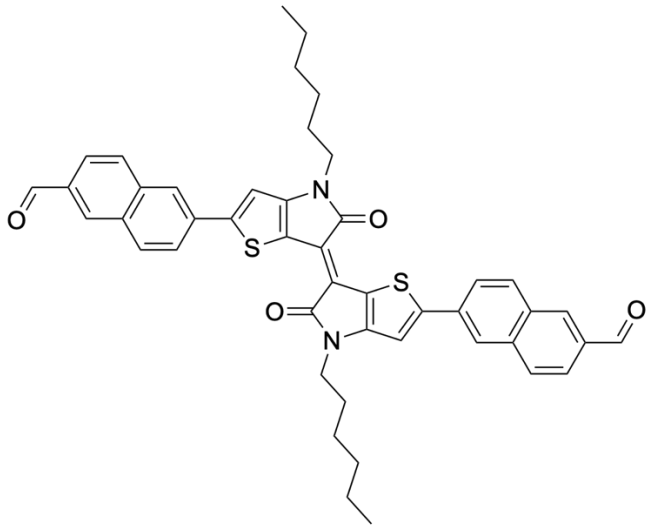

To a solution of compound **10** (572 mg, 0.62 mmol, 1.0 eq.) dissolved in 60 mL $CHCl_3$, trifluoroacetic acid (12 mL) and H_2O (1.2 mL) were added dropwise and left to stir at room temperature for 4 h under argon atmosphere. The reaction was neutralized by the dropwise addition into saturated aqueous $NaHCO_3$ (150 mL) and extracted with $CHCl_3$. The product was precipitated by the addition of MeOH (50 mL), collected by filtration, and washed with H_2O (200 mL), acetone (30 mL) and $CHCl_3$ (20 mL). Drying under high vacuum yielded the title compound as a dark green powder (375 mg, 0.50 mmol, 81%).

^{1}H NMR (400 MHz, $CDCl_3$): 10.15 (s, 2H), 8.30 (s, 2H), 8.25 (s, 2H), 8.03 – 7.90 (m, 8H), 7.24 (s, 2H), 3.90 (t, *J* = 7.3 Hz, 4H), 1.87 – 1.77 (m, 4H), 1.42 – 1.28 (m, 12H), 0.91 (t, *J* = 7.0 Hz, 6H).

HR-EI-MS: *m*/*z* 750.26 (M^+, calculated for $C_{46}H_{42}N_2O_4S_2$: 750.26).

Section K – NMR spectra of the TII building blocks

^{1}H and ^{13}C NMR spectra. Residual (undeuterated) solvent peaks and H_2O/HDO are marked with asterisks.

$TII(CHO)_2$

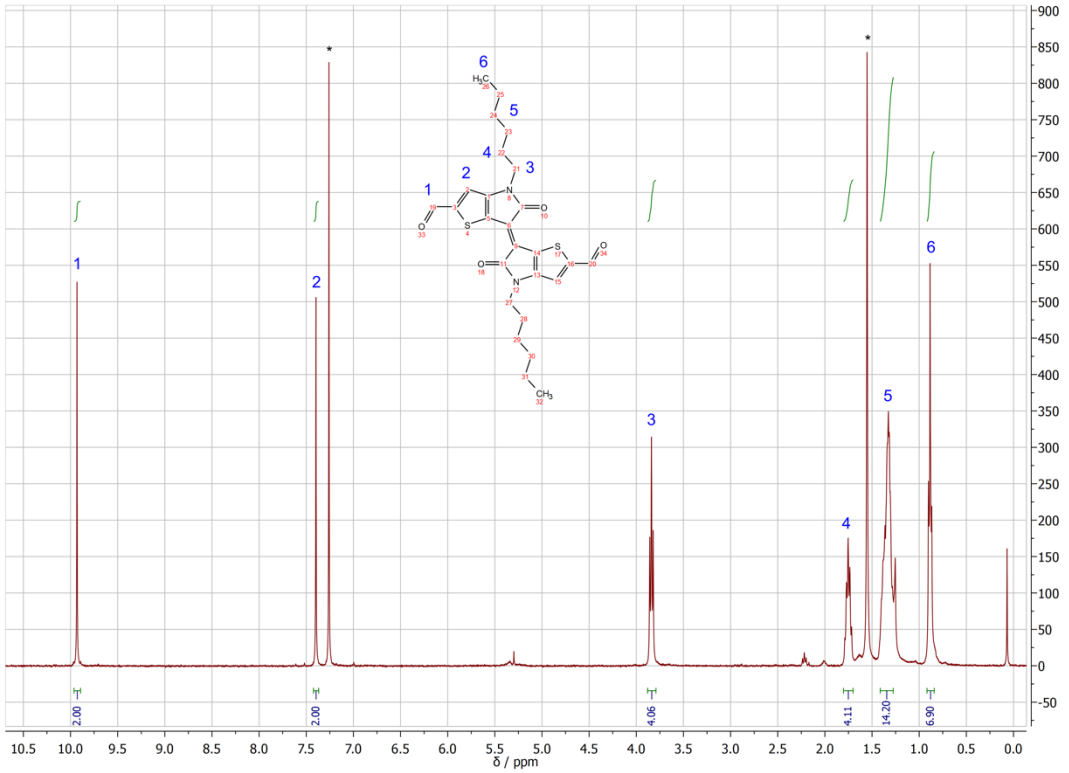

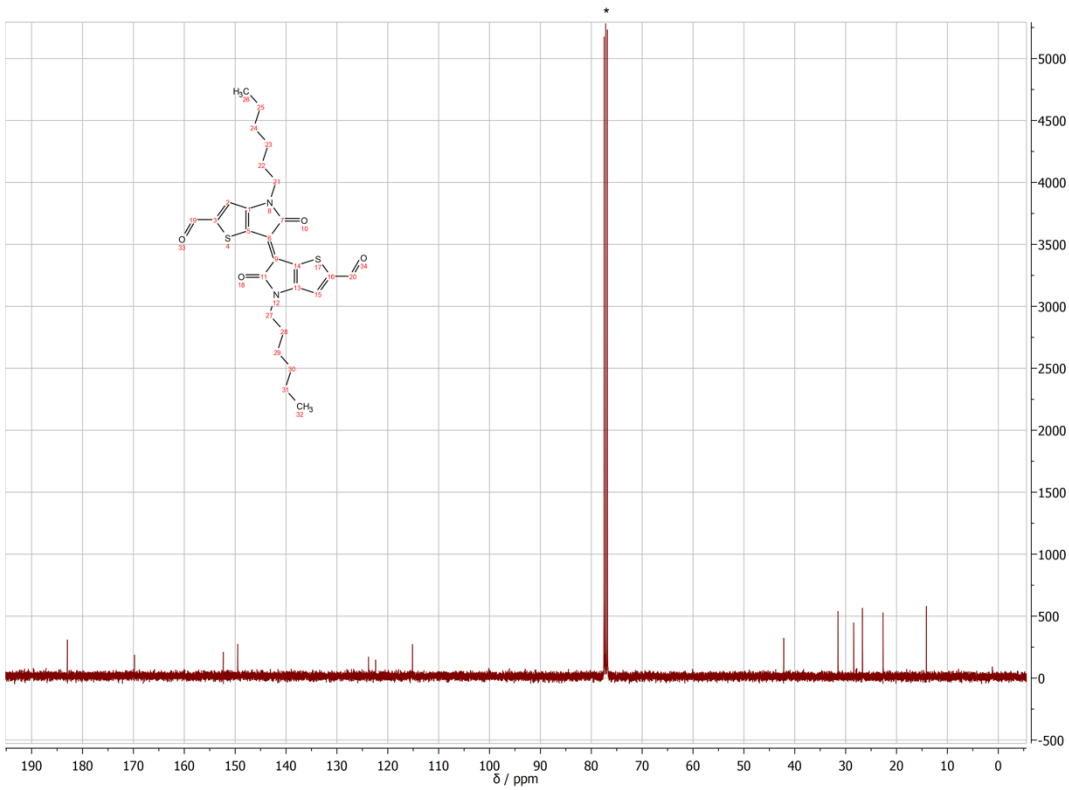

ttTII(CHO)$_2$

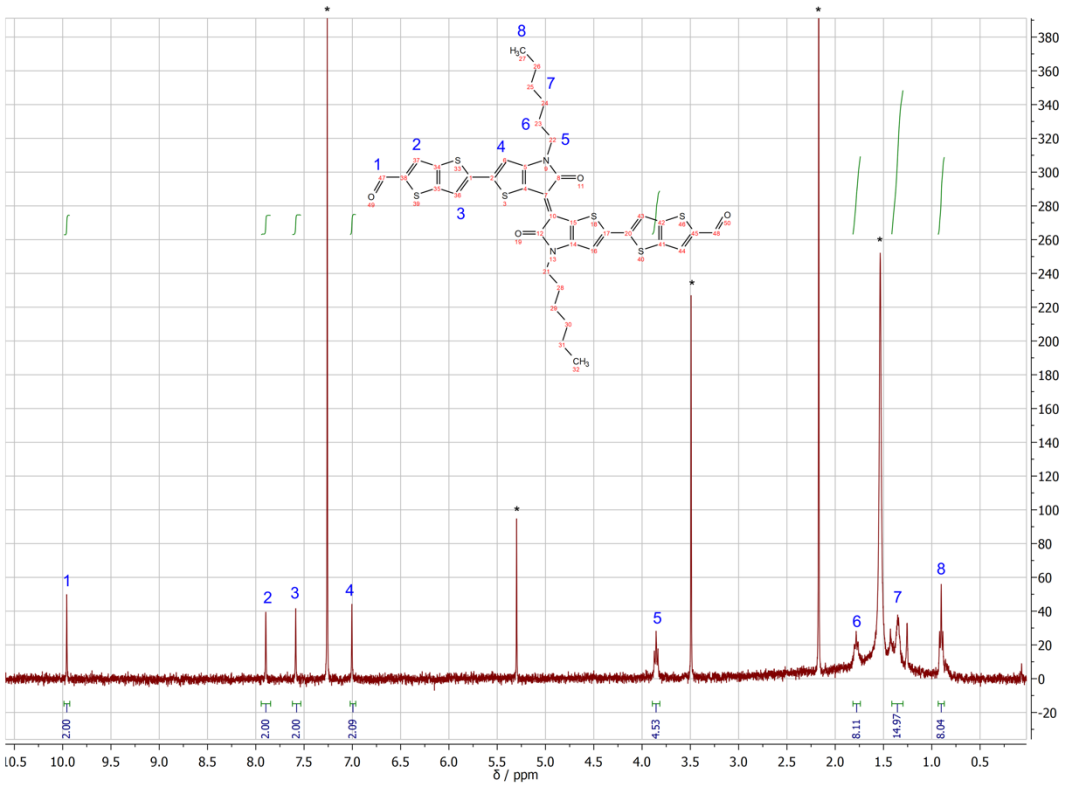

nTII(CHO)$_2$

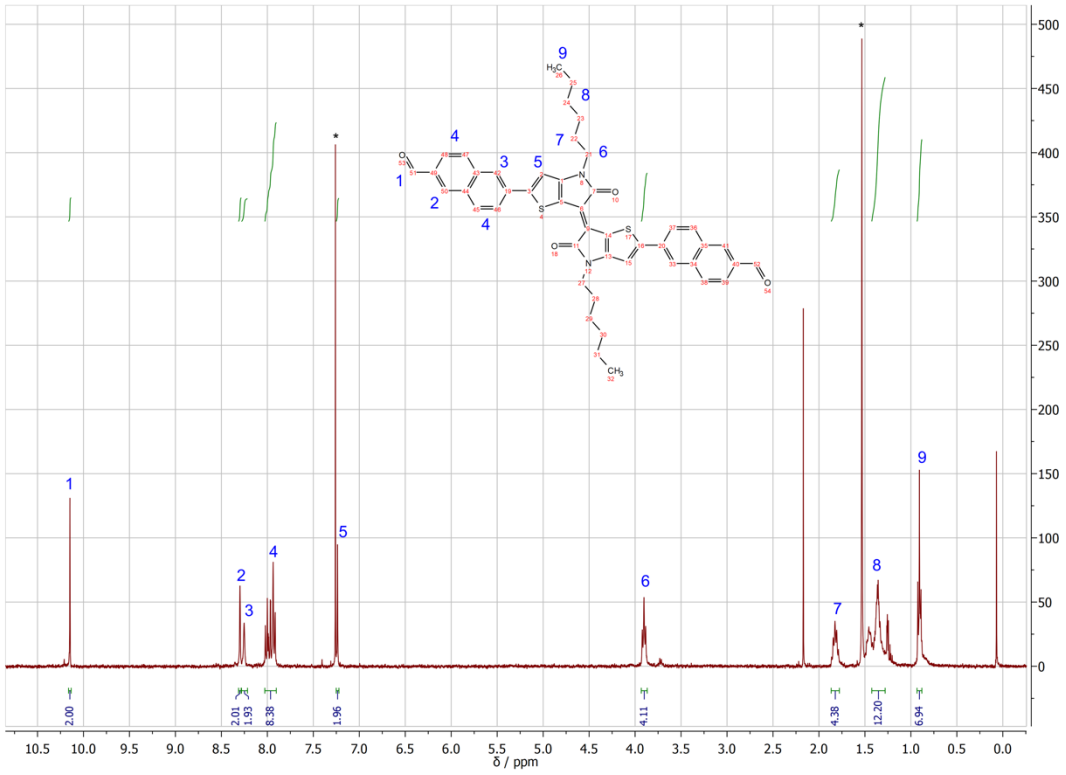

Section L – Solid-state NMR spectra

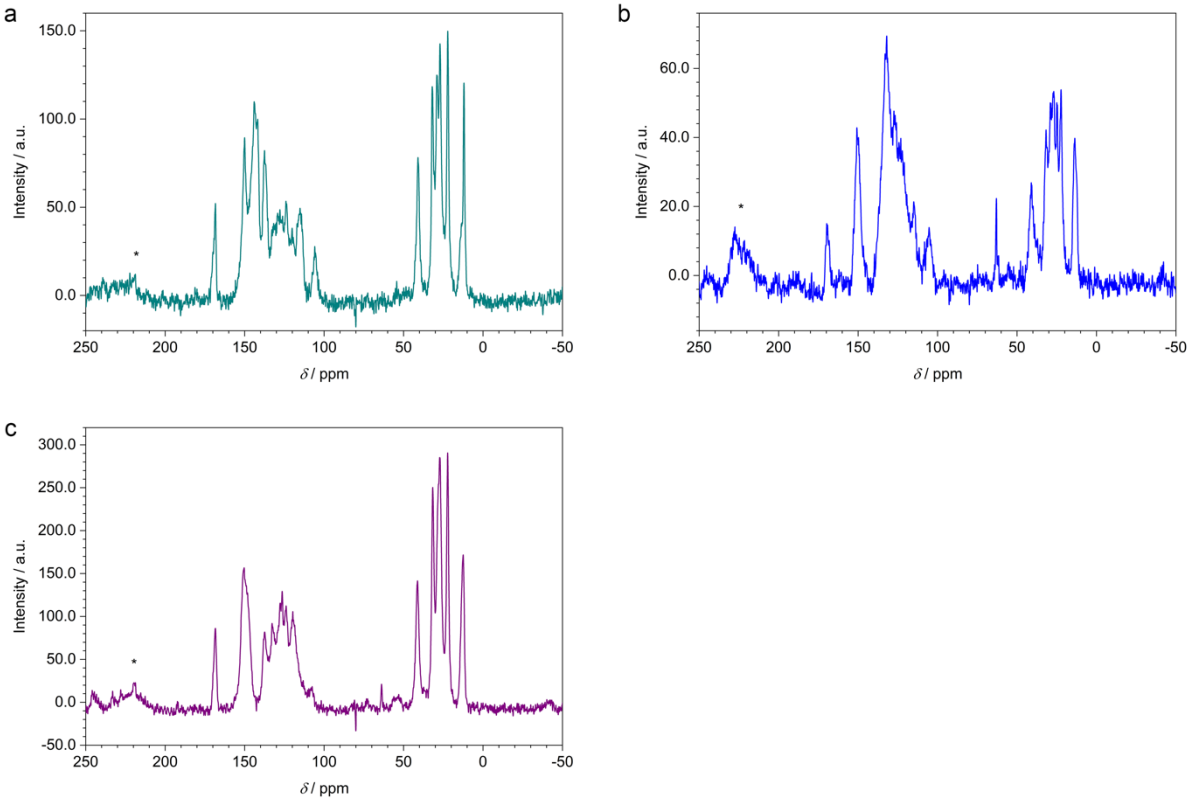

Figure 4.25. Solid-state ^{13}C cross-polarization magic angle spinning (CP-MAS) NMR spectra of the thienoisoindigo COFs. (**a**) Py-ttTII COF, (**b**) Py-nTII COF, (**c**) Py-TII COF. The appearance of the characteristic imine C=N resonance at around 170 ppm and the absence of residual aldehyde signals around 190 ppm confirm the successful COF formation.[42] The signals in the 100-150 ppm range originate from the (hetero)aromatic framework backbone, while the six well-resolved signals below 50 ppm are due to the hexyl chains. Spinning sidebands are marked with asterisks.

3.7 References

1. Côte, A. P.; Benin, A. I.; Ockwig, N. W.; O'Keeffe, M.; Matzger, A. J.; Yaghi, O. M., Porous, Crystalline, Covalent Organic Frameworks. *Science* **2005,** *310*, 1166-1170.
2. Jin, E.; Asada, M.; Xu, Q.; Dalapati, S.; Addicoat, M. A.; Brady, M. A.; Xu, H.; Nakamura, T.; Heine, T.; Chen, Q.; Jiang, D., Two-dimensional sp2 carbon–conjugated covalent organic frameworks. *Science* **2017,** *357*, 673-676.
3. Ma, T.; Kapustin, E. A.; Yin, S. X.; Liang, L.; Zhou, Z.; Niu, J.; Li, L.-H.; Wang, Y.; Su, J.; Li, J.; Wang, X.; Wang, W. D.; Wang, W.; Sun, J.; Yaghi, O. M., Single-crystal x-ray diffraction structures of covalent organic frameworks. *Science* **2018,** *361*, 48-52.
4. Xu, H.; Gao, J.; Jiang, D., Stable, crystalline, porous, covalent organic frameworks as a platform for chiral organocatalysts. *Nat. Chem.* **2015,** *7*, 905-912.
5. Li, R. L.; Flanders, N. C.; Evans, A. M.; Ji, W.; Castano, I.; Chen, L. X.; Gianneschi, N. C.; Dichtel, W. R., Controlled growth of imine-linked twodimensional covalent organic framework nanoparticles. *Chem. Sci.* **2019,** *10*, 3796-3801.
6. Ascherl, L.; Sick, T.; Margraf, J. T.; Lapidus, S. H.; Calik, M.; Hettstedt, C.; Karaghiosoff, K.; Döblinger, M.; Clark, T.; Chapman, K. W.; Auras, F.; Bein, T., Molecular docking sites designed for the generation of highly crystalline covalent organic frameworks. *Nat. Chem.* **2016,** *8*, 310-316.
7. Spitler, E. L.; Dichtel, W. R., Lewis acid-catalysed formation of two-dimensional phthalocyanine covalent organic frameworks. *Nat. Chem.* **2010,** *2*, 672-677.
8. Dogru, M.; Handloser, M.; Auras, F.; Kunz, T.; Medina, D.; Hartschuh, A.; Knochel, P.; Bein, T., A Photoconductive Thienothiophene-Based Covalent Organic Framework Showing Charge Transfer Towards Included Fullerene. *Angew. Chem. Int. Ed.* **2013,** *52*, 2920-2924.
9. Calik, M.; Auras, F.; Salonen, L. M.; Bader, K.; Grill, I.; Handloser, M.; Medina, D. D.; Dogru, M.; Löbermann, F.; Trauner, D.; Hartschuh, A.; Bein, T., Extraction of Photogenerated Electrons and Holes from a Covalent Organic Framework Integrated Heterojunction. *J. Am. Chem. Soc.* **2014,** *136*, 17802-17807.
10. Stegbauer, L.; Schwinghammer, K.; Lotsch, B. V., A Hydrazone-based Covalent Organic Framework for Photocatalytic Hydrogen Production. *Chem. Sci.* **2014,** *5*, 2789-2793.
11. Wang, X.; Chen, L.; Y., C. S.; Little, M. A.; Wu, Y.; Zhu, W.-H.; Clowes, R.; Yan, Y.; Zwijnenburg, M. A.; Sprick, R. S.; Cooper, A. I., Sulfone-containing covalent organic

frameworks for photocatalytic hydrogen evolution from water. *Nat. Chem.* **2018,** *10*, 1180-1189.

12. Rauh, R. D., Electrochromic windows: an overview. *Electrochim. Acta* **1999,** *44*, 3165-3176.
13. Cheng, C.-P.; Kuo, Y.; Chou, C.-P.; Cheng, C.-H.; Teng, T. P., Performance improvement of electrochromic display devices employing micro-size precipitates of tungsten oxide. *Appl. Phys. A* **2014,** *116*, 1553-1559.
14. Wu, L.; Sun, Y.; Sugimoto, K.; Luo, Z.; Ishigaki, Y.; Pu, K.; Suzuki, T.; Chen, H.-Y.; Ye, D., Engineering of Electrochromic Materials as Activatable Probes for Molecular Imaging and Photodynamic Therapy. *J. Am. Chem. Soc.* **2018,** *140*, 16340-16352.
15. Knott, E. P.; Craig, M. R.; Liu, D. Y.; Babiarz, J. E.; Dyer, A. L.; Reynolds, J. R., A minimally coloured dioxypyrrole polymer as a counter electrode material in polymeric electrochromic window devices. *J. Mater. Chem.* **2012,** *22*, 4953-4962.
16. Gu, H.; Ming, S.; Lin, K.; Chen, S.; Liu, X.; Lu, B.; Xu, J., Isoindigo as an electron-deficient unit for high-performance polymeric electrochromics. *Electrochim. Acta* **2018,** *260*, 772-782.
17. Arockiam, J. B.; Son, H.; Han, S. H.; Balamurugan, G.; Kim, Y.-H.; Park, J. S., Iron Phthalocyanine Incorporated Metallo-Supramolecular Polymer for Superior Electrochromic Performance with High Coloration Efficiency and Switching Stability. *ACS Appl. Energy Mater.* **2019,** *2*, 8416-8424.
18. Beaujuge, P. M.; Ellinger, S.; Reynolds, J. R., The donor–acceptor approach allows a black-to-transmissive switching polymeric electrochrome. *Nat. Mater.* **2008,** *7*, 795-799.
19. Sapp, S. A.; Sotzing, G. A.; Reynolds, J. R., High Contrast Ratio and Fast-Switching Dual Polymer Electrochromic Devices. *Chem. Mater.* **1998,** *10*, 2101-2108.
20. Hao, Q.; Li, Z.-J.; Lu, C.; Sun, B.; Zhong, Y.-W.; Wan, L.-J.; Wang, D., Oriented Two-Dimensional Covalent Organic Framework Films for Near-Infrared Electrochromic Application. *J. Am. Chem. Soc.* **2019,** *141*, 19831-19838.
21. Yu, F.; Liu, W.; Ke, S.-W.; Kurmoo, M.; Zuo, J.-L.; Zhang, Q., Electrochromic two-dimensional covalent organic framework with a reversible dark-to-transparent switch. *Nat. Commun.* **2020,** *11*, 5534.

22. Beaujuge, P. M.; Amb, C. M.; Reynolds, J. R., Spectral Engineering in π-Conjugated Polymers with Intramolecular Donor-Acceptor Interactions. *Acc. Chem. Res.* **2010,** *43*, 1396-1407.

23. Stalder, R.; Mei, J.; Reynolds, J. R., Isoindigo-Based Donor-Acceptor Conjugated Polymers. *Macromolecules* **2010,** *43*, 8348-8352.

24. Ho, C.-C.; Chen, C.-A.; Chang, C.-Y.; Darling, S. B.; Su, W.-F., Isoindigo-based copolymers for polymer solar cells with efficiency over 7%. *J. Mater. Chem. A* **2014,** *2*, 8026-8032.

25. Auras, F.; Ascherl, L.; Hakimioun, A. H.; Margraf, J. T.; Hanusch, F. C.; Reuter, S.; Bessinger, D.; Döblinger, M.; Hettstedt, C.; Karaghiosoff, K.; Herbert, S.; Knochel, P.; Clark, T.; Bein, T., Synchronized Offset Stacking: A Concept for Growing Large-Domain and Highly Crystalline 2D Covalent Organic Frameworks. *J. Am. Chem. Soc.* **2016,** *138*, 16703-16710.

26. Keller, N.; Bessinger, D.; Reuter, S.; Calik, M.; Ascherl, L.; Hanusch, F. C.; Auras, F.; Bein, T., Oligothiophene-Bridged Conjugated Covalent Organic Frameworks. *J. Am. Chem. Soc.* **2017,** *139*, 8194-8199.

27. Bessinger, D.; Ascherl, L.; Auras, F.; Bein, T., Spectrally Switchable Photodetection with Near-Infrared-Absorbing Covalent Organic Frameworks. *J. Am. Chem. Soc.* **2017,** *139*, 12035-12042.

28. Ascherl, L.; Evans, E. W.; Hennemann, M.; Di Nuzzo, D.; Hufnagel, A. G.; Beetz, M.; Friend, R. H.; Clark, T.; Bein, T.; Auras, F., Solvatochromic covalent organic frameworks. *Nat. Commun.* **2018,** *9*, 3802.

29. Ascherl, L.; Evans, E. W.; Gorman, J.; Orsborne, S.; Bessinger, D.; Bein, T.; Friend, R. H.; Auras, F., Perylene-Based Covalent Organic Frameworks for Acid Vapor Sensing. *J. Am. Chem. Soc.* **2019,** *141*, 15693-15699.

30. Hasegawa, T.; Ashizawa, M.; Matsumoto, H., Design and structure–property relationship of benzothienoisoindigo in organic field effect transistors. *RSC Adv.* **2015,** *5*, 61035-61043.

31. Yoo, D.; Hasegawa, T.; Ashizawa, M.; Kawamoto, T.; Masunaga, H.; Hikima, T.; Matsumoto, H.; Mori, T., *N*-Unsubstituted thienoisoindigos: preparation, molecular packing and ambipolar organic field-effect transistors. *J. Mater. Chem. C* **2017,** *5*, 2509-2512.

32. Cychosz, K. A.; Guillet-Nicolas, R.; García-Martínez, J.; Thommes, M., Recent advances in the textural characterization of hierarchically structured nanoporous materials. *Chem. Soc. Rev.* **2017,** *46*, 389-414.

33. Matsumoto, M.; Dasari, R. R.; Ji, W.; Feriante, C. H.; Parker, T. C.; Marder, S. R.; Dichtel, W. R., Rapid, Low Temperature Formation of Imine-Linked Covalent Organic Frameworks Catalyzed by Metal Triflates. *J. Am. Chem. Soc.* **2017,** *139*, 4999-5002.

34. Dutta, G. K.; Han, A.-R.; Lee, J.; Kim, Y.; Oh, J. H.; Yang, C., Visible-Near Infrared Absorbing Polymers Containing Thienoisoindigo and Electron-Rich Units for Organic Transistors with Tunable Polarity. *Adv. Funct. Mater.* **2013,** *23*, 5317-5325.

35. Oleson, A.; Zhu, T.; Dunn, I. S.; Bialas, D.; Bai, Y.; Zhang, W.; Dai, M.; Reichman, D. R.; Tempelaar, R.; Huang, L.; Spano, F. C., Perylene Diimide-Based Hj- and hJ-Aggregates: The Prospect of Exciton Band Shape Engineering in Organic Materials. *J. Phys. Chem. C* **2019,** *123*, 20567-20578.

36. Feng, J. f.; Liu, T. F.; Cao, R., An Electrochromic Hydrogen-Bonded Organic Framework Film. *Angew. Chem. Int. Ed.* **2020,** *59*, 22392-22396.

37. Wade, C. R.; Li, M.; Dincă, M., Facile Deposition of Multicolored Electrochromic Metal–Organic Framework Thin Films. *Angew. Chem. Int. Ed.* **2013,** *52*, 13377-13381.

38. Cai, G.; Cui, M.; Kumar, V.; Darmawan, P.; Wang, J.; Wang, X.; Eh, A. L.-S.; Qian, K.; Lee, P. S., Ultra-large optical modulation of electrochromic porous WO_3 film and the local monitoring of redox activity. *Chem. Sci.* **2016,** *7*, 1373-1382.

39. Düren, T.; Millange, F.; Férey, G.; Walton, K. S.; Snurr, R. Q., Calculating Geometric Surface Areas as a Characterization Tool for Metal-Organic Frameworks. *J. Phys. Chem. C* **2007,** *111*, 15350-15356.

40. Koizumi, Y.; Ide, M.; Saeki, A.; Vijayakumar, C.; Balan, B.; Kawamotoa, M.; Seki, S., Thienoisoindigo-based low-band gap polymers for organic electronic devices. *Polym. Chem.* **2013,** *4*, 484-494.

41. Hasegawa, T.; Ashizawa, M.; Hiyoshi, J.; Kawauchi, S.; Mei, J.; Bao, Z.; Matsumoto, H., An ultra-narrow bandgap derived from thienoisoindigo polymers: structural influence on reducing the bandgap and self-organization. *Polym. Chem.* **2016,** *7*, 1181-1190.

42. Nguyen, H. L.; Gropp, C.; Ma, Y.; Zhu, C.; Yaghi, O. M., 3D Covalent Organic Frameworks Selectively Crystallized through Conformational Design. *J. Am. Chem. Soc.* **2020,** *142*, 20335-20339.

4. Electrically conductive carbazole and thienoisoindigo-based COFs showing fast and stable electrochromism

This chapter is based on the following publication:

Katharina Muggli, Laura Spies, Derya Bessinger, Florian Auras, and Thomas Bein*

ACS Nanoscience Au. **2023**, *3*, 153-160.

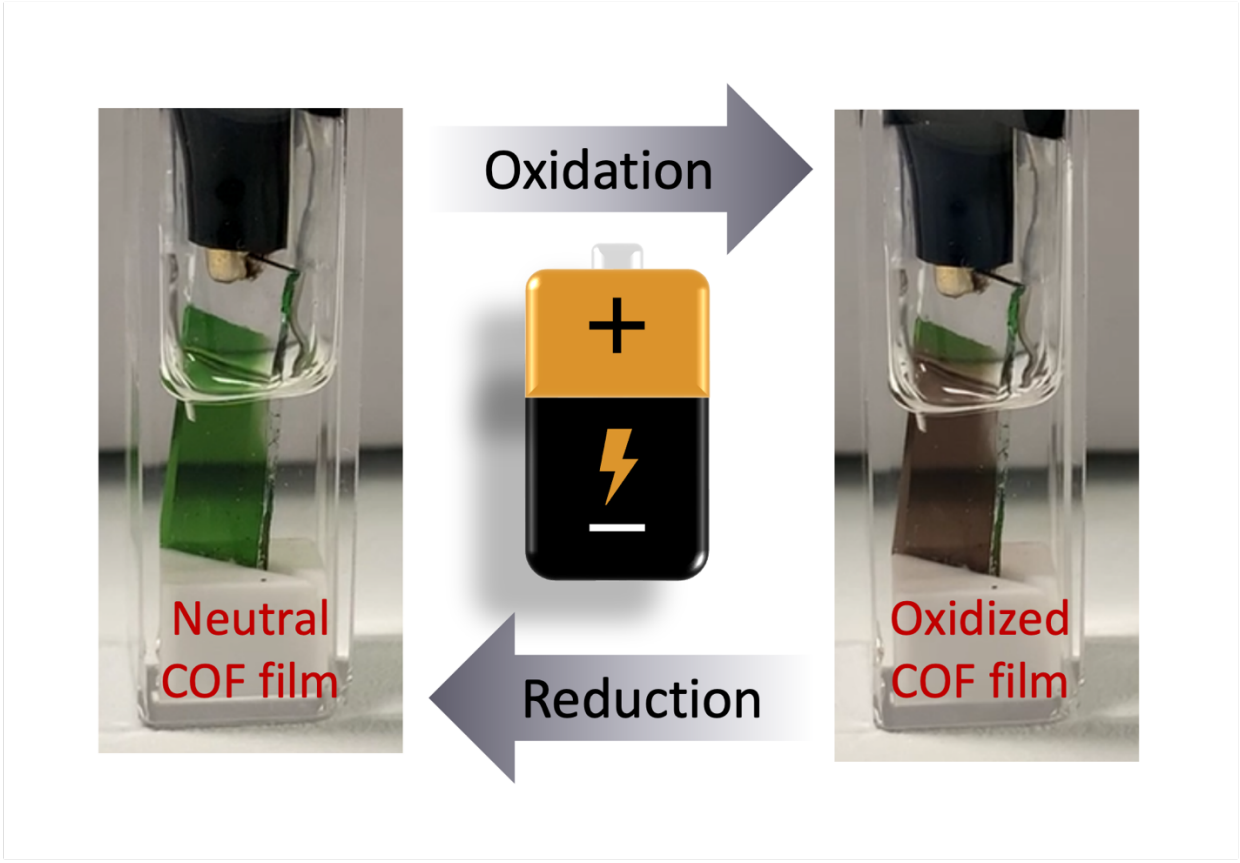

4. Electrically conductive carbazole and thienoisoindigo-based COFs showing fast and stable electrochromism

4.1 Abstract

Thienothiophene thienoisoindigo (ttTII)-based COFs have been shown to offer low band gaps and intriguing optical and electrochromic properties. So far, only one tetragonal thienothiophene thienoisoindigo-based covalent organic framework (COF) has been reported showing stable and fast electrochromism and good coloration efficiencies. We have developed two novel COFs using this versatile and nearly linear ttTII building block in a tetragonal and a hexagonal framework geometry to demonstrate their attractive features for optoelectronic applications of thienoisoindigo-based COFs.

Both COFs exhibit good electrical conductivities, show promising optical absorption features, are redox-active, and exhibit a strong electrochromic behavior when applying an external electrical stimulus, shifting the optical absorption even farther into the NIR region of the electromagnetic spectrum and achieving absorbance changes of up to 2.5 OD. Cycle-stable cyclic voltammograms with distinct oxidation and reduction waves reveal excellent reversibility and electrochromic switching over 200 cycles and confirm the high stability of the frameworks. Furthermore, high coloration efficiencies in the NIR region and fast switching speeds for coloration/decoloration as fast as 0.75 s/0.37 s for the Cz-ttTII COF and 0.61 s/0.29 s for the TAPB-ttTII COF at 550 nm excitation were observed, outperforming many known electrochromic materials, and offering options for a great variety of applications, such as stimuli-responsive coatings, optical information processing, or thermal control.

4.2 Introduction

Covalent organic frameworks (COFs) constructed from organic building blocks represent a highly ordered and porous group of materials offering large internal surface areas and high crystallinity.[1-5] So far, COFs have demonstrated intriguing and highly promising characteristics for applications in different fields, including photocatalysis,[6-8] or gas storage and separation.[9-11] After metal organic frameworks (MOFs) had already exhibited good electrochromic properties,[12, 13] the ever-expanding scope of covalent organic frameworks has now also provided access to their use in this optoelectronic field, with visible and near-infrared (NIR) electrochromic COFs being promising candidates for modern applications, such

as smart windows, stimuli-response materials or as a molecular logic gate.[14-17] Here, electrochromism describes the phenomenon of an electrically induced reversible color change of a given material.

A high degree of order and continuous electronic connectivity of the π-conjugated COF materials represent ideal prerequisites for a good and stable electrochromism. To date, an increasing number of COFs with high intrinsic electrical conductivities has been reported.[18-21]

Thienoisoindigo, a thiophene-analogue of isoindigo, represents an electron-deficient moiety commonly used in molecular donor-acceptor designs for promoting enhanced optical, electronic and photophysical properties of the corresponding polymers.[22-25] In this context, thienothiophene thienoisoindigo (ttTII)-based COFs have proven to show intriguing electrochromic properties with high stabilities, remarkable coloration efficiencies, fast switching speeds and fully reversible vis-NIR absorption changes.[14]

Taking advantage of the modular concept of reticular chemistry, here we expanded the group of two-dimensional electrochromic ttTII-based COFs and covalently connected the versatile linear building block with promising counterparts: A functionalized biscarbazole-based building block (Cz) was used for the synthesis of the tetragonal Cz-ttTII COF, and the established trigonal TAPB moiety was employed for the generation of the hexagonal TAPB-ttTII COF.

The well-known carbazole moiety has already proven of value in host materials of optoelectronic devices or in organic light emitting diodes (OLEDs),[26-29] as well as hole transporting materials.[30] Recently, carbazole-based building blocks have been integrated into crystalline COF materials and showed their strong performance in various application fields, e.g. for sensing,[31-33] in catalysis [7], or as a supercapacitor.[34]

Likewise, the trigonal 1,3,5-tris(4-aminophenyl)benzene (TAPB) building block has been incorporated in several COF systems, which were utilized as cathode materials in electrochemical applications,[35, 36] and have been shown to offer good characteristics in electrochemical sensors[37, 38].

We will show that the newly developed ttTII-based COFs meet important criteria that render these materials suitable for high-performing electrochromism.

4. Electrically conductive carbazole and thienoisoindigo-based COFs showing fast and stable electrochromism

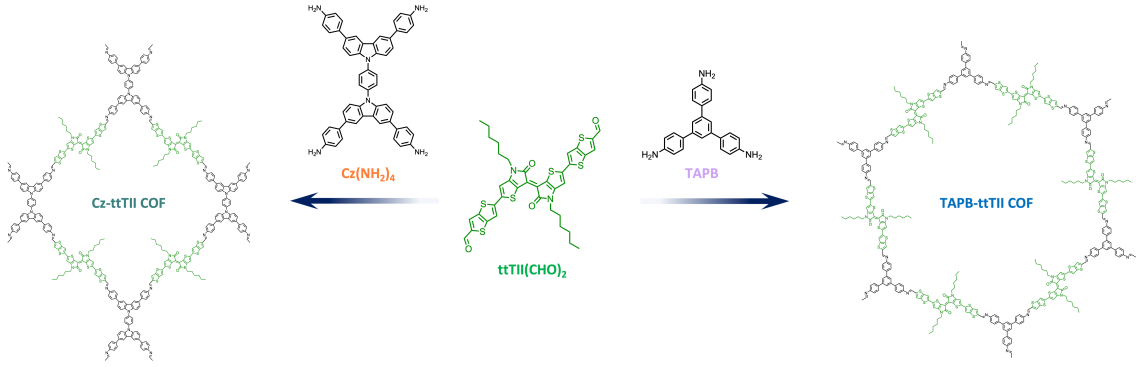

Figure 1. Synthesis of the new Cz-ttTII and TAPB-ttTII COFs. The co-condensation of the nearly linear ttTII(CHO)$_2$ building block with the tetragonal carbazole-based precursor and the trigonal TAPB unit, respectively, yields a tetragonal and a hexagonal two-dimensional framework.

4.3 Results and Discussion

COF synthesis

For the construction of ttTII-based covalent organic frameworks, we designed a functionalized biscarbazole-based, tetragonal building block (Cz), with carbazole molecules interconnected by a linking phenylene moiety. The single crystal structure data of a biscarbazole-phenylene derivative exhibits a virtual coplanarity of the carbazole units,[39] which may be favorable for a close slip-stacked aggregation of a building block with a similar molecular design. Here, a slip-stacked packing was already reported for the tetragonal pyrene counterpart that produced various highly ordered COFs,[40] amongst others the previously published Py-ttTII.[14] Therefore, we anticipated that a building block with an analogous stacking behavior, directing the slip-stacked packing of 2D COF layers, would promote crystalline growth. On the other hand, we expanded the tetragonal geometry of existing ttTII-based COFs and developed a hexagonal framework by imine-linking the nearly linear ttTII to the well-established trigonal TAPB node. The hexagonal pore geometry provides larger pores than the tetragonal structure and sufficient space between the extended hexyl chains that reach into the pores.

The two new imine-linked COFs were synthesized under solvothermal conditions, condensing the nearly linear 5,5'-bis(2-formylthienothiophen-5-yl)-*N*,*N*'-dihexyl-thienoisoindigo (ttTII(CHO)$_2$) building block with the novel tetradentate 4,4',4'',4'''-(1,4-phenylenebis(9*H*-carbazole-9,3,6-triyl)) tetra-aniline (Cz(NH$_2$)$_4$) building block, as well as with the trigonal 1,3,5-tris(4-aminophenyl)benzene (TAPB) unit, forming the tetragonal Cz-ttTII COF and the

hexagonal TAPB-ttTII COF, respectively (Figure 1). For experimental details see Methods section

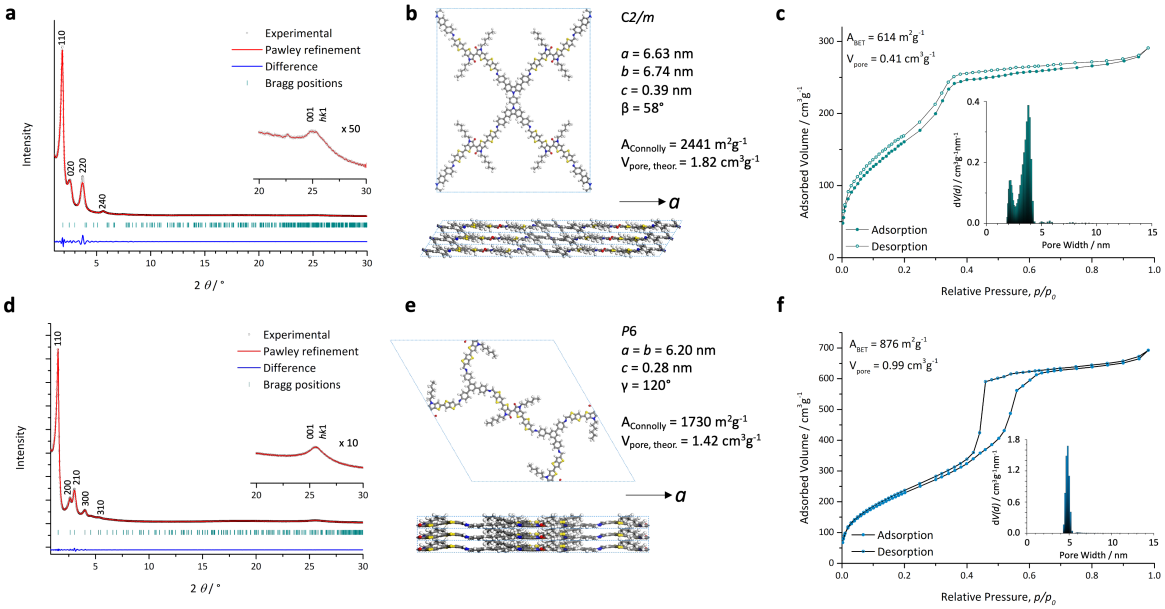

Figure 2. Structural analysis of the Cz-ttTII and the TAPB-ttTII COFs. **(a)** Experimental PXRD pattern of the Cz-ttTII COF powder (black dots). Pawley refinement of the simulated structure model (red line) based on the monoclinic space group C*2/m*, providing a good fit for the experimental data with only minor differences (blue line). R_{wp} = 3.63% and R_p = 2.13%. The corresponding Bragg positions are indicated by green ticks. Inset: magnification of the 2θ > 20° region. **(b)** View onto the crystallographic *a*-*b* plane of the Pawley-refined Cz-ttTII COF structure model. The COF exhibits a quasi-square topology with slip-stacked layers and high porosity with a calculated Connolly surface area of 2241 $m^2\ g^{-1}$ and a pore volume of 1.33 $cm^3\ g^{-1}$. **(c)** Nitrogen sorption analysis of the Cz-ttTII COF bulk material at 77 K shows a type IVb isotherm. Inset: Pore size distribution (PSD) of the Cz-ttTII COF. The bimodal PSD is derived from a fit of the isotherm based on a QSDFT equilibrium model for cylindrical pores. Peaks are found at 2.2 and 3.8 nm, which is in very good agreement with the wall-to-wall distances of the refined COF structure, confirming the shamrock-like pore shape. **(d)** Experimental PXRD pattern of the TAPB-ttTII COF powder (black dots). Pawley refinement of the structure model (red line) in the hexagonal space group *P*6, providing a good fit to the experimental data with only minor differences (blue line). R_{wp} = 3.24% and R_p = 4.18%. The corresponding Bragg positions are indicated by green ticks. Inset: magnification of the 2θ > 20° region. **(e)** View onto the crystallographic *a*-*b* plane of the Pawley-refined TAPB-ttTII COF structure model. The COF exhibits a hexagonal topology with eclipsed layers and high porosity with a calculated Connolly surface area of 1730 $m^2\ g^{-1}$ and a pore volume of 1.42 $cm^3\ g^{-1}$. **(f)** Nitrogen sorption analysis of the TAPB-ttTII COF bulk material at 77 K shows a type IVa isotherm. Inset: Pore size distribution (PSD) of the TAPB-ttTII COF. The unimodal PSD is derived from a fit of the isotherm based on a QSDFT equilibrium model for cylindrical pores. The peak is found at 4.8 nm, which is in very good agreement with the wall-to-wall distances of the refined COF structure model.

Structural and morphological investigations

Structural characterization *via* powder X-ray diffraction (PXRD) reveals high crystallinity of the two-dimensional Cz-ttTII and TAPB-ttTII COFs (Figure 2a, d). The black dots represent the experimentally obtained PXRD patterns and confirm the high crystallinity of the new materials. The simulated structure of the quasi-square Cz-ttTII COF was Pawley-refined based on the monoclinic space group C*2/m*, and that of the hexagonal TAPB-ttTII COF based on the space group *P*6. The respective refined patterns (red lines) provide a good fit for the experimentally obtained data, with only minor differences, confirmed by the difference plots (blue lines). Refined unit cell parameters are a = 6.63 nm, b = 6.74 nm, c = 0.39 nm, and β = 58° for the Cz-ttTII COF and $a = b$ = 6.20 nm, c = 0.28 nm and γ = 120° for the TAPB-ttTII COF (Figure 2b, e). Nitrogen sorption at 77 K of the materials (Figure 2c, f) confirms their porosity, yielding a type IVb isotherm for the Cz-ttTII COF, typical for smaller mesopores. The TAPB-ttTII COF isotherm exhibits a type IVa shape, known for larger mesopores. Brunauer-Emmett-Teller (BET) surface areas amount to 614 $m^2 g^{-1}$ for the Cz-ttTII COF and 876 $m^2 g^{-1}$ for the TAPB-ttTII COF, with the respective total pore volumes being 0.41 $cm^3 g^{-1}$ and 0.99 $cm^3 g^{-1}$. Deviations from the theoretically calculated values could be attributed to building block residues or oligomeric fragments trapped in the porous structure of the COF, despite extensive extraction. Pore size distributions (PSD) were calculated based on a quenched solid density functional theory (QSDFT) equilibrium model for cylindrical pores, showing a bimodal shape with peaks at 2.2 and 3.8 nm for the Cz-ttTII COF and a unimodal shape peaking at 4.8 nm in case of the TAPB-ttTII COF, being in very good agreement with the simulated wall-to-wall distances (Figure S1a, b). The bimodal shape of the Cz-ttTII PSD derives from the modelling based on the QSDFT method, describing a noncylindrical pore shape.

High-resolution transmission electron microscopy (TEM) images of the polycrystalline COF powders reveal highly crystalline domains, confirming the tetragonal structure of the Cz-ttTII COF and the hexagonal structure of the TAPB-ttTII COF (Figure S1c, d). The determined periodicities of 4.7 nm for the Cz-ttTII COF and 6.0 nm for the TAPB-ttTII COF are in very good agreement with the according refined structure models.

COF thin films

For further investigations of the properties of the newly synthesized COFs, thin films of both structures were prepared in a solvothermal procedure. The crystallinity and oriented growth of thin films was confirmed *via* grazing-incidence wide-angle X-ray scattering (GIWAXS) analyses. The GIWAXS patterns of the films display a preferential orientation with the COFs' *a*-*b* planes growing parallelly to the surface of the substrate, confirmed by the high intensities near the sample horizon and the lack of semicircular reflections (Figure S6a, d).
Scanning electron microscopy (SEM) cross-sections of the thin films reveal an approximate thickness of 240 nm in the case of the Cz-ttTII COF and 790 nm for the TAPB-ttTII COF. SEM top view images confirm a homogenously grown dense COF film on top of the substrates with Cz-ttTII showing a pillar-like and TAPB-ttTII displaying a web-like morphology (Figure S6c, f).

Electrical conductivity

For the investigation of the COF films' vertical electrical conductivity performance, a COF thin film was grown on a partially etched ITO substrate. Subsequently, gold electrodes were evaporated onto the COF film and a gold counter electrode onto the blank ITO surface (Figure S13). The electrodes were contacted under exclusion of light and *I*-*V* curves for both COFs were measured. Here, the potential was increased from 0 V to 1000 mV in 100 mV s^{-1} steps, then decreased to –400 mV and finally again increased to 0 V. The resulting *I*-*V* curves were fitted with a linear fit, yielding the respective slope values of 0.03799 A V^{-1} for the Cz-ttTII COF film and 0.02527 A V^{-1} for the TAPB-ttTII COF film. The current density plots were calculated based on the electrode area of 3 × 4 mm (Figure S12). The electrical conductivities of the COFs were calculated using the equations described in the Supporting Information, section J and based on film thicknesses of 240 nm for the Cz-ttTII COF film and 790 nm for the TAPB-ttTII COF film. Good electrical conductivities of 7.60×10^{-4} S m^{-1} for the Cz-ttTII COF and 1.66×10^{-3} S m^{-1} for the TAPB-ttTII COF were found, confirming their good electrical connectivity and suitability for electrochromic experiments.

Optoelectronic and electrochromic properties

Both COFs are dark green colored materials and were investigated *via* UV-Vis/NIR absorption spectroscopy. The examined bulk powders exhibit a strong dual-band absorption in the visible spectrum with the respective higher-energy absorption band deriving from π→π* interactions and the respective lower energy absorption band being assigned to intramolecular charge transfer (ICT) processes (Figure S3 a, b).[41, 42] This absorption behavior has already been observed for the previously reported Py-ttTII COF.[14] The Cz-ttTII COF has an absorption onset at approximately 980 nm and the TAPB-ttTII COF an onset at about 955 nm. Comparing the absorption characteristics of the COF materials to the bare ttTII(CHO)$_2$ building block, a redshift of approximately 70 nm is found (FWHM) for the Cz-ttTII COF, whilst the TAPB-ttTII COF exhibits a respective red shift of up to 55 nm, assigned to the electronic integration of the precursors and hence the expansion of the conjugated π-system in the COFs. Low band gaps of 1.35 eV for the Cz-ttTII COF and 1.40 eV for the TAPB-ttTII COF were calculated using Tauc plots, assuming a direct transition for both materials (Figure S3 c, d).

Likewise, the absorption spectra of the respective COF thin films on indium tin oxide (ITO) display an analogous dual-band shape, also confirming the successful growth of the COFs as thin films.

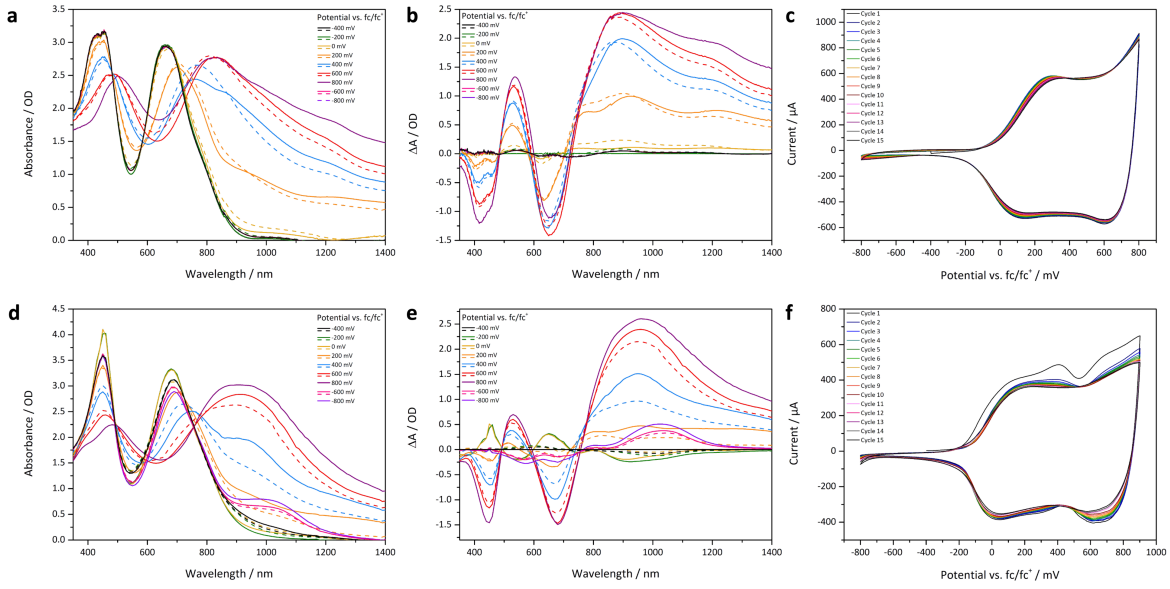

Figure 3. Investigations on the electrochromic behavior of the Cz-ttTII COF films **(a – c)** and the TAPB-ttTII COF films **(d – f)**. Voltage-dependent absorption spectra of **(a)** the Cz-ttTII COF and **(d)** the TAPB-ttTII COF, scanning from –400 mV to 800 mV, subsequently down to –800 mV and back to –400 mV vs.

fc/fc$^+$ in 200 mV steps, featuring a strong shift in absorption to the NIR region. The respective changes in absorption are shown for **(b)** the Cz-ttTII COF and **(e)** the TAPB-ttTII COF, illustrating an extraordinary increase in absorption of both materials for wavelengths above approximately 730 nm (Cz-ttTII COF) and 755 nm (TAPB-ttTII COF). Parallel to this absorption increase, an attenuation of the absorption bands at 420 nm and 650 nm (Cz-ttTII COF) and 445 nm and 680 nm (TAPB-ttTII COF) of the electronically neutral state is observed, whilst new absorption bands appear at 535 nm (Cz-ttTII COF) and 530 nm (TAPB-ttTII COF). The solid and dashed lines of the optical spectra indicate the forward and backward scanning direction, respectively. CV curves were recorded for the **(c)** Cz-ttTII COF and **(f)** TAPB-ttTII COF, displaying well-defined oxidation and reduction peaks. In order to examine the stability and reversibility, the voltage was cycled 15 times between –800 mV and 800 mV vs. fc/fc$^+$.

Both COFs were investigated in terms of their electrochromic behavior. Here, the COF thin film acts as the active material of the working electrode, a platinum wire as the counter electrode, a silver wire as the quasi-reference electrode and a 0.1 M solution of tetrabutylammonium hexafluorophosphate ($TBAPF_6$) in acetonitrile as the electrolyte. The voltage was cycled in a range between –800 mV and 800 mV vs. the ferrocene couple fc/fc$^+$ in 200 mV steps. UV-Vis/NIR absorption spectra were recorded between 350 and 1400 nm at every voltage step, keeping the voltage constant when recording the respective spectrum.
Increasing the applied potential oxidizes the respective COF film, leading to a darkening of the color from dark green to nearly black. Here, a strong redshift of the absorption spectra is found starting at 200 mV vs. fc/fc$^+$. The two main absorption bands of the neutral state with peaks at 420 nm and 650 nm for the Cz-ttTII COF (Figure 3a) and at 445 nm and 680 nm for the TAPB-ttTII COF (Figure 3d), respectively, are attenuated while new absorption features are found at 535 nm and above 720 nm for the Cz-ttTII COF and at 530 nm and above 755 nm for the TAPB-ttTII COF (Figures 3b, e). For the Cz-ttTII COF, an extraordinary increase of almost 2.5 OD at 895 nm between the neutral state (–400 mV) and the oxidized state (800 mV) can be reported. Likewise, the TAPB-ttTII COF also shows a very strong increase in absorption of even above 2.5 OD at 960 nm between the neutral and the fully oxidized state. When reversing the scanning direction, the absorption characteristics of the COFs exhibit a reversible behavior with only slight differences between the spectra in the forward and the backward scanning directions at a certain voltage, which can be assigned to charging effects that are entirely overcome by further reducing the potential.

To monitor the cycle stability, CV curves for both COFs were recorded by cycling the potential between –800 mV and 800 mV vs. fc/fc$^+$ (Cz-ttTII), respectively 900 mV (TAPB-ttTII) at a scan

speed of 100 mV s^{-1} for 15 times. For the Cz-ttTII COF (Figure 3c), a first distinct oxidation peak is found at approximately 280 mV and a second oxidation process starts for potentials above 600 mV. To reduce stress on the COF film caused by higher potentials and ensure the chemical stability of the electrolyte solution, the scanning direction was reversed at 800 mV. After reversing the scanning direction, the oxidized COF is gradually reduced with the corresponding reduction peaks at 600 mV and 120 mV. The COF film shows good stability, with nearly no degradation over the course of 15 cycles. In case of the TAPB-ttTII COF film (Figure 3f), two oxidation peaks are found at 165 mV and 405 mV, and a third oxidation process starts at potential values above 525 mV, but could also not completely be measured due to stability limitations of the COF film and the electrolyte. The corresponding reduction peaks occur at 615 mV, 285 mV and 45 mV. The COF also exhibits a high stability after the 15 cycles, with only minor drift between the first and the second cycle.

In addition, the reversibility of the electrochromic color change of both COFs was monitored at two wavelengths, 550 nm and 900 nm, by switching the applied potentials between –600 mV and 600 mV vs. fc/fc^+ with a dwell time of 4 s after each potential step for 200 oxidation/reduction cycles (Figure S8). At a wavelength of 550 nm, the Cz-ttTII COF exhibits a change in absorbance of approximately 1.0 OD, retaining > 90% of the initial electrochromic response after 200 cycles. The second absorption feature at 900 nm, which is assignable to different transition processes as described above, exhibits a distinct absorption change of approximately 1.5 OD. The small performance drift of 6 % after 200 cycles confirms the exceptional stability of this COF in this potential range. We attribute the deviations of the absorption change between the long-term stability tests and the absorption spectra in this wavelength region to the different measurement conditions of both measurements. The stability tests were conducted under more conservative potential settings not fully applying the maximal possible voltage to the films in order to reduce strain on the frameworks and ensure the best possible tradeoff between performance and material protection. While the Cz-ttTII COF can reach the fully oxidized state with the set potential settings of the UV-Vis spectra scans, the long-term cycling measurements aim to test the stability under fast switching conditions in the optimally functioning window, still exhibiting considerable absorption changes in the NIR.

For the TAPB-ttTII COF, monitoring the electrochromic switching at 550 nm showed an initial absorbance change of about 0.9 OD, retaining > 83% of the initial electrochromic response over the course of 200 cycles. When monitoring at a wavelength of 900 nm with a new thin film, an absorption change of 1.9 OD was found, which only showed a minor drift of approximately 5%, also confirming the good stability of the COF film at this wavelength.

Additionally, the response times of the oxidation and reduction processes, i.e., the electrochromic switching speeds, were determined. Using the data from the electrochromic cycling stability measurements, the averages of the respective first ten cycles for each COF and wavelength were calculated (Figure S9). The switching speeds for the oxidation and reduction processes were subsequently determined between the 10% and 90% boundaries of the respective total absorbance change at excitation wavelengths of 550 and 900 nm. At 550 nm, coloration/decoloration times of 0.75 s/0.37 s were determined for the Cz-ttTII COF, with the respective times for the absorbance change at 900 nm being 1.22 s/0.29 s. The corresponding switching times of the TAPB-ttTII COF are 0.61 s/0.29 s recorded at 550 nm excitation and 1.26 s/0.47 s at 900 nm, with both COFs outperforming many known organic and inorganic electrochromic materials.[15, 17, 43-46] This overall fast and stable electrochromic response of the TAPB-ttTII COF confirms the initial considerations of building an extended hexagonal pore geometry. Our design concept with sufficient space between the alkyl chains reaching into the pore aims for the unimpeded diffusion of counterions which balance the oxidized porous framework.

Finally, the coloration efficiencies were determined according to the equation described in the Supporting Information, section H. Here, the calculated efficiencies at 900 and 550 nm for the single-oxidized Cz-ttTII COF were found be 807 and 272 $cm^2\ C^{-1}$ at a potential of 400 mV. The respective values at 400 mV of the double-oxidized TAPB-ttTII COF are 596 and 114 $cm^2\ C^{-1}$, confirming the highly efficient electrochromic performance of the COFs in the NIR-region, which exceeds that of known covalent organic and hybrid frameworks.[15, 17, 43]

4.4 Conclusion

We have developed two novel and highly crystalline thienothiophene thienoisoindigo-based imine-linked 2D COFs – one with a tetragonal geometry using a newly designed tetradentate

carbazole-based node as the counterpart, and the other one in a hexagonal geometry fused with the established trigonal TAPB building block. Both COFs, grown as thin films, exhibit good vertical conductivities in the range of 10^{-4} - 10^{-3} S m^{-1}, which represent an important factor for excellent electrochromic performance. The COFs show intriguing optical properties with a very broad absorption in the visible range, reaching into the NIR region of the electromagnetic spectrum. To highlight the versatility and the excellent optoelectronic features of the ttTII building block, we investigated the COFs' fast and stable electrochromic behavior, showing strong absorption changes of up to 2.5 OD in the NIR region. Electrochromic stability monitoring over 200 cycles showed a high stability of the frameworks. Cyclic voltammetry measurements exhibited distinct redox waves, revealing a high cycle stability and reversibility of the redox processes. Additionally, highly efficient coloration efficiencies in the NIR region and response times as fast as 0.75 s/0.37 s for the Cz-ttTII COF and 0.61 s/0.29 s for the TAPB-ttTII COF at 550 nm excitation were established. Despite the slightly faster electrochromic response of Py-ttTII,[14] these switching speeds exceed those of many known covalent organic and hybrid frameworks, further demonstrating the high electrochromic performance level of thienoisoindigo-based covalent organic frameworks, and making them highly promising candidates for NIR optoelectronic applications, such as optical information processing or thermal control.

In this context, we have discovered that the ttTII unit not only performs well when embedded in a tetragonal framework geometry but that it can also be incorporated in a hexagonal COF structure whilst maintaining its excellent electrochromic behavior. It is envisioned that additional thienoisoindigo-based materials with different geometries could be incorporated in stimuli-responsive coatings and high-performing electrochromic devices.

4.5 Methods

The COF building blocks were synthesized according to the procedures described in Section K. All reagents and solvents are commercially available and were obtained in high-purity grades. Unless stated otherwise, solvents were degassed and saturated with argon before use.

COF bulk powder syntheses were performed under argon atmosphere in PTFE-sealed glass reaction tubes (6 mL volume).

Cz-ttTII COF

$Cz(NH_2)_4$ (3.86 mg, 5.0 µmol, 1.0 eq.) and $ttTII(CHO)_2$ (7.75 mg, 10 µmol, 2.0 eq.) were filled into a 6 mL reaction tube. Mesitylene (167 µL), benzyl alcohol (83 µL), and 6 M aqueous acetic acid (25 µL) were added to the tube, which was then sealed and heated to 120 °C for 5 d. After cooling to room temperature, the precipitate was collected by filtration and subsequently extracted with supercritical CO_2 for 2 h to remove by-products, yielding the COF as a dark green powder.

Elemental analysis (calculated, found for $C_{260}H_{204}N_{20}O_8S_{24}$): C (69.30, 69.64), H (4.56, 4.67), N (6.22, 5.34), S (17.08, 16.04).

TAPB-ttTII COF

TAPB (1.8 mg, 5.0 µmol, 1.0 eq.) and $ttTII(CHO)_2$ (5.8 mg, 7.5 µmol, 1.5 eq.) were filled into a 6 mL reaction tube. Mesitylene (167 µL), benzyl alcohol (83 µL), and 6 M aqueous acetic acid (25 µL) were added to the tube, which was then sealed and heated to 120 °C for 5 d. After cooling to room temperature, the precipitate was collected by filtration and subsequently extracted with supercritical CO_2 for 2 h to remove by-products, yielding the COF as a dark green powder.

Elemental analysis (calculated, found for $C_{162}H_{132}N_{12}O_6S_{18}$): C (66.64, 66.91), H (4.56, 4.50), N (5.76, 5.42), S (19.76, 19.45).

COF thin films were synthesised in 100 mL autoclaves equipped with a 28 mm diameter glass liner. ITO-coated glass substrates were cleaned in detergent solution (Hellmanex III, 0.5% *v*/*v*), water, acetone, and isopropanol, and treated with an O_2-plasma for 10 min directly before use. For the COF thin film syntheses, substrates were placed horizontally in PTFE sample holders with the plasma-treated surface face-down.

Cz-ttTII COF film

$Cz(NH_2)_4$ (3.86 mg, 5.0 µmol, 1.0 eq.) and $ttTII(CHO)_2$ (7.75 mg, 10 µmol, 2.0 eq.) were filled into an autoclave. Mesitylene (1333 µL) and benzyl alcohol (667 µL) were added, and an ITO/glass substrate was placed in the autoclave with the ITO side facing upside-down. 6 M aqueous acetic acid (200 µL) was added, and the autoclave was sealed and heated to 120 °C

for 3 d. After cooling to room temperature, the rear side of the substrate was cleaned with MeCN and the COF film was dried with a stream of nitrogen.

The COF film exhibits a dark green color with a thickness of approximately 240 nm (determined by cross-sectional SEM).

TAPB-ttTII COF film

TAPB (1.8 mg, 5.0 µmol, 1.0 eq.) and ttTII$(CHO)_2$ (5.8 mg, 7.5 µmol, 1.5 eq.) were filled into an autoclave. Mesitylene (1333 µL) and benzyl alcohol (667 µL) were added, and an ITO/glass substrate was placed in the autoclave with the ITO side facing down. 6 M aqueous acetic acid (200 µL) was added, and the autoclave was sealed and heated to 120 °C for 3 d. After cooling to room temperature, the rear side of the substrate was cleaned with MeCN and the COF film was dried with a stream of nitrogen.

The COF film exhibits a dark green color with a thickness of approximately 790 nm (determined by cross-sectional SEM).

Characterization methods

Nuclear magnetic resonance (NMR) spectra were recorded on Bruker Avance III HD spectrometers. Chemical shifts of the protons are expressed in parts per million (ppm, δ scale) and are calibrated using residual undeuterated solvent peaks as an internal reference (^{1}H NMR: $CDCl_3$: 7.26, DMSO-d_6: 2.50, THF-d_8: 3.58). Data for ^{1}H NMR spectra are reported in the following manner: chemical shift (δ ppm) (multiplicity, coupling constant, integration). Multiplicities are reported as follows: s = singlet, d = doublet, t = triplet, m = multiplet, or combinations thereof.

Powder X-ray diffraction (PXRD) patterns were measured on a Bruker D8 Advance diffractometer equipped with a Cu K_α source (0.1 mm divergence slit, knife edge air scatter screen) and a LynxEye detector. K_β radiation was attenuated with a 0.0125 mm Ni filter.

2D grazing-incidence wide angle X-ray scattering (GIWAXS) data were recorded on an Anton Paar SAXSpoint 2.0 system equipped with a Primux 100 micro Cu K_α source and a Dectris EIGER R 1M detector. The COF films were positioned at a sample-detector distance of 140 mm and were measured with an incidence angle of 0.22°.

The **structure models of the COFs** were simulated using the Accelrys Materials Studio software package. The highest possible symmetry was applied for the COFs. The structure models were optimized using the Forcite module with the Universal force-field. **Structure refinements** were carried out with the Reflex module using the Pawley method. Pseudo-Voigt peak profiles were used, and peak asymmetry was corrected using the Finger-Cox-Jephcoat method. **Connolly surfaces** and accessible surfaces were generated using a N_2-sized probe (r = 0.184 nm) at a 0.025 nm grid interval.[47]

Nitrogen sorption analyses were conducted with a Quantachrome Autosorb 1 instrument at 77 K. The samples were first extracted with supercritical CO_2, and subsequently degassed at 120 °C under high vacuum for 5 h prior to the measurements. BET areas were calculated based on the pressure range $0.05 \leq p/p_0 \leq 0.2$. Pore size distributions were determined using the QSDFT equilibrium model with a carbon kernel for cylindrical pores.

Scanning electron microscopy (SEM) images were recorded with an FEI Helios NanoLab G3 UC microscope equipped with a Schottky field-emission electron source operated at 1 – 30 kV.

Transmission electron microscopy (TEM) images were recorded with an FEI Titan Themis microscope equipped with a field emission gun operated at 300 kV.

Fourier-transform infrared (FTIR) spectra were recorded on a Bruker Vertex 70 FTIR instrument using a liquid nitrogen-cooled MCT detector and a germanium ATR crystal.

UV-Vis-NIR spectra were measured with a Perkin-Elmer Lambda 1050 spectrometer equipped with a 150 mm InGaAs integrating sphere. **Diffuse reflectance spectra** were recorded with a Harrick Praying Mantis accessory kit and were referenced to barium sulfate powder as the white standard.

Electrochemical measurements were performed with a Metrohm Autolab PGSTAT potentiostat/galvanostat. **Cyclic voltammetry (CV)** scans were recorded with the respective COF film on ITO/glass as the working electrode, a Pt wire counter electrode and a Ag wire quasi-reference electrode, and referenced to fc/fc^+ as the internal standard with a potential of 400 mV. 0.1 M tetrabutylammonium hexafluorophosphate ($TBAPF_6$) in MeCN was chosen as the electrolyte. The measurements were conducted with a scan speed of 100 mV s^{-1}.

For the **spectroelectrochemical measurements**, the COF films were placed inside a fused silica cuvette (10 mm path length) equipped with a Pt wire counter electrode, an Ag wire quasi

reference electrode and 0.1 M $TBAPF_6$/MeCN electrolyte under argon atmosphere. The potential was increased/decreased in 200 mV intervals using a 20 mV s^{-1} ramp and then held constant for the duration of the UV-Vis scan (ca. 6 min per spectrum). For the **stability and response time measurements**, the applied potential was switched between –600 mV and +600 mV vs fc/fc^+ and held constant for 4 s between each step. In order to reduce the instrument response time, absorption changes were tracked with the Lambda 1050 photomultiplier tube (Vis) and InGaAs (NIR) detectors set to fixed gain mode.

For the **conductivity measurements**, COF films were grown onto an etched ITO substrate (see Figure S13). The films were fastened in a specifically designed mold, the COF film was removed from the counter electrode opening using acetone, and gold electrodes (40 nm thickness) were evaporated on the COF film/substrate. The conductivity was subsequently determined in the dark using a vertical conductivity measurement setup and a Metrohm Autolab PGSTAT potentiostat/galvanostat, scanning from –400 mV to +1000 mV.

4.6 Supporting Information

Abbreviations

BET	Brunauer-Emmett-Teller
CV	cyclic voltammetry
DCM	dichloromethane
DMF	*N,N*-dimethylformamide
DMSO	dimethyl sulfoxide
eq.	equivalent(s)
FWHM	full width at half maximum
ICT	intramolecular charge transfer
ITO	indium tin oxide
NBS	*N*-bromosuccinimide
NIR	near-infrared
OD	optical density
PSD	pore size distribution
PTFE	poly(tetrafluoroethylene)
QSDFT	quenched solid density functional theory
rt	room temperature
$TBAPF_6$	tetrabutylammonium hexafluorophosphate
TFA	trifluoroacetic acid
THF	tetrahydrofuran

4. Electrically conductive carbazole and thienoisoindigo-based COFs showing fast and stable electrochromism

COF structure analysis

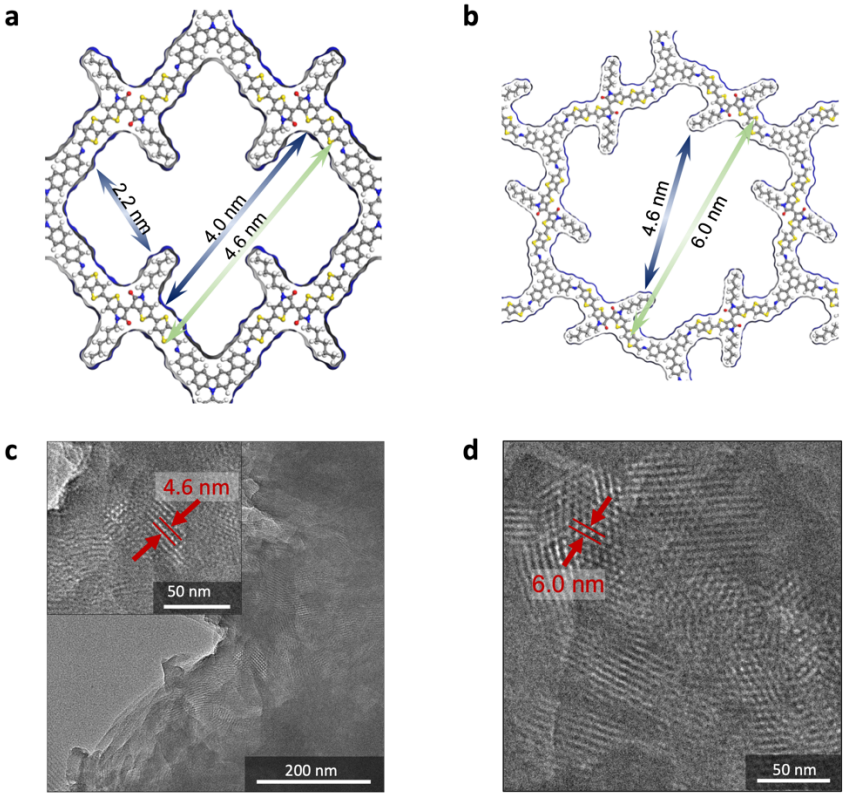

Figure S1. (a) Illustration of the pore structure of the Cz-ttTII COF viewed along the *c*-axis, showing a shamrock-like shape, induced by the hexyl chains reaching into the pore (assumed to be stiff in the model). The refined structure indicates a periodicity of 4.6 nm and wall-to-wall distances of 4.0 nm (excluding the hexyl chains) and 2.2 nm (including the hexyl chains). (**b)** Illustration of the pore structure of the TAPB-ttTII COF viewed along the *c*-axis, showing a honeycomb shape. The refined structure indicates a periodicity of 6.0 nm and wall-to-wall distances of 4.6 nm. **(c)** High-resolution TEM image of a polycrystalline Cz-ttTII COF powder sample exhibiting crystallites with a tetragonal pore structure. Inset: Magnification of a crystalline domain with the view along the crystallographic *c*-axis, showing a periodicity of 4.6 nm, which is in excellent agreement with the structure model. **(d)** High-resolution TEM image of a polycrystalline TAPB-ttTII COF powder sample exhibiting crystallites with a hexagonal pore structure with the view along the crystallographic *c*-axis, showing a periodicity of 6.0 nm, which is in excellent agreement with the structure model.

FTIR spectroscopy

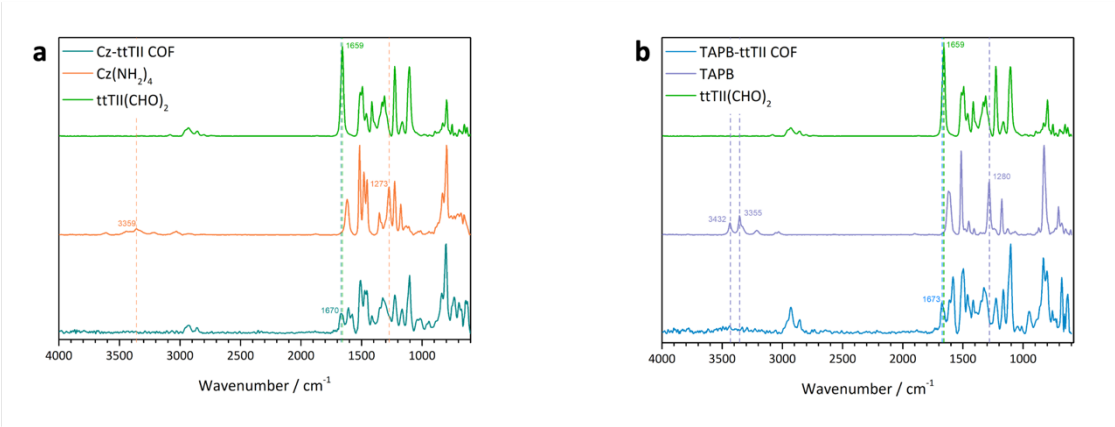

Figure S2. IR spectra of **(a)** the Cz-ttTII COF powder and **(b)** the TAPB-ttTII COF powder with the respective precursors $Cz(NH_2)_4$, TAPB, and $ttTII(CHO)_2$. The spectra of $Cz(NH_2)_4$ and TAPB show characteristic amine stretching and bending vibrations, whilst the $ttTII(CHO)_2$ precursor spectrum exhibits stretching vibrations typical for aldehydes. The decrease of these signals and the evolution of the C=N stretching vibrations deriving from the formation of imine bonds confirm the successful formation of the COFs.

Table S1. Assignment of selected IR vibrations.

	Wavenumber / cm^{-1}	**Assignment**
$Cz(NH_2)_4$	3359	N-H stretching
	3440	N-H stretching
	1620	N-H bending
	1273	C-NH_2 stretching
TAPB	3432	N-H stretching
	3355	N-H stretching
	1619	N-H bending
	1280	C-NH_2 stretching
$ttTII(CHO)_2$	2927	C-H stretching
	1659	C=O stretching
Cz-ttTII	1670	C=N stretching
TAPB-ttTII	1673	C=N stretching

UV-Vis spectroscopy

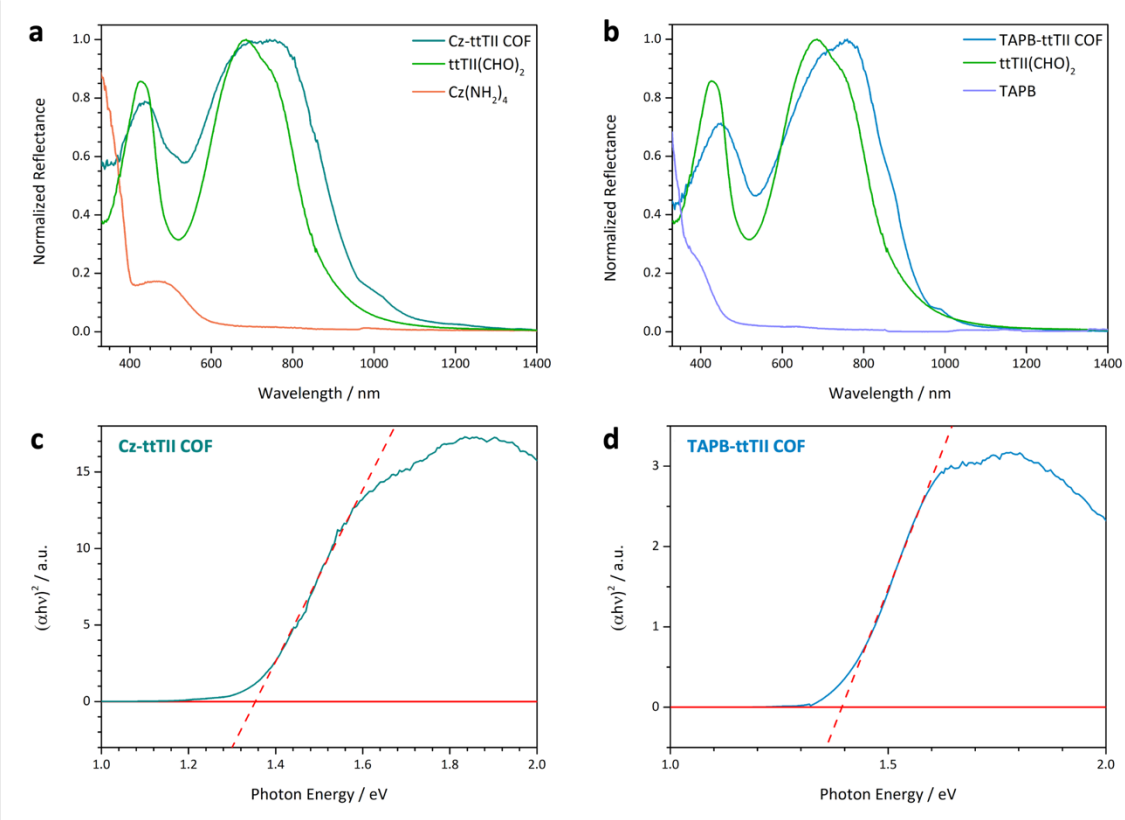

Figure S3. UV-vis absorption spectra of solid precursors $Cz(NH_2)_4$, TAPB, and $ttTII(CHO)_2$ and of the corresponding COF powders. **(a)** Cz-ttTII COF, **(b)** TAPB-ttTII COF. **(c)** And **(d)** display the respective Tauc plots of the COFs assuming a direct band gap of E_{gap} = 1.35 eV for the Cz-ttTII COF and E_{gap} = 1.40 eV for the TAPB-ttTII COF.

The $ttTII(CHO)_2$ exhibits a dual band absorption. The higher-energy band between 350 and 500 nm is attributed to a π→π* transition, while the lower-energy absorption band between 600 and 850 nm represents intramolecular charge transfer (ICT) transitions.[41]

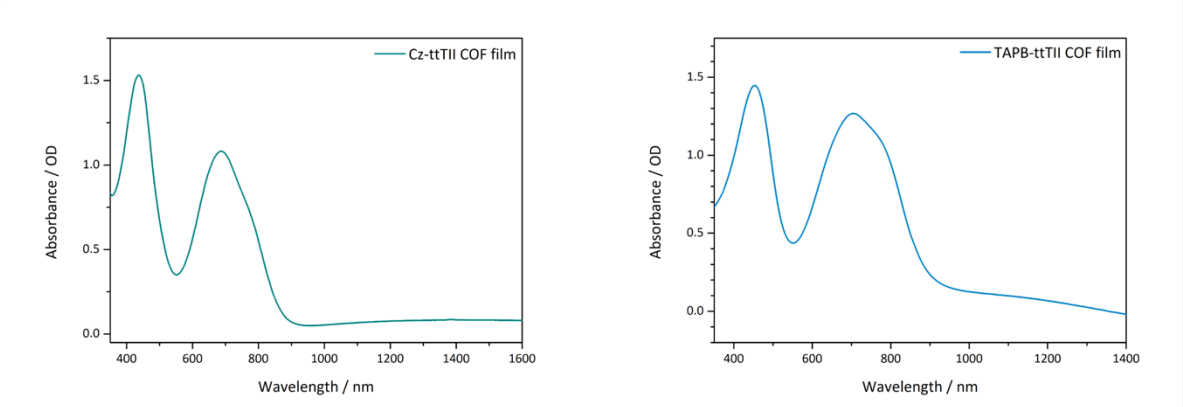

Figure S4. UV-vis absorption spectra of the **(a)** Cz-ttTII COF thin film on ITO and **(b)** the TAPB-ttTII COF thin film on ITO. Both films exhibit the typical dual-band absorption spectra, typical for ttTII-COFs.

Scanning electron microscopy

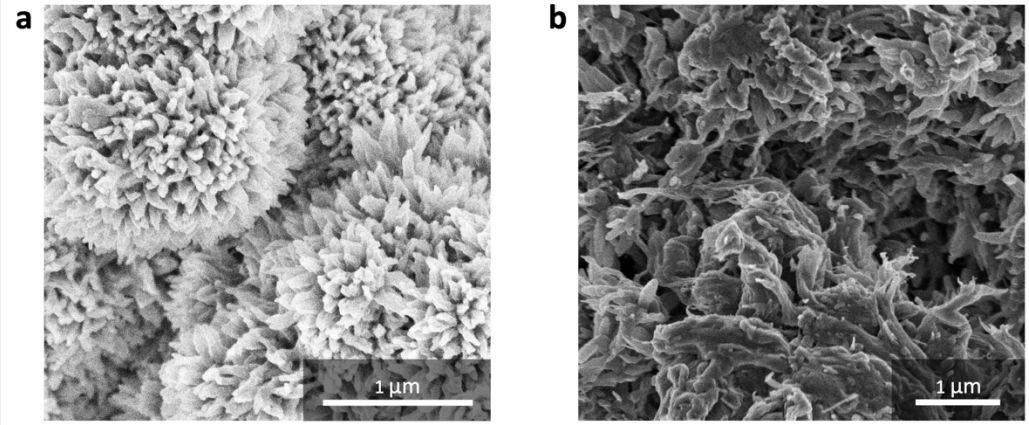

Figure S5. Scanning electron microscopy images of the COF powders. **(a)** shows the rod-like morphology of the Cz-ttTII COF and **(b)** the sponge-like morphology of the TAPB-ttTII COF.

4. Electrically conductive carbazole and thienoisoindigo-based COFs showing fast and stable electrochromism

GIWAXS and SEM analyses of the COF films

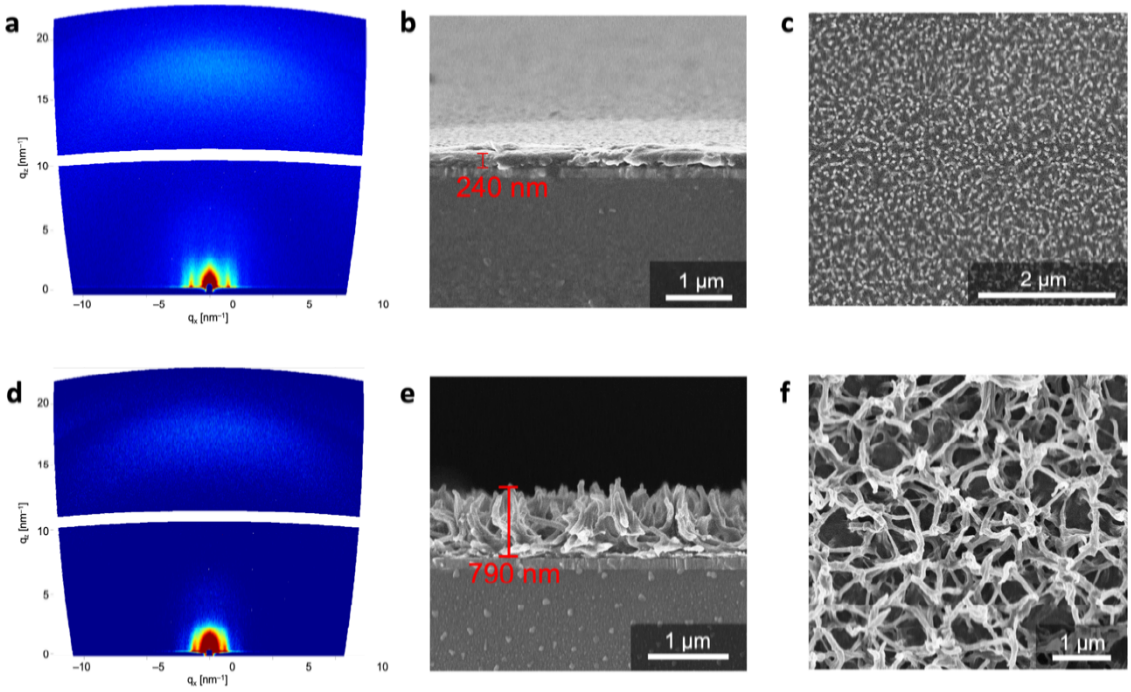

Figure S6. (a) 2D GIWAXS pattern of a Cz-ttTII thin film on ITO showing the crystallinity and preferential orientation of the COF film. The COF *a*-*b* plane is oriented parallel to the substrate surface. **(b)** Cross-sectional SEM image of a Cz-ttTII COF film on ITO displaying the full coverage of the substrate and an approximate film thickness of 240 ± 10 nm. **(c)** SEM-top view image of the Cz-ttTII COF film surface, exhibiting a pillar-like morphology. **(d)** 2D GIWAXS pattern of a TAPB-ttTII film on ITO showing the crystallinity and preferential orientation of the COF film. The COF *a*-*b* plane is oriented parallel to the substrate surface. **(e)** Cross-sectional SEM image of a TAPB-ttTII COF thin film on ITO displaying the full coverage of the substrate and an approximate film thickness of 790 ±10 nm. **(f)** SEM-top view image of the COF film surface, showing a web-like morphology.

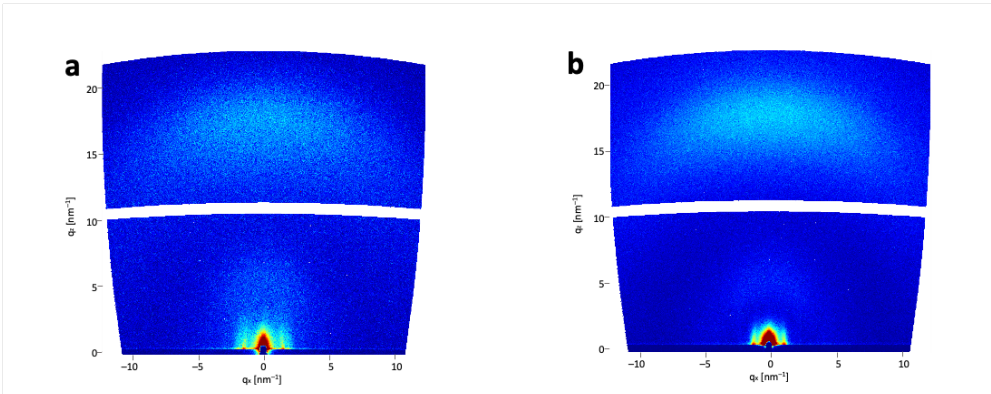

Figure S7. GIWAXS patterns of the measured **(a)** Cz-ttTII COF film and **(b)** TAPB-ttTII COF film, showing the crystallinity and the preferential orientation of the COF films after the electrochromic measurements.

Stability cycling measurements

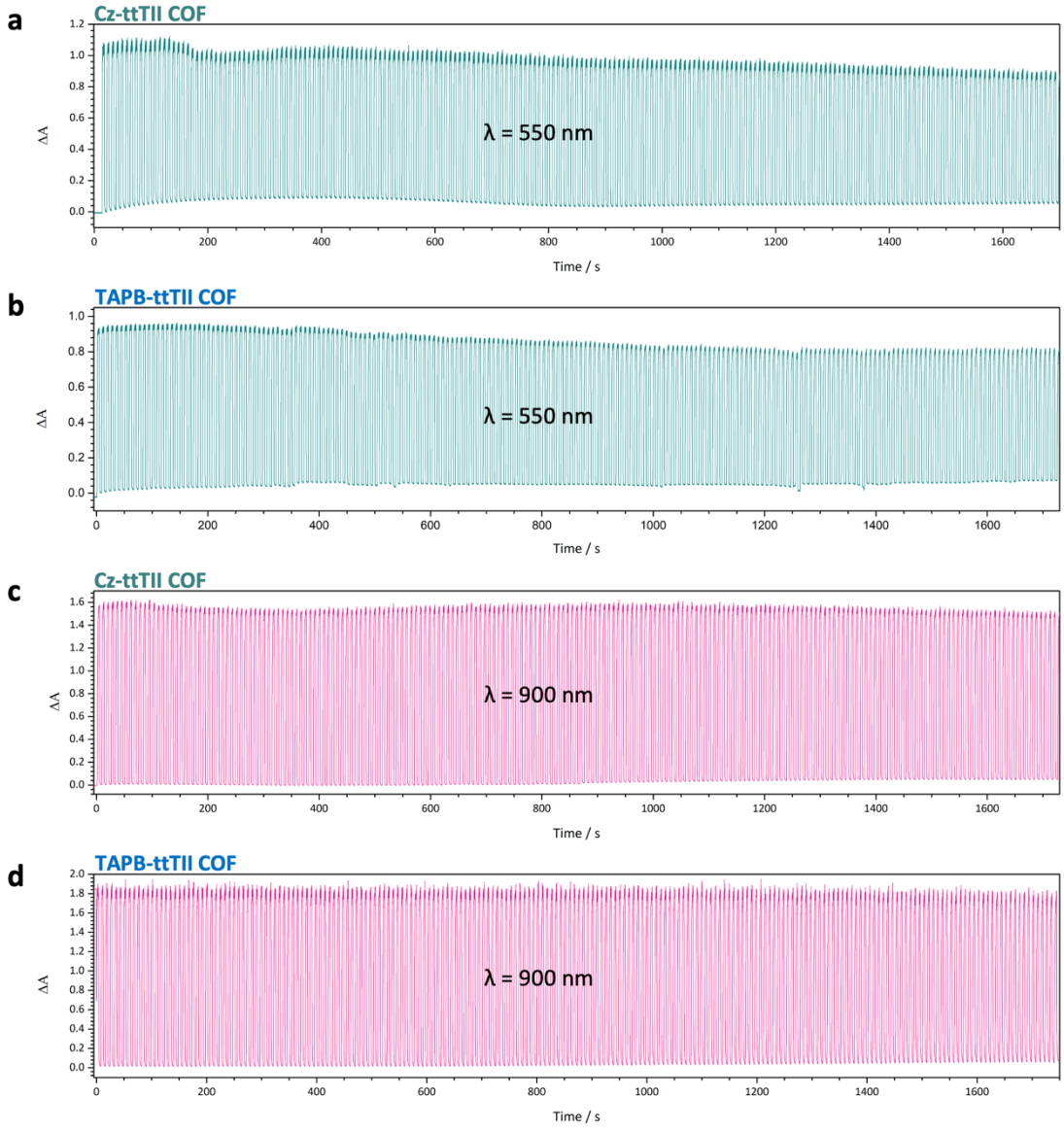

Figure S8. Electrochromic stability cycling measurements of the Cz-ttTII COF film and the TAPB-ttTII COF film on ITO substrates. The films were cycled between –600 mV and 600 mV vs. fc/fc$^+$ for more than 200 times and the potential was held constant for 4 s after each potential step. The change in absorbance was observed at 550 nm and at 900 nm. The Cz-ttTII COF film exhibits a change in absorbance of **(a)** approximately 1.0 OD at 550 nm, and **(b)** 1.5 OD at 900 nm. For both wavelengths the COF shows a minor degradation of 10% and 6%, respectively, over 200 cycles. The TAPB-ttTII COF film also shows a strong change in absorbance of **(c)** up to 0.9 OD at 550 nm and **(d)** 1.9 OD at 900 nm. The film is stable over 200 cycles measured at 900 nm wavelength with virtually no degradation, whilst the change in absorbance at 550 nm decreases to approximately 0.8 OD over 200 cycles.

.

Response times

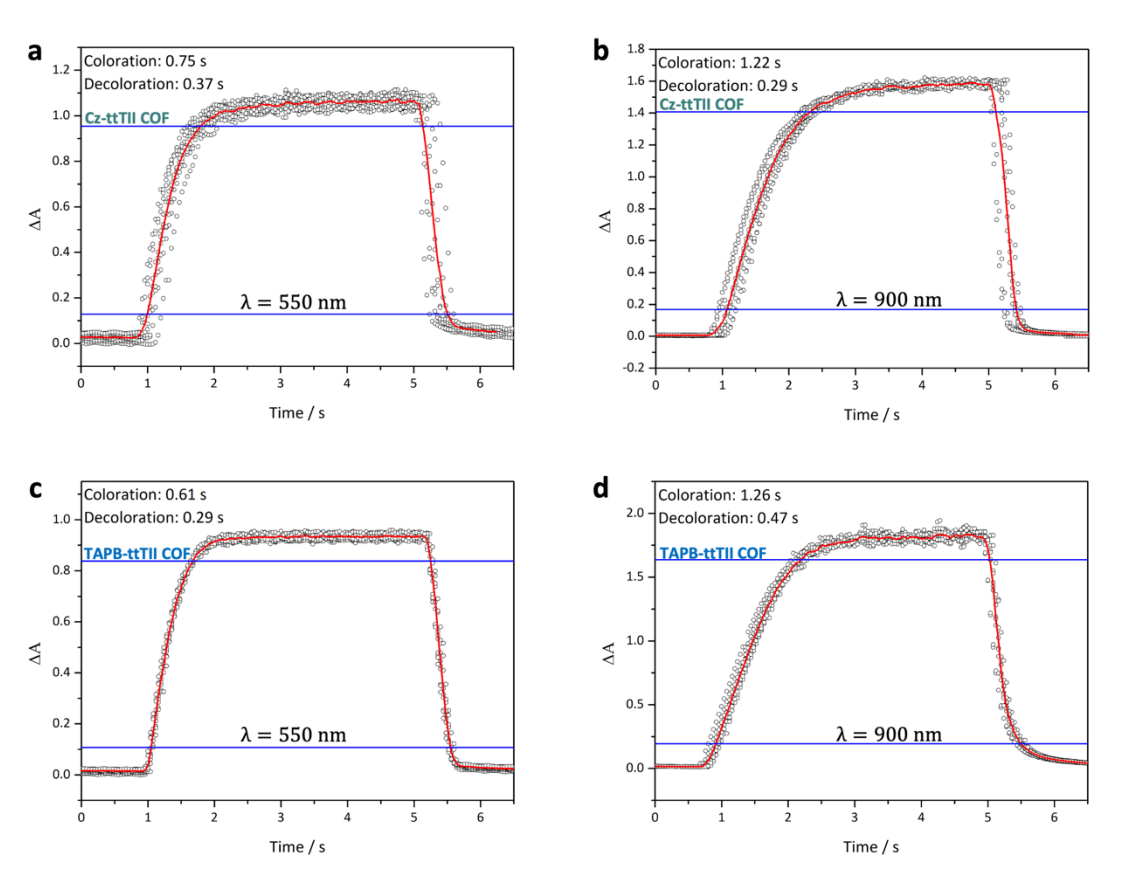

Figure S9. Electrochromic response times of the Cz-ttTII COF film and the TAPB-ttTII COF film. The first ten cycles of the respective electrochromic stability cycling measurement (Figure S8) are averaged and the coloration and decoloration times are determined between the respective 10% and 90% boundaries. For the Cz-ttTII COF film coloration times between 0.75 – 1.22 s and decoloration times between 0.29 – 0.37 s were observed (**(a)** and **(b)**). The corresponding response times for the TAPB-ttTII COF are 0.61 – 1.26 s for coloration and 0.29 – 0.47 s for decoloration (**(c)** and **(d)**).

Table S2: Comparison of response times of a selection of electrochromic COFs.

Material	Wavelength [nm]	Coloration [s]	Decoloration [s]	Year
$COF_{3PA\text{-}TT}$[15]	610 1300	18.5 20	7 2.5	2019
EC-COF-1[17]	574 730	1.8 2.6	7.2 3.5	2020
Py-ttTII[14]	550 660 900	0.38 0.29 0.47	0.20 0.14 0.20	2021
PPTA[43]	668	1.8	3.3	2022
FAF1[48]	1420 765 515 374	11.5 6.8 2.4 6.7	4.9 5.8 1.4 9.0	2022
FAF2[48]	1630 980 526	8.2 7.0 12.8	5.8 3.1 4.2	

Coloration efficiency

The coloration efficiencies were calculated according to the following formula:

$$CE = \frac{\Delta OD}{\frac{Q}{A}}$$

The calculations are based on the respective OD values at a potential of 400 mV. The scan speed of the CV measurements is 100 mV s^{-1}. Q represents the extracted charge from the first oxidation calculated from the oxidation scan (see Figure S10).

Cz-ttTII	TAPB-ttTII
ΔOD_{900nm}: 1.99	ΔOD_{900nm}: 1.41
ΔOD_{550nm}: 0.72	ΔOD_{550nm}: 0.27
A = 0.70 cm^2	A = 0.69 cm^2
Q = 1.84996 × 10^{-3} C	Q = 1.63259 × 10^{-3} C
$CE_{900\ nm}$ = 807 $cm^2\ C^{-1} \pm$ 81 $cm^2\ C^{-1}$	**$CE_{900\ nm}$ = 596 $cm^2\ C^{-1} \pm$ 60$cm^2\ C^{-1}$**
$CE_{550\ nm}$ = 272 $cm^2\ C^{-1} \pm$ 27 $cm^2\ C^{-1}$	**$CE_{550\ nm}$ = 114 $cm^2\ C^{-1} \pm$ 11 $cm^2\ C^{-1}$**

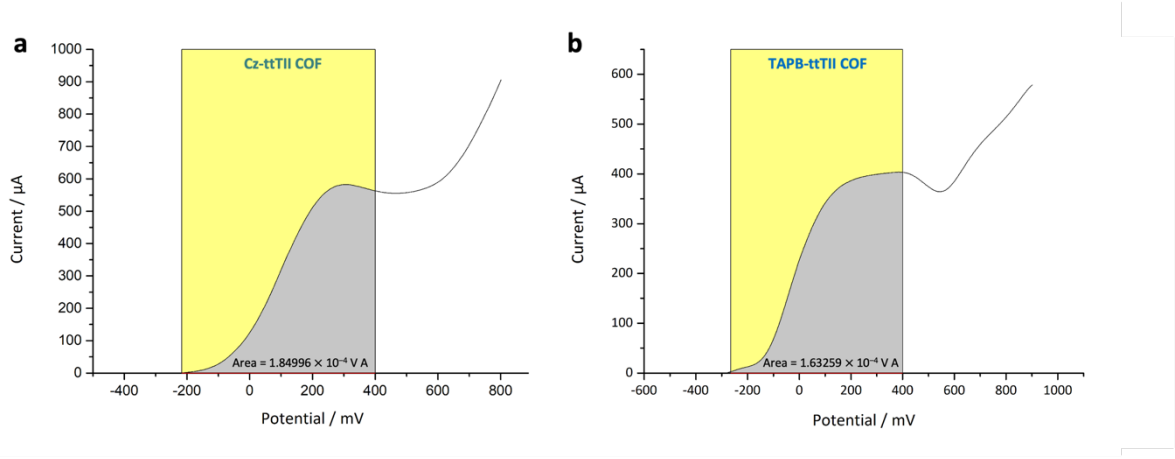

Figure S10. Integration of the CV curves of **(a)** the Cz-ttTII COF and **(b)** the TAPB-ttTII COF until the first oxidation process of both COFs is complete. The integrated areas (grey) of the Cz-ttTII COF and the TAPB-ttTII COFs are 1.84996×10^{-4} V A and 1.63259×10^{-4} V A, respectively. Dividing these areas by the scan speed of 0.1 V s^{-1} yields the respective extracted charges Q used for the calculation above.

Photographic images of the COF films' electrochromism

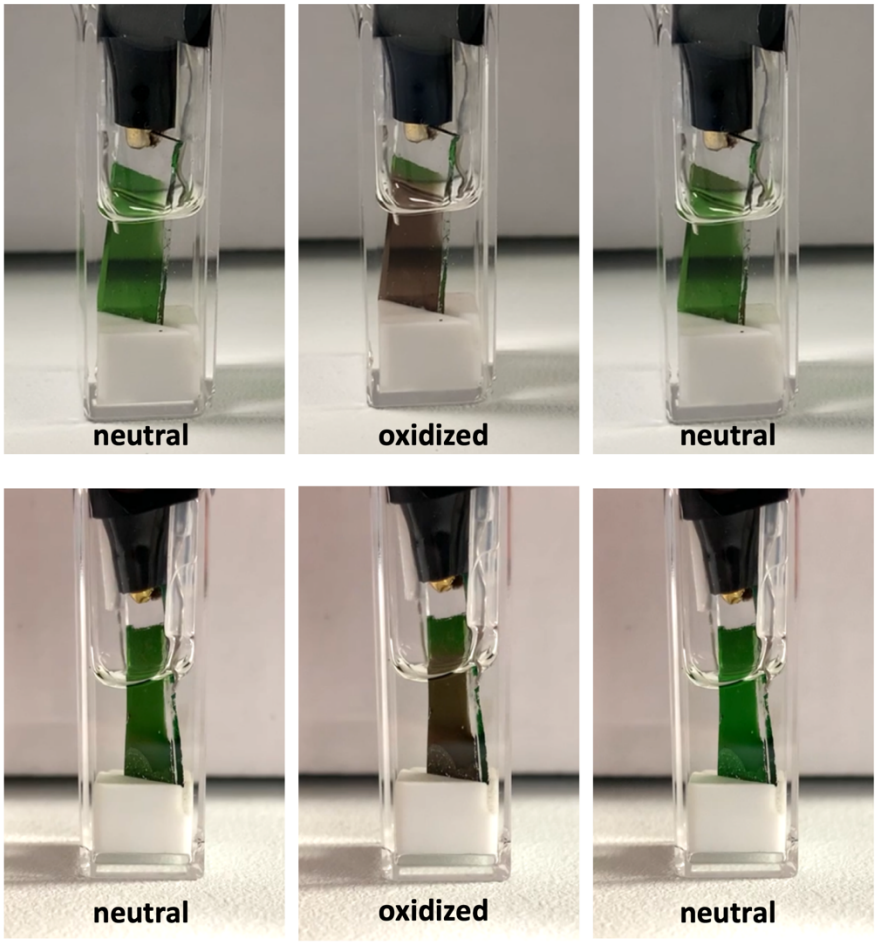

Figure S11. Photographic images of the **(a)** Cz-ttTII COF and **(b)** TAPB-ttTII COF from the neutral (before oxidation), oxidized and neutral (after oxidation). The color of both COF films changes from dark green (neutral) to almost black (oxidized) and back to dark green (neutral) upon the application of a potential.

Vertical electrical conductivity

Electrical conductivity measurements of the COFs were performed using the following sample setup:

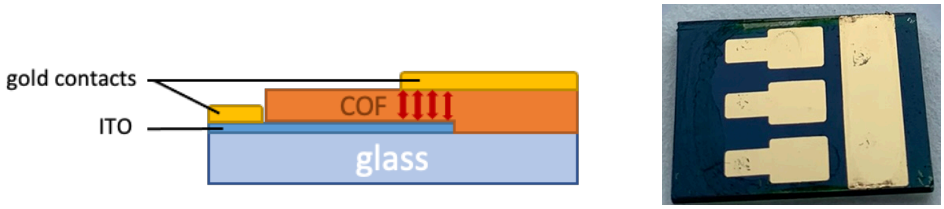

Figure S12. Left: Schematic cross-section of the sample setup. A COF film is grown onto a specifically etched ITO substrate. Gold electrodes were evaporated onto the surface of the COF film and the ITO layer respectively. **Right:** Photographic picture of a measured Cz-ttTII COF film with three gold electrodes on the COF film and the counter electrode on the ITO substrate.

Calculation of the electrical conductivity

Resistance R:

$$\mathrm{R} = \frac{1}{slope}$$

Specific electrical resistance ρ through-plane:

$$\rho = \mathrm{R}\,\frac{\mathrm{A}}{\mathrm{l}} = \mathrm{R}\,\frac{length\ a\ (electrode)\ \times\ length\ b\ (electrode)}{film\ thickness}$$

Electrical conductivity

$$\sigma = \frac{1}{\rho}$$

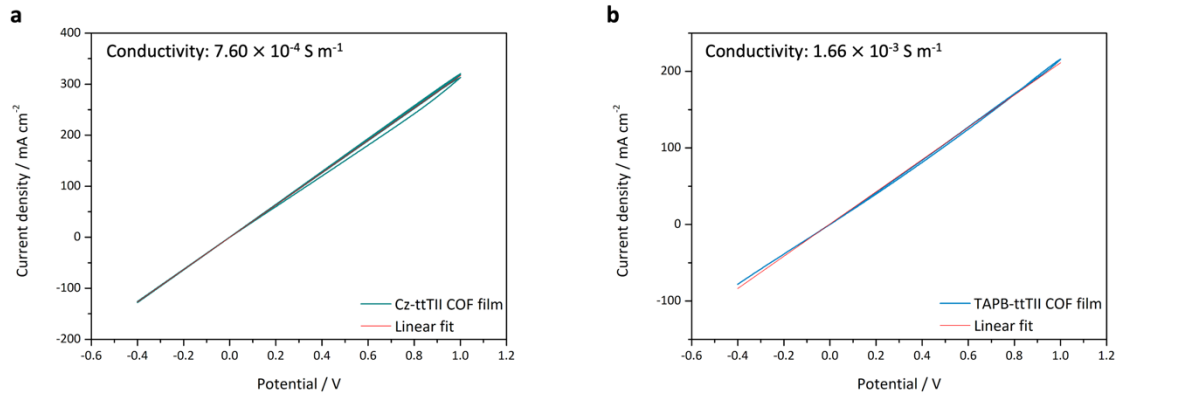

Figure S13. *I-V* curves of the **(a)** Cz-ttTII (green line) and **(b)** TAPB-ttTII (blue line) COF films and the respective linear fits (red lines). The curves were measured between –400 mV and 1000 mV using a vertical conductivity setup shown in Figure S12. Based on the measurement setup, there will be systematic errors due to the porous morphology of the films, where the measured thickness includes air.

Building block syntheses

Reactions were performed using oven-dried glassware and standard Schlenk and glovebox techniques under argon atmosphere. For the reactions, commercially available and high-purity reagents and solvents were used, and if not shipped under inert gas, degassed and saturated with argon prior to use. Flash column chromatography was conducted using silica gel (Acros Organics, 60 Å, 35 – 70 µm), with continuous monitoring *via* thin layer chromatography (TLC) using silica gel coated aluminum plates (Merck, 60 Å, F254).

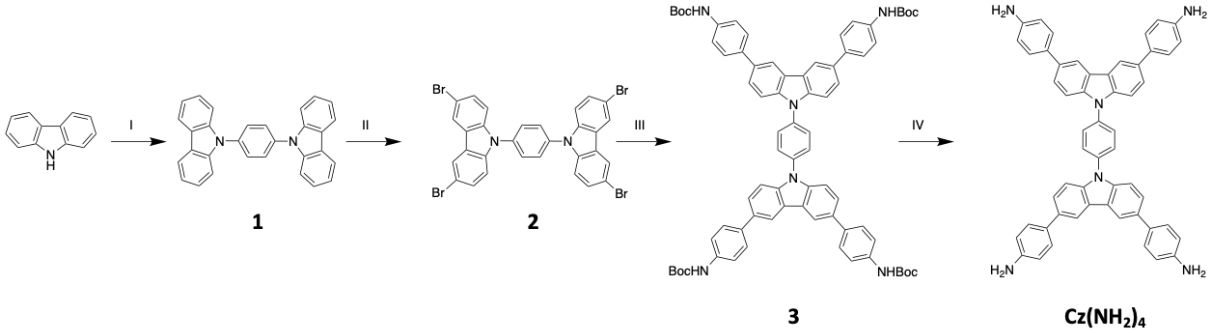

Figure S14. Synthesis path of the new $Cz(NH_2)_4$ building block. Reagents and synthesis conditions: (I) 1,4-Diiodobenzene, DMSO, 90 °C, 61%. (II) NBS, DMF, rt/160 °C, 98 %. (III) (*N*-Boc-amino)phenylboronic acid pinacol ester, 1,4-dioxane/water, 111°C, 60%. (IV) TFA, DCM/water, rt, 56%.

1,4-Di(9*H*-carbazol-9-yl)benzene (1)[49]

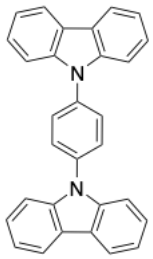

A reaction mixture of 1,4-diiodobenzene (1.23 g, 3.74 mmol, 1.0 eq.), carbazole (1.50 g, 8,97 mmol, 2.4 eq.), copper (I) iodide (142 mg, 0.75 mmol, 0.2 eq.), *L*-proline (172 mg, 1.90 mmol, 0.4 eq.), and potassium carbonate (2.07 g, 15.0 mmol, 4.0 eq.) in DMSO was stirred under argon atmosphere at 90 °C for 3 d. The reaction was quenched with 50 mL of 0.2 M HCl, stirred for 30 min, the product collected by filtration, and washed with 300 mL water and 200 mL of a water and acetonitrile mixture (1:1). The crude product was dried under high vacuum,

dissolved in DCM / cyclohexane (1:1) and purified by column chromatography (silica gel, DCM / cyclohexane, 1:1) to yield the title compound as a white-yellow solid (1.12 g, 2.74 mmol, 61%).

^{1}H NMR (400 MHz, $CDCl_3$): 8.19 (d, *J* = 7.6 Hz, 4H), 7.83 (s, 4H), 7.57 (d, *J* = 8.4 Hz, 4H), 7.49 (td, *J* = 6.0, 1.2 Hz, 4H), 7.34 (t, *J* = 5.6 Hz, 4H).

1,4-Bis(3,6-dibromo-9*H*-carbazol-9-yl)benzene (2)

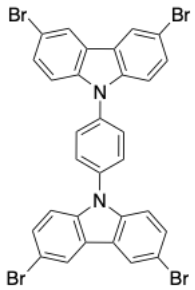

A reaction mixture containing compound **1** (1.02 g, 2.5 mmol, 1.0 eq.) and NBS (2.04 g, 11.5 mmol, 4.6 eq.) in anhydrous DMF (60 mL) was stirred at room temperature for 48 h. Subsequently, the reaction temperature was increased to 160 °C for another 3 h before letting the mixture cool down to room temperature again. The mixture was then quenched with water (50 mL), stirred for 60 min, the product collected by filtration and washed with water (300 mL) and a mixture of water and acetonitrile (300 mL, 1:1). The product was dried under high vacuum, yielding a yellow solid (1.77 g, 2.44 mmol, 98 %)

^{1}H NMR (400 MHz, THF-d_8): 8.43 (s, *J* = 2.0 Hz, 4H), 7.92 (s, 4H), 7.60 (dd, *J* = 6.8, 2.0 Hz, 4H), 7.51 (d, *J* = 8.8 Hz, 4H).

Tetra-*tert*-butyl((1,4-phenylenebis(9*H*-carbazole-9,3,6-triyl))tetrakis(benzene-4,1-diyl))tetracarbamate (3)

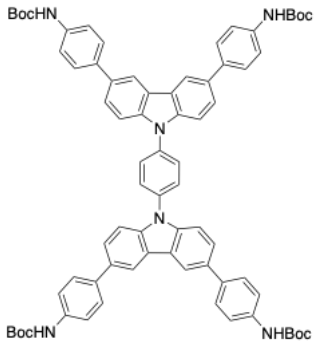

A reaction mixture of compound **2** (700 mg, 0.97 mmol, 1.0 eq.), 4-(*N*-Boc-amino)phenylboronic acid pinacol ester (1.85 mg, 5.80 mmol, 6.0 eq.), potassium carbonate (1.07 g, 7.73 mmol, 8.0 eq.) and $Pd(PPh_3)_4$ (223 mg, 0.19 mmol, 0.2 eq.) in 1,4-dioxane (18.3 mL) and water (4.6 mL) was stirred at 111 °C for 4 d. Once cooled down to room temperature, the mixture was quenched with water (50 mL), stirred for another 30 min and extracted with DCM. The organic phase was dried over $MgSO_4$ and concentrated under reduced pressure. Purification by column chromatography (silica gel, DCM /EtOAc, 99:1) yielded the title compound as a white-yellow solid (683 mg, 0.58 mmol, 60%).

^{1}H NMR (400 MHz, $CDCl_3$): 8.38 (s, 4H), 7.83 (s, 4H), 7.70 – 7.67 (m, 12H), 7.60 (d, *J* = 8.8 Hz, 4H), 7.49 (d, *J* = 8.4 Hz, 8H), 6.62 (s, 4H), 1.56 (s, 36H).

Cz(NH_2)$_4$: 4,4',4'',4'''-(1,4-Phenylenebis(9*H*-carbazole-9,3,6-triyl))tetraaniline (4)

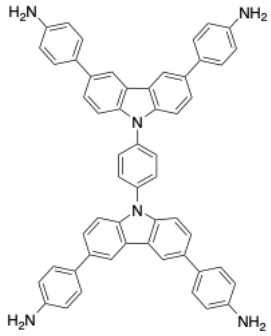

Compound **3** (617 mg, 0.53 mmol, 1.0 eq.) was dissolved in 25 mL of DCM and 0.7 mL of water and stirred at room temperature. TFA (6.83 mL) was added dropwise to the reaction mixture, leading to a color change to dark green. The mixture was stirred for 1 h, with the color changing turquoise, and slowly added to a saturated solution of $NaHCO_3$, turning the color to orange. After stirring for 30 min, the product was collected by filtration, washed with a mixture of water and methanol (100 mL, 1:1) and dried under high vacuum, yielding a light orange solid (229 mg, 0.30 mmol, 56%).

^{1}H NMR (400 MHz, DMSO-d_6): 8.61 (s, *J* = 1.6 Hz, 4H), 7.71 (dd, *J* = 6,8, 2.0 Hz, 4H), 7.63 (d, *J* = 8.4 Hz, 4H), 7.55 (d, *J* = 8.4 Hz, 8H), 6.72 (d, *J* = 8.4 Hz, 8H), 5.18 (s, 8H).

Given the low solubility of the compound, no ^{13}C NMR spectrum could be recorded.

MS-EI: *m*/*z* 772.3313 (M^+, calculated for $C_{54}H_{40}N_6$: 772.3314).

The synthesis of the ttTII($CHO)_2$ building block was conducted according to the procedure reported elsewhere.[14]

NMR spectroscopy

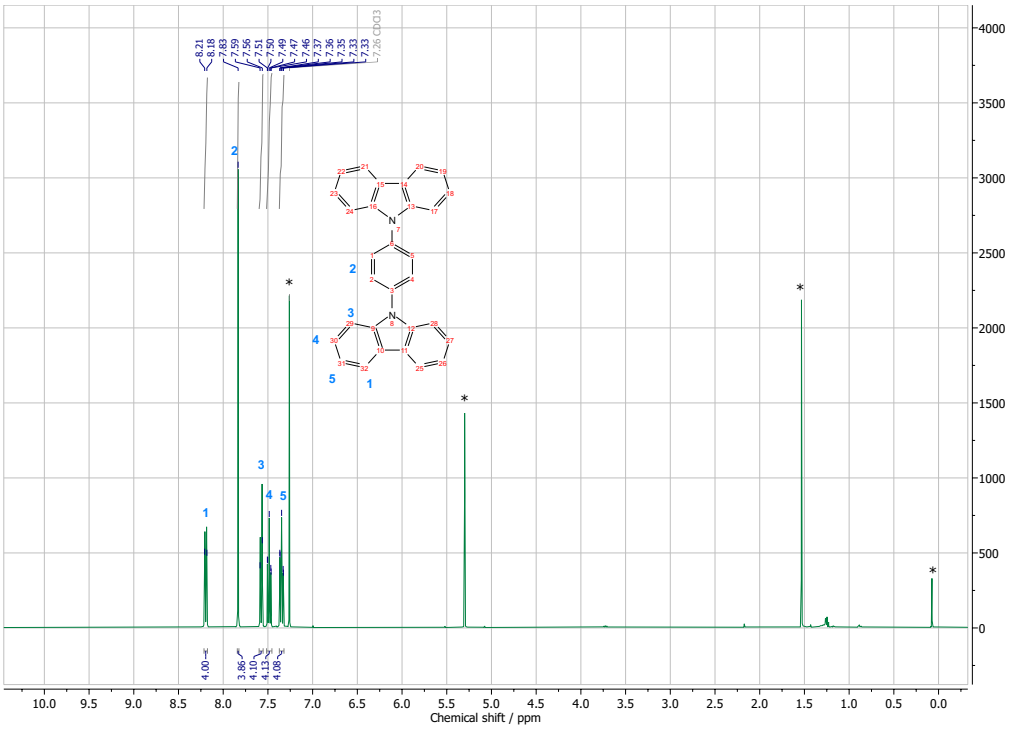

Figure S15. ^{1}H NMR spectrum of compound 1, measured in $CDCl_3$. Residual solvent signals are marked with asterisks.

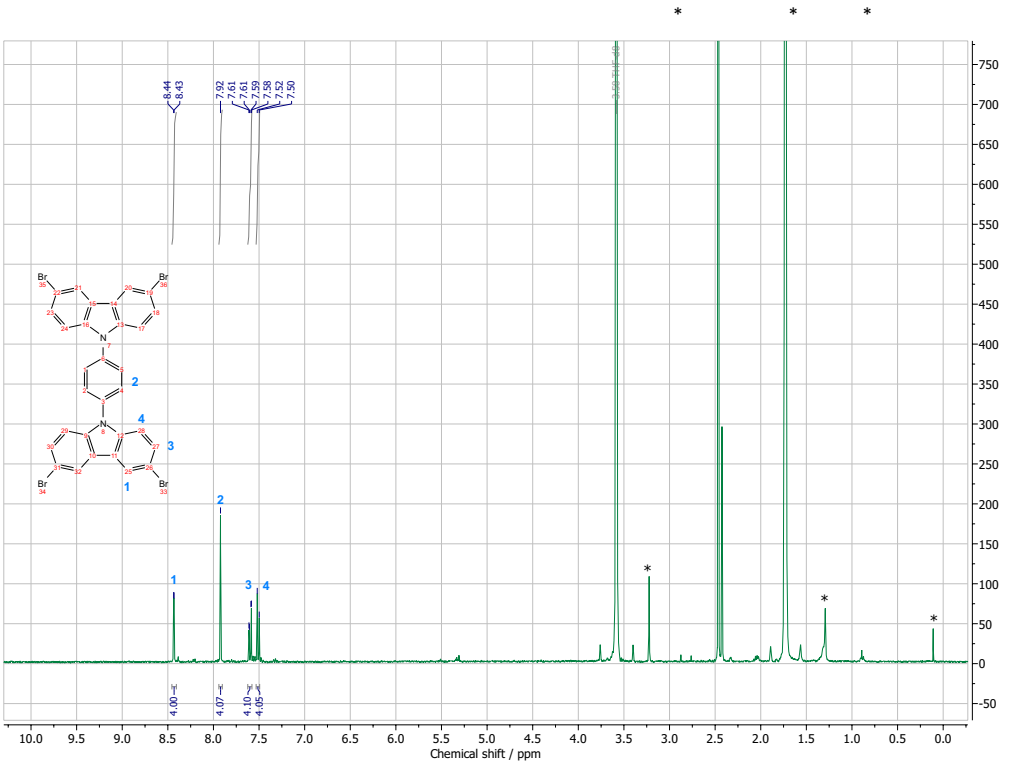

Figure S16. ^{1}H NMR spectrum of compound 2, measured in THF-d_8. Residual solvent signals are marked with asterisks.

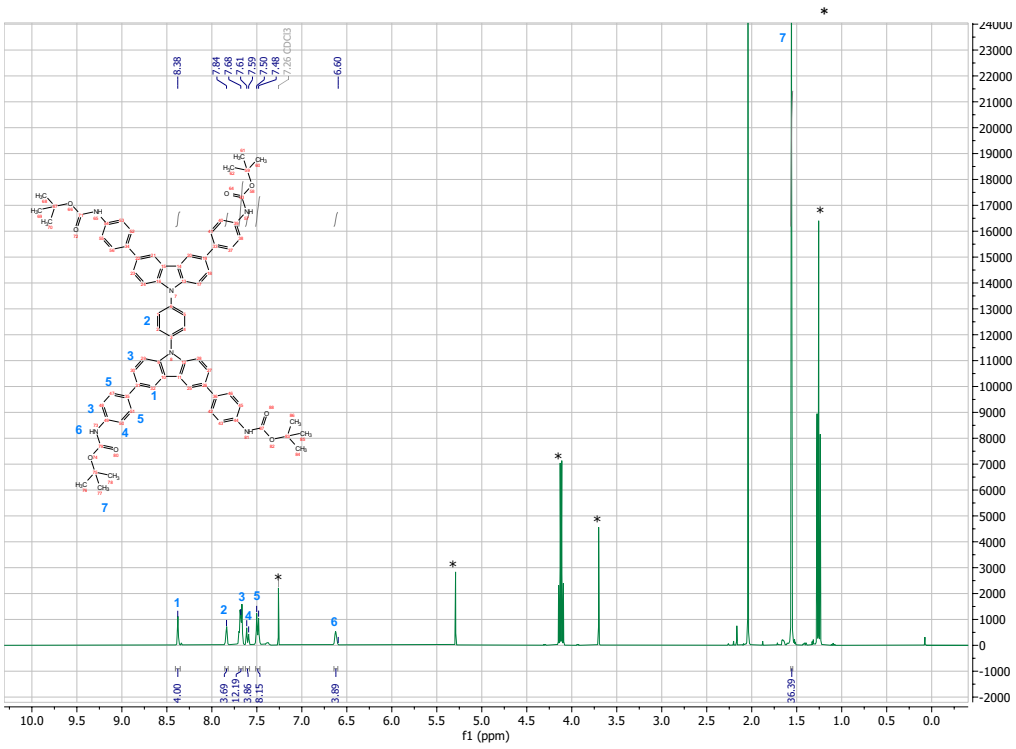

Figure S17. ^{1}H NMR spectrum of compound 3, measured in $CDCl_3$. Residual solvent signals are marked with asterisks.

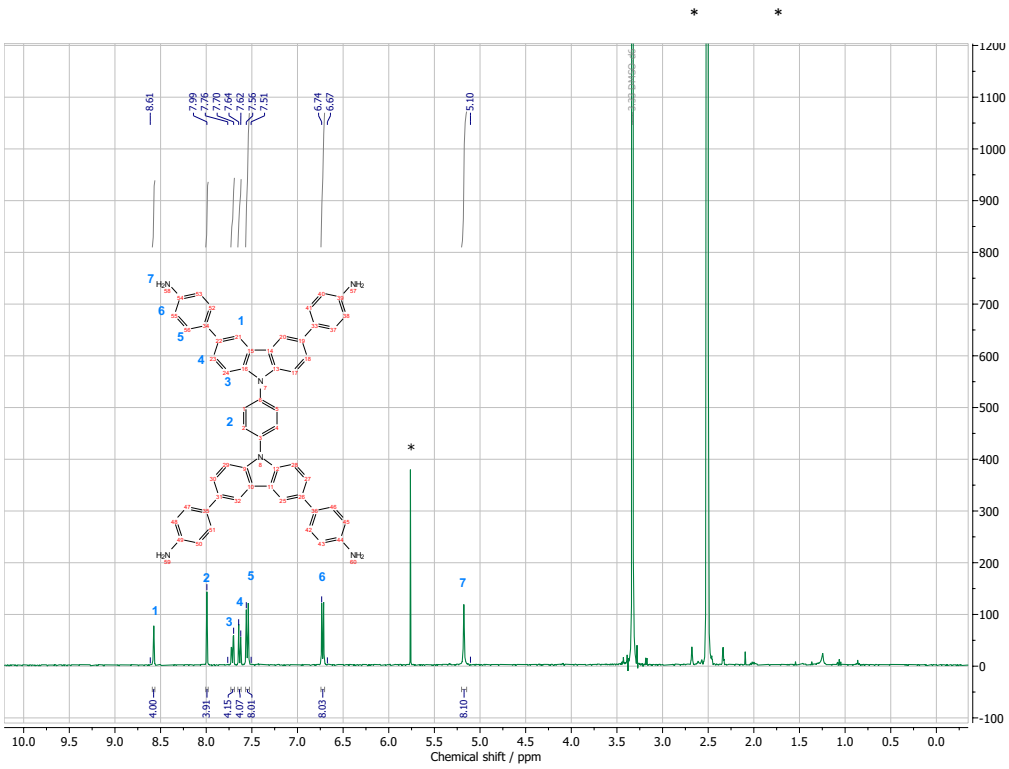

Figure S18. ^{1}H NMR spectrum of the $Cz(NH_2)_4$ building block (compound 4), measured in DMSO-d_6. Residual solvent signals are marked with asterisks.

4.7 References

1. Côté, A. P.; Benin, A. I.; Ockwig, N. W.; O'Keeffe, M.; Matzger, A. J.; Yaghi, O. M., Porous, Crystalline, Covalent Organic Frameworks. *Science* **2005,** *310*, 1166-1170.
2. Côté, A. P.; El-Kaderi, H. M.; Furukawa, H.; Hunt, J. R.; Yaghi, O. M., Reticular Synthesis of Microporous and Mesoporous 2D Covalent Organic Frameworks. *J. Am. Chem. Soc.* **2007,** *129*, 12914-12915.
3. Xu, H.; Gao, J.; Jiang, D., Stable, crystalline, porous, covalent organic frameworks as a platform for chiral organocatalysts. *Nat. Chem.* **2015,** *7*, 905-912.
4. Uribe-Romo, F. J.; Hunt, J. R.; Furukawa, H.; Klock, C.; O'Keeffe, M.; Yaghi, O. M., A Crystalline Imine-Linked 3-D Porous Covalent Organic Framework. *J. Am. Chem. Soc.* **2009,** *131*, 4570-4571.
5. Li, Rebecca L.; Flanders, N. C.; Evans, A. M.; Ji, W.; Castano, I.; Chen, L. X.; Gianneschi, N. C.; Dichtel, W. R., Controlled growth of imine-linked two-dimensional covalent organic framework nanoparticles. *Chem. Sci.* **2019,** *10*, 3796-3801.
6. Jati, A.; Dey, K.; Nurhuda, M.; Addicoat, M. A.; Banerjee, R.; Maji, B., Dual Metalation in a Two-Dimensional Covalent Organic Framework for Photocatalytic C–N Cross-Coupling Reactions. *Journal of the American Chemical Society* **2022,** *144*, 7822-7833.
7. Lei, K.; Wang, D.; Ye, L.; Kou, M.; Deng, Y.; Ma, Z.; Wang, L.; Kong, Y., A Metal-Free Donor–Acceptor Covalent Organic Framework Photocatalyst for Visible-Light-Driven Reduction of CO2 with H2O. *ChemSusChem* **2020,** *13*, 1725-1729.
8. Yang, J.; Acharjya, A.; Ye, M.-Y.; Rabeah, J.; Li, S.; Kochovski, Z.; Youk, S.; Roeser, J.; Grüneberg, J.; Penschke, C.; Schwarze, M.; Wang, T.; Lu, Y.; van de Krol, R.; Oschatz, M.; Schomäcker, R.; Saalfrank, P.; Thomas, A., Protonated Imine-Linked Covalent Organic Frameworks for Photocatalytic Hydrogen Evolution. *Angew. Chem. Int. Ed.* **2021,** *60*, 19797-19803.
9. Li, Z.; Zhi, Y.; Feng, X.; Ding, X.; Zou, Y.; Liu, X.; Y., M., An Azine-Linked Covalent Organic Framework: Synthesis, Characterization and Efficient Gas Storage. *Chem. Eur. J.* **2015,** *21*, 12079-12084.
10. Dey, K.; Pal, M.; Rout, K. C.; Kunjattu H, S.; Das, A.; Mukherjee, R.; Kharul, U. K.; Banerjee, R., Selective Molecular Separation by Interfacially Crystallized Covalent Organic Framework Thin Films. *J. Am. Chem. Soc.* **2017,** *139*, 13083-13091.

11. Ying, Y.; Peh, S. B.; Yang, H.; Yang, Z.; Zhao, D., Ultrathin Covalent Organic Framework Membranes via a Multi-Interfacial Engineering Strategy for Gas Separation. *Adv. Mater.* **2022,** *34*, 2104946.

12. AlKaabi, K.; Wade, Casey R.; Dincă, M., Transparent-to-Dark Electrochromic Behavior in Naphthalene-Diimide-Based Mesoporous MOF-74 Analogs. *Chem* **2016,** *1*, 264-272.

13. Zhang, N.; Jin, Y.; Zhang, Q.; Liu, J.; Zhang, Y.; Wang, H., Direct fabrication of electrochromic Ni-MOF 74 film on ITO with high-stable performance. *Ionics* **2021,** *27*, 3655-3662.

14. Bessinger, D.; Muggli, K.; Beetz, M.; Auras, F.; Bein, T., Fast-Switching Vis–IR Electrochromic Covalent Organic Frameworks. *J. Am. Chem. Soc.* **2021,** *143*, 7351-7357.

15. Hao, Q.; Li, Z.-J.; Lu, C.; Sun, B.; Zhong, Y.-W.; Wan, L.-J.; Wang, D., Oriented Two-Dimensional Covalent Organic Framework Films for Near-Infrared Electrochromic Application. *J. Am. Chem. Soc.* **2019,** *141*, 19831-19838.

16. Hao, Q.; Li, Z.-J.; Bai, B.; Zhang, X.; Zhong, Y.-W.; Wan, L.-J.; Wang, D., A Covalent Organic Framework Film for Three-State Near-Infrared Electrochromism and a Molecular Logic Gate. *Angew. Chem. Int. Ed* **2021,** *60*, 12498-12503.

17. Yu, F.; Liu, W.; Ke, S.-W.; Kurmoo, M.; Zuo, J.-L.; Zhang, Q., Electrochromic two-dimensional covalent organic framework with a reversible dark-to-transparent switch. *Nat. Commun.* **2020,** *11*, 5534.

18. Meng, Z.; Stolz, R. M.; Mirica, K. A., Two-Dimensional Chemiresistive Covalent Organic Framework with High Intrinsic Conductivity. *J. Am. Chem. Soc.* **2019,** *141*, 11929-11937.

19. Zhang, J.-L.; Yao, L.-Y.; Yang, Y.; Liang, W.-B.; Yuan, R.; Xiao, D.-R., Conductive Covalent Organic Frameworks with Conductivity- and Pre-Reduction-Enhanced Electrochemiluminescence for Ultrasensitive Biosensor Construction. *Anal. Chem.* **2022,** *94*, 3685-3692.

20. Rotter, J. M.; Guntermann, R.; Auth, M.; Mähringer, A.; Sperlich, A.; Dyakonov, V.; Medina, D. D.; Bein, T., Highly conducting Wurster-type twisted covalent organic frameworks. *Chem. Sci.* **2020,** *11*, 12843-12853.

21. Cai, S.-L.; Zhang, Y.-B.; Pun, A. B.; He, B.; Yang, J.; Toma, F. M.; Sharp, I. D.; Yaghi, O. M.; Fan, J.; Zheng, S.-R.; Zhang, W.-G.; Liu, Y., Tunable electrical conductivity in

oriented thin films of tetrathiafulvalene-based covalent organic framework. *Chem. Sci.* **2014,** *5*, 4693-4700.

22. Koizumi, Y.; Ide, M.; Saeki, A.; Vijayakumar, C.; Balan, B.; Kawamoto, M.; Seki, S., Thienoisoindigo-based low-band gap polymers for organic electronic devices. *Polym. Chem.* **2013,** *4*, 484-494.
23. Xia, R.; Li, C.; Yuan, X.; Wu, Q.; Jiang, B.; Xie, Z., Facile Preparation of a Thienoisoindigo-Based Nanoscale Covalent Organic Framework with Robust Photothermal Activity for Cancer Therapy. *ACS Appl. Mater. Interfaces* **2022,** *14*, 19129-19138.
24. Liu, F.; Wang, H.; Zhang, Y.; Wang, X.; Zhang, S., Synthesis of low band-gap 2D conjugated polymers and their application for organic field effect transistors and solar cells. *Organ. Electron.* **2019,** *64*, 27-36.
25. Bessinger, D.; Ascherl, L.; Auras, F.; Bein, T., Spectrally Switchable Photodetection with Near-Infrared-Absorbing Covalent Organic Frameworks. *J. Am. Chem. Soc.* **2017,** *139*, 12035-12042.
26. Shizu, K.; Lee, J.; Tanaka, H.; Nomura, H.; Yasuda, T.; Kaji, H.; Adachi, C., Highly efficient electroluminescence from purely organic donor–acceptor systems. *Pure Appl. Chem.* **2015,** *87*, 627-638.
27. Grybauskaite-Kaminskiene, G.; Ivaniuk, K.; Bagdziunas, G.; Turyk, P.; Stakhira, P.; Baryshnikov, G.; Volyniuk, D.; Cherpak, V.; Minaev, B.; Hotra, Z.; Ågren, H.; Grazulevicius, J. V., Contribution of TADF and exciplex emission for efficient "warm-white" OLEDs. *J. Mater. Chem. C* **2018,** *6*, 1543-1550.
28. Yokoyama, M.; Inada, K.; Tsuchiya, Y.; Nakanotani, H.; Adachi, C., Trifluoromethane modification of thermally activated delayed fluorescence molecules for high-efficiency blue organic light-emitting diodes. *Chem Commun (Camb)* **2018,** *54*, 8261-8264.
29. Oda, S.; Kumano, W.; Hama, T.; Kawasumi, R.; Yoshiura, K.; Hatakeyama, T., Carbazole-Based DABNA Analogues as Highly Efficient Thermally Activated Delayed Fluorescence Materials for Narrowband Organic Light-Emitting Diodes. *Angew. Chem. Int. Ed* **2021,** *60*, 2882-2886.
30. Yu, W.; Yang, Q.; Zhang, J.; Tu, D.; Wang, X.; Liu, X.; Li, G.; Guo, X.; Li, C., Simple Is Best: A p-Phenylene Bridging Methoxydiphenylamine-Substituted Carbazole Hole

Transporter for High-Performance Perovskite Solar Cells. *ACS Appl. Mater. Interfaces* **2019,** *11*, 30065-30071.

31. Gilmanova, L.; Bon, V.; Shupletsov, L.; Pohl, D.; Rauche, M.; Brunner, E.; Kaskel, S., Chemically Stable Carbazole-Based Imine Covalent Organic Frameworks with Acidochromic Response for Humidity Control Applications. *J. Am. Chem. Soc.* **2021,** *143*, 18368-18373.
32. El-Mahdy, A. F. M.; Lai, M.-Y.; Kuo, S.-W., A highly fluorescent covalent organic framework as a hydrogen chloride sensor: roles of Schiff base bonding and π-stacking. *J. Mater. Chem. C* **2020,** *8*, 9520-9528.
33. Zhang, N.; Wei, B.; Ma, T.; Tian, Y.; Wang, G., A carbazole-grafted covalent organic framework as turn-on fluorescence chemosensor for recognition and detection of Pb2+ ions with high selectivity and sensitivity. *J. Mater. Sci.* **2021,** *56*, 11789-11800.
34. El-Mahdy, A. F. M.; Young, C.; Kim, J.; You, J.; Yamauchi, Y.; Kuo, S.-W., Hollow Microspherical and Microtubular [3 + 3] Carbazole-Based Covalent Organic Frameworks and Their Gas and Energy Storage Applications. *ACS Appl. Mater. Interfaces* **2019,** *11*, 9343-9354.
35. Wang, D.-G.; Li, N.; Hu, Y.; Wan, S.; Song, M.; Yu, G.; Jin, Y.; Wei, W.; Han, K.; Kuang, G.-C.; Zhang, W., Highly Fluoro-Substituted Covalent Organic Framework and Its Application in Lithium–Sulfur Batteries. *ACS Appl. Mater. Interfaces* **2018,** *10*, 42233-42240.
36. Jiang, Q.; Li, Y.; Zhao, X.; Xiong, P.; Yu, X.; Xu, Y.; Chen, L., Inverse-vulcanization of vinyl functionalized covalent organic frameworks as efficient cathode materials for Li–S batteries. *J. Mater. Chem. A* **2018,** *6*, 17977-17981.
37. Zhang, T.; Gao, C.; Huang, W.; Chen, Y.; Wang, Y.; Wang, J., Covalent organic framework as a novel electrochemical platform for highly sensitive and stable detection of lead. *Talanta* **2018,** *188*, 578-583.
38. Sun, X.; Wang, N.; Xie, Y.; Chu, H.; Wang, Y.; Wang, Y., In-situ anchoring bimetallic nanoparticles on covalent organic framework as an ultrasensitive electrochemical sensor for levodopa detection. *Talanta* **2021,** *225*, 122072.
39. Colin-Molina, A.; Pérez-Estrada, S.; Roa, A. E.; Villagrana-Garcia, A.; Hernández-Ortega, S.; Rodríguez, M.; Brown, S. E.; Rodríguez-Molina, B., Isotropic rotation in

amphidynamic crystals of stacked carbazole-based rotors featuring halogen-bonded stators. *Chem. Commun.* **2016,** *52*, 12833-12836.

40. Auras, F.; Ascherl, L.; Hakimioun, A. H.; Margraf, J. T.; Hanusch, F. C.; Reuter, S.; Bessinger, D.; Döblinger, M.; Hettstedt, C.; Karaghiosoff, K.; Herbert, S.; Knochel, P.; Clark, T.; Bein, T., Synchronized Offset Stacking: A Concept for Growing Large-Domain and Highly Crystalline 2D Covalent Organic Frameworks. *J. Am. Chem. Soc.* **2016,** *138*, 16703-16710.
41. Stalder, R.; Mei, J.; Reynolds, J. R., Isoindigo-Based Donor−Acceptor Conjugated Polymers. *Macromol.* **2010,** *43*, 8348-8352.
42. Ho, C.-C.; Chen, C.-A.; Chang, C.-Y.; Darling, S. B.; Su, W.-F., Isoindigo-based copolymers for polymer solar cells with efficiency over 7%. *J. Mater. Chem. A* **2014,** *2*, 8026-8032.
43. Liu, J.; Li, M.; Yu, J., High-Performance Electrochromic Covalent Hybrid Framework Membranes via a Facile One-Pot Synthesis. *ACS Appl. Mater. Interfaces* **2022,** *14*, 2051-2057.
44. Wang, B.; Huang, Y.; Han, Y.; Zhang, W.; Zhou, C.; Jiang, Q.; Chen, F.; Wu, X.; Li, R.; Lyu, P.; Zhao, S.; Wang, F.; Zhang, R., A Facile Strategy To Construct Au@VxO2x+1 Nanoflowers as a Multicolor Electrochromic Material for Adaptive Camouflage. *Nano Lett.* **2022,** *22*, 3713-3720.
45. Zhang, W.; Li, H.; Hopmann, E.; Elezzabi, A. Y., Nanostructured inorganic electrochromic materials for light applications. *Nanophotonics* **2021,** *10*, 825-850.
46. Li, H.; Zhang, W.; Elezzabi, A. Y., Transparent Zinc-Mesh Electrodes for Solar-Charging Electrochromic Windows. *Adv. Mater.* **2020,** *32*, 2003574.
47. Düren, T.; Millange, F.; Férey, G.; Walton, K. S.; Snurr, R. Q., Calculating Geometric Surface Areas as a Characterization Tool for Metal-Organic Frameworks. *J. Phys. Chem. C* **2007,** *111*, 15350-15356.
48. Li, M.; Ma, J.; Pan, B.; Wang, J., Cage-Based Covalent Organic Framework for the Effective and Efficient Removal of Malachite Green from Wastewater. *ACS Appl. Mater. Interfaces* **2022,** *14*, 57180-57188.
49. Krause, S.; Evans, J. D.; Bon, V.; Senkovska, I.; Ehrling, S.; Stoeck, U.; Yot, P. G.; Iacomi, P.; Llewellyn, P.; Maurin, G.; Coudert, F.-X.; Kaskel, S., Adsorption Contraction

4. Electrically conductive carbazole and thienoisoindigo-based COFs showing fast and stable electrochromism

Mechanics: Understanding Breathing Energetics in Isoreticular Metal–Organic Frameworks. *J. Phys. Chem. C* **2018,** *122*, 19171-19179.

5. Carbazole-based Covalent Organic Frameworks for Water and Dye Adsorption Applications

Katharina Muggli[1], Christoph Kremser[1], and Thomas Bein[1]*

[1]Department of Chemistry and Center for NanoScience (CeNS), University of Munich (LMU), Butenandtstraße 5-13, 81377 Munich, Germany
*Email: bein@lmu.de

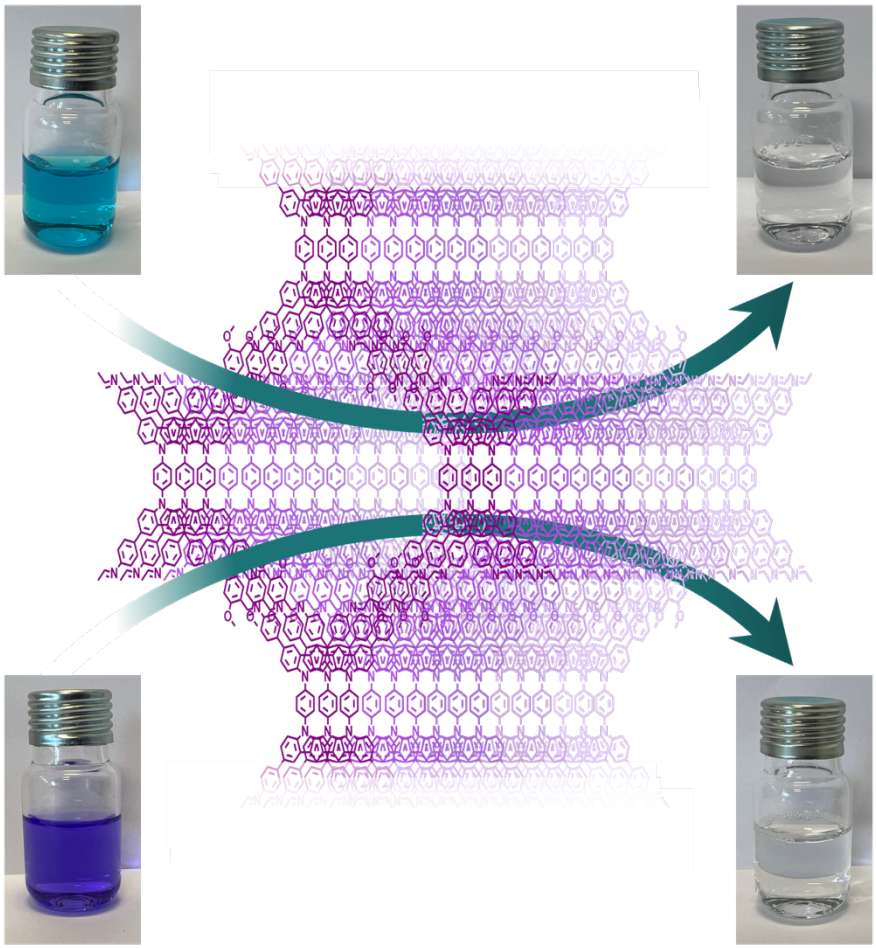

5.1 Abstract

The generation of new materials for targeted adsorption is an important challenge. Covalent organic frameworks (COFs) are a modern materials class that can be easily functionalized and modified. To show the applicational versatility of carbazole-based COFs, we have developed two new rectangular COFs based on a biscarbazole building block: Cz-1P COF and Cz-DM1P COF. Both materials exhibit a high surface area and a permanent porosity of the predesigned structure with an adjusted pore size, which facilitates a successful adsorption process. The conjugated structure of the nearly co-planar carbazole moieties is furthermore beneficial for the adsorption of conjugated triphenylmethane dye molecules via π-π-interactions, irrespective of the pH conditions. Additionally incorporating methoxy groups into the porous structure of the Cz-DM1P COF improves the wetting properties, yielding a hydrophobic material in contrast to the superhydrophobic Cz-1P COF, which is confirmed by a greater water uptake capacity of the Cz-DM1P COF. To examine their dye adsorption behavior, both materials were tested for the adsorption of the two triphenylmethane dyes, crystal violet (CV) and malachite green (MG), from aqueous solutions. The more hydrophilic Cz-DM1P COF exhibits an overall superior uptake capacity for both dyes than the superhydrophobic Cz-1P COF, due to the incorporation of methoxy groups as additional active sites for dipole-ion interactions and hydrogen bonding between the adsorbent and the adsorbate, stressing the importance and options offered by COF pore engineering. Both materials exhibit dye adsorption efficiencies of up to 100% for lower concentration samples, with the Cz-DM1P COF showing a superior efficiency at higher initial dye concentrations. Cycling experiments with only small adsorption performance losses indicate the good reusability of the materials. The evaluation of the adsorption kinetics shows a pseudo-second order uptake behavior of the adsorption process.

5.2 Introduction

Increasing global population and industrial activity in various fields such as textile, printing, leather, plastics or rubber have led to an ever-growing water demand as well as to serious environmental damage by industrial effluents. The pollution of water is amongst the major issues related to environmental damage, causing severe risks for nature and human health.[1]

Here, oily pollutants and organic dyes represent a great part of water pollution, with triphenylmethane dyes being one of the largest dye classes used in industrial processes.[2] These dyes are highly toxic and in parts carcinogenic, highly water soluble and therefore represent a serious threat to aquatic life.[3, 4] Dyes released into natural environments can absorb sunlight and impede photosynthesis, without significantly degrading by exposure to sunlight.[5] As a result, effective removal methods for these organic dyes are of great importance, and various methods have been investigated for dye-contaminated wastewater treatment: photodegradation,[6, 7] electrochemical degradation,[8, 9] membrane filtration,[10, 11] separation and adsorption,[12, 13] as well as biological approaches.[14]

Here, adsorption represents a simple and cost-effective method for wastewater treatment. Advantages of this technique include good reproducibility, high efficiency, no secondary pollution, and a large choice of possible adsorbents[5] such as zeolites,[15, 16] activated carbon,[17] carbon nanotubes,[18, 19] porous organic polymers,[20, 21] or metal-organic frameworks.[22, 23] With the adsorption process mainly relying on electrostatic or π-π-interactions between adsorbent and adsorbate, a large and accessible surface area is an important prerequisite for an effective adsorbent.

Covalent organic frameworks (COFs) have gained increasing interest for various fields of application over the past years, due to their fully organic nature, their high crystallinity paired with high porosity and therefore large surface area.[24, 25] Furthermore, their modular composition allows for a virtually unlimited number of possible geometries and structures, and enables tailor-made design that specifically targets the desired application. The possibility to modify COF building blocks and COF pore walls by pre- and post-synthetic pore engineering represents a key element for the successful usage of these materials for optoelectronic,[26, 27] catalytic[28, 29] and sensing[30, 31] applications as well as adsorption[32, 33] processes.

Given the good water uptake capacity of the carbazole-based DUT-175 COF,[34] we aimed at the generation of carbazole-based COFs for selective organic dye adsorption. In order to be independent from pH conditions for good adsorption performances, which is a major factor for the dominating electrostatic interactions between adsorbing COFs and ionic triphenylmethane dye molecules, we targeted the design of the framework in such way that the π-π-interactions between adsorbent and adsorbate are promoted. We therefore reduced the COF pore size to enable enhanced guest molecule-pore wall interactions, facilitating the formation of relatively weak π-π-interactions while maintaining the high stability, porosity,

and conjugation of the carbazole-based COF system. This was achieved by taking advantage of the modular building principle and incorporating a smaller biscarbazole building block,[35] which contains a linking phenyl ring between the two carbazole moieties, for the formation of two novel COFs with highly similar geometries. The large surface area and the permanent porosity combined with the highly conjugated carbazole-based building blocks allow for an efficient dye adsorption at small concentration levels of the two triphenylmethane-based dyes, crystal violet (CV) and malachite green (MG). Additional slight pore wall modification based on the incorporation of dimethoxy groups into the porous framework of one of the COFs alters the material's wetting properties by adding additional active sites for adsorbent-adsorbate interactions,[36, 37] enabling an improved adsorption behavior and emphasizing the significance of appropriate pore design and tunability as well as the multitude of possibilities for targeted application offered by this intriguing materials class.

5.3 Results and Discussion

COF synthesis

For the synthesis of the two new imine-linked covalent organic frameworks, we chose to use the previously described tetradentate biscarbazole-based 4,4',4'',4'''-(1,4-phenylenebis(9*H*-carbazole-9,3,6-triyl)) tetra-aniline ($Cz(NH_2)_4$) building block as the node, condensing it under solvothermal conditions with the established linear terephthalaldehyde ($1P(CHO)_2$), and 2,5-dimethoxy terephthalaldehyde ($DM1P(CHO)_2$) building units, respectively, forming the Cz-1P COF and the Cz-DM1P COF (Figure 5.1). For experimental details see Methods section.

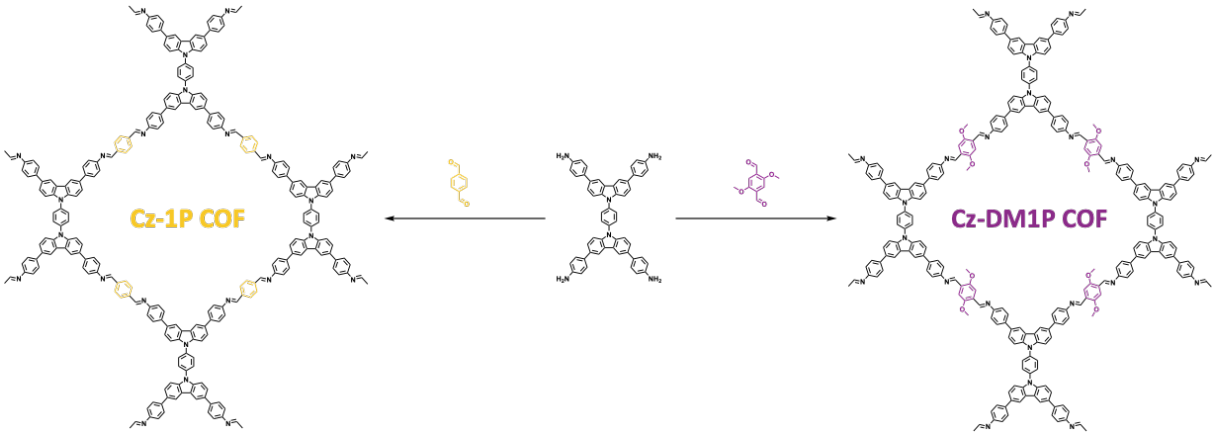

Figure 5.1. Synthesis of the new Cz-1P and Cz-DM1P COFs. The co-condensation of the rectangular $Cz(NH_2)_4$ node with the two linear $1P(CHO)_2$ and $DM1P(CHO)_2$ building blocks, respectively, yields two two-dimensional and imine-linked frameworks with rectangular pore structures.

The biscarbazole-based building block was chosen as it has been shown to form highly crystalline covalent organic frameworks. For this study the structural similarity of the investigated COF materials is vital for being able to evaluate the impact of pore surface engineering, so linear building blocks that only differ in their side chains were used. Here, in case of the Cz-DM1P COF, methoxy side chains were incorporated into the porous network, whilst the Cz-1P COF does not feature any additional side chains. The aim of this slight structural modification is the alteration and investigation of the materials' wetting properties by adding additional active sites for interactions between guest molecules and the COF pore wall, which is discussed below.

Structural and morphological investigations

Both materials were structurally characterized via powder X-ray diffraction (PXRD), revealing high crystallinity of the two-dimensional Cz-1P and Cz-DM1P COFs (Figure 5.2 a, c).
The experimentally obtained PXRD patterns are shown by the black dots, confirming the high crystallinity of both structures. The Cz-1P COF with a rectangular geometry was structurally simulated and Pawley-refined based on the monoclinic space group C*2/m*, and the also rectangular Cz-DM1P COF based on the monoclinic space group P*2/m*, showing the slip-stacked arrangement of the materials. The resulting refined PXRD patterns (red lines) represent a very good fit for the experimentally obtained patterns, with the minor differences, as shown in the difference plots (blue lines). The refined unit cell parameters are a = 4.52 nm,

b = 4.97 nm, *c* = 0.35 nm, and *ß* = 76° for the Cz-1P COF, and *a* = 4.54 nm, *b* = 4.69 nm, *c* = 0.35 nm, and *ß* = 72° for the Cz-DM1P COF.

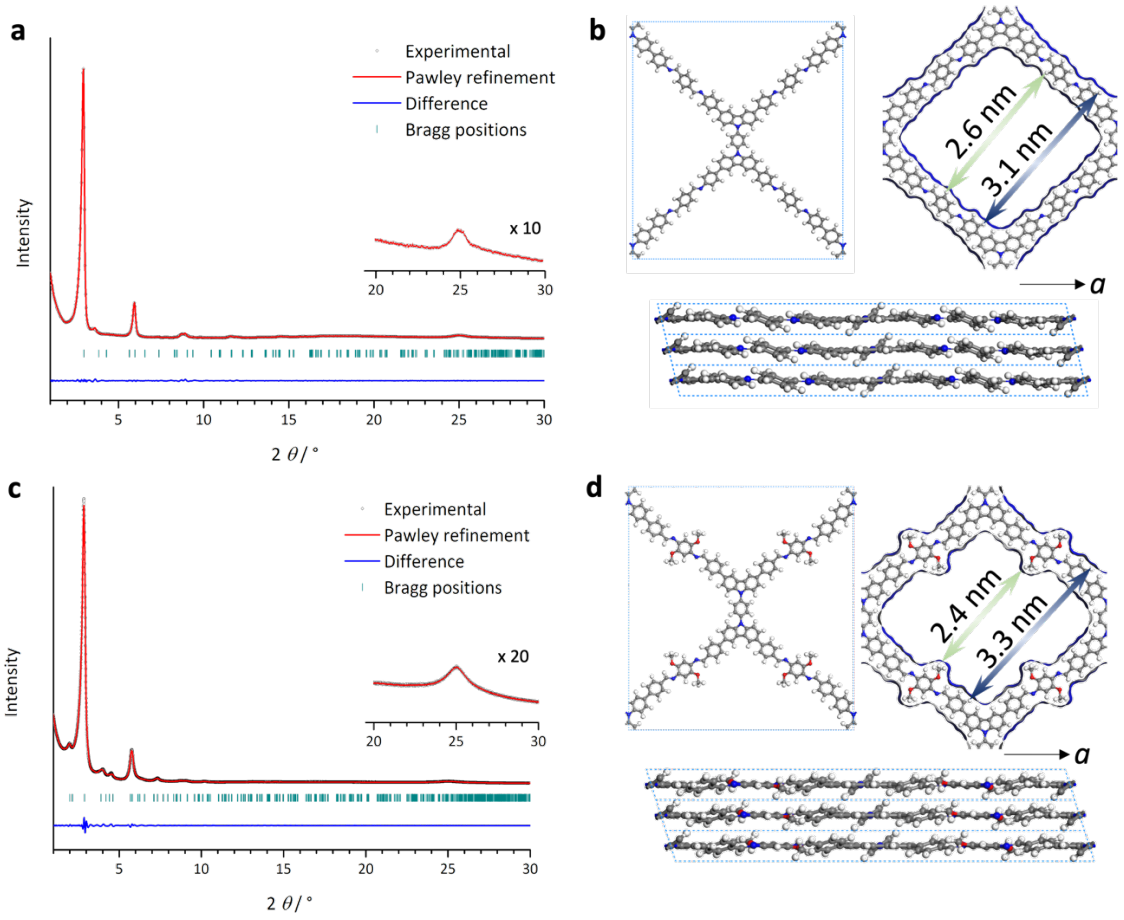

Figure 5.2. Structural analysis of the Cz-1P and the Cz-DM1P COFs. **(a)** Experimental PXRD pattern of the Cz-1P COF powder (black dots). Pawley refinement of the simulated structure model (red line) based on the monoclinic space group C*2/m*, providing a good fit for the experimental data with only minor differences (blue line). R_{wp} = 2.96% and R_p = 1.65%. The corresponding Bragg positions are indicated by green ticks. Inset: magnification of the 2θ > 20° region. **(b)** View onto the crystallographic *a*-*b* plane of the Pawley-refined Cz-1P COF structure model. The COF exhibits a rectangular topology with slip-stacked layers and high porosity with a calculated Connolly surface area of 2488 $m^2 g^{-1}$ and a pore volume of 1.65 $cm^3 g^{-1}$. **(c)** Experimental PXRD pattern of the Cz-DM1P COF powder (black dots). Pawley refinement of the structure model (red line) based on the monoclinic space group *P*2/m, providing a good fit to the experimental data with only minor differences (blue line). R_{wp} = 2.50% and R_p = 1.60%. The corresponding Bragg positions are indicated by green ticks. Inset: magnification of the 2θ > 20° region. **(d)** View onto the crystallographic *a*-*b* plane of the Pawley-refined Cz-DM1P COF structure model. The COF exhibits a rectangular topology with slip-stacked layers and high porosity with a calculated Connolly surface area of 2275 $m^2 g^{-1}$ and a pore volume of 1.27 $cm^3 g^{-1}$.

Nitrogen sorption analyses at 77 K of the materials (Figure 5.3 a, b) confirm the high porosity of the COFs, with a type IVb isotherm, which is typical for small mesopores, in case of the Cz-1P COF, and a type Ib isotherm, common for larger micropores and small mesopores, in case

of the Cz-DM1P COF. Despite extensive pore extraction with CO_2, a vertical offset between the adsorption and desorption branches remained, which is typical for some micro- and mesoporous materials and may be due to swelling of non-rigid pores or chemical interactions.[38]

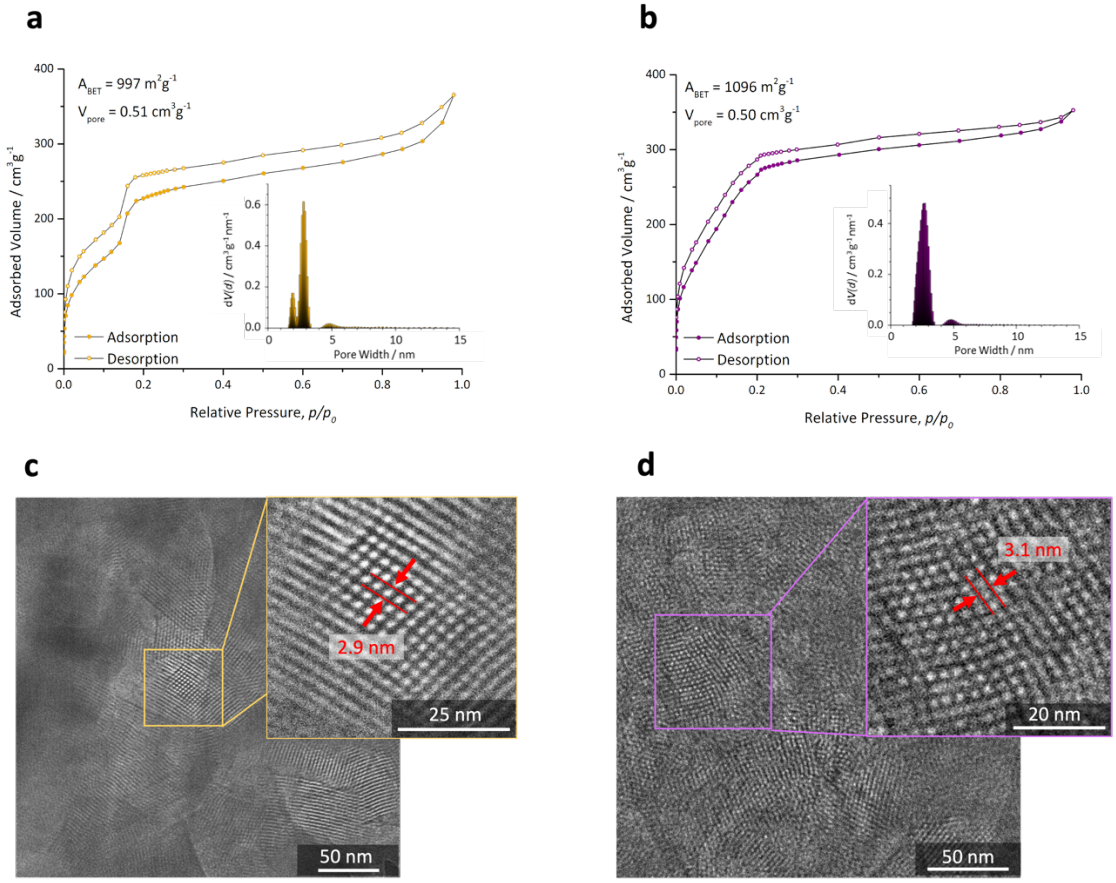

Figure 5.3. (a) Nitrogen sorption analysis of the Cz-1P COF bulk material at 77 K shows a type IVb isotherm. Inset: Pore size distribution (PSD) of the Cz-1P COF. The PSD is derived from a fit of the isotherm based on a QSDFT equilibrium model for cylindrical pores, peaking at 2.7 mm, which is in very good agreement with the wall-to-wall distance of the refined COF structure. **(b)** Nitrogen sorption analysis of the Cz-1P COF bulk material at 77 K shows a type Ib isotherm. Inset: Pore size distribution (PSD) of the Cz-DM1P COF. The unimodal PSD is derived from a fit of the isotherm based on a QSDFT equilibrium model for cylindrical pores. The peak is found at 2.5 nm, which is in very good agreement with the wall-to-wall distances of the refined COF structure model. **(c)** Transmission electron microscopy (TEM) image of the Cz-1P COF powder with the viewing direction along the crystallographic *c*-axis onto the *a*-*b* plane, showing a highly crystalline domain with a rectangular pore structure and a periodicity of 2.9 nm. **(d)** TEM image of the Cz-DM1P COF powder with the viewing direction along the crystallographic *c*-axis onto the *a*-*b* plane, showing a highly crystalline domain with a rectangular pore structure and a periodicity of 3.1 nm.

The respective Brunauer-Emmett-Teller (BET) surface areas were determined to be 997 $m^2 g^{-1}$ for the Cz-1P COF and 1096 $m^2 g^{-1}$ for the Cz-DM1P COF, with the corresponding total pore

volumes amounting to 0.51 $cm^3\ g^{-1}$ and 0.50 $cm^3\ g^{-1}$. Despite extensive extraction, building block residues and/or oligomeric fragments trapped in the pores of the COF structure may lead to deviations from the theoretically calculated Connolly surface areas and total pore volumes of 2488 $m^2\ g^{-1}$ and 1.65 $cm^3\ g^{-1}$ (Cz-1P COF), and 2275 $m^2\ g^{-1}$ and 1.27 $cm^3\ g^{-1}$ (Cz-DM1P COF).

Pore size distributions (PSD) were calculated based on a quenched solid density functional theory (QSDFT) equilibrium model for cylindrical pores, showing pore size distribution maxima at 2.7 nm for the Cz-1P COF and 2.5 nm for the Cz-DM1P COF, respectively. These PSD peak values are in very good agreement with the wall-to-wall distances of the simulated COF structures (Figure 5.2 b, d).

High-resolution transmission electron microscopy (TEM) images of the polycrystalline COF powders show domains of high crystallinity and confirm the rectangular geometries of both COFs (Figure 5.3 c, d). The measured periodicities are 2.9 nm for the Cz-1P COF, and 3.1 nm in case of the Cz-DM1P COF and are thus in very good agreement with the respective periodicities of the refined structure models (Cz-1P COF: 3.1 nm, Cz-DM1P COF: 3.3 nm).

Spectroscopic characterization

In addition to the structural analysis, both COFs were spectroscopically characterized with UV-vis, photoluminescence and Fourier-transform infrared spectroscopy.

The bulk powder of the Cz-1P COF has a yellow-orange and the Cz-DM1P COF a brownish color, respectively. In the UV-vis spectra, the COFs exhibit broad absorptions in the visible spectrum with the major absorption onset of the Cz-1P COF being 525 nm and that of the Cz-DM1P COF being 534 nm, in addition to an absorption tail reaching into the near infrared for Cz-DM1P COF (Figure S5.3 a, c). Maxima in the UV-vis absorption are found at 394 nm for the Cz-1P COF and at 412 nm for the Cz-DM1P COF. The comparison of the COF absorption bands to the pure $1P(CHO)_2$ and $DM1P(CHO)_2$ building blocks shows a redshift of 132 nm for the Cz-1P COF and 64 nm for the Cz-DM1P COF (FWHM), illustrating the electronic integration of the precursors and the expansion of the conjugated π-systems. Using the powder UV-vis data, Tauc plots for both materials were calculated assuming a direct transition, yielding band gaps of 2.60 eV for the Cz-1P COF and 2.59 eV for the Cz-DM1P COF (Figure S5.3 b, d).

In addition, photoluminescence (PL) measurements were conducted, with both spectra exhibiting a unimodal shape and the respective emissions showing maxima at 580 nm (Cz-1P COF) and 710 nm (Cz-DM1P COF) (Figure S5.4). Considering the UV-vis data, Stokes shifts of 182 nm for the Cz-1P COF and 294 nm for the Cz-DM1P COF were calculated.

Finally, Fourier-transform infrared (FTIR) spectra of the COFs and the precursors were recorded (Figure S5.5). Here, the successful formation of the COFs was confirmed by the appearance of the C=N stretching vibration of the imine linkages and the attenuation of the C=O vibration of the linear aldehydes $1P(CHO)_2$ and $DM1P(CHO)_2$, and the N-H vibrations of the $Cz(NH_2)_4$ building block.

Wetting and water adsorption properties

To gain deeper understanding of the wetting properties of the two COFs, water contact angle (WCA) measurements were performed. For this, the respective COF powder was finely ground in a mortar, mixed with additional 15 mass% of polyvinylidene fluoride as the binder dispersed in *N*-methyl-2-pyrrolidone, drop-casted onto a glass substrate and dried on a hotplate at 50 °C for 10 minutes. The use of a binder was necessary to enable to generation of COF films with a very good and homogeneous coverage of the glass substrates. Using these films, water contact angles were measured (Figure 5.4 a, c).

The Cz-1P COF showed a WCA of 168°, confirming its superhydrophobicity.[39] For the Cz-DM1P COF, a WCA of 142° was found, which represents a hydrophobic surface. Due to the incorporation of the methoxy side chains in the Cz-DM1P COF structure, the material has a more hydrophilic nature than the Cz-1P COF, demonstrating the impact of pore surface modifications. The two photographic images illustrate the water droplet on the respective COF surface. For reference and to demonstrate that the binder does not bias the WCA measurements, the WCA of the pure binder on a glass substrate was measured, yielding an angle of 89° (Figure S5.6). With materials with WCA > 90° being referred to as hydrophobic, and WCA < 90° as hydrophilic, the polyvinylidene fluoride binder does not qualify for either of these properties and hence is expected to not significantly impact the COF WCA measurements. Yet, a minor influence of the binder cannot fully be precluded, so that we focus on the relative comparisons of the WCA values. Furthermore, the WCA of the bare glass

substrate was determined to be 43° and therefore is not expected to strongly influence the COFs' (super)hydrophobic nature.

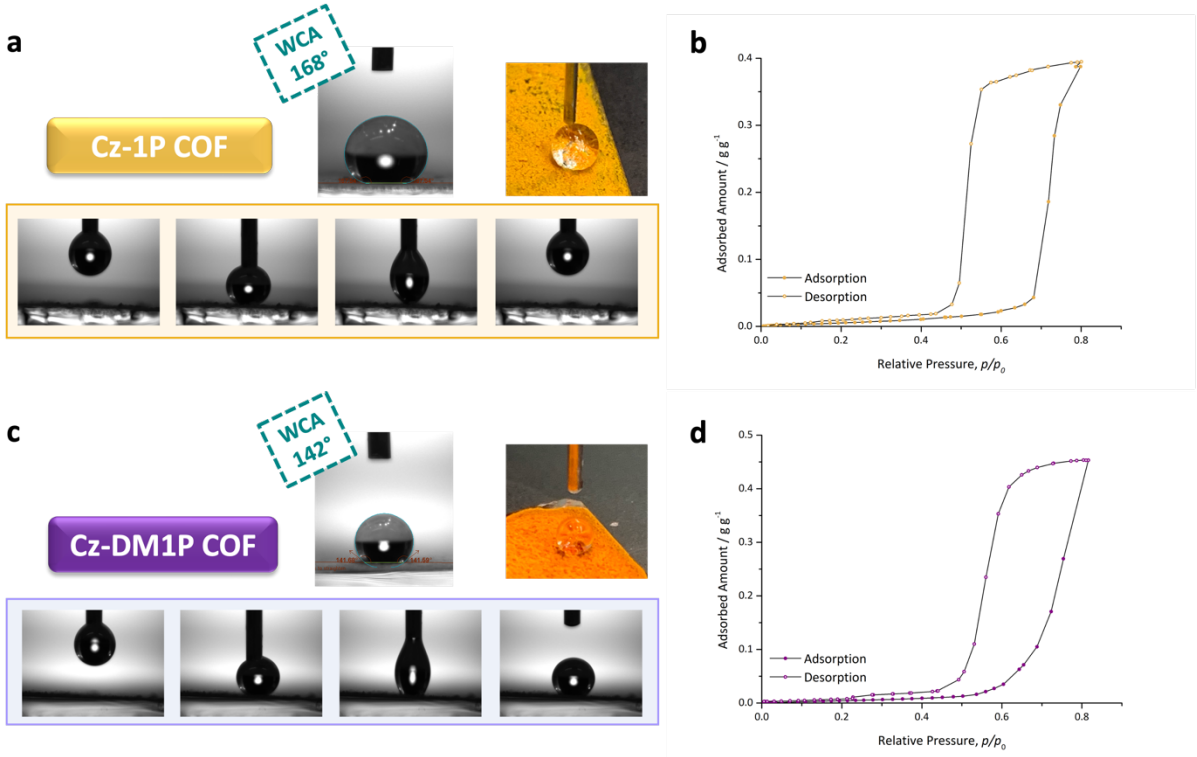

Figure 5.4. Analysis of the wetting properties of the Cz-1P and the Cz-DM1P COFs. **(a)** Water contact angle (WCA) measurement of the Cz-1P COF, confirming the superhydrophobicity of the material with an angle of 168°. The photographic image illustrates the water drop on the superhydrophobic COF surface. Orange box: Adhesion experiment on the Cz-1P COF surface, demonstrating the material's superhydrophobicity, with the water droplet not sticking to the COF surface when the syringe tip is withdrawn. **(b)** Water vapor sorption analysis of the Cz-1P COF, showing a maximum water vapor uptake of 0.40 g g^{-1} **(c)** Water contact angle (WCA) measurement of the Cz-DM1P COF, showing the hydrophobicity of the material with a WCA of 142°. The photographic image illustrates the water drop on the hydrophobic COF surface. Violet box: Adhesion experiment on the Cz-DM1P COF surface, demonstrating the material's increased hydrophilicity in comparison to the Cz-1P COF, with the water droplet sticking to the COF surface when the syringe tip is withdrawn. **(d)** Water vapor sorption analysis of the Cz-DM1P COF, yielding a maximum water vapor uptake of 0.46 g g^{-1}.

To further illustrate the wetting properties of the COFs, adhesion experiments were performed (Figure 5.4 a (orange box), c (violet box)). Here, the syringe with a water droplet at its tip was lowered to the COF films until the water droplet touches the film surface and then is slightly pushed further down into a squeezed state. When releasing the pressure and withdrawing the syringe, the water drop on the Cz-1P COF film exhibits a stretched state and is then fully withdrawn from the COF surface, illustrating the superhydrophobic nature of the material. In contrast, when withdrawing the syringe with the water droplet from the Cz-DM1P

COF film, the water droplet sticks to the film surface after the stretched state, showing the more hydrophilic properties of the Cz-DM1P COF.

In addition, water vapor sorption analyses were conducted with both COF powders to further investigate their wetting properties. Before the analyses, the COFs were extensively extracted with CO_2 and heated to 120 °C overnight. At 20 °C, the Cz-1P COF isotherm (Figure 5.3 b) exhibits an S-shape with an induction pressure zone (p/p_0) between 0 and 0.66, which then changes to a sudden steep water uptake between relative pressure values of 0.68 and 0.80. For the Cz-DM1P COF (Figure 5.3 d), the respective induction pressure zone was determined to be > 0.58, followed by a less steep increase in the water uptake between relative pressure values of 0.60 and 0.82. Both isotherms exhibit a strong hysteresis loop, with the desorption process starting at a relative pressure of 0.55 for the Cz-1P COF and at 0.62 in case of the Cz-DM1P COF. The delayed adsorption is attributed to strong repulsive interactions between the hydrophobic COF pores and the water molecules. Hysteresis loops in water vapor adsorption isotherms have already been described for mesoporous COFs.[40] A maximum water vapor uptake of 0.40 g g^{-1} was measured for the Cz-1P COF, whilst for the Cz-DM1P COF, a larger maximum water vapor uptake of 0.46 g g^{-1} was determined, and is attributed to the more hydrophilic nature based on the methoxy side chains. Given the strategy of reducing the pore size for the purpose of enhanced interaction between organic dye molecules and COF under neutral conditions, i.e. without the contribution of strong electrostatic interactions, both uptakes are considerably lower than that of the carbazole-based DUT-175 COF.[34]

Considering the water vapor sorption process, Jiang and coworkers state that the polarized, and therefore hydrophilic, C=N linkages of the imine bond act as nucleation sites for water clusters in the pore channels. By increasing the pressure, a growth of the water clusters starts and eventually leads to an instant pore filling via capillary condensation.[40] In addition, the wetting properties strongly determine the required uptake pressures with more hydrophobic materials requiring higher uptake pressures, but being able to release the captured water at lower desorption temperatures.

Furthermore, the methoxy side chains may act as steric barriers, hindering the adsorption process and leading to a smaller working capacity.[33] Working capacities were calculated by firstly determining the relative pressure at half of the respective maximum adsorption value. Secondly, a range of + / – 0.05 p/p_0 from these relative pressure values was chosen and the

respective difference of the adsorption capacity within the range was calculated, representing the respective working capacities. For the Cz-1P COF a working capacity of 0.32 g g^{-1} was found, whilst that of the Cz-DM1P COF was calculated to be 0.27 g g^{-1}, which represents an approximate decrease by 15%.

Dye adsorption

For the dye adsorption experiments, two triphenylmethane dyes, crystal violet (CV) and malachite green (MG), were used. These organic dyes, commonly used in industry, are toxic and hydrophobic compounds, which are, however, sufficiently water soluble for generating aqueous dye solutions. Approaches to adsorb organic dyes with ionic covalent organic frameworks have been studied.[5, 41-43] It was shown that one of the main promoters for dye adsorption are the electrostatic interaction between the charged adsorbent and adsorbate which can be influenced by the pH conditions.[5, 43, 44] However, it was found that the adsorption process is not solely based on the electrostatic forces between the charged COFs and dye molecules but rather is a synergy of various interaction mechanisms leading to an effective uptake of aromatic dye molecules. Thus, another determining driving factor for the effective adsorption lies in the π-π-interactions between the large π-conjugated COF structures and the benzene-containing dyes.[5, 41, 43, 45, 46]

For not being dependent on pH conditions during the dye adsorption process and thus operating without surface charge of the respective COF material, we instead utilized the above-mentioned π-π-interactions, ion-dipole-interactions and hydrogen-bonding between COF and adsorbate and aimed to design a neutral framework structure with optimal characteristics for the effective adsorption of triphenylmethane dyes. Therefore, we used the biscarbazole building block with its nearly co-planar carbazole moieties that promote a high degree of conjugation, which is beneficial for a successful adsorption process at small concentration levels.

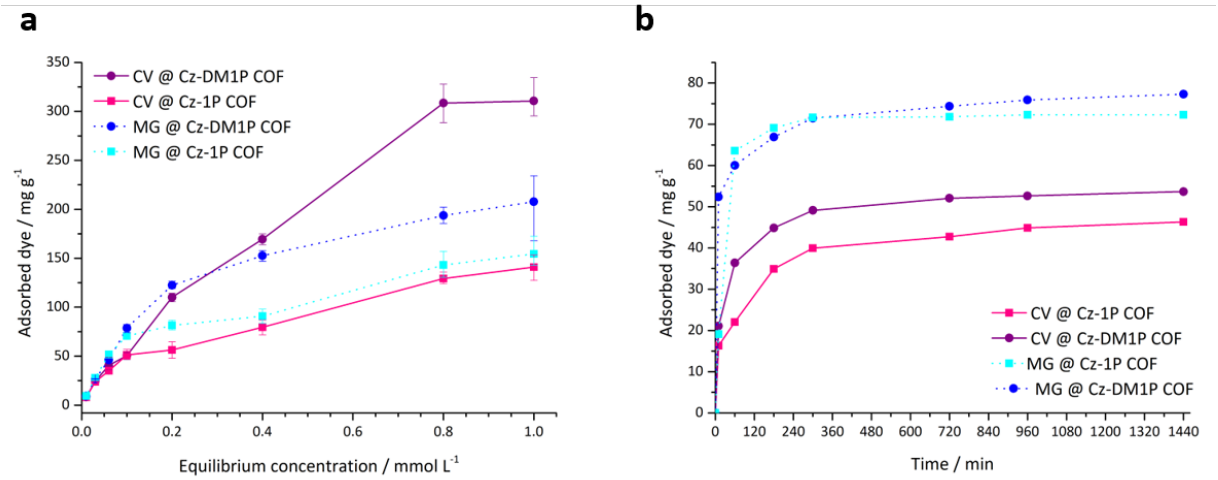

Figure 5.5. (a) Dye adsorption capacity of the Cz-1P COF (square symbols) and Cz-DM1P COF (round symbols) after a 24 hour treatment of crystal violet solutions (solid lines) and malachite green solutions (dashed lines) of different initial concentrations: 0.01 mmol L^{-1}, 0.03 mmol L^{-1}, 0.06 mmol L^{-1}, 0.1 mmol L^{-1}, 0.2 mmol L^{-1}, 0.4 mmol L^{-1}, 0.8 mmol L^{-1}, and 1.0 mmol L^{-1}, showing an overall better adsorption performance of the Cz-DM1P COF. **(b)** Time-dependent adsorption of the Cz-1P COF and Cz-DM1P COF for 0.1 mmol L^{-1} solutions of crystal violet and malachite green with respective exposure times of 10 min, 1 hour, 3 hours, 5 hours, 12 hours, 16 hours, and 24 hours.

Dye adsorption experiments were conducted with aqueous solutions with different initial concentrations: 0.01 mmol L^{-1}, 0.03 mmol L^{-1}, 0.06 mmol L^{-1}, 0.1 mmol L^{-1}, 0.2 mmol L^{-1}, 0.4 mmol L^{-1}, 0.8 mmol L^{-1}, and 1.0 mmol L^{-1}. The solutions were treated with Cz-1P COF or Cz-DM1P COF for 24 hours. After the treatment, the COF powder was filtered off and the filtrate was analyzed photometrically (Figure 5.5 a). For a more detailed description of the experimental setup, see Methods section.

The dye adsorption capacity of both COFs for crystal violet and malachite green solutions shows a saturation behavior with a generally steeper adsorption performance for lower concentrations and a reduced adsorption performance for higher concentration samples. An overall superior dye adsorption capacity was found for the Cz-DM1P COF in comparison to the Cz-1P COF. The Cz-DM1P COF showed a malachite green uptake of 208 mg g^{-1} for the 1.0 mmol L^{-1} sample after 24 hours – a 33% performance increase to the corresponding 155 mg g^{-1} uptake of the Cz-1P COF. An even larger performance increase of 125 % was found for the adsorption of crystal violet for the Cz-DM1P COF (treating the 1.0 mmol L^{-1} sample for 24 hours). A maximum uptake of 311 mg g^{-1} was found in comparison to 141 mg g^{-1} for the corresponding Cz-1P COF sample. We attribute the improved dye adsorption performance of the Cz-DM1P COF to two main factors: on the one hand, the altered wetting properties based

on the incorporation of polar methoxy side chains into the porous framework. On the other hand, additional ion-dipole-interactions and hydrogen-bonding between the methoxy side chains of the Cz-DM1P COF and the triphenylmethane dye molecules cause the enhanced adsorption behavior.[36] With crystal violet offering an additional dimethylamino-moiety in its structure in comparison to malachite green, the formation of further hydrogen bonds to the methoxy side chains of the Cz-DM1P COF is facilitated, leading to the superior adsorption performance. It is shown that by a minor adjustment of the COFs' pore design via building block modification, the adsorption performance can be strongly improved. Yet, in comparison to other approaches, such as the above-mentioned adsorption via electrostatic interactions, the biscarbazole-based COFs with weaker interactions exhibits lower adsorption capacities.

The adsorption efficiency, i.e. the percentage of dye that could be adsorbed in relation to the initial dye concentration, was calculated for all samples based on the dye adsorption capacity data (Table S5.3). All COFs exhibit very good efficiencies above 90% and even up to 100% for samples with lower initial concentrations (0.01 mmol L^{-1} and 0.03 mmol L^{-1}) and above 80% for 0.06 mmol L^{-1} initial concentration samples for both Cz-DM1P treated solutions and for the MG @ Cz-1P sample. For higher concentrations, the Cz-DM1P COF treated samples show an overall better adsorption efficiency compared to the Cz-1P COF samples, attributed to the above-mentioned pore modification.

The dye adsorption performance of the covalent organic frameworks was furthermore investigated for five consecutive cycles each. Here, 0.05 mmol L^{-1} solutions of crystal violet and malachite green were treated with the respective COF powder for 24 hours. After filtration, the COF powders were repeatedly washed with ethanol, dried, and used for the next cycle, whilst the filtrate was analyzed photometrically. Both, the Cz-1P COF and the Cz-DM1P COF, exhibit an excellent reusability with merely slight performance losses of 1 to 3 % (Figure S5.11), demonstrating the high stability of the COF powders.

In addition, the time-dependent adsorption was determined experimentally. To this end, 0.1 mmol L^{-1} dye solutions of malachite green and crystal violet were treated with Cz-1P COF or Cz-DM1P COF. Here, exposure times of 10 min, 1 hour, 3 hours, 5 hours, 12 hours, 16 hours, and 24 hours were investigated (Figure 5.5 b). As for the dye adsorption capacity

measurements, the COF powder was filtered off after the treatment and the filtrate was analyzed photometrically (see Methods section). After an initial steep adsorption onset in the first 60 minutes of exposure, all curves exhibit a flattened shape up to 5 hours of exposure time due to an increased pore filling, followed by an equilibrium state of the curve. In equilibrium, both samples treated with malachite green show a higher uptake capacity than those treated with crystal violet, confirming the findings of the dye adsorption capacity tests.

Adsorption kinetics

Investigating the adsorption kinetics, the time-dependent adsorption data were fitted with pseudo-first order and pseudo-second order models using the following equations:[41, 47]

1. Pseudo-first order equation:

$$\ln(q_e - q_t) = \ln(q_e) - k_1 t$$

   with k_1 being the pseudo-first order rate constant.

2. Pseudo-second order equation:

$$\frac{t}{q_t} = \frac{1}{k_2\, q_e^2} + \frac{1}{q_e}\, t$$

   with q_t being the uptake capacity at a given a time t, q_e the uptake capacity at equilibrium, and k_2 the pseudo-second order rate constant.

The respective fitting plots and results are shown in Figure S5.10. The linear fit for the pseudo-second order better matched the data with overall higher correlation coefficients R^2 (Table S5.1), indicating that the chemical surface adsorption process was the rate-limiting step, depending on interactions between adsorbate and adsorbent.[5, 41, 44] Here, the slope represents the rate constant k_2, which ranges between 0.01312 and 0.02219 g mg^{-1} min^{-1}. Compared to adsorption rates of other dye-adsorbing COFs, these adsorption rates are

obviously lower due to the absence of strong electrostatic interactions but rather deploying weaker interactions, such as π-π interactions (see Table S5.2).

5.4 Conclusion

Using the tetragonal biscarbazole node and the two linear building blocks terephthalaldehyde and 2,5-dimethoxy terephthalaldehyde, we have developed two novel and highly crystalline and porous covalent organic frameworks (COFs): Cz-1P and Cz-DM1P. The materials exhibit a large surface area and permanent porosity, which is beneficial for a successful adsorption behavior. Moreover, the nearly co-planar structure of the carbazole moieties promotes a high degree of conjugation and thus facilitates π-π-interactions between the adsorbent and the adsorbate, whilst being independent of pH conditions. Furthermore, we chose the carbazole-based building block to deliberately reduce the pore size of the COFs, also allowing for improved adsorbent-adsorbate interactions.

The two investigated COFs are structurally similar, with the Cz-DM1P COF incorporating methoxy moieties in its pore channels. Due to this incorporation, we could alter the wetting properties of the material, rendering it hydrophobic in contrast to the superhydrophobic Cz-1P COF, determined by water contact angle measurements. This was also confirmed by water vapor sorption analyses with a great water uptake capacity of the Cz-DM1P COF.

The dye adsorption capacity from aqueous solutions of the triphenylmethane dyes crystal violet and malachite green was investigated. The Cz-DM1P COF exhibited an overall superior adsorption capacity, attributed to its greater hydrophilicity based on the additional active sites for ion-dipole interactions as well as hydrogen bonds between the COF and the guest molecules. However, COFs using electrostatic interaction for the adsorption process, could generally achieve higher adsorption capacities, illustrating the need for further optimizations of the investigated materials. Here, the smaller pore size of the COFs may lead to an impeded water uptake and therefore a reduced dye adsorption performance. Finding the sweet spot between water uptake capacity and guest molecule-pore wall interaction therefore remains a challenge.

Nevertheless, the COFs exhibit very good adsorption efficiencies of above 90 and even up to 100 % for samples with initially lower concentrations. Here, an overall superior separation

performance for the Cz-DM1P COF for higher concentration samples was found, which is attributed to the COF's pore modification. Dye adsorption cycling experiments with merely slight performance losses after five consecutive adsorption cycles furthermore demonstrated the good reusability of the COF powders. The significance of adsorbate-adsorbent interactions and thus the pore surface for the adsorption process was additionally underlined by adsorption kinetics studies, showing a pseudo-second order behavior. Hence, pore engineering by incorporation of the polar and thus more hydrophilic dimethoxy moieties was shown to play a key role for achieving a superior adsorption performance. It is envisioned that further research regarding COF pore size and pore modifications will lead to a continuous improvement towards targeting specific pollutants in industrial wastewater.

5.5 Methods

The biscarbazole-based building block $Cz(NH_2)_4$ was synthesized according to the procedures described elsewhere.[35] The terephthalaldehyde $1P(CHO)_2$ and the 2,5-dimethoxy terephthalaldehyde $DM1P(CHO)_2$ building blocks are commercially available. All other reagents and solvents are also commercially available and were obtained in high-purity grades. Unless stated otherwise, solvents were degassed and saturated with argon before use. **COF bulk powder syntheses** were performed under argon atmosphere in PTFE-sealed glass reaction tubes (6 mL volume).

Cz-1P COF

$Cz(NH_2)_4$ (3.86 mg, 5.0 µmol, 1.0 eq.) and $1P(CHO)_2$ (1.34 mg, 10 µmol, 2.0 eq.) were filled into a 6 mL reaction tube. Mesitylene (167 µL), benzyl alcohol (83 µL), and 6 M aqueous acetic acid (25 µL) were added to the tube, which was then sealed and heated to 120 °C for 3 d. After cooling to room temperature, the precipitate was collected by filtration and subsequently extracted with supercritical CO_2 for 3 h to remove by-products, yielding the COF as a yellow-orange powder.

Elemental analysis (calculated, found for $C_{140}H_{92}N_{12}$): C (86.57, 86.21), H (4.77, 4.82), N (8.65, 8.61)

Cz-DM1P COF

$Cz(NH_2)_4$ (3.86 mg, 5.0 µmol, 1.0 eq.) and $DM1P(CHO)_2$ (1.94 mg, 10 µmol, 2.0 eq.) were filled into a 6 mL reaction tube. Mesitylene (167 µL), benzyl alcohol (83 µL), and 6 M aqueous acetic acid (25 µL) were added to the tube, which was then sealed and heated to 120 °C for 3 d. After cooling to room temperature, the precipitate was collected by filtration and subsequently extracted with supercritical CO_2 for 3 h to remove by-products, yielding the COF as a brown powder.

Elemental analysis (calculated, found for $C_{140}H_{108}N_{12}O_8$): C (81.45, 81.33), H (4.99, 5.04), N (7.70, 7.66)

Characterization methods

Powder X-ray diffraction (PXRD) patterns were measured on a Bruker D8 Advance diffractometer equipped with a Cu K_α source (0.1 mm divergence slit, knife edge air scatter screen) and a LynxEye detector. K_β radiation was attenuated with a 0.0125 mm Ni filter.

The **structure models of the COFs** were simulated using the Accelrys Materials Studio software package. The highest possible symmetry was applied for the COFs. The structure models were optimized using the Forcite module with the Universal force-field. **Structure refinements** were carried out with the Reflex module using the Pawley method. Pseudo-Voigt peak profiles were used, and peak asymmetry was corrected using the Finger-Cox-Jephcoat method. **Connolly surfaces** and accessible surfaces were generated using a N_2-sized probe (r = 0.184 nm) at a 0.025 nm grid interval.[48]

Nitrogen sorption analyses were conducted with a Quantachrome Autosorb 1 instrument at 77 K. The samples were first extracted with supercritical CO_2, and subsequently degassed at 120 °C under high vacuum for 5 h prior to the measurements. BET areas were calculated based on the pressure range $0.05 \leq p/p_0 \leq 0.2$. Pore size distributions were determined using the QSDFT equilibrium model with a carbon kernel for cylindrical pores.

Water sorption analyses were conducted with a Quantachrome Autosorb 1 instrument set to water vapor sorption mode at room temperature. The samples were first extracted with supercritical CO_2, and subsequently degassed at 120 °C under high vacuum for 24 h prior to the measurements.

Scanning electron microscopy (SEM) images were recorded with an FEI Helios NanoLab G3 UC microscope equipped with a Schottky field-emission electron source operated at 1 – 30 kV.

Transmission electron microscopy (TEM) images were recorded with an FEI Titan Themis microscope equipped with a field emission gun operated at 300 kV.

Fourier-transform infrared (FTIR) spectra were recorded on a Bruker Vertex 70 FTIR instrument using a liquid nitrogen-cooled MCT detector and a germanium ATR crystal.

UV-Vis-NIR spectra were measured with a Perkin-Elmer Lambda 1050 spectrometer equipped with a 150 mm InGaAs integrating sphere. **Diffuse reflectance spectra** were recorded with a

Harrick Praying Mantis accessory kit and were referenced to barium sulfate powder as the white standard.

Dye adsorption experiments were conducted using 1.5 mg COF for the treatment of 3 mL dye solution in a small glass vial. To minimize weighing errors, the COF powder was weighed using an analytical balance in an argon filled glove box with the circulation being switched off. The closed vials were left in a shaker for the respective treatment time. Directly after the treatment, the COF powder was filtered off using a Chromafil® PET-45/15 MS syringe filter and the filtrate was analyzed photometrically.

For the determination of the dye uptake, linear calibration curves of crystal violet and malachite green were measured (Figure S5.9). The respective concentration of the COF treated sample was determined using these calibration curves and the dye uptake was calculated as the difference of the initial concentration and the final filtrate concentration. In order to enable photometric analyses of high concentration samples, the samples were diluted by a certain factor before the measurement and the determined final concentration was multiplied by the same factor.

Dye adsorption cycling experiments of the respective COF were conducted by preparing 0.05 mmol L^{-1} dye solutions of crystal violet and malachite green. 6 mL of the respective solution were treated with 3 mg of either Cz-1P COF or Cz-DM1P COF for 24 hours. The filtrate was collected, and the COF powder was washed with EtOH (3 x 10 mL) and dried at 60°C before the consecutive cycle.

.

5.6 Supporting Information

Abbreviations

BET	Brunauer-Emmett-Teller
CV	crystal violet
eq.	equivalent(s)
FWHM	full width at half maximum
MG	malachite green
OD	optical density
PSD	pore size distribution
PTFE	poly(tetrafluoroethylene)
QSDFT	quenched solid density functional theory
rt	room temperature
SE	separation efficiency
UV	ultraviolet
Vis	visible
WCA	water contact angle

Photographic images of the COF powders

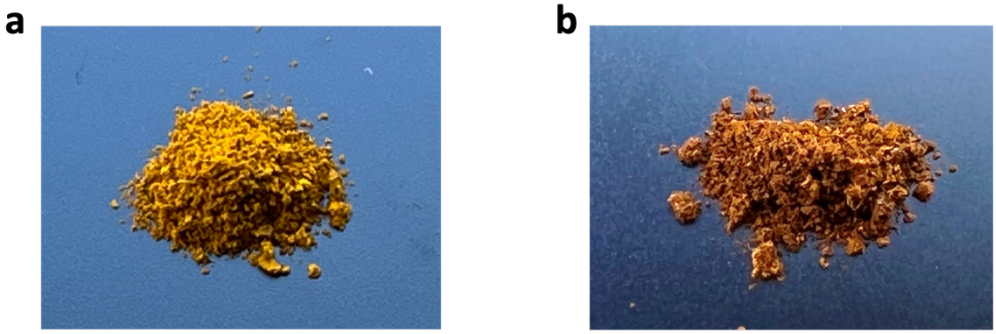

Figure S5.1. Photographic images of the **(a)** Cz-1P COF and **(b)** Cz-DM1P COF bulk powders, showing a yellow-orange color for the former and a brownish color for the latter.

Scanning electron microscopy (SEM)

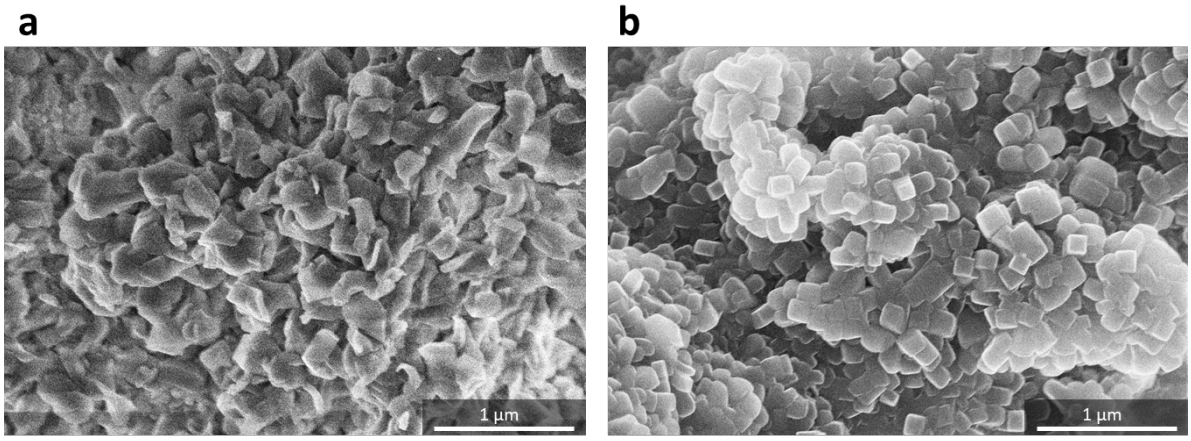

Figure S5.2. Scanning electron microscopy (SEM) images of **(a)** the Cz-1P COF and **(b)** the Cz-DM1P COF, exhibiting a platelet-like morphology in case of the former, and a cube-like morphology with edge lengths of about 120 to 150 nm in case of the latter.

UV-vis spectroscopy

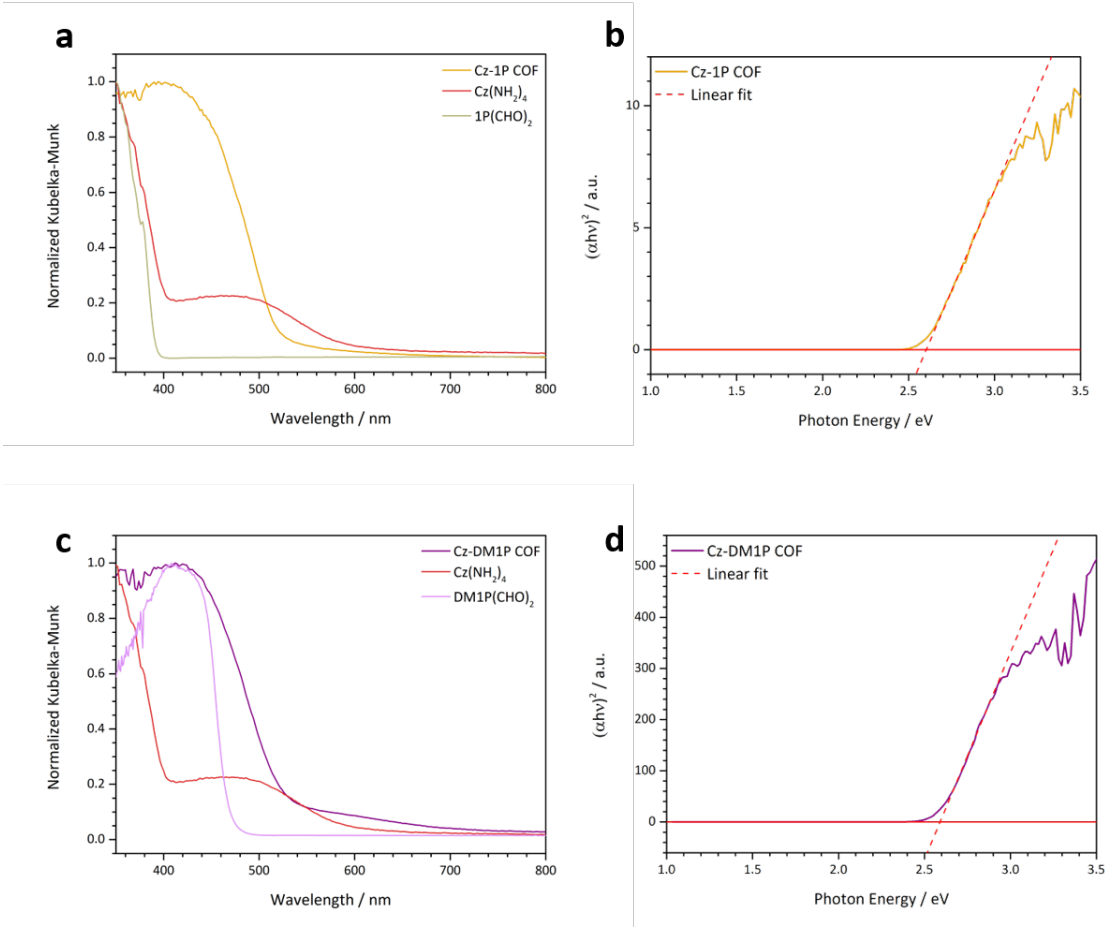

Figure S5.3. UV-vis absorption spectra of solid precursors $Cz(NH_2)_4$, $1P(CHO)_2$, and $DM1P(CHO)_2$ and of the corresponding COF powders. **(a)** Cz-1P COF, **(c)** Cz-DM1P COF. **(b)** and **(d)** display the respective Tauc plots of the COFs assuming a direct band gap of E_{gap} = 2.60 eV for the Cz-1P COF and E_{gap} = 2.59 eV for the Cz-DM1P COF.

Photoluminescence spectroscopy

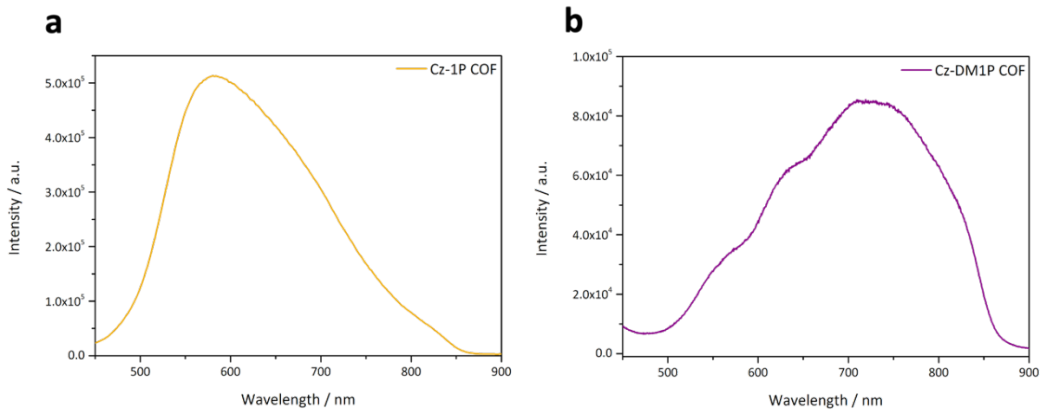

Figure S5.4. Photoluminescence spectra of the **(a)** Cz-1P COF powder and **(b)** Cz-DM1P COF powder, with their respective peaks at 580 nm and 710 nm. An excitation wavelength of 375 nm was used for the measurements.

Infrared spectroscopy

a

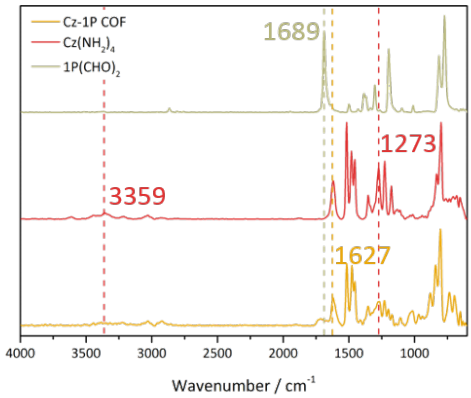

b

	Wavenumber / cm^{-1}	Assignment
$Cz(NH_2)_4$	1273	C-NH_2 stretching
	3359, 3440	N-H stretching
	1620	N-H bending
$1P(CHO)_2$	1689	C=O stretching
Cz-1P COF	1627	C=N stretching

c

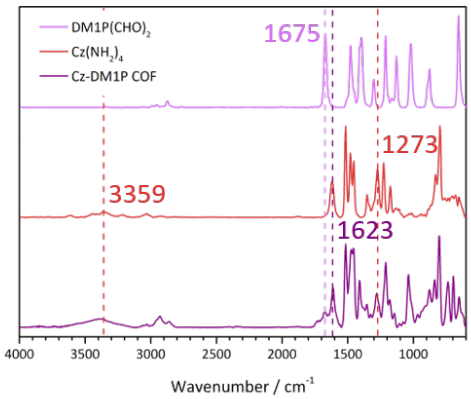

d

	Wavenumber / cm^{-1}	Assignment
$Cz(NH_2)_4$	1273	C-NH_2 stretching
	3359, 3440	N-H stretching
	1620	N-H bending
$DM1P(CHO)_2$	1675	C=O stretching
Cz-DM1P COF	1623	C=N stretching

Figure S5.5. Fourier-transform infrared spectra of the **(a)** Cz-1P COF and **(c)** Cz-DM1P COF. Important vibrational peaks are listed in the tables **(b)** and **(d)**, showing characteristic vibrations of the precursors and the COFs including C=N stretching vibrations of the COFs' imine linkages.

Water contact angle

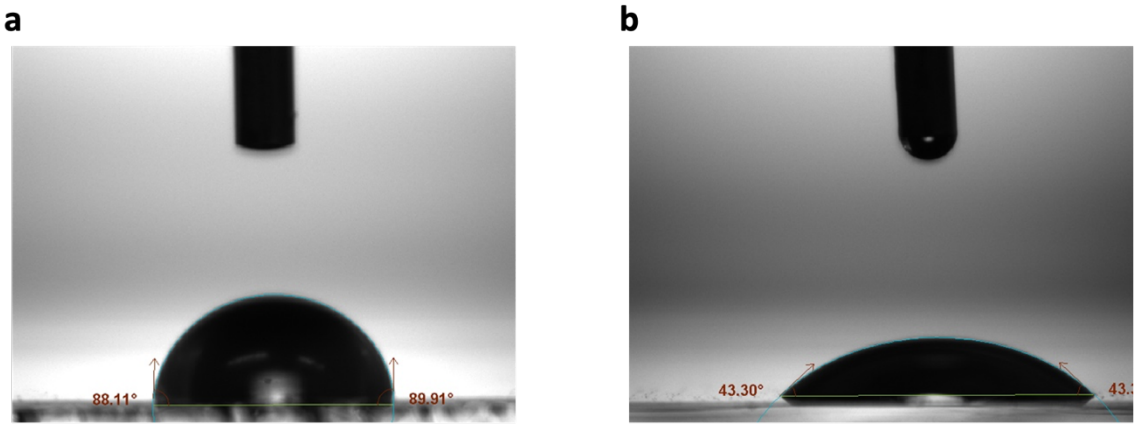

Figure S5.6. Water contact angle (WCA) measurement on the **(a)** pure polyvinylidene fluoride binder on a glass substrate with a WCA of 89°, and **(b)** bare glass substrate with a WCA of 43°. The glass substrate was cleaned in detergent solution (Hellmanex III, 0.5% *v*/*v*), water, acetone, and isopropanol, and activated with an O_2-plasma for 5 min directly before the measurement. The polyvinylidene fluoride binder was dispensed in *N*-methyl-2-pyrrolidone, drop-casted onto a glass substrate and dried on a hotplate at 50 °C for 10 minutes.

Dye adsorption photographic images

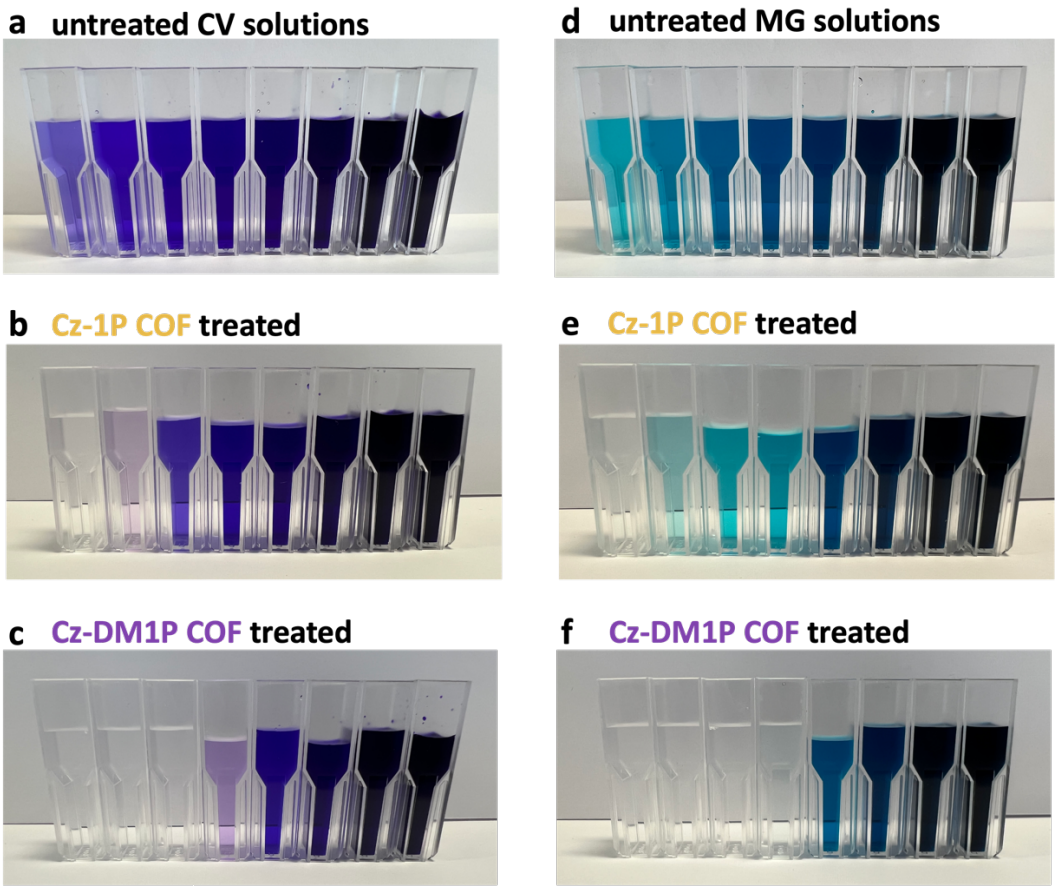

Figure S5.7. Photographic images of untreated dye solutions of **(a)** crystal violet and **(d)** malachite green, as well as the respective COF treated solutions of **(b)** & **(c)** crystal violet and **(e)** & **(f)** malachite green with different initial concentrations: 0.01 mmol L^{-1}, 0.03 mmol L^{-1}, 0.06 mmol L^{-1}, 0.1 mmol L^{-1}, 0.2 mmol L^{-1}, 0.4 mmol L^{-1}, 0.8 mmol L^{-1}, and 1.0 mmol L^{-1} from left to right. The series in **(b)** & **(e)** were treated with Cz-1P COF and those in **(c)** & **(f)** with Cz-DM1P COF for 24 hours at room temperature. Dye solutions treated with Cz-DM1P COF exhibit an overall stronger decoloration, and thus an enhanced dye adsorption capacity in comparison to those treated with Cz-1P COF. The plotted data are shown in Figure 5.5.

Stability after dye adsorption

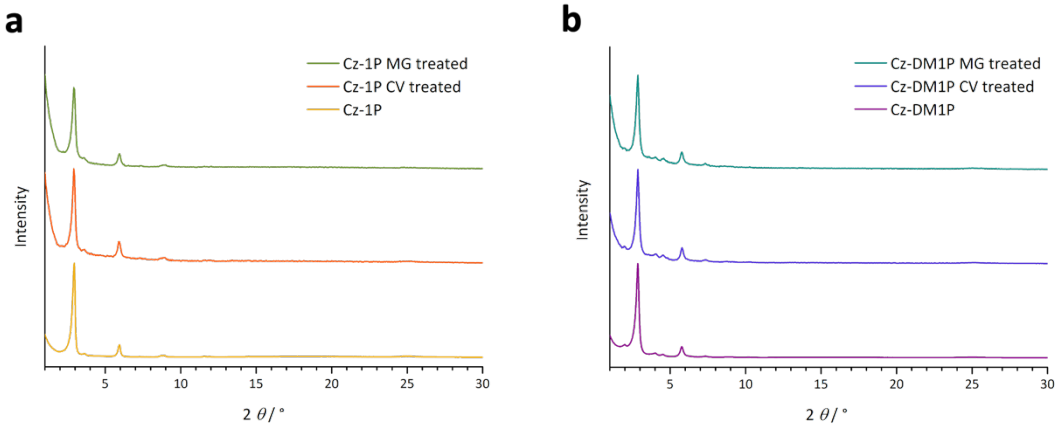

Figure S5.8. PXRD patterns of the **(a)** Cz-1P COF and **(b)** Cz-DM1P COF before **(bottom)** and after a 24 hour treatment with 0.1 mmol L^{-1} crystal violet solution **(middle)**, and 0.1 mmol L^{-1} malachite green solution **(top)** in water at room temperature. After the treatment, the COF powders were washed with ethanol three times and dried at 60°C for 3 hours. All patterns exhibit distinct reflections, indicating that the COFs' crystallinity is maintained throughout and after the treatment and confirming the high stability of the materials.

Linear calibration curves

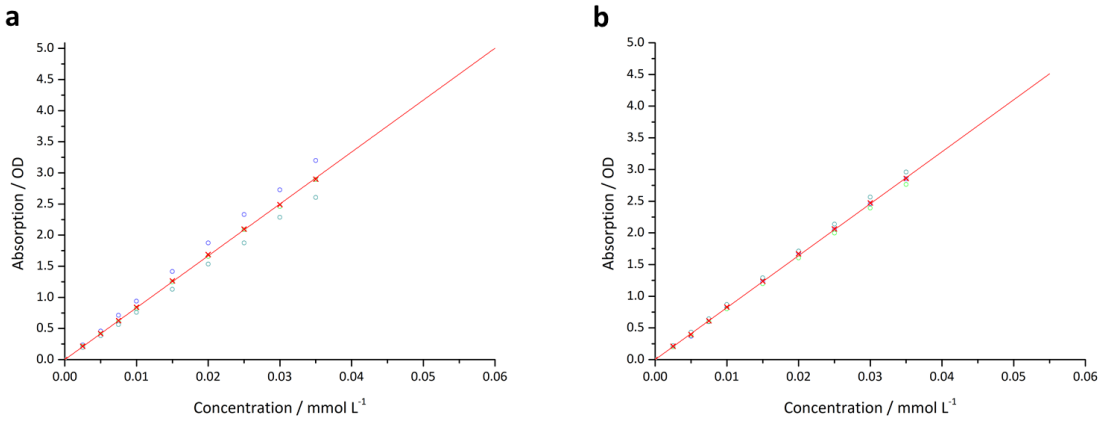

Figure S5.9. Linear calibration curves of **(a)** aqueous crystal violet solutions and **(b)** aqueous malachite green solutions, used for the determination of the concentration of COF-treated dye solutions.

Adsorption kinetics

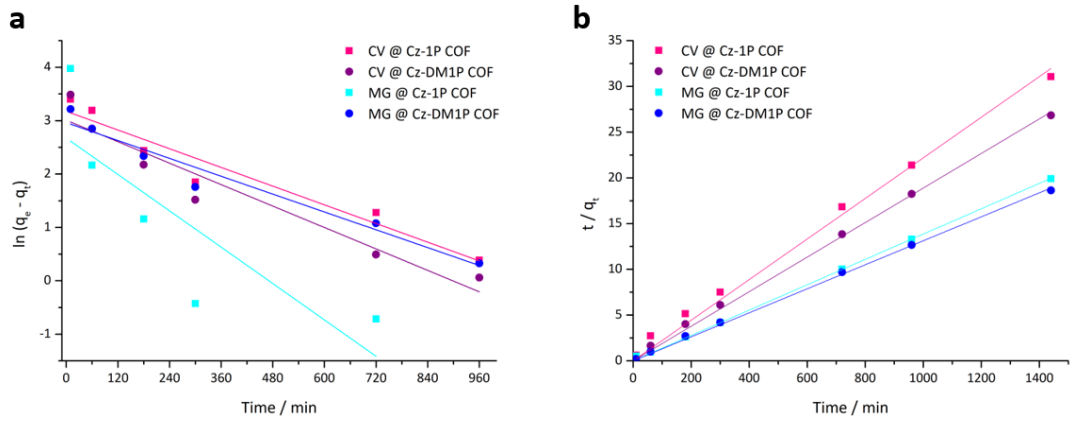

Figure S5.10. Adsorption kinetics plots of the time-dependent adsorption data of the Cz-1P COF and the Cz-DM1P COF treated with crystal violet (CV) and malachite green (MG) respectively. **(a)** First-order adsorption plot. The linear fits do not match the plotted data. **(b)** Second-order adsorption plot, exhibiting a good agreement of the plotted data points with the respective linear fits.

Table S5.1. Summary of the values of the adsorption constant *k*, the R^2 values and the standard error values of the adsorption constant *k*, obtained from the adsorption kinetics plots (Figure S5.10).

	COF	*k* [g mg^{-1} min^{-1}]	R^2	Standard Error
First-order plot data	Cz-DM1P @ CV	-0.00292	0.92676	3.6428 * 10^{-4}
	Cz-1P @ CV	-0.00335	0.91131	4.62865 * 10^{-4}
	Cz-DM1P@ MG	-0.00279	0.94797	2.90355 * 10^{-4}
	Cz-1P @ MG	-0.00568	0.59340	0.00217
Second-order plot	Cz-DM1P @ CV	0.01889	0.99899	2.2683 * 10^{-4}
	Cz-1P @ CV	0.02219	0.99631	5.1022 * 10^{-4}
	Cz-DM1P@ MG	0.01386	0.99970	9.0350 * 10^{-5}
	Cz-1P @ MG	0.01312	0.99935	1.2680 * 10^{-4}

Comparison of COF adsorption capacities of different dyes

Table S5.2. Non-exclusive list of dye-adsorbing covalent organic frameworks.

Material	Dye	Adsorption capacity [mg g^{-1}]	Rate constant k_2 [g mg^{-1} min^{-1}]	Reference
TFPB-Pa-SO_3H TFPB-BDSA	Crystal violet	1559 1288	0.085 0.094	*New J. Chem.* **2022**, *46*, 22185-22194.[5]
COPN	Crystal violet Methylene blue	361 263	$0.0484 \cdot 10^{-2}$ $0.0395 \cdot 10^{-2}$	*Langmuir* **2022***, 38, 4310–4320.*[49]
Cz-DM1P Cz-1P	Crystal violet	311 141	0.02219 0.01889	This thesis
TzBBd	Crystal violet Brilliant green	307.7 276.1	9.86 7.10	*ACS Appl. Nano Mater.* **2019**, *2*, 7290-7298.[41]
Cage-COF-TP	Malachite green	1805	10.7	*ACS Appl. Mater. Interfaces* **2022**, *14*, 57180-57188.[44]
YCOF1 YCOF2	Malachite green	650 573	$0.1133 \cdot 10^{-4}$ $0.5666 \cdot 10^{-4}$	*New J. Chem.* **2023**,*47*, 19672-19678.[50]
COF-CNT	Malachite green Methyl orange	604 235	$4.32 \cdot 10^{-4}$ $2.34 \cdot 10^{-4}$	*J. Environ. Chem. Eng.* **2023***, 11,* 109890.[51]
Cz-DM1P Cz-1P	Malachite green	208 155	0.01312 0.01386	This thesis
BFTB-PyTA BFTB-BFTB BFTB-BCTA	Rhodamine B	2127 1854 1605	-	*J. Mater. Chem. A*, **2020**, *8*, 25148-25155.[52]
Ttba-TPDA	Rhodamine B	833	0.136	*Ind. Eng. Chem. Res*. **2020**, *59*, 8315-8322.[53]
BTA-BDSA	Methylene blue	1280	$6.58 \cdot 10^{-2}$	*New J. Chem.* **2022**, *35*, 17016-17025.[42]
COFZ1	Methylene blue Gentian violet	510 564	0.0103 0.0099	*Langmuir* **2023***, 39,* 16367–16373.[54]
TpPa-COOH	Methylene blue Safranine T	410 1135	-	*Chem. Eur. J.* **2021**, *27*, 2692-2698.[55]

Dye adsorption cycles

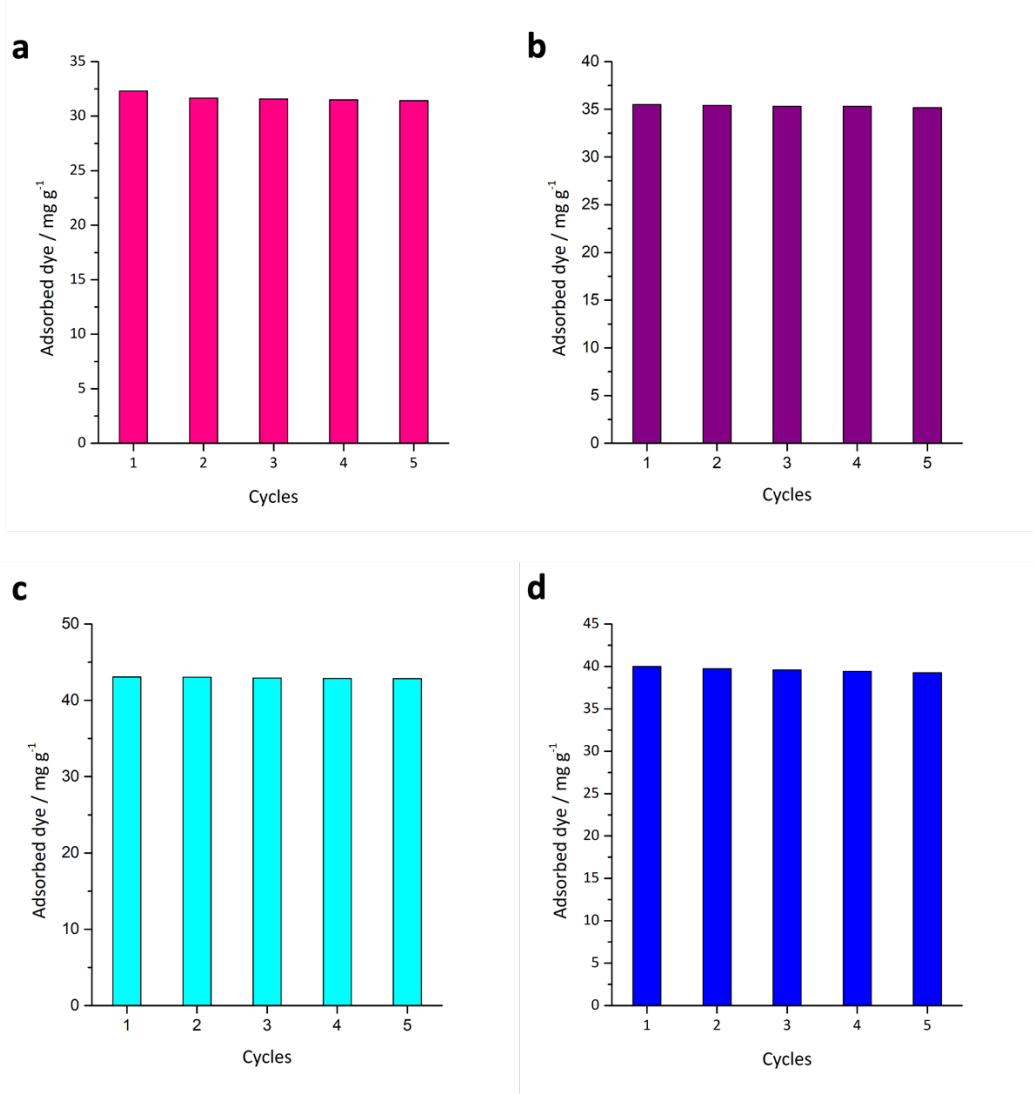

Figure S5.11. Adsorption cycles of 0.05 mmol L^1 crystal violet solutions treated with **(a)** Cz-1P COF and **(b)** Cz-DM1P COF; and 0.05 mmol L^1 malachite green solutions treated with **(c)** Cz-1P COF and **(d)** Cz-DM1P COF for five times respectively. Before a consecutive cycle, the COF powders were washed with EtOH for three times and dried at 60°C. All dye adsorption cycling experiments show excellent reusability of the COF powders with merely slight performance decreases of **(a)** 3%, **(b)** 1%, **(c)** 1% and **(d)** 2% after five adsorption cycles.

Adsorption efficiency

The adsorption efficiency *AE* was calculated according to the following equation:

$$\%AE = \frac{(C_0 - C)}{C_0} \times 100$$

with C_0 being the initial dye concentration and *C* the respective dye concentration in the filtrate after the COF treatment.

Table S5.3. Calculated adsorption efficiencies in per cent based on the dye adsorption capacity data.

Initial dye concentration [mmol L^{-1}]	**CV @ Cz-1P COF**	**MG @ Cz-1P COF**	**CV @ Cz-DM1P COF**	**MG @ Cz-DM1P COF**
0.01	100.0	100.0	100.0	100.0
0.03	97.5	100.0	99.7	95.8
0.06	71.8	92.9	82.7	83.1
0.1	62.8	82.6	59.6	72.9
0.2	34.5	43.9	67.5	66.1
0.4	24.4	24.5	51.9	41.1
0.8	19.8	19.3	47.3	26.1
1.0	17.3	16.7	38.1	22.4

5.7 References

1. Lellis, B.; Fávaro-Polonio, C. Z.; Pamphile, J. A.; Polonio, J. C., Effects of textile dyes on health and the environment and bioremediation potential of living organisms. *Biotechnol. Res. Innov.* **2019,** *3*, 275-290.
2. Okesola, B. O.; Smith, D. K., Applying low-molecular weight supramolecular gelators in an environmental setting – self-assembled gels as smart materials for pollutant removal. *Chem. Soc. Rev.* **2016,** *45*, 4226-4251.
3. Ye, J.; Jin, L.; Zhao, X.; Qian, X.; Dong, M., Superior adsorption performance of metal-organic-frameworks derived magnetic cobalt-embedded carbon microrods for triphenylmethane dyes. *J. Colloid Interface Sci.* **2019,** *536*, 483-492.
4. German-Federal-Institute-for-Risk-Assessment Malachite green identified as an environmental contaminant. https://www.bfr.bund.de/en/press_information/2007/17/malachite_green_identified_as_an_environmental_contaminant-10136.html (accessed 08.01.2024).
5. Zheng, W.; Li, A.; Wang, X.; Li, Z.; Zhao, B.; Wang, L.; Kan, W.; Sun, L.; Qi, X., Construction of hydrophilic covalent organic frameworks and their fast and efficient adsorption of cationic dyes from aqueous solution. *New J. Chem.* **2022,** *46*, 22185-22194.
6. Amirilargani, M.; Merlet, R. B.; Hedayati, P.; Nijmeijer, A.; Winnubst, L.; de Smet, L. C. P. M.; Sudhölter, E. J. R., MIL-53(Al) and NH2-MIL-53(Al) modified α-alumina membranes for efficient adsorption of dyes from organic solvents. *Chem. Comm.* **2019,** *55*, 4119-4122.
7. Wang, S.; Li, D.; Sun, C.; Yang, S.; Guan, Y.; He, H., Synthesis and characterization of g-C3N4/Ag3VO4 composites with significantly enhanced visible-light photocatalytic activity for triphenylmethane dye degradation. *Appl. Catal. B* **2014,** *144*, 885-892.
8. Sirés, I.; Guivarch, E.; Oturan, N.; Oturan, M. A., Efficient removal of triphenylmethane dyes from aqueous medium by in situ electrogenerated Fenton's reagent at carbon-felt cathode. *Chemosphere* **2008,** *72*, 592-600.
9. Abdel-Aziz, M. H.; Bassyouni, M.; Zoromba, M. S.; Alshehri, A. A., Removal of Dyes from Waste Solutions by Anodic Oxidation on an Array of Horizontal Graphite Rods Anodes. *Ind. Eng. Chem.* **2019,** *58*, 1004-1018.

10. Yang, G.; Zhang, D.; Zhu, G.; Zhou, T.; Song, M.; Qu, L.; Xiong, K.; Li, H., A Sm-MOF/GO nanocomposite membrane for efficient organic dye removal from wastewater. *RSC Adv.* **2020,** *10*, 8540-8547.
11. Kong, G.; Pang, J.; Tang, Y.; Fan, L.; Sun, H.; Wang, R.; Feng, S.; Feng, Y.; Fan, W.; Kang, W.; Guo, H.; Kang, Z.; Sun, D., Efficient dye nanofiltration of a graphene oxide membrane via combination with a covalent organic framework by hot pressing. *J. Mater. Chem. A* **2019,** *7*, 24301-24310.
12. Alsbaiee, A.; Smith, B. J.; Xiao, L.; Ling, Y.; Helbling, D. E.; Dichtel, W. R., Rapid removal of organic micropollutants from water by a porous β-cyclodextrin polymer. *Nature* **2016,** *529*, 190-194.
13. Karmakar, A.; Paul, A.; Santos, I. R. M.; Santos, P. M. R.; Sabatini, E. P.; Gurbanov, A. V.; Guedes da Silva, M. F. C.; Pombeiro, A. J. L., Highly Efficient Adsorptive Removal of Organic Dyes from Aqueous Solutions Using Polyaromatic Group-Containing Zn(II)-Based Coordination Polymers. *Cryst. Growth Des.* **2022,** *22*, 2248-2265.
14. Chen, S. H.; Yien Ting, A. S., Biodecolorization and biodegradation potential of recalcitrant triphenylmethane dyes by Coriolopsis sp. isolated from compost. *J. Environ. Manag.* **2015,** *150*, 274-280.
15. Alver, E.; Metin, A. Ü., Anionic dye removal from aqueous solutions using modified zeolite: Adsorption kinetics and isotherm studies. *Chem. Eng. J.* **2012,** *200-202*, 59-67.
16. Karadag, D.; Akgul, E.; Tok, S.; Erturk, F.; Kaya, M. A.; Turan, M., Basic and Reactive Dye Removal Using Natural and Modified Zeolites. *J. Chem. Eng. Data* **2007,** *52*, 2436-2441.
17. Völker, J.; Stapf, M.; Miehe, U.; Wagner, M., Systematic Review of Toxicity Removal by Advanced Wastewater Treatment Technologies via Ozonation and Activated Carbon. *Environ. Sci. Technol.* **2019,** *53*, 7215-7233.
18. Bhaumik, M.; Agarwal, S.; Gupta, V. K.; Maity, A., Enhanced removal of Cr(VI) from aqueous solutions using polypyrrole wrapped oxidized MWCNTs nanocomposites adsorbent. *J. Colloid Interface Sci.* **2016,** *470*, 257-267.
19. Madrakian, T.; Afkhami, A.; Ahmadi, M.; Bagheri, H., Removal of some cationic dyes from aqueous solutions using magnetic-modified multi-walled carbon nanotubes. *J. Hazard. Mater.* **2011,** *196*, 109-114.

20. Zhang, H.-J.; Wang, J.-H.; Zhang, Y.-H.; Hu, T.-L., Hollow porous organic polymer: High-performance adsorption for organic dye in aqueous solution. *J. Polym. Sci., Part A: Polym. Chem.* **2017,** *55*, 1329-1337.

21. Xu, T.; He, Y.; Qin, Y.; Zhao, C.; Peng, C.; Hu, J.; Liu, H., Facile preparation of porous organic copolymer based on triptycene and crown ether for efficient organic dye adsorption. *RSC Adv.* **2018,** *8*, 4963-4968.

22. Hasan, Z.; Jhung, S. H., Removal of hazardous organics from water using metal-organic frameworks (MOFs): Plausible mechanisms for selective adsorptions. *J. Hazard. Mater.* **2015,** *283*, 329-339.

23. Fu, H.-R.; Wang, N.; Qin, J.-H.; Han, M.-L.; Ma, L.-F.; Wang, F., Spatial confinement of a cationic MOF: a SC–SC approach for high capacity Cr(vi)-oxyanion capture in aqueous solution. *Chem. Comm.* **2018,** *54*, 11645-11648.

24. Keller, N.; Sick, T.; Bach, N. N.; Koszalkowski, A.; Rotter, J. M.; Medina, D. D.; Bein, T., Dibenzochrysene enables tightly controlled docking and stabilizes photoexcited states in dual-pore covalent organic frameworks. *Nanoscale* **2019,** *11*, 23338-23345.

25. Lohse, M. S.; Bein, T., Covalent Organic Frameworks: Structures, Synthesis and Application. *Adv. Funct. Mater.* **2018,** *28*, 1705553.

26. Wan, S.; Guo, J.; Kim, J.; Ihee, H.; Jiang, D., A Photoconductive Covalent Organic Framework: Self-Condensed Arene Cubes Composed of Eclipsed 2D Polypyrene Sheets for Photocurrent Generation. *Angew. Chem. Int. Ed.* **2009,** *48*, 5439-5442.

27. Bessinger, D.; Muggli, K.; Beetz, M.; Auras, F.; Bein, T., Fast-Switching Vis–IR Electrochromic Covalent Organic Frameworks. *J. Am. Chem. Soc.* **2021,** *143*, 7351-7357.

28. Wang, X.; Chen, L.; Y., C. S.; Little, M. A.; Wu, Y.; Zhu, W.-H.; Clowes, R.; Yan, Y.; Zwijnenburg, M. A.; Sprick, R. S.; Cooper, A. I., Sulfone-containing covalent organic frameworks for photocatalytic hydrogen evolution from water. *Nat. Chem.* **2018,** *10*, 1180-1189.

29. Yang, J.; Acharjya, A.; Ye, M.-Y.; Rabeah, J.; Li, S.; Kochovski, Z.; Youk, S.; Roeser, J.; Grüneberg, J.; Penschke, C.; Schwarze, M.; Wang, T.; Lu, Y.; van de Krol, R.; Oschatz, M.; Schomäcker, R.; Saalfrank, P.; Thomas, A., Protonated Imine-Linked Covalent Organic Frameworks for Photocatalytic Hydrogen Evolution. *Angew. Chem. Int. Ed.* **2021,** *60*, 19797-19803.

30. Ascherl, L.; Evans, E. W.; Gorman, J.; Orsborne, S.; Bessinger, D.; Bein, T.; Friend, R. H.; Auras, F., Perylene-Based Covalent Organic Frameworks for Acid Vapor Sensing. *J. Am. Chem. Soc.* **2019,** *141*, 15693-15699.

31. Jhulki, S.; Evans, A. M.; Hao, X.-L.; Cooper, M. W.; Feriante, C. H.; Leisen, J.; Li, H.; Lam, D.; Hersam, M. C.; Barlow, S.; Brédas, J.-L.; Dichtel, W. R.; Marder, S. R., Humidity Sensing through Reversible Isomerization of a Covalent Organic Framework. *J. Am. Chem. Soc.* **2020,** *142*, 783-791.

32. Sun, C.; Zhu, Y.; Shao, P.; Chen, L.; Huang, X.; Zhao, S.; Ma, D.; Jing, X.; Wang, B.; Feng, X., 2D Covalent Organic Framework for Water Harvesting with Fast Kinetics and Low Regeneration Temperature. *Angew. Chem. Int. Ed.* **2023,** *62*, e202217103.

33. Nguyen, H. L., Covalent Organic Frameworks for Atmospheric Water Harvesting. *Adv. Mater.* **2023,** *35*, 2300018.

34. Gilmanova, L.; Bon, V.; Shupletsov, L.; Pohl, D.; Rauche, M.; Brunner, E.; Kaskel, S., Chemically Stable Carbazole-Based Imine Covalent Organic Frameworks with Acidochromic Response for Humidity Control Applications. *J. Am. Chem. Soc.* **2021,** *143*, 18368-18373.

35. Muggli, K.; Spies, L.; Bessinger, D.; Auras, F.; Bein, T., Electrically Conductive Carbazole and Thienoisoindigo-Based COFs Showing Fast and Stable Electrochromism. *ACS Nanosci. Au* **2023,** *3*, 153-160.

36. Mohamad Yusop, M. F.; Abdullah, A. Z.; Ahmad, M. A., Malachite green dye adsorption by jackfruit based activated carbon: Optimization, mass transfer simulation and surface area prediction. *Diam. Relat. Mater.* **2023,** *136*, 109991.

37. Trieu, T. N. D.; Nguyen, N. T. T.; Nguyen, T. T. T.; Nguyen, D. T. C.; Tran, T. V., A comparative study on the malachite green dye adsorption of chemically synthesized and green MgFe2O4 nanoparticles using gerbera floral waste extract. *Environ Sci Pollut Res* **2023**.

38. Bardestani, R.; Patience, G. S.; Kaliaguine, S., Experimental methods in chemical engineering: specific surface area and pore size distribution measurements—BET, BJH, and DFT. *Can. J. Chem. Eng.* **2019,** *97*, 2781-2791.

39. Wang, S.; Jiang, L., Definition of Superhydrophobic States. *Adv. Mater.* **2007,** *19*, 3423-3424.

40. Tan, K. T.; Tao, S.; Huang, N.; Jiang, D., Water cluster in hydrophobic crystalline porous covalent organic frameworks. *Nat. Commun.* **2021,** *12*, 6747.

41. Li, Y.; Yang, C.-X.; Qian, H.-L.; Zhao, X.; Yan, X.-P., Carboxyl-Functionalized Covalent Organic Frameworks for the Adsorption and Removal of Triphenylmethane Dyes. *ACS Appl. Nano Mater.* **2019,** *2*, 7290-7298.

42. Li, L.; Li, A.; Zhao, B.; Kan, W.; Bi, C.; Zheng, W.; Wang, X.; Sun, L.; Wang, L.; Zhang, H., Multi-sulfonated functionalized hydrophilic covalent organic framework for highly efficient dye removal from real samples. *New J. Chem.* **2022,** *46*, 17016-17025.

43. Li, R.; Zhang, K.; Yang, X.; Xiao, R.; Xie, Y.; Tang, X.; Miao, G.; Fan, J.; Zhang, W.; Zheng, S.; Cai, S., Construction of a carboxyl-functionalized clover-like covalent organic framework for selective adsorption of organic dyes. *Separation and Purification Technology* **2024,** *340*, 126765.

44. Li, M.; Ma, J.; Pan, B.; Wang, J., Cage-Based Covalent Organic Framework for the Effective and Efficient Removal of Malachite Green from Wastewater. *ACS Appl. Mater. Interfaces* **2022,** *14*, 57180-57188.

45. Liu, J.; Li, G.; Yu, Y.; Zhou, X., Hierarchically porous covalent organic framework for adsorption and removal of triphenylmethane dyes. *Microporous and Mesoporous Materials* **2021,** *312*, 110703.

46. Wang, L.; Tao, Y.; Wang, J.; Tian, M.; Liu, S.; Quan, T.; Yang, L.; Wang, D.; Li, X.; Gao, D., A novel hydroxyl-riched covalent organic framework as an advanced adsorbent for the adsorption of anionic azo dyes. *Analytica Chimica Acta* **2022,** *1227*, 340329.

47. Ho, Y. S.; McKay, G., Sorption of dye from aqueous solution by peat. *Chem. Eng. J.* **1998,** *70*, 115-124.

48. Düren, T.; Millange, F.; Férey, G.; Walton, K. S.; Snurr, R. Q., Calculating Geometric Surface Areas as a Characterization Tool for Metal-Organic Frameworks. *J. Phys. Chem. C* **2007,** *111*, 15350-15356.

49. Anbazhagan, R.; Krishnamoorthi, R.; Thankachan, D.; Van Dinh, T. T.; Wang, C.-F.; Yang, J. M.; Chang, Y.-H.; Tsai, H.-C., Fluorine-Free Superhydrophobic Covalent-Organic-Polymer Nanosheet Coating for Selective Dye and Emulsion Separation. *Langmuir* **2022,** *38*, 4310-4320.

50. Liu, Y.-F.; Yang, L.; Shen, X.; Zhao, J.; He, Y.; Zou, R.-Y., Phenoxazine-based COFs for CO2/N2 separation and organic dye adsorption. *New J. Chem.* **2023,** *47*, 19672-19678.

51. Thakkar, H.; Bhatt, M.; Thakore, S., Barbituric acid derived covalent organic framework and its CNT composite as high-performance adsorbents for organic dye removal. *J. Environ. Chem. Eng.* **2023,** *11*, 109890.

52. El-Mahdy, A. F. M.; Zakaria, M. B.; Wang, H.-X.; Chen, T.; Yamauchi, Y.; Kuo, S.-W., Heteroporous bifluorenylidene-based covalent organic frameworks displaying exceptional dye adsorption behavior and high energy storage. *J. Mater. Chem. A* **2020,** *8*, 25148-25155.

53. Xu, T.; An, S.; Peng, C.; Hu, J.; Liu, H., Construction of Large-Pore Crystalline Covalent Organic Framework as High-Performance Adsorbent for Rhodamine B Dye Removal. *Ind. Eng. Chem.* **2020,** *59*, 8315-8322.

54. Zhao, J.; Shen, X.; Liu, Y.-F.; Zou, R.-Y., (3,3)-Connected Triazine-Based Covalent Organic Frameworks for Efficient CO2 Separation over N2 and Dye Adsorption. *Langmuir* **2023,** *39*, 16367-16373.

55. Dong, B.; Wang, W.-J.; Xi, S.-C.; Wang, D.-Y.; Wang, R., A Carboxyl-Functionalized Covalent Organic Framework Synthesized in a Deep Eutectic Solvent for Dye Adsorption. *Chem. Eur. J.* **2021,** *27*, 2692-2698.

6. Summary and Outlook

This thesis was focused on the development and investigations of novel functional covalent organic frameworks (COFs). The appropriate choice and thoughtful design of the organic building blocks used for the syntheses of these porous nanomaterials played a vital role for targeting specific needs and applications.

In the first project, two new organic building blocks based on the thienoisoindigo (TII) motif were developed by respectively fusing two thienothiophene (tt) or naphthalene (n) moieties on either side of the TII core, yielding the ttTII and nTII units. Electronically speaking, the electron-deficient TII core was extended by electron-rich moieties, generating a donor-acceptor-donor (D-A-D) design with an enhanced π-conjugation that is favorable for certain (opto-)electronic properties. These include improved charge carrier separation and migration properties and the band gap tunability enabling a broader optical absorption. Combining these two new building blocks with the well-established tetradentate pyrene (Py) node, respectively, yielded the pseudo-square Py-ttTII and Py-nTII COFs. Both materials exhibited high crystallinity and permanent porosity with large surface areas. Due to the D-A-D design of the (nearly) linear building blocks, the COFs featured very dark colors and showed a broad absorption in the UV-vis spectra, virtually covering the visible part of the electromagnetic spectrum. This broad absorption results from the characteristic intramolecular charge transfer (ICT) between the donor and acceptor parts of the building blocks, which narrows the band gap and leads to a redshift in the absorption.

The new Py-ttTII and Py-nTII COFs were successfully grown as oriented thin films on conducting substrates, allowing for their investigation as electrochromic materials. Both COFs exhibited a fully reversible electrochromism that is stable for more than 200 cycles. In comparison to three additional reference COFs (Py-TII, Py-TT, and Py-N; TII: thienoisoindigo, TT: thienothiophene, N: naphthalene) that were also tested regarding their electrochromic behavior, it could be shown that the Py-ttTII COF exhibits a superior electrochromic performance with absorption changes close to 3 OD, due to its targeted, deliberate building block design.

In addition, the electrochromic switching speeds of the new COFs were measured, showing very short time constants of up to 0.4 s for coloration and 0.2 s for decoloration,

outperforming many other electrochromic materials. Here, the planarity and rigidity of the COFs combined with their accessible pores that allow for a fast and free diffusion of charge-balancing counter ions in and out of the porous framework were identified as design guidelines for achieving a good and stable electrochromic performance. Finally, the high coloration efficiencies of up to 858 $cm^2\ C^{-1}$ emphasized the suitability of ttTII-based COFs for opto-electronic applications.

In the second project, the well-performing ttTII building block was used for the generation of further ttTII-based COFs. Here, the pyrene node was substituted by a novel tetradentate building block, based on two fused carbazole moieties. The biscarbazole (Cz) building block was synthesized in a four-step reaction by fusing two carbazole moieties *via* an inner phenyl ring, brominating the core, coupling protected aniline moieties to it, and unprotecting the molecule in a final step. Due to the incorporation of two electron-rich carbazole moieties, and a high planarity with the two carbazole moieties being nearly coplanar, the new Cz building block is well-suited for (opto-)electronic applications. Using this new building block and combining it with the ttTII unit, the Cz-ttTII COF with a rectangular geometry was successfully synthesized. To also vary the geometry of ttTII-based COFs, the hexagonal TAPB-ttTII COF was generated, using the well-established trigonal TAPB node. The new materials exhibited high crystallinity, high porosity, and large surface areas. Both COF powders featured dark colors and exhibited a broad vis-NIR absorption in the electromagnetic spectrum.
The Cz-ttTII and TAPB-ttTII COFs were successfully grown as oriented thin films on ITO substrates, and good vertical electrical conductivity values of up to $1.66 \times 10^{-3}\ S\ m^{-1}$ based on the oriented stacking of the COF layers and the resulting good electronic connectivity were measured. Furthermore, their electrochromic performance was investigated, showing a fully reversible redox behavior with strong absorption changes and high coloration efficiencies. Cycling tests with 200 cycles showed the good stability of these redox-active materials, with short switching times for coloration/decoloration as fast as 0.75 s/0.37 s for the Cz-ttTII COF and 0.61 s/0.29 s for the TAPB- ttTII COF, demonstrating the versatility of the ttTII building block in a variety of different covalent organic frameworks and its suitability for (opto-)-electronic applications.

In the third project, the significance for targeted COF design using a pore modification strategy for specific application purposes was demonstrated. The biscarbazole (Cz) building block was used for the generation of two structurally similar COFs, by combining it with terephthalaldehyde (1P) and 2,5-dimethoxy terephthalaldehyde (DM1P), yielding the Cz-1P and Cz-DM1P COFs. Both materials exhibit high crystallinity, permanent porosity, and a large surface area. The incorporation of dimethoxy moieties into the porous framework of the Cz-DM1P COF alters the wetting properties of this material by adding additional polar sites, which was demonstrated using water contact angle (WCA) measurements. Here, the Cz-1P COF exhibited a WCA of 168°, corresponding to a superhydrophobic surface, whilst the Cz-DM1P COF was somewhat more hydrophilic with a WCA of 142°, overall representing a hydrophobic material. Water vapor sorption analyses confirmed these findings, with the Cz-DM1P COF exhibiting a higher water uptake capacity than the Cz-1P COF. Both materials were investigated regarding their dye adsorption performance for aqueous solutions of two organic triphenylmethane dyes, crystal violet and malachite green. The Cz-DM1P COF showed an overall superior adsorption capacity for both dyes, due to enhanced guest molecule-pore wall interactions. Both materials exhibited very good adsorption efficiencies above 90 and even up to 100 % for samples with lower initial concentration. Again, the Cz-DM1P COF also showed superior efficiency for higher concentration samples, which is attributed to its pore modification. Dye adsorption cycling experiments confirmed a good reusability of the COF powders with only minor performance losses after five consecutive cycles. Furthermore, adsorption kinetics investigations showed a pseudo-second order adsorption behavior, underlining the importance of adsorbent-adsorbate interactions for the adsorption process. Thus, targeted pore size and surface engineering is of key importance for improved dye adsorption performance, as shown by the incorporation of dimethoxy side chains in the Cz-DM1P COF. Here, further optimization of the COF structure and the choice of appropriate side chains to allow for an ideal dye solution flux in and out of the pores, whilst achieving efficient interactions between the guest molecules and the COF pore walls remains a challenge for future research.

In conclusion, this thesis illustrates the many design options and the great potential of covalent organic frameworks defined by the principle of reticular chemistry underlying their synthesis. The possibility to design new tailor-made building blocks according to specific needs

was shown to be of great benefit for the generation of redox-active and electrically conductive COFs. Engineering the porous framework of these materials also offers opportunities for specific adsorption applications. The virtually unlimited number of possible building block designs and combinations and therefore of COF architectures offer the opportunity to generate materials tailored for many different future applications.

7. Publications and Presentations

7.1 Publications

1. Electrically conductive carbazole and thienoisoindigo-based COFs showing fast and stable electrochromism

   Katharina Muggli, Laura Spies, Derya Bessinger, Florian Auras, and Thomas Bein*
   ACS Nanoscience Au. **2023**, *3*, 153-160.

2. Fast-Switching Vis–IR Electrochromic Covalent Organic Frameworks

   Derya Bessinger, Katharina Muggli, Michael Beetz, Florian Auras*****, and Thomas Bein*****
   J. Am. Chem. Soc. **2021**, *143*, 7351-7357.

3. A Flavin-inspired Covalent Organic Framework for Photocatalytic Alcohol Oxidation

   Stefan Trenker, Lars Grunenberg, Tanmay Banerjee, Gökcen Savasci, Laura Poller, Katharina Muggli, Frederik Haase, Christian Ochsenfeld, and Bettina Lotsch*
   Chem. Sci. **2021**, *12*, 15143-15150.

4. Investigations of Croconic Acid in Superacidic Media

   Manuel Schickinger, Christoph Jessen, Yvonne Morgenstern, Katharina Muggli, Florian Zischka, Andreas Kornath*
   Eur. J. Org. Chem. **2018**, 6223-6229.

7.2 Oral and Poster Presentations

- International Conference on Metal-Organic Frameworks 2022
  Poster Presentation

- Deutsche Zeolith Tagung 2023
  Oral Presentation

- European Conference on Metal-Organic Frameworks 2023
  Poster Presentation